

MARSQUITO: Final Report

Mars Atmospheric Reconnaissance, Soil Acquisition, Imaging, and Terrain Observation

Course Code: AE3200

DSE Group 27

Delft University of Technology



MARSQUITO: Final Report

Mars Atmospheric Reconnaissance, Soil Acquisition, Imaging, and Terrain Observation

by

DSE Group 27

Student Name	Student Number
Rafaël Beckers	4854446
Irmak Çavdar	4782364
Tobias de Jong	4863763
Matthias Mandl	4789903
Rónán McIntyre	4865529
Crina Mihalache	4827333
Nigel van Nierop	4868722
Pim Ottenhoff	4675843
Aman Singhvi	4772059
Roy Vorster	4556720

Instructors: Sander van Zuijlen, Ferry Schrijer, Stefano di Mascio
Teaching Assistant: Anique Altena
Institution: Delft University of Technology
Place: Faculty of Aerospace Engineering, Delft
Project Duration: April 2021 - June 2021

Executive Summary

The purpose of this report is to design and iterate all the subsystems of a drone for Mars exploration. Based on a design option analysis and trade-off, the vehicle is designed to be a VTOL tilt rotor. The mission need statement is: *Enable large-scale targeted exploration of the atmosphere and surface of currently inaccessible areas of Mars.* This mission statement resulted in two expedition types: collect and return expeditions in which soil samples are collected, and remote sensing expeditions where visual mapping, height mapping, gas analyzing and dust composition data is collected and. The project objective statement is: *Design a semi-autonomous unpiloted atmospheric vehicle that can assist human Martian exploration by observing remote areas and collecting atmosphere and soil samples from difficult-to-reach places. This design will be performed by 10 students in 10 weeks.*

Before developing each separate subsystem a final sizing process was carried out to provide the layout and dimensions of the final design. This skeleton was then built on and the final design is displayed below:

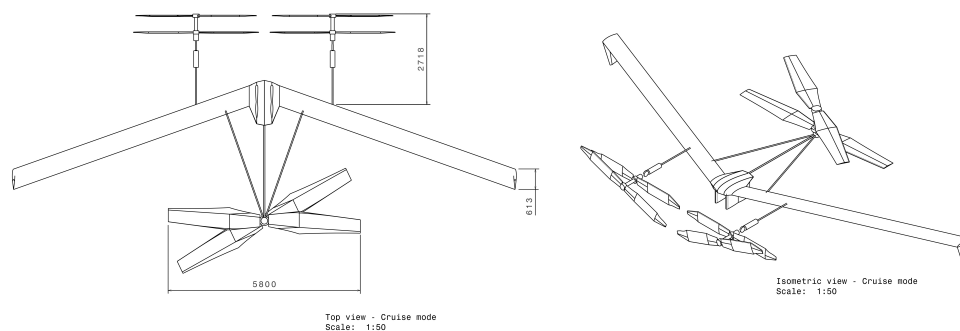


Figure 1: Multi-view technical drawings of external layout of the design (dimensions in millimeters)

The payload subsystem is at the heart of the design as it houses the instruments required to collect data on the Martian environment. For each top-level requirement a model was made to ensure the instruments chosen were capable of performing the required measurements in flight. The payload was split into two parts being the collect and return part and the remote sensing part. For the first part a model was made to size a sample collection robotic arm with an ultrasonic coring tool attachment. It was also determined how long collection would take. The results were a 9.5 [kg] arm with two cylinders of length 0.4 [m] and collection times of 30 minutes per 20 [g] sample for the hardest rock on Mars which is Basalt rock. For remote sensing a number of instruments were selected such as cameras, a ground penetrating radar and a gas analyzer thus completing all the top level requirements.

The flight operations subsystem ensures that the UAV is capable of performing autonomous and human controlled flights. It also covered procedures with respect to take-off, landing, safety and emergency situations essential for the proper functioning of the aircraft. The autonomy system consists of an inertial measuring unit and cameras to determine position and attitude, a laser altimeter for height measurements, a laser sensor for airspeed, a thermometer to measure air temperature and extensive computer hardware to process all the data inputs.

The communications subsystem ensures that the UAV can communicate with the base for control command and data transfers. Three scenarios were modelled which were a network of beacons, a single beacon at the base and a network of beacons in combination with a satellite. Based on the selection of communication strategy a model was made to analyze the beacon coverage based on the location and height of each beacon. The result was that using a network of beacons would be the most efficient strategy. If the UAV were flying at 100 [m], using two beacons away from the base 10 [m] off the ground results in 92% coverage in a 50 [km] radius from the base. The power usage of the beacons is covered by placing solar panels on the beacon tower. The beacon tower needs to be constructed by the astronauts however, due to its light weight structure does not pose issues.

The structures and materials subsystem ensure that the UAV does not fail under the loads that it experiences during the mission. It was one of the first subsystems to be addressed as it provides the skeleton to package the payload. A model was made to analyze the propeller carrying structure, main body structure and the wing box structure. For each model launch loads and operational load cases were analyzed. As a result of these analyses a structure was designed capable of withstanding critical load cases.

The aerodynamics subsystem was focused on producing sufficient lift during flight while also minimizing drag to be able to fly with minimal thrust. The components of the UAV taken into account when making a drag estimation were the wing, landing gear, vertical rotor, vertical rotor structure and forward propulsion structure originating from the structures subsystem. For the landing gear struts an airfoil selection was carried out instead of simply using cylinders to reduce the drag produced by these structures. This resulted in the RAF MOD 30 airfoil being used. The

largest part of this subsystem is however the wing sizing which depends on aerodynamics, structures and flight stability. Taking into account aspects the Reynolds number, wing geometry, surface areas, twist and dihedral the aerodynamics polars of the final design were outputted. The maximum C_L was 1.28 with stall occurring after 9° . The trim angle of the aircraft in cruise was 6° .

The flight control and stability subsystem was focused on ensuring the stability and controlability of the drone. The landing and take-off maneuvers present a large risk to the drone as they occur at high velocities and close to the ground. The VTOL sequences were designed to ensure sufficient lift at all moment while minimizing the energy requirement for these operations. The elevon sizing resulted in elevons which take up 27% of the chord and have a length of 2 [m] on each side of the wing.

The power subsystem provides the necessary electrical power all the subsystems of the drone. Power is generated on board using solar cells for which a model was made based on the amount of solar power that could be salvaged on Mars. Based on this 1.26 [m²] of solar panel were required with a mass of 0.63 [kg] and producing 146.58 [Ah]. To store the power lithium ion batteries were selected as they are rechargeable. The total energy they can store is 4659 [Wh] with a capacity of 194 [Ah] and a mass of 16.64 [kg]. The next decision made for the power subsystem was its placement as this played a significant role in ensuring longitudinal stability. The battery is divided into two arrays and placed in either wing. Lastly, the power management and distribution strategy was designed. A source controller is used as the solar panels do not provide direct energy to the components but simply charge the batteries. A storage controller is used to regulate battery charging. An output controller ensures that powerlines with the correct current and voltage reach the instruments.

The propulsion subsystem ensures that the UAV has sufficient thrust in the forward and vertical directions staying within the limits of the power subsystem. Analysis was done on the main parameters that influence rotor design which were the chord, taper and revolutions per minute. Based on these QBlade was used to optimize the forward and tilt rotor. The challenge was that they both require different optimization techniques. It was concluded that the vertical rotor would be a co-axial bi-rotor to achieve the required performance. The results of this analysis were that the tilt rotor cruise thrust is 17.5 [N] with an efficiency of 74%, the tilt rotor hover thrust is 55.2 [N] with an efficiency of 50.6% and the vertical rotor hover thrust is 122 [N] with an efficiency of 53.8%. During VTOL each forward propeller requires 2200 [W] and each rear propeller requires 2311 [W]. During cruise, one forward propeller requires 2400 [W]. Based on these values a brushless DC motor was selected for propulsion with an optimum efficiency torque of 34.27 [Nm] and an RPM between 1500 and 3000.

The thermal control system has one requirement and that is: to keep the temperature of all the subsystems within their operational ranges during expeditions. This was the last consideration as it required a lot of design decisions to be finalized before it was designed. The biggest consideration when making a model for the thermal controller was the temperature range in the Hellas Planitia from -96 to 0°C . The heat contributions taken into account were radiation, conduction between components and convection between the gases in the atmosphere and components. The model is based on a heat balance equation taking each instrument as a thermal node and making a network from this. Based on this balance it was determined which components needed thermal finishing and insulation. For the motors a separate thermal analysis was also done which resulted in a radiator being required to prevent overheating. Lastly, a thermal analysis was done for the batteries which resulted in no active heat control being required.

Having designed all the subsystems the final system had to be verified and validated to ensure it was built right and the right system was built. Each individual subsystem model was verified using a range of unit and system tests. To model the system the subsystem models were integrated. To verify the system only the iterative loop that uses all the verified inputs needed to be checked. This was done using a convergence test for the total mass of the design. For product verification a method of testing, analyzing, demonstrating or inspecting the vehicle for each top level requirement was devised and for production validation tests were devised to to check the integration of the final system.

To conclude, the goal of this report was to design the subsystems of a drone for Mars exploration proving its feasibility. The result of this can be seen in Figure 1 where the integration of all these separate subsystems results in a single product.

A number of main recommendations for future research have been identified as vital to the design. To improve the aerodynamic, controllability and propulsion analysis, Computational Fluid Dynamics simulations or wind tunnel tests should be performed for a better understanding of the stall characteristics. For structures a Finite Element Analysis should be done on the entire structure, furthermore, more failure cases can be identified and analyzed, for example where one propeller breaks off. For communication a detailed analysis of the beacon network could have been performed by creating a numerical model that considers the limitations due to surface characteristics. The thermal analysis consists of separate analyses and only takes convection into account once. Integrating these analyses and analysing convection would lead to more realistic results. For improved power analysis, the degradation of the solar and battery cells has to be accounted for. The orientation of the drone during charging can be analysed for optimum solar incidence angle.

Contents

Executive Summary	i
Nomenclature	v
1 Introduction	1
2 Project Overview	2
2.1 Mission Background	2
2.2 Literature Review	2
2.3 Sustainability Strategy	3
2.4 Design Concept Generation	5
2.5 Trade-Off and Selected Design	6
3 Market Analysis	8
3.1 Stakeholder Identification	8
3.2 The Future Space Market	9
3.3 Establishing of New Markets	9
3.4 Foreseeable Share in New Markets	9
3.5 Cost Analysis	10
4 Resource Analysis and Budget Breakdown	11
5 Mission Analysis	13
5.1 Functional Flow Diagram	13
5.2 Functional Breakdown Diagram	13
5.3 Expedition Profiles	13
5.4 Altitude Considerations	15
5.5 Assumptions About the Mars Base	15
6 Final Sizing Process	17
6.1 Layout of the Design	17
6.2 Sizing Methodology	17
7 Payload Analysis	20
7.1 Requirements	20
7.2 Model and Analysis	21
7.3 Layout	24
7.4 Risk Analysis	25
7.5 Verification and Validation	26
8 Flight Operations Analysis	28
8.1 Requirements	28
8.2 Autonomy System	28
8.3 Human Remote Control	33
8.4 Onboard Computer	34
8.5 Layout	34
8.6 Procedures	36
8.7 Risk Analysis	37
9 Communications Analysis	39
9.1 Requirements	39
9.2 Model and Analysis	39
9.3 Risk Analysis	43
9.4 Communication Flow Diagram	44
9.5 Verification and Validation	44
10 Structures and Materials Analysis	47
10.1 Requirements	47
10.2 Layout	47
10.3 Model and Analysis	48
10.4 Risk Analysis	54
10.5 Verification and Validation	55
10.6 Validation Strategy	56
11 Aerodynamic Analysis	57
11.1 Requirements	57
11.2 Drag	57
11.3 Aerodynamic Model	58
11.4 Wing Sizing	59
11.5 Layout	60
11.6 Risk Analysis	60

11.7 Verification and Validation	61
12 Flight Control, Stability, and Performance Analysis	62
12.1 Requirements	62
12.2 Model and Analysis	62
12.3 Risk Analysis	76
12.4 Verification and Validation	77
13 Propulsion Analysis	78
13.1 Requirements	78
13.2 Model and Analysis	78
13.3 Performance Analysis and Sizing	81
13.4 Layout	87
13.5 Risk Analysis	87
13.6 Verification and Validation	88
14 Power Analysis	89
14.1 Requirements and Constraints	89
14.2 Model and Analysis	89
14.3 Risk Analysis	94
14.4 Layout	95
14.5 Verification and Validation	96
15 Thermal Control Analysis	97
15.1 Requirements	97
15.2 Model and Analysis	97
15.3 Risk Analysis	104
15.4 Verification and Validation	104
16 Ground Operations and Logistics Description	106
16.1 Requirements	106
16.2 Earth Operations (Prior to Operational Life)	106
16.3 Mars Operations (Prior to Operational Life)	107
16.4 Ground Equipment	108
16.5 Storage	108
16.6 Ground Transportability	109
16.7 Expedition Procedures	109
16.8 Inspection, Maintenance, and Repair	109
16.9 Earth Operations (During Operational Life)	110
16.10End of Life Operations	110
17 System Description	111
17.1 Final Configuration	111
17.2 Hardware Block Diagram	112
17.3 Software Block Diagram	113
17.4 Technical Drawings	113
17.5 Data Handling Block Diagram	114
18 Analysis of the Final Design	115
18.1 Sensitivity Analysis	115
18.2 RAMS Analysis	116
18.3 Risk Analysis	118
18.4 Sustainability Analysis	120
19 System Verification and Validation	122
19.1 Verification of Subsystem Code Modules Integration	122
19.2 Compliance Matrix and Feasibility Analysis	122
19.3 Product Validation	124
20 Project Design and Development	126
20.1 Project Design and Development Logic	126
20.2 Project Gantt Chart	127
20.3 Production Plan	127
20.4 Cost Breakdown Structure	127
20.5 Cost Analysis of Different Components	129
20.6 Fiscal Year	131
20.7 Margins	132
20.8 Total Costs	132
21 Conclusion	133
A Appendix	140

Nomenclature

Abbreviation	Definition	Abbreviation	Definition
AU	Astronomical Unit	OBC	Onboard Computer
BOL	Beginning of Life	ROP	Rate of Penetration
BEM	Blade Element Momentum	SRV	Surface Rover Vehicle
EOL	End of Life	UAV	Unpiloted Atmospheric Vehicle
FOV	Field of View	USD	United States Dollars
FY	Fiscal Year	VIO	Visual-Inertial Odometry
GPR	Ground Penetrating Radar	WOB	Weight on Bit
IMU	Inertial Measurement Unit	XTE-LILT	XTJ Targeted Environment - Low Intensity Low Temperature
ISA	International Standard Atmosphere		

Symbol	Definition	Unit
A	Surface area	[m ²]
C_a	Abrasive particle concentration on drill	[-]
C_P	Power coefficient	[-]
C_{P_i}	Induced power coefficient	[-]
C_{P_o}	Profile power coefficient	[-]
C_T	Thrust coefficient	[-]
D_{avg}	Average diameter of coring tool	[m]
d	Depth of GPR penetration	[m]
E	Young's Modulus	[GPa]
F	Load	[N]
G_2	Rate of penetration constant	[-]
G_b	Direct beam irradiance at Mars surface	[W/m ²]
G_{ob}	Beam irradiance at the top of Mars atmosphere	[W/m ²]
g	Gravitational acceleration	[m/s ²]
H_v	Vickers hardness	[Pa]
h	Convection heat transfer coefficient	[W/(m ² K)]
I	Moment of inertia	[m ⁴]
K	Column effective length factor	[-]
K	Permittivity of material	[A]
K_{IC}	Fracture toughness	[Pa m ^{0.5}]
L	Length	[m]
L_s	Aerocentric latitude	[°]
M	Moment	[Nm]
P	Required power	[W]
P_i	Induced power	[W]
P_o	Profile power	[W]
r	Ground resolution	[m]
S	Speed of the drill bit	[s ⁻¹]
S_a	Abrasive particle size on drill	[m]
t	Thickness	[m]
V	Velocity	[m/s]
v	Deflection	[m]
ν	Poisson ratio	[-]
z	Zenith angle	[°]
β	Scattering limit GPR	[°]
δ	Declination Angle	[°]
ρ	Density	[kg/m ³]
σ	Stress	[MPa]
σ	Stefan-Boltzmann constant	[W/(m ² K ⁴)]
τ	Shear	[MPa]
τ	Optical Depth	[-]
ϕ	Latitude	[°]

1 Introduction

The search for extraterrestrial life has consistently pushed technology to its limits over the past decades. As the search for life beyond Earth carries on, the technology being used to do so continues to advance with leaps and bounds. One of the planets that is of most interest is Mars, due to the presence of water in the soil and the relatively favorable conditions. A number of successful Mars rover missions have already been carried out which have explored the surface, but after human missions have landed on Mars and a base has been established, the next paradigm shift in exploration capabilities is to use a flying vehicle to quickly scout large areas near the base in great detail. The challenge that this poses is immense, since the Martian atmosphere is extremely thin compared to Earth's and the environment is harsher in many ways, including large temperature fluctuations, damaging solar radiation, and fine dust particles. The importance of overcoming these obstacles is of interest when considering the possibilities of future homes for mankind. As human missions to Mars are already planned for the mid 2030s, doing more extensive research is necessary.

The aim of this report is to develop the design of a semi-autonomous unpiloted atmospheric vehicle (UAV) and to integrate all the main subsystems to prove its feasibility. Based on the trade-off of potential design concept options completed in the previous report, the starting point for this report is a VTOL Tilt Rotor concept. To fulfil this aim, extensive research and design work is carried out for the ten most important subsystems, with the customer's requirements serving as the basis for all design decisions made. Based on this research, models are made and analyses are carried out on each subsystem to develop the initial concept into a full design. After this, a risk analysis is carried out and the models made are verified and validated to ensure that the results are reliable.

The report is structured as follows: first, a summary is given of the three reports which detailed the design process prior to this report. After this, a market analysis is presented to establish the cost and volume of the market for such a vehicle. Then a budget breakdown is shown to set boundaries for the amount of power, mass, and volume that can be used. The next chapter is a mission analysis to better understand what the functionalities of the vehicle must be. After this, the overall sizing methodology is explained, setting up the general framework into which the ten individual subsystems can fit. Once all of the subsystems are designed and explained in detail, the final integrated system is presented. This is followed by an analysis of the final design as a whole, and system-level verification and validation. The final chapter looks at the future outlook and prospects of the project from a manufacturing point of view and also an organizational point of view. A conclusion then summarizes the main findings from the report and the lessons learnt throughout the design process.

2 Project Overview

The purpose of this chapter is to give an overview of the project and the work that has been completed prior to this report. For more detail on any of this work, please refer to the Project Plan [3], Baseline Report [1], and/or Midterm Report [2]. First, the background of the mission is described in Section 2.1, including the purpose statements of the mission. This is followed by a description of the operational conditions and comparable past mission in Section 2.2. The sustainability strategy is discussed in Section 2.3. In Section 2.4, the different design concepts are given, leading to a summary of the trade-off in Section 2.5, where the final design choice is presented.

2.1 Mission Background

The first human missions to Mars are planned for the around the mid 2030s. Once a base is established on the surface, it would be of great scientific value if a semi-autonomous UAV could fly to areas of interest in the vicinity of the base to explore and take measurements. Such a vehicle could take high resolution images, make detailed height maps, analyze atmospheric gas and dust particle composition, detect the presence of underground ice, and even collect soil samples to take back to the base for analysis. An aerial vehicle would be advantageous because rover vehicles are slow-moving and limited by rough terrain. Satellites are capable of imaging and height mapping, but not to the same level of resolution as an aircraft. Furthermore, satellites are not capable of in-situ measurements of gas and dust, nor can they collect soil samples. Thus, the purpose of this project is to design a UAV to assist with the exploration of the areas surrounding a Mars base.

2.1.1 Purpose Statements

The statements below were devised to solidify the goals and purposes of the project. All steps and decisions in the design process are in service of achieving what is set out in these statements.

Mission Need Statement:

Enable large-scale targeted exploration of the atmosphere and surface of currently inaccessible areas of Mars.

Project Objective Statement:

Design a semi-autonomous unpiloted atmospheric vehicle that can assist human Martian exploration by observing remote areas and collecting atmosphere and soil samples from difficult-to-reach places. This design will be performed by 10 students in 10 weeks.

2.1.2 Customer Requirements

The task at hand comes with some requirements as specified by the customer. These lay out the scientific capabilities which the drone must possess, as well as setting some minimum values for performance. Some of the most important requirements which drive the design include needing to be able to carry out expeditions in which the drone can:

- Perform semi-autonomous remote sensing of areas of 50 [km²] up to 50 [km] from the base. This includes:
 - Visual imaging at 10 [cm] ground resolution
 - Height mapping at 10 [cm] ground and height resolution
 - Shallow ground ice deposit detection at 10 [m] depth
 - Dust composition and particle size measurements
 - Atmospheric gas proportion measurements
- Perform (subsurface) soil sample collect-and-return missions. The requirements for this depend on whether the expedition is semi-autonomous or remotely piloted by a human.
 - Semi-autonomous: up to 50 [km] from the base, soil sample of 0.1 [kg], between -1 and +2 [km] height relative to base elevation
 - Human remote control: up to 10 [km] from the base, soil sample of 0.5 [kg], between -2 and +4 [km] height relative to base elevation

The full set of these top-level requirements can be found in Table 19.1. In the Baseline Report, a larger set of lower-level or subsystem requirements were developed to guide the design of more specific aspects of the mission. These can be found in compliance matrices in their respective subsystem chapters throughout this report.

2.2 Literature Review

The goal of the literature study was to better understand the environmental conditions on Mars and to better understand the mission as a whole. In addition, past missions and studies were identified which could be used as references for the design of the vehicle.

2.2.1 Operational Conditions

The Martian environment presents unique challenges which make flight a much more difficult task than on Earth. For the purposes of some initial calculations, the location of the Mars base was taken to be in Hellas Planitia, an

area within the impact basin Hellas in Mars' southern hemisphere. This places the base at about -5.5 [km] elevation with respect to the Martian vertical datum and at a latitude of 40° south.

The "air" in Mars' atmosphere is mostly composed of carbon dioxide and has a surface pressure of about 700 [Pa] at the vertical datum, only 0.7% of sea-level pressure on Earth. The surface air density is 0.015 [kg/m³] and surface air temperature is 242 [K] on average [87]. Wind speeds are generally in the range of 0-10 [m/s]; wind speeds up to 32 [m/s] have been observed during dust storms [163]. Dust storms are a significant threat to the mission, due to potential damage from the dust's abrasive properties [89]. At the assumed base location, the conditions are slightly more favourable to flight, with an air density of 0.024 [kg/m³]. The speed of sound is 20% lower than on Earth, which limits the maximum speed of propellers if transonic tip speeds are to be avoided.

The gravitational acceleration on Mars is 3.72 [m/s²] (38% of sea-level gravitational acceleration on Earth). This leads to high-extending dust storms and causes dust to be suspended in the atmosphere for longer periods of time. However, it also provides an advantage since less lift is required for the same mass and structures can be made lighter.

Since Mars is further away from the Sun than Earth, it receives less solar irradiance: around 590 [W/m²] compared to Earth's ~1360 [W/m²]. Solar irradiance can drop further in the event of dust storms [91]. Due to the lack of a magnetic field and a dense atmosphere, dangerous solar radiation reaches Mars' surface. This is a hazard to humans and to sensitive components. Hellas Planitia has some of the lowest radiation levels on all of Mars [90], at about 0.1 [Sv/year] - this is roughly double the exposure astronauts experience on the ISS [133].

2.2.2 Past Missions

A variety of missions were considered as relevant for this literature study. One is a Mars mission and the other two are high altitude Earth designs which are representative of the options for lift generation and propulsion on Mars. These missions were later used as references to help in the sizing of the four design concepts.

The only successful powered flights on another planet have been performed by the Ingenuity helicopter, whose primary mission was to be a technology demonstration. It uses large lightweight contra-rotating coaxial rotors spinning at high rotational speeds to perform vertical take-offs and landings. It has a total mass of 1.8 [kg] and has no scientific payload.

The JP Aerospace Tandem high altitude airship has been able to fly up to an altitude of 29 [km] on Earth (where air density is 0.0214 [kg/m³]). Using its propellers, it is able to achieve a maximum speed of around 3 [m/s]. This proof-of-concept shows that it is not unrealistic to use a lighter than air solution to create lift in the thin Martian atmosphere. However, additional challenges arising from the Mars environment would include: wind speeds of up to 10 [m/s], low temperatures which can cause rubber to become brittle, and including a significant payload mass.

Helios HP01 is an extremely high altitude and high aspect ratio flying wing developed by AeroVironment. It has been able to attain a maximum altitude of 29.5 [km] on Earth (where air density is 0.0194 [kg/m³]). The design presents an inspiration for an optimized propeller design for low density and low Reynolds numbers. Additionally, it provides proof that generating lift with flying wings at these densities is realistic. The design has an empty mass of 600 [kg] and a maximum payload mass of 329 [kg].

2.3 Sustainability Strategy

The purpose of developing the sustainability strategy was to ensure that the mission will have a minimal negative impact on both the Earth environment and the Mars environment. By taking proper precautions and by devising appropriate requirements, sustainability was taken into account throughout the design process and any damages can be minimized.

The sustainability strategy was based upon a framework of 15 sustainability principles for engineering projects from [52]. This framework can be seen in Figure 2.1. The principles were situated based on their relation to the three pillars of sustainability: environment, society, and economy.

The mission was then split into stages, divided by time (from the design stage to the end of life) and location (Earth operations and Mars operations). For each stage, the most relevant principles were identified. An overview of this can be seen in Table 2.1.

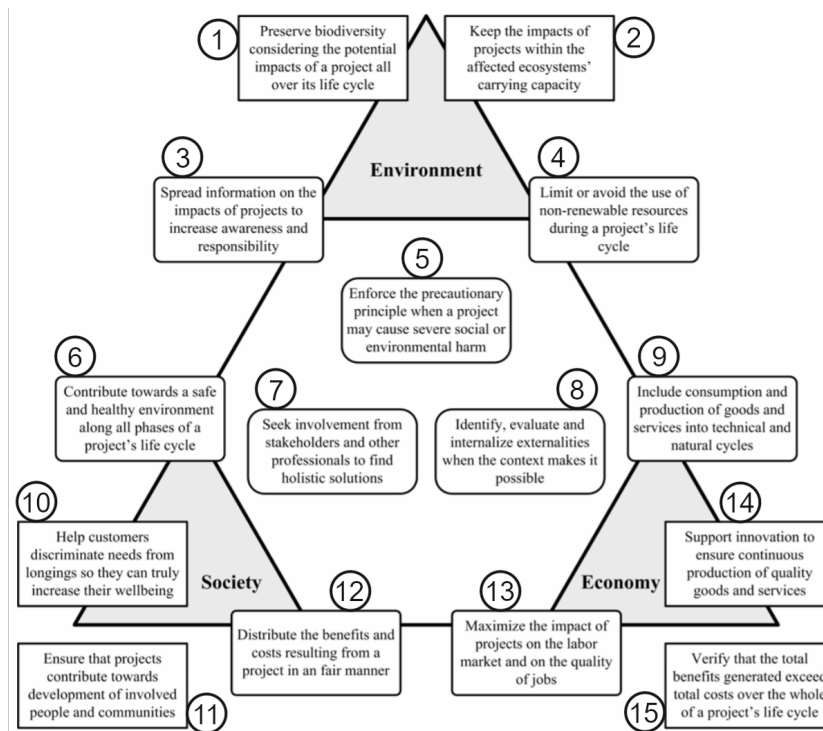


Figure 2.1: Triangle of sustainable engineering principles compiled by Gagnon, Leduc, and Savard in 2008 [52], with number labels added for referencing

Table 2.1: Division of mission into stages and the relevant sustainability aspects for each stage

Stage	Earth	Mars
1. Design	1E	1M
	(4) Using green energy/transportation, etc. (7) Consulting experts about design, close communication with customer (14) Taking innovative ideas into account when designing (15) Comparing expected benefits of mission to estimated costs	-
2. Production and testing	2E	2M
	(4) Using green energy/materials, etc. (6) Avoiding use of toxic/dangerous materials (9) Accounting for consumption of goods and services	-
3. Pre-launch, launch and journey to Mars	3E	3M
	(1) Sterilizing to prevent forward contamination	-
4. Arrival and assembly on Mars	4E	4M
	-	(1) Preventing forward contamination (6) Ensuring safety of Mars astronauts and their base
5. Operational life	5E	5M
	(3) Including info about impacts in social media, PR campaigns, etc. (12) Benefits (scientific data) should be made available to scientific personnel and institutions	(1) Preventing forward contamination (2) Some impacts are inevitable, but should be limited (4) Using renewable resources available on Mars (6) Ensuring safety of Mars astronauts and their base
6. End of life	6E	6M
	(12) Benefits (scientific data) should be made available to scientific personnel and institutions	(4) Using reusable equipment after EOL (6) Ensuring safety of Mars astronauts and their base

For the justifications and explanations of why certain principles are relevant to certain stages, please refer to the Baseline Report [1].

The sustainability strategy was implemented through the requirements which arose from it. By meeting these requirements, it could be guaranteed that all mission stages could be carried out in a sustainable manner. These requirements were created per stage and were based on the top-level sustainability requirements and the above sustainability analysis. They are listed below, with the relevant stage(s) and principle(s) given after in parentheses.

- DME-REQ-STN-01:** At least 15% of the materials used in the design (by mass) shall be from recycled sources. (Principle (4) in stage 2E)
- DME-REQ-STN-02:** The process of manufacturing the design shall not involve any toxic/hazardous processes which would endanger the production workers past the threshold set by local guidelines. (Principle (6) in stage 2E).
- DME-REQ-STN-03:** All parts, components, and peripheral equipment which are part of the design and which are to be delivered to Mars shall be sterilized on Earth before launch such that the entire UAV is restricted to a surface biological burden level of ≤ 30 spores. (Principle (1) in stage 3E).
- DME-REQ-STN-04:** Information about the sustainability risks and impacts of the mission shall be made publicly available via the mission website, media coverage, and social media posts. (Principle (3) in stage 5E).
- DME-REQ-STN-05:** The scientific data resulting from the mission shall be made available to scientists and scientific institutions for which this data is relevant to research. (Principle (12) in stages 5E and 6E).
- DME-REQ-STN-06:** During the operational phase, components of the UAV relating to soil collection shall be sterilized at the base such that these components are restricted to a surface biological burden level of ≤ 30 spores before they are used for soil collection purposes. (Principle (1) in stages 4M and 5M).
- DME-REQ-STN-07:** The design shall not leave behind any stray material on the Martian surface during mission operations. (Principle (2) in stage 5M).
- DME-REQ-STN-08:** It shall be possible for the operators on Mars to disassemble the UAV to access reusable components after end-of-life. (Principle (4) in stage 6M).
- DME-REQ-STN-09:** The instruments and sensors used on the UAV shall have expected minimum lifetimes of 2 years. (Principle (4) in stage 6M).
- DME-REQ-STN-10:** All parts, components, and spares needed to sustain the mission for 10 years shall be included in a single launch vehicle.

2.4 Design Concept Generation

In order to create feasible design concepts, inspiration was taken from the previously described past missions. First, design options were generated with the help of a design option tree. This tree was then systematically pruned: if a particular branch or design solution could not feasibly be used for this mission, it was eliminated. More details on this process can be found in the Baseline Report [1]. The options that were not eliminated are listed below.

- **Lift:** Fixed wing (conventional configuration or flying wing), gas balloon (dirigible).
- **Propulsion:** Fixed rotors, tilted rotors, cold gas thrusters, mono propellant.
- **Ascent and descent:** Externally powered launching and catching systems, not landing at all, vertical ascent/descent (fixed rotors or tilt rotors).
- **Control in flight:** Thrusters, rotors, aerodynamic control surfaces.
- **Power storage:** Batteries, fuel tank.
- **Soil collection:** Grabber, drill, scoop.
- **Storing soil samples:** Hanging under aircraft flying, store internally.
- **Site strategy:** Hover above site, drop/pick-up, vertical take-off/landing.
- **Power generation:** Nuclear energy (RTGs), solar panels, fuel cells.
- **Communication strategy:** Using satellites in Mars orbit, using central beacon at base, using beacon network.

From these remaining design options, four concepts were generated: a dirigible, a fixed rotor VTOL airplane, a tilt rotor VTOL airplane, and a STOL aircraft with a soil collection pod to be dropped and recovered in flight.

Dirigible Concept

The dirigible concept is a lighter-than-air design, meaning it could hover without a power source. Additionally, it was designed such that the payload would hang beneath the balloon so that the entire craft would not need to land for soil collection. However, the dirigible also has disadvantages. The use of a large envelope to store the lifting gas created significant risks. The most significant risk identified was the envelope rupturing. The large frontal area causes significant drag, meaning that this design would require a powerful propulsion system. A conceptual sketch of this concept can be seen in Figure 2.2a.

VTOL Fixed Rotor Concept

This concept uses dedicated vertical rotors to perform vertical take-offs and landings, separate horizontal rotors to generate thrust during flight, and a wing to generate lift during flight. Its estimated total mass is much lower than that of the dirigible concept. The use of separate propellers for VTOL and forward thrust in a relatively heavy but simple propulsion system. A conceptual sketch of this concept is shown below in Figure 2.2b.

VTOL Tilt Wing Concept

This concept makes use of the same propellers for take-off/landing as for producing forward thrust during flight. Compared to the VTOL Fixed Rotor, this results in lower system mass, but at the price of added complexity (as a tilting mechanism is required to orient some of the rotors). The tilt mechanism also limits the level to which the propellers can be optimized, as they must be efficient for VTOL and during flight. Figure 2.2c presents a sketch of this design concept.

STOL with Pod Concept

The final concept was a winged aircraft without VTOL capabilities. Visually, the aircraft was similar to the above concept (Figure 2.2c), however the rotors are fixed and only used for forward propulsion. This simplifies the design and reduces required thrust capacity of the rotors significantly. Note that VTOL capabilities are a significant contribution to aircraft mass. Given the lack of VTOL capabilities, soil sampling would be carried out by dropping the required soil sampling payload in a pod. The aircraft then loiters over the area until the soil sample has been collected, after which it descends and picks up the pod using a grabbing mechanism. Note that this adds significant complexity in terms of the soil collection payload, the inclusion of the grabbing mechanism, and the required autonomy considerations. Furthermore, the UAV would require external ground infrastructure to assist with take-off and landing: a launching system would be used to quickly accelerate the aircraft to flight speed for take-off and a catching system would help to slow it down over a short distance for landing.

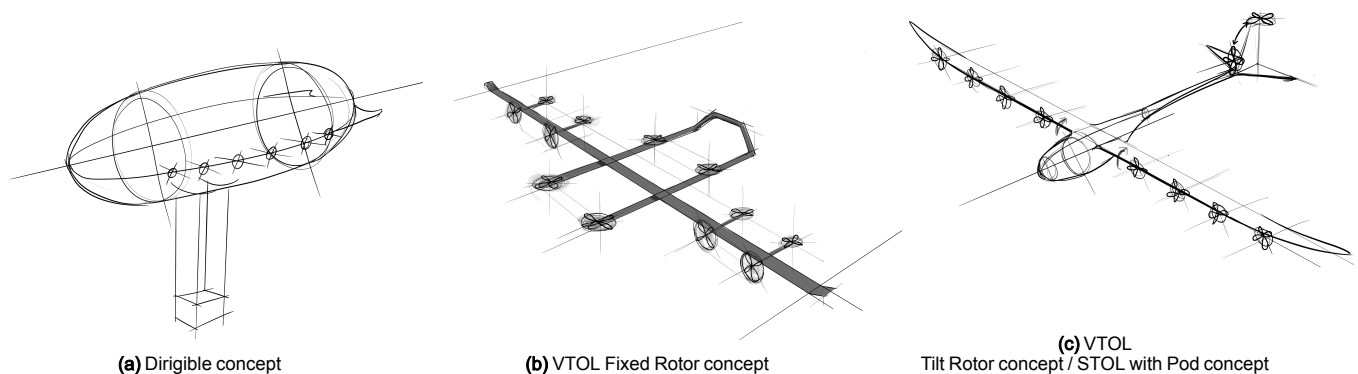


Figure 2.2: Overview of the main concept design for the UAV for Mars exploration

2.5 Trade-Off and Selected Design

One of the four concepts needed to be chosen to be able to produce a detailed design. When comparing design options, the focus was on how well the concepts could be expected to exceed the requirements, as it was assumed that each of the designs could at least meet the requirements. The process of selecting a final design was done by means of a trade-off. First, the design criteria were established - these are listed below with their associated weights. The criteria were selected and weighted based on the requirements set by the customer.

- Reliability and Durability: 17.8%
- Safety: 17.3%
- Total mass: 15.6%
- Payload Choice Flexibility: 10.4%
- Transport dimensions: 9.1%
- Distance per month: 7.6%
- Resources and Maintenance: 6.8%
- Sustainability: 4.7%
- Flight operations: 4.4%
- Cost: 2.8%
- Ground transportability: 2.3%
- Assembly: 1.2%

Before scoring each design with respect to these criteria, a preliminary analysis was done. This analysis took into account some important characteristics of the design, such as the autonomy system characteristics, the power system, and the aerodynamics. In addition, the functionality of the communications subsystem was initially designed and the payload instruments were selected. An overview of these payload instruments is given below in Table 2.2. As a final part of the preliminary analysis, an initial sizing was done on each of the design options.

Table 2.2: Summary of payload instruments and specifications

Subsystem	Mass [kg]	Power [W]	Dimensions [cm]	ESA Mass and Power Margin
Drill and Arm	7.16	50	50×30×30	20%
Soil Containers	2.2	0	15×15×15	20%
Camera	0.056	3.1	3.8×3.8×3.6	10%
Ground Penetrating Radar	3.3	8.25	41×31×18	20%
Gas Analyser	16	70	30.5×30.5×28	10%
Magnetic Disks	1	0	3×2.5×0.9	10%
Total Including Margins	33.95	150.31	-	-

The communication subsystem of the design must support constant contact with the UAV in order to obtain visual telemetry and assess the state of the UAV. Therefore, a combination of a beacon network and an orbiter around Mars was chosen. The beacon network functions as a primary link and the orbiter as a secondary/emergency link, due to the significant amount of delay.

For the initial sizing of the design options, two separate models were written; one for the dirigible concept and one for the winged concepts. The models used the payload mass, required range, and air density as inputs, among others. The payload mass for the Dirigible and STOL Pod were assumed to be a bit larger due to the addition of suspension cables and a drop pod, respectively. This resulted in an initial mass estimation of 315.3 [kg] for the Dirigible, 113.6 [kg] for the VTOL Fixed Rotor, 98.0 [kg] for the VTOL Tilt Rotor and 94.1 [kg] for the STOL Pod concept. The calculated dimensions were also taken into account in the scoring.

Finally, the trade-off between the different design options was performed. The four design options were analyzed with respect to each of the criteria. The purpose of this analysis was to identify all of the factors affecting each concept's expected performance for each criterion. Based on this, each concept was given a score from 1 to 10 for each criterion. The VTOL Tilt Rotor concept received the highest score in terms of mass, dimensions, and assembly, with the VTOL Fixed Rotor coming in second place. For resources and maintenance, flight operations, and reliability and durability, the VTOL Fixed Rotor came in first with the VTOL Tilt Rotor in second place. This is due to the tilt design, allowing the propellers to be used for both upward and forward thrust, making it more mass efficient, but also resulting in more complexity. For ground transportability, the Dirigible received the highest score, since it would support its own weight, making it easier to move around. For the distance per month and cost criteria, the STOL with Pod concept received the highest score. This was due to the fact that this design has the lowest battery mass, resulting in lower costs and lower recharging time. However, the main issues for this design were the use of a pod and an external launching/catching system. This led to a low score in the design's payload flexibility criterion score, as well as the ground transportability criterion. The Dirigible's main issues were its size and thin skin, which resulted in low scores for the dimensions, assembly, reliability and durability, and resources and maintenance criteria.

The assigned scores were then multiplied by the criteria weights to give an overall score for each design. Overall, the VTOL Tilt Rotor came out on top, with the VTOL Fixed Rotor design in a close second place. The Dirigible and STOL with Pod concepts received significantly lower scores than the two VTOL designs.

In order to select the best design for the mission, the two best options were analyzed further. The fact that the VTOL Tilt Rotor scored slightly higher in the trade-off did not ensure that it would be the best design. Therefore, a technical sensitivity analysis as well as a trade-off sensitivity analysis were performed. The technical sensitivity analysis introduced changes in the requirements for altitude, range, and payload mass. The result of this analysis showed that the VTOL concepts were robust against range and altitude, but not against changing payload mass. For the trade-off sensitivity analysis, the criteria weights were changed randomly between -100% and 100% and the winning concept was identified; VTOL Tilt Rotor was chosen in 96% of the cases. All in all, the results of the sensitivity analyses showed that the VTOL Tilt Rotor design was the most robust.

Thus, the design concept chosen for the final design was the *VTOL Tilt Rotor* design. The focus of the rest of this report is on the further design of this concept into a complete design.

3 Market Analysis

Interest in Mars as a new habitat has grown significantly in the past years. With the current growth of large private space companies, investments in the exploration of Mars are increasing. In this chapter, the future market of drone exploration on Mars is analyzed. First, a market segmentation is done with regard to stakeholders, followed by an analysis of these. Then, an analysis is done on the future and possible new market of drone exploration on Mars. Finally, a SWOT analysis is completed to distinguish the strengths, weaknesses, opportunities, and threats of this market.

3.1 Stakeholder Identification

In order to distinguish segments of the market, market segmentation is done with regard to the different stakeholders of the mission. This section provides a comprehensive overview on these stakeholders. First, the stakeholders and their needs are identified. Stakeholders are companies, individuals, or institutes that have an interest in the mission and the outcome of the mission. Therefore, they either affect or are affected by the mission. In order to identify the stakeholders, it is important to consider the entire mission from getting approval from the government to assembling the drone on Mars. Each stakeholder has primary needs, which are derived from their expectations and concerns. These stakeholders with corresponding roles and needs are presented in Table 3.1. From these stakeholders, the key players in the future market are identified. These key stakeholders, as well as their position in the future market will be analyzed below.

Table 3.1: Stakeholder identification

Stakeholder	Identifier	Definition and Role	Primary Needs
Launcher company	LC	A company that provides a platform to transport the drone to Mars.	Provide a platform that is safe both for the launcher and for the drone.
Payload providers	PP	Companies that provides payloads to be sent to Mars on board with the drone.	To be able to fulfil the science objectives of the drone.
Government	G	Departments and groups of people that have the authority to govern a country.	A successful mission that meets the regulations set by the government.
Insurers	I	A company that assess the risks and provides an insurance coverage.	A reliable and safe drone.
National/International space agencies	SA	Space agencies which ensure that innovations in the field of space continue. Responsible from organization of the launch, tracking, data acquisition.	Perform and manage a successful launch to transfer the drone to Mars.
Assembly team	AT	A team of astronauts on Mars that are responsible from assembling the drone.	Perform assembly safely and without any difficulties on Mars.
Operators	O	A team of astronauts on Mars that are responsible from operating the drone.	Operate the drone on Mars without any difficulties.
End users	EU	Scientists/individuals who are employed by academia that use the data gathered by the drone to enhance the level of knowledge in the field.	Scientific data that is gathered by the drone.
Educators	EDU	Individuals/institutions that provide education to various age groups.	Access to scientific knowledge.
Public	PUB	The general society and their view.	Access to scientific knowledge.

National/International Space Agencies

Several governmental institutions have been working on exploring Mars for decades. Examples are NASA, ESA, Roscosmos, and the UAE Space Agency. Alternatively, companies such as Boeing and SpaceX have also started to play an important role in the space industry in the past few years. Some of these institutions currently have scientific missions on the Martian surface and schedules for upcoming tasks as early as 2022. This proves it is of high interest currently to perform such scientific missions. Therefore, it can be concluded that these institutions are interested in the product delivered by this project and can be seen as customers.

Launcher Companies

For past missions to Mars, launchers were provided by a small group of launcher companies. For this mission, the Atlas V launcher is selected, since this launcher provided a safe journey to Mars for the Perseverance Rover, which is a comparable mission. These launch costs are taken as a guideline for the future launch costs. However, when looking at the future launch market regarding new technologies, the costs reduce. It is said that the launcher costs can be reduced by approximately \$25 million USD when using refurbished rocket boosters. This is a realistic

view of the future launcher costs, since the US Space Force is planning on launching two satellites with refurbished rocket boosters by 2022 [130].

Payload Providers

In order to execute the mission requirements, several scientific instruments are needed. These scientific instruments are included in the payload of the spacecraft. An overview of the costs of these instruments is given in the next chapter. Although the space instrument sector is a constantly evolving field, the cost of these instruments do not vary greatly. However, due to the increase in interest in space exploration, it will be expected that the space instrument sector will grow a lot in the coming years. This is due to the opportunities to provide scientific instruments for new missions. Therefore, the competition in this market will grow and it is likely that the design and manufacturing prices for scientific instruments will decrease slightly [119].

Government

The government is interested in the exploration of space as well. This can be seen by the various space institutions that are funded by the government in order to do research. In the future, it is expected that these funds will increase [60]. However, there are some regulations and rules on space exploration set by governments as well. Before executing a mission, for example, there are specific tests which have to be performed in order to ensure that the spacecraft can adhere to these rules and regulations. Most governmental institutions, such as NASA provide these testing facilities as a service when the spacecraft is manufactured. In the future market, there are going to be rules and regulations set by the government as well. Moreover, it is to be expected that the amount of rules and regulations increase, looking at the trend of the past years [60]. In this way, governments will play a big role in the future market.

Insurers

Since space missions introduce many risks, it is important to make sure that these risks are partly covered. This is done by insurers. They provide insurance when there is critical damage due to unforeseen circumstances. This is not only for assembly and integration, but also for pre-launch risk, in-orbit life insurance, and more. Since the costs for space exploration are so high, so are the covering costs for the insurance companies. Due to decreasing premiums, some companies are reviewing their position in the market, and some are even stepping out [66]. However, with the growing amount of space activities, it is expected that these premiums will increase again and remain high for the coming decades [108].

3.2 The Future Space Market

The future space market will look significantly different to the current space market. It is estimated that the space market global economy will double by 2030 [97]. This is because launch costs are expected to decrease, and new technologies are expected to enter the market. One example of this is the company SpaceX, which already introduced several launchers and aims to bring humans to Mars and back. With developing launch vehicle technologies, such as reusable rocket boosters, they aim to launch for under \$22 per kilogram in the coming years. In this way, launch prices will decrease in the next few years due to competition in the space sector. Therefore, it can be assumed that the interest in space exploration will only grow in the future, thereby expanding the space market and the number of stakeholders.

3.3 Establishing of New Markets

Government institutions have long dominated space exploration; however, the emerging commercial space market, NewSpace, offers the chance for more stakeholders to participate. Numerous start-ups and companies interested in NewSpace are leading to the formation of larger commercial space market for space transportation, research and development, in-situ resource extraction, orbital and suborbital space tourism, in-orbit satellite servicing, and space debris prevention [150]. From this division, it is clear that the product of this mission will enter the research and development market as a technology demonstrator. Since the exploration of Mars is a relatively new concept in the space market, it will be expected that this mission will be one of the great pioneers in exploration on Mars with drones. So far, only the Ingenuity helicopter has been able to perform powered flight on Mars. This mission was, however, not capable of retrieving ground samples, for instance. Looking at sample retrieval and atmospheric measurements, the Perseverance Rover has been able to perform such measurements. However, since this rover is not able to cover such a large area, the drone for this mission will have a lot more scientific value. In this way, it will be one of the first of its kind and therefore will be able to set the standards for the future drone exploration market. In the next section, the foreseeable share in this new market will be discussed, as well as the opportunities and strengths that this design has compared to previous missions.

3.4 Foreseeable Share in New Markets

As mentioned above, there is not yet a specific market for drones designed for exploration on other planets. The technology currently available would fall under the category of research and development in the market. There has been only one previous mission of a robotic flying vehicle on Mars (the Ingenuity helicopter), which was conducted by a governmental institution (NASA). No public records attest to the development of such technology from Europe as of today. Therefore, if the design were to enter the market, it would be the only product of its type in the European

market. In 2021, the market for non-satellite technology accounts for approximately 21% of all expenditure in the space industry market. It is expected that the overall amount invested in such missions will increase by 20% by 2031 [97]. To better understand the aspects influencing a break into this new market, a SWOT analysis has been performed; it is presented in Figure 3.1 and contains the strengths, weaknesses, opportunities, and threats of the future market for our specific design. As already mentioned, the opportunities for drone exploration in space create an enormous gap in the future market of space drones, as can be seen Figure 3.1. On the other hand, this leads to a lot of emerging competitors in the future market, as can be seen on the right bottom of this figure. However, since this design is one of the first of its kind, it will set the standards for the new market, being able to be ahead of the emerging competitors. It has characteristics that are unique and new to the environment of Mars, being a scientific pioneer in the analysis of Mars. Also, the required investment of the customer can be realized, due to the growing interest in life on other planets from big companies.

	HELPFUL	HARMFUL
INTERNAL	S 1.Vision and Creativity 2.Sustainable development 3.World-renowned expertise of TU Delft applications in aerospace industry 4.Design that is able to fly for 100 km and perform analysis of the environment on Mars	W 1.Limited work experience of the team 2.Required investment of customer
EXTERNAL	O 1. Market growth potential 2. Aging government organizations 3. Interest on life on other planets 4. Improving strengths of design for further development in the future	T 1. Emerging competitors 2. Limited testing facilities 3. Contract dependability 4. Bargaining power of launching services providers

miro

Figure 3.1: SWOT analysis for the entrance in new markets of the UAV for Mars exploration [1]

3.5 Cost Analysis

The development costs usually account for about 70-75% of the missions' total costs. This is primarily the case in space missions, since they require high precision and considerable time and resources. The operational costs as a proportion of the total costs vary between missions, based on the operational lifetime and complexity. The launcher costs, however, are approximately the same per mass unit.

Due to the complexity and long operational lifetime of this mission, it is decided that the distribution of the costs can be best compared to the Perseverance Rover mission. An approximate distribution of the costs for this mission will therefore be: 75% for design and development, 10% for the launcher, and 15% for the operations.

The launcher cost for the Perseverance Rover mission to Mars was about \$243 million USD, not including the use of reusable rocket boosters. This will however be available in the future, thus for our design, a launcher cost of \$218 million USD is used. Using the above distribution, this leads to a total mission cost approximation of \$2.18 billion USD. As a preliminary estimate the costs here are uncertain. That is why there are margins for the cost budget. According to NASA, it is a ground rule to take 20% margin for design and development and 10% for operation [100]. Using the approximate distribution of cost segments of these past missions, this leads to the following budget breakdown:

- **Design and Development:** \$1635 million USD + \$327 million USD (20%)
- **Launch and launch vehicle:** \$218 million USD
- **Operations:** \$327 million USD + \$32.7 million USD (10%)

4 Resource Analysis and Budget Breakdown

Budgeting is an important part of the design process, since the use of resources such as mass and power tends to grow as design of a product develops. In this chapter, an analysis on the resources used during the mission is presented with the aim to set targets with contingencies for the final design. The breakdown is presented per subsystem with margins based on ESA standards [47].

In previous reports, a complete budget breakdown per subsystem was not presented. The reason for this was because the four design options were far too different to the extent that different subsystems would have been required for each one. However, in the detailed design phase, these budgets can now be defined thus ensuring maximum values are set before the detailed design phase is begun. The budgets are based on the initial sizing performed in phase 2 of the project [2]. This sizing primarily focused on the mass and power usage of the payload and of the communications subsystems, as these would have been constant over all design options. Extrapolating these budgets for the winning design options provides the final values.

Mass Budget

As the primary goal of the UAV is to explore Mars, the payload's mass and power usage was one of the first design parameters that was fixed. The sizing program uses that payload mass as input and provides good mass estimates for the main heavy components, which includes the wing box, battery, and propulsion system. Additionally, an extra percentage was added for the other subsystems, based on statistics. Subsystems represented by this miscellaneous mass were: all structures not part of the wing box; the harness of the power subsystem; the communications subsystem; the thermal control subsystem; and the onboard data handling subsystem, which also runs the main software. However, in order for the mass budget to be a useful tool for the detailed design on subsystem level, the masses had to be rearranged and summed into appropriate subsystems.

To achieve this, the miscellaneous mass has to be divided. The communication subsystem had already been analysed in phase 2, yielding a 2 [kg] mass including 20% margin [47]. Furthermore, due to the likeness of the drone subsystems to spacecraft subsystems, which makes sense due to its intended use on Mars, spacecraft mass fractions were used to estimate the harness mass (4% of dry mass), thermal subsystem mass (3.4% of dry mass), and OBDH subsystem mass (3.8% of dry mass) [161]. The leftover mass was used for the non-wing box structural components.

Subsystem masses then follow from the numbers above. The structures subsystem consists of the wing box mass and the miscellaneous structures mass. The propulsion subsystem consists of the forward and VTOL propulsion mass estimates. The power subsystem consists of the battery and harness masses. The communications subsystem is 2 [kg] including 20% margin as mentioned above. The Thermal control and onboard data handling subsystems are the masses as found by the mass fractions. Finally, the payload subsystem is the selected payload mass.

Margins have to be defined in order to have a contingency on the masses in the mass budget. Since all masses except for the payload are based on initial sizing estimates and still have to be newly designed, they were given a margin of 20%. The payload mass on the other hand is primarily based on existing off-the-shelf components. Some of the components may need minor modifications, meaning the payload was given a 10% margin. The mass budget to be adhered to for the detailed design can be seen in Table 4.1

Table 4.1: Mass budget

Subsystem	Mass [kg]	Margin [%]	Mass Including Margin [kg]
Structures	17.6	20	21.1
Propulsion	20.0	20	24
Power	17.7	20	21.2
Communications	1.7	20	2.0
Thermal Control	3.3	20	4.0
Payload	34.0	10	37.4
Onboard Data Handling	3.7	20	4.4
Total	98.0		114.1

Power Budget

The power budget is more difficult to create, due to the preliminary state the analysis was in during phase 2. Only power requirements for the forward and VTOL propulsion systems were sized in the initial sizing program. Moreover, in the Payload and Communications Selection chapter, a required power for the entire payload and the communication subsystem was identified. Proper preliminary sizing on the power requirements for the structures subsystem, the power subsystem, the thermal control subsystem, and the onboard data handling subsystem was not performed yet. In order to be able to produce power budgets, an estimate had to be made for these missing subsystems. This was done by using statistics on typical power consumption breakdowns.

It was decided that the thermal subsystem takes 2% of total operating power. The onboard data handling subsystem takes 4%. Furthermore, the power subsystem takes 2% to make up for losses in the long wiring in the wings.

Finally the structures subsystem takes 0% power according to the statistics; however, since the actuators for tilting the rotors and for moving the control surfaces are considered part of the structure, a higher percentage had to be chosen. It is decided to keep it in line with the power and thermal subsystems and thus set it at 2%.

By using the known values for the propulsion, communication and payload subsystems, along with the percentages above, an iteration could be done to find total system power. This was done twice, one time based on peak propulsion power, which can be seen in Table 4.2, and a second time with nominal propulsion power, which can be seen in Table 4.3.

Table 4.2: Power budget based on peak power.

Subsystem	Peak Power [W]	Margin	Peak Power Including Margin [W]
Structures	323	20	388
Propulsion	14368	20	17242
Power	323	20	388
Communications	17	20	20
Thermal Control	323	20	388
Payload	150	10	165
Onboard Data Handling	646	20	775
Total	16150		19366

Table 4.3: Power budget based on nominal power.

Subsystem	Nominal Power [W]	Margin	Nominal Power Including Margin [W]
Structures	158	20	190
Propulsion	6960	20	8352
Power	158	20	190
Communications	17	20	20
Thermal Control	158	20	190
Payload	150	10	165
Onboard Data Handling	317	20	380
Total	7918		9487

5 Mission Analysis

This chapter gives some context as to how the expeditions will be carried out. While the term "mission" refers to the overall, years-long operations of the drone, the term "expedition" is used to denote individual flights and tasks of the drone which occur on a daily basis. The functional flow and functional breakdown diagrams in Sections 5.1 and 5.2 give an overview of the operations of the drone from the beginning of the mission to the end, including expedition procedures. Section 5.3 gives a rundown of the two main expedition types, and Section 5.4 discusses the altitude ceiling and more distant exploration. Finally, assumptions regarding what will be available at the Mars base throughout the mission are outlined in Section 5.5.

5.1 Functional Flow Diagram

The first part of analysing the mission was to make a functional flow diagram. This diagram present top level functions and the order in which they occur. The diagram is presented in Appendix A. It is important to note the use of a number of color indicators on the diagram. The blue blocks refer to sub-routines within a block. For example, the blue block, "4.8 Perform soil sample collection" has a sub-routine displayed at the bottom of the diagram. The green reference circles at the ends of sub-routines direct the reader back to the appropriate block from which to continue through the flow. The red boxes denote abort sequences as also stated in the legend of the diagram. Any of the 'Assess X' blocks that are colored in red thus mean 'Assess X and abort when wrong'. The reason this is included is because this missions focuses heavily on autonomy. In addition, the added cost and impracticality of having to perform repairs or replace the UAV would be far too great as a result of being on Mars. The dashed lines without an arrow head denote going a level deeper in to the routine and the orange lines denote going up one level.

There are a number of different mission profiles for the UAV thus it was decided that the diagram should reflect this so that it encompasses all the functionalities of the design. For example, some missions may require the astronauts to move the drone to a specified location first. The focus of the UAV is to function as a tool for scientific research thus any mission profile suiting this goal is feasible. The main form of mission profile reflected on the diagram is a mission that involves, flying to a target location, doing remote sensing at this target location, landing to collect soil samples and lastly flying back to the base.

5.2 Functional Breakdown Diagram

The second part of analysing the mission was to make a functional breakdown diagram. This goes a level deeper in to each task in the functional flow diagram. The diagram is displayed in Figure A.4 in Appendix A. An important decision that was made for this diagram was that the focus of the diagram should be on the operation of the UAV. This means top level mission tasks such as, "Perform launch" or "Perform Mars landing" are not expanded on as they are not in the scope of this report. This decision was made based on instructions from the customer.

5.3 Expedition Profiles

The expedition profiles are the basic types of expeditions that the drone will carry out on a daily basis. They are defined by their scientific purposes, which impose certain requirements on the drone's flight.

5.3.1 Expedition Profile 1: Remote Sensing

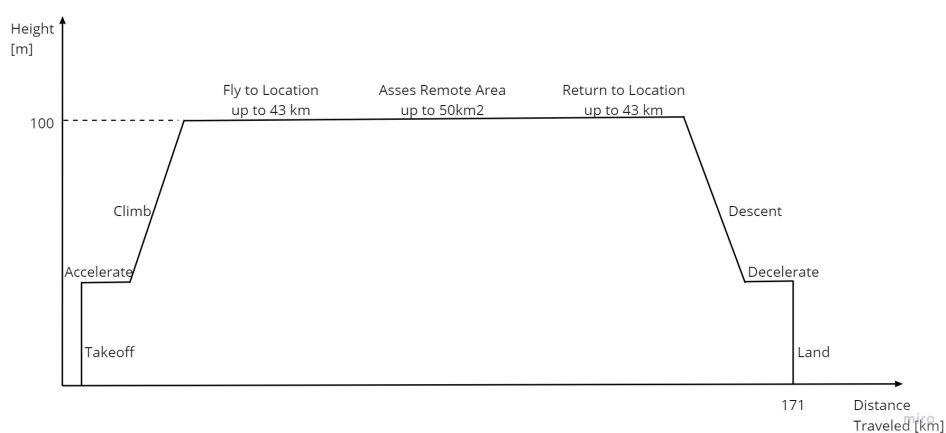


Figure 5.1: Profile for expedition profile 1: remote sensing.

The first mission profile is one in which the drone's scientific mission is to survey an area of interest on the Martian surface to perform visual imaging, height mapping, underground ice deposit detection, atmospheric gas detection, and dust sample collection. The drone must be capable of surveying these parameters at the specified minimum

resolutions over an area of at least 50 [km²] in a single flight. It may also be desired to survey areas of different sizes: larger areas may be achievable by a single flight depending on conditions and performance, and smaller areas may be used if very high resolution is desired for a specific region of interest (higher resolution requires flying at lower altitudes, thereby reducing the swath width of the camera and thus the area covered per distance travelled).

The local region around the base, defined by a 50 [km] radius from the base location, covers an area of around 7854 [km²]. Assuming expeditions which survey 50 [km²] at a time, it would take 157 remote sensing expeditions to survey the entire region. Note that certain strategies for fully covering this region are more efficient than others. For example, surveying long and narrow strips would require fewer turns to cover the same area as a square region. Of course, the exact areas to be surveyed and the order in which to survey them will depend on the astronauts, the scientists on Earth, and weather conditions at the time of the mission.

To determine at the altitude above the ground at which the UAV should fly to achieve sufficient resolution for visual imaging and height mapping, the geometry of the situation must be considered. This can be seen in Figure 5.2, where FOV stands for Field of View, h is the altitude above the ground, and r is the ground resolution at the edge of the field of view. This diagram applies to both swath directions (perpendicular and parallel to the direction of flight).

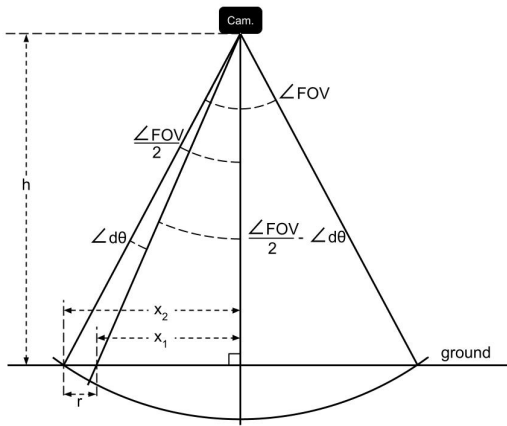


Figure 5.2: Geometry of downward-pointing payload camera's field of view and swath

The angle $d\theta$ is defined as

$$d\theta = \frac{\angle FOV}{N_{\text{pixel}}}$$

where N_{pixel} is the number of pixels of the camera. From the geometry seen in Figure 5.2:

$$\begin{aligned} r &= x_2 - x_1 \\ &= h \cdot \tan\left(\frac{FOV}{2}\right) - h \cdot \tan\left(\frac{FOV}{2} - d\theta\right) \\ \therefore h &= \frac{r}{\tan\left(\frac{FOV}{2}\right) - \tan\left(\frac{FOV}{2} - d\theta\right)} \end{aligned}$$

The swath width is simply:

$$2h \cdot \tan\left(\frac{FOV}{2}\right)$$

The top-level requirements specify that the ground resolution for visual imaging and height mapping should be 10 [cm] or better. Since ground resolution is always better at the center of the field of view, the outer edge of the field of view is taken as the limiting factor for resolution. It is assumed that a wide-angle lens will not be used, so image distortion at the edges of the frame should be minimal.

By assuming a camera with $FOV = 72^\circ$ and $N_{\text{pixel}} = 4000$, and with the minimum requirement that $r = 0.1$ [m], the maximum altitude at which the drone should fly can be calculated to be 208 [m]. By flying at or below this altitude, a drone equipped with such a camera would meet the relevant payload requirements. The corresponding swath width is 303 [m]. To cover an area of 50 [km²] in a single flight at this altitude would require a range of at least 165 [km]. This range does not include the initial distance to the area of interest (which would depend on the expedition), nor does it include the distance that would be required for making turns to cover adjacent swaths (which would depend on the shape of the area to be surveyed). It must be noted that flying slightly lower than the maximum altitude would be required to account for sudden (downward) changes in the terrain below.

If flying at a lower altitude of 100 [m], for example, resolution would improve to 4.8 [cm] at the edge of the field of view, but the swath width would decrease to 145 [m], thereby increasing requiring more than 344 [km] of range to survey an area of 50 [km²] in a single flight.

5.3.2 Expedition Profile 2: Soil Collection

The aim of the second mission profile is to collect a soil sample within 50 [km] of the base when operating semi-autonomously, or 10 [km] if operating human controlled. Hence, the primary difference from expedition profile 1 is that the drone needs to perform an additional landing and take-off at the soil sampling site. At the soil sampling site the drone collects between 100 and 500 grams depending on whether it is an autonomous mission or a human controlled mission.

The altitude at which the drone flies is less important if all remote sensing equipment is turned off. However, since these instruments are on the drone anyway, it is likely that they are just turned on to collect additional information on the route flown - this is to be chosen by the operators for each expedition. This would give an upper limit to fly at of 208 [m] above the surface as described in Section 5.3.1.

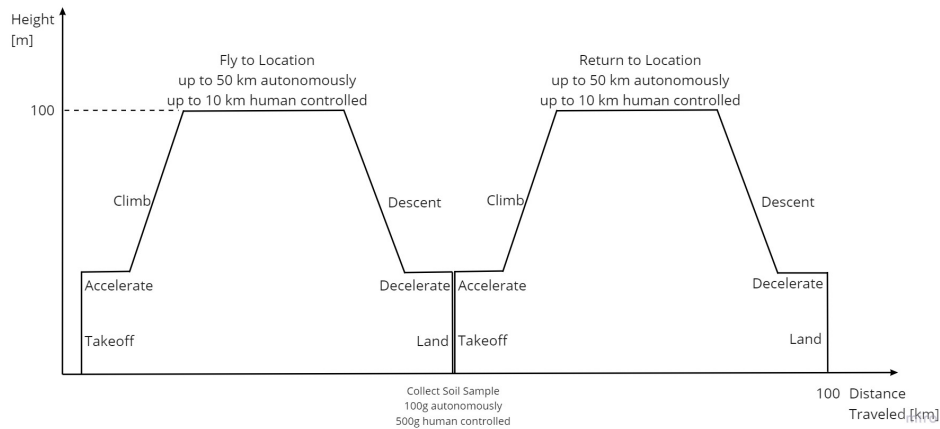


Figure 5.3: Profile for expedition profile 2: soil collection.

5.4 Altitude Considerations

In order to make a decision about what altitude ceiling to choose for the UAV, a program was written to investigate which parts of the Martian surface can be explored for a given maximum flying altitude with respect to the Martian vertical datum - the geoid. This calculation is performed under the assumption that the flight is performed 100 [m] above the surface, so a flying altitude of 1000 [m] allows for exploration of all regions with a surface altitude of 900 [m] or lower. This results in the area distribution shown in Figure 5.4. As can be seen, staying under the vertical datum (corresponding to the dark and light purple regions) severely limits the versatility of the UAV in exploring different regions of Mars. Choosing a maximum flying altitude of 1500 [m] (corresponding to all the colored regions) above the vertical datum allows for exploration of a much larger portion of the Martian surface, as well as crossing between all the regions situated at low altitude, such as Hellas Planitia (bottom left), Argyre Planitia (bottom right) and the large region of low altitude in the Northern hemisphere. While visiting multiple of these locations in a single flight would require a range in the order of thousands of kilometers, this versatility is useful for allowing the utilisation of the UAV at various potential base locations. It was thus chosen to design for a maximum flying altitude of 1500 [m] above the vertical datum.

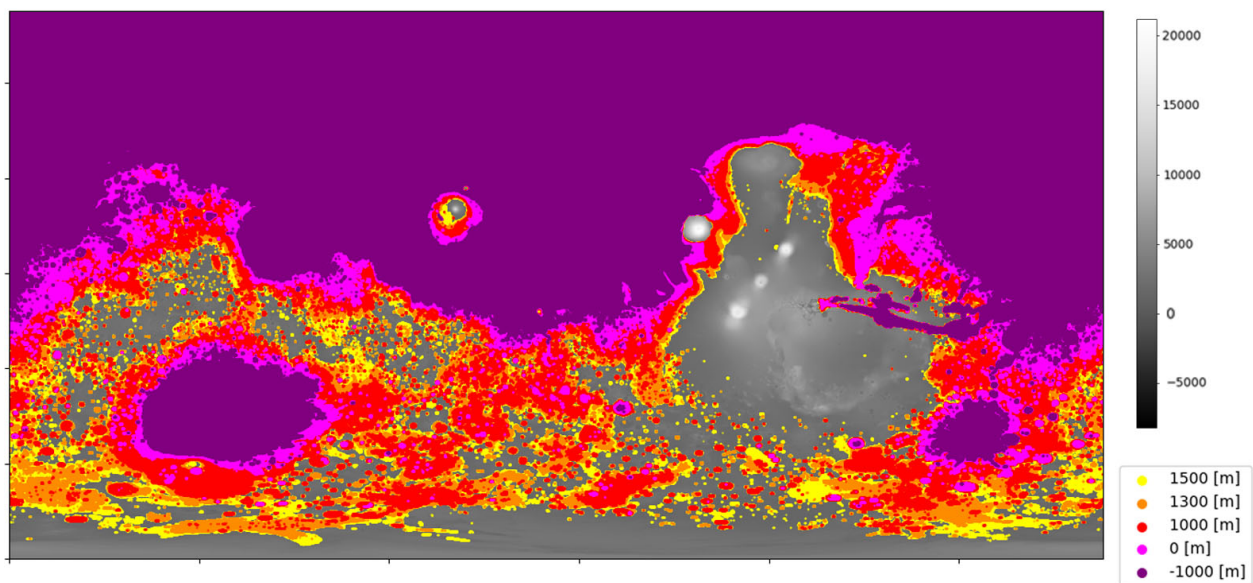


Figure 5.4: The areas of Mars that are explorable for different maximum flying altitudes

5.5 Assumptions About the Mars Base

The first human missions to Mars are planned for the 2030s. A significant amount of equipment and life support systems would be needed on the Martian surface to accommodate sustained or even short-term human presence on Mars. For example, astronauts would need pressurized habitation modules, communication equipment, facilities for growing food, systems for generating and/or recycling oxygen and water, medical equipment, and power

generation as a bare minimum. The most likely strategy for setting up such a base would be to first send all of these components to Mars through multiple robotic missions. Then a human-rated spacecraft could carry the first crew to the surface, where the base components would be ready and waiting.

As of 2021, there are many technological challenges still to overcome before a crewed Mars mission is feasible and safe. There are currently no detailed plans from a major space agency outlining what a Mars base may look like, how it would function, or what facilities would be present; only loose concepts have been published to date. As a result, a number of assumptions about the base have been made to assist with the development of the designs and procedures in the following chapters. They are listed and explained below.

It is assumed that:

- *This mission takes place at a point in the future when humans have a semi-permanent presence at the Mars base.* The first crewed missions will likely be discontinuous and will involve a ~500 day surface stay each; such a mission profile allows for orbital transfer to and from Mars using the minimum amount of energy [162]. The initial non-permanence allows findings to be assessed between missions (such as physiological effects on the crew) and allows procedures or hardware to be refined if any issues were found. Additionally, the operations involved in the first human missions may not be conducive to the operation of a drone like the one detailed in this report. The crew would likely be focusing on becoming familiar with the environment, building and improving the base itself, and testing out equipment and procedures. The operation of a UAV for exploration may be more suited to later in the timeline when the more foundational work has been completed, when regular trips to Mars are more routine, and when there is a continuous human presence at the base (as there is on the International Space Station today). Therefore, it is assumed that the base will be relatively advanced, well equipped, and well functioning.
- *The base will have its own power generation capabilities.* The most likely methods are solar and nuclear and the system would be easily expandable to allow for future growth. It is assumed that this power network will be accessible for the drone to use for charging.
- *There will be a communication link between the Mars base and the primary ground station on Earth.* This communication link will likely make use of the Deep Space Network (DSN) and will provide continuous contact, albeit with delays due to distance.
- *There will be at least one Surface Rover Vehicle (SRV) present at the base which is capable of transporting astronauts and cargo.* This may be similar to NASA's Space Exploration Vehicle concept, which is electrically powered and can provide life support to two astronauts for up to 14 days. This concept can also function as a cargo transport vehicle when the pressurized cabin is detached [83].
- *The base will have facilities for the sterilization of equipment.* The first crewed Mars missions will almost certainly have scientific goals which involve searching for or analyzing signs of Martian life. Forward contamination will be a risk to the success of these goals and therefore measures to prevent this will be an important aspect of the design of the Mars base. This will include proper containment of human living spaces as well as high-grade sterilization equipment of potentially contaminated equipment.
- *3D printing technology will be present at the base.* These 3D printers would be capable of producing miscellaneous spare parts, such as screws or other connectors. Therefore, spare parts of this kind will not need to be included in the design of this mission. It is not assumed that they are capable of printing entire sensors or instruments.
- *The instruments required to analyze soil and dust samples will be present at the base.* As mentioned, a large part of the early human exploration of Mars will be grounded in looking for signs of extraterrestrial life. As a result, an important activity for the crew will be the analyzing of rocks, soil, and dust using laboratory instruments at the base.
- *There will be weather prediction systems in place which will be capable of predicting dust storms and other weather events.* Martian weather is relatively predictable due to Mars' lack of an ocean or thick atmosphere, which contribute to making Earth's weather quite difficult to predict in comparison [94]. Dust storms, especially larger regional or global ones, can be more unpredictable [94, 12]. However, current models which use data assimilation are already capable of predicting dust storms up to "about a sol in advance" [12] (a sol is a Martian day, or around 25 hours). Furthermore, as more data is gathered about Martian weather by current and future orbiting satellites, the understanding of the climate will increase further and predictions will become more accurate [76].

It must be again asserted that there are no concrete plans for the exact composition and functioning of a future Mars base. The assumptions are estimations based on currently available information and may need to be altered later depending on the developments of the planned missions to Mars.

6 Final Sizing Process

This chapter will describe the process used to determine the layout and dimensions of the final design. First the layout choices for the design are described followed by the optimization methodology used to create the final system.

6.1 Layout of the Design

The final design option has been chosen in the midterm, it was determined to be the VTOL tilt rotor design. The theory behind this design was to use one (or two) main VTOL rotors behind the wing which are optimized for take-off while the forward rotors would tilt upwards during take-off to assist in the balance and then tilt forwards during flight. Based on an initial analysis of the propulsion system and stability requirements a layout of one large VTOL rotor behind the wing and two (smaller) tilting rotors in front of the wing was chosen. Figure 6.1 shows the internal layout of the drone for reference when reading about the different subsystems in subsequent chapters.

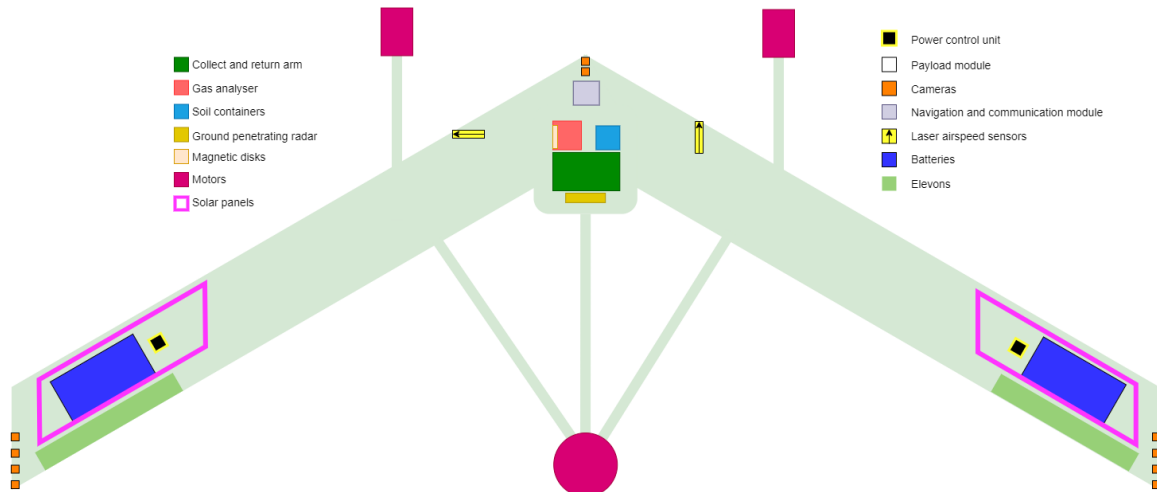


Figure 6.1: Internal drone layout (not to scale)

6.2 Sizing Methodology

After the determination of the design layout a final sizing must be performed which optimizes over a number of parameters and determines the best final design. The chosen parameters have positive and negative effects on various subsystems and hence it is not clear (without optimization) what the optimal values for these are. For example, a higher cruise speed is beneficial for aerodynamics (as it allows for higher Reynolds numbers) but it is detrimental for the energy required for phase 2 of the take-off as it will take longer for the drone to reach the desired speed.

6.2.1 Iterative Sizing Model

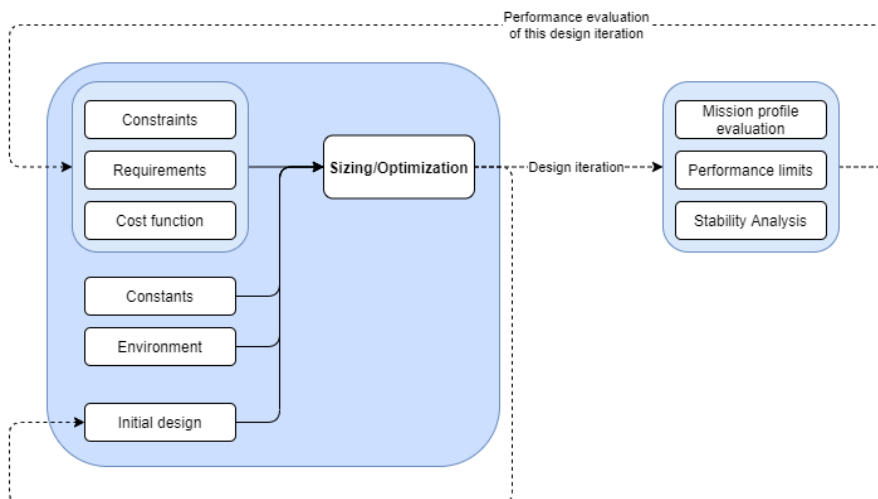


Figure 6.2: Overview of the iterative sizing model

Figure 6.2 presents a simplified overview of the sizing model. There are a number of environmental factors and constants which do not change during the optimization process. These often depend on the desired service ceiling which is chosen based on Section 5.4. The drone mass for a certain set of parameters is calculated by performing an iterative loop which converges to a final mass with a tolerance of 0.005 [kg]. The optimization is performed by determining this final mass for a large number of parameter combinations with the goal of finding the option which minimizes the cost function. The cost function is equal to the mass of the design and a small adjustment which favors designs that have a larger stability margin (as this increases the reliability of the design).

The parameters which are included in the optimization are presented in Section 6.2.2 below as well as a justification for why the parameter has been chosen to be included.

Sizing Model General Flow

Based on the above inputs and a starting mass, an optimal wing planform is computed (except for the sweep angle θ). Based on this wing planform and estimates for aerodynamic coefficients (refer to Chapter 11), this design's lift- and drag figures feed into the sizing of the forward- and VTOL rotors (refer to Chapter 13). This constrains the center of gravity position (see Section 12.2.2) and based on a desired stability margin the required sweep angle is computed (refer to Chapter 12). The efficiency loss from the elevons is dependent on this sweep angle as well as other parameters, including the stability margin and the constant pitching moment of the wing. The required cruise elevator trim has a non-negligible effect on cruise lift-over-drag performance and is thus included here already (refer to Chapter 12). This design is then fed into a mission profile simulation where the required energy for a desired worst-case mission profile is estimated (refer to Chapter 12), which then feeds into battery and power system sizing (refer to Chapter 14). The wing box- and body structure mass is computed based on a structural model (refer to Chapter 10). The total mass follows from these computed masses as well as constant estimates for other components and the iteration is repeated until the loop converges.

6.2.2 Parameters for Optimization

The number of parameters included in the optimization should be limited in order to reduce run-time. However, it is desired that a somewhat optimal design is determined. Hence, the parameters chosen for the optimization must be selected to have a large impact on the overall design. Parameters with little interplay (such as landing gear strut radius) were set to realistic values and not varied during this process. Furthermore, there turned out to be parameters (such as the length of the body or the spanwise position of the forward rotors) that had clear, consistent optima toward some limit. In which case they are simply set to these optima and left there.

This section presents the selected parameters as well as their expected effects (advantages and disadvantages) on the design.

1. **Excess forward thrust** ($\frac{T_{Fw}}{F_D}$)
2. **Cruise velocity** (v)
3. **VTOL rotor radius** (r_{VTOL})
4. **Stability margin**
5. **Spanwise forward rotor positioning**
6. **Body/fuselage length**
7. **Airfoil Selection**

Excess Forward Thrust

It is necessary to size the forward facing rotor so that they can produce sufficient thrust to overcome the drag during cruise. However, increasing the size (and power) of the forward rotors beyond this point provides additional benefits. Firstly, the second phase of the take-off will take less time (and energy) as the drone will be able to accelerate faster. Additionally, larger forward rotors will be able to produce more thrust in front of the wing during take-off which makes it possible to shift the center of gravity forward (thereby increasing the stability margin). The main disadvantage of increasing the front rotor size is that it adds mass to the system. Hence, an optimal point must be found for the sizing of this subsystem.

Cruise Speed

Cruise speed is included as a parameter as it will determine the required chord length to achieve the desired Reynolds number (this is elaborated upon further in Chapter 11). A high cruise speed will increase the power usage for take-off and landing. Additionally, a higher cruise speed will also lead to higher parasite drag due to the landing gear, vertical rotor etc. However, when the cruise speed is increased a lower wing area is required to produce sufficient lift during cruise.

VTOL Rotor Radius

Increasing the VTOL rotor radius will increase the newtons per watt that can be produced by the vertical rotor. This results in a more efficient take-off sequence. However, the propeller cannot overlap with the wing which means that increasing the rotor radius will also force the center of the rotor to be moved back further, hence increasing the size of the support structure. Additionally, a rotor with larger radius will produce more parasite drag during cruise.

Stability Margin

The stability margin allows for a design which is statically stable and will return to its original angle of attack in case of perturbations. However, a stability margin which is too large will require a large elevator deflection (or wing tip twist) in order to be trimmed during cruise. The sweep angle of the wing increases the stability margin as it moves the aerodynamic center of the wing more aft. However, a large sweep has a negative effect on structures as it increases the moment arm and effectively makes the wing longer. It is important to note that this is a significant interplay between the mentioned parameters. For example, the C_m of the airfoil will influence the required sweep angle for stability.

Spanwise Forward Rotor Positioning

The spanwise position of the forward rotors will determine their location with respect to the center of gravity. This influences their moment arm during take-off which has a large influence on the sizing of the forward rotors. However, the spanwise location of these rotors also has an influence of the sizing of the wingbox since the load must be transferred through the structure.

Body/Fuselage Length

The minimum length of the fuselage is sized such that it is able to fit the payload and other subsystems. However, increasing the length could be beneficial as it allows the center of gravity to be moved back which influences the thrust balance during take-off. However, a larger body will influence the placement of the VTOL rotor and the parasite drag on the design which is detrimental to the design.

Airfoil Selection

For the airfoil selection an initial selection of 15 low Re airfoils was made and a swept wing was simulated for each airfoil to determine aerodynamic characteristic in flight. The chosen airfoil of the wing has a large impact on the; aerodynamics, structures and stability of the drone. While it is difficult to perfectly quantify all of the effects, a number of aerodynamic characteristics were chosen to assist in the airfoil selection. Specifically; C_L , $\frac{C_L}{C_D}$ and C_m at $\frac{C_L}{C_D}$ max were chosen as the most important characteristics for the aerodynamics and stability. For the structures the geometry of the airfoil (as well as the thickness to chord ratio) plays a large role. It is not easy to determine the optimal airfoil due to the interplay between subsystems and parameters. For example a negative C_{m_α} is preferred for stability which will require the aerodynamic center to be behind the center of gravity. In this case it is beneficial to have a positive airfoil C_m at the trim condition to reduce the required elevon deflection for the drone to be trimmed. However, for structures a high C_L (which usually corresponds to a large negative C_m) is preferred as it results in a shorter wing. The 15 airfoils that have been considered are shown in Figure 6.3.

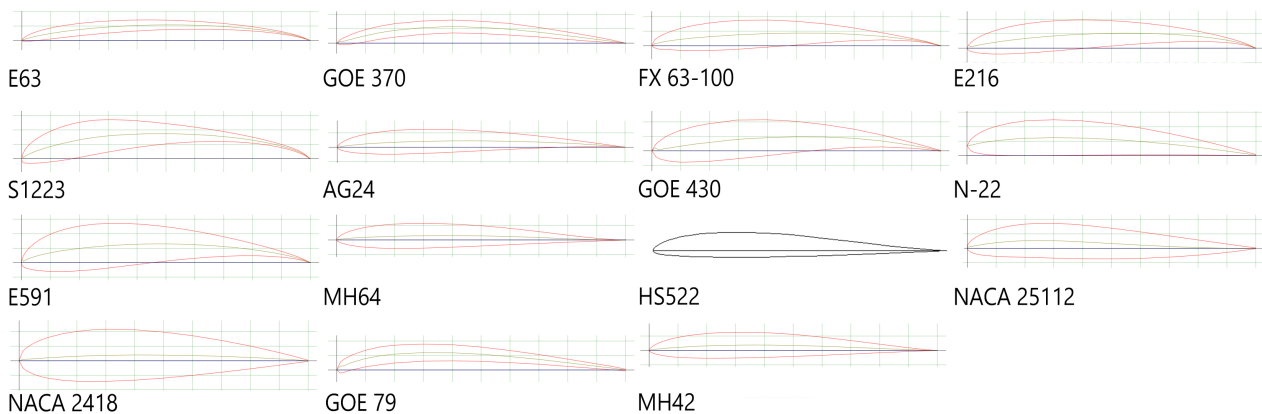


Figure 6.3: The different airfoils that have been considered for the main wing of the UAV (adapted from [8, 5])

7 Payload Analysis

In the first section it is detailed what the requirements and constraints are for the payload subsystem. After this, each part of the payload is detailed using a CAD model to detail the connection of the payload to the rest of the design and a program showing how the payload software functions when doing measurements. After this, a risk analysis is done based on the functioning of the instruments looking at the probability and severity of certain of events that could negatively impact the payload subsystem. Finally all the models and programming done is verified and validated to ensure it is of sufficient accuracy.

7.1 Requirements

Based on the requirements listed below, the payload is split up into six parts. Each part focuses on completing a number of requirements using a specific scientific instrument. For most of the instruments, a CAD model is made showing how the instrument interacts with the rest of the aircraft. In some cases a model is made to show what specifications the instrument will need to be set to, to complete the requirement and show that the requirement can be feasibly fulfilled.

Table 7.1: Requirements related to aerodynamics and their expected compliance

Index: DME-REQ-	Requirement	Compliance
SYS-PAY-01	(Key) The remote sensing system shall provide visual imaging with 10 [cm] resolution.	Satisfied
SYS-PAY-02	The remote sensing system shall provide visual imaging with at least 100 [m] swath width.	Satisfied
SYS-PAY-03	(Key) The remote sensing system shall provide height mapping with 10 [cm] ground resolution.	Satisfied
SYS-PAY-04	(Key) The remote sensing system shall provide height mapping with 10 [cm] height resolution.	Satisfied
SYS-PAY-05	The remote sensing system shall provide height mapping with at least 100 [m] swath width.	Satisfied
SYS-PAY-06	(Key) The remote sensing system shall be able to analyse atmospheric dust particle size distribution up to 1.5 [km] altitude.	Satisfied
SYS-PAY-07	(Key) The remote sensing system shall be able to measure dust particle sizes in the range of 1-40 [μ m].	Satisfied
SYS-PAY-08	(Key) The remote sensing system shall be able to monitor trace gas emissions every 500 [m] during cruising flight.	Satisfied
SYS-PAY-09	(Key) The remote sensing system shall be able to measure the presence of carbon dioxide with an accuracy of ± 0.06 [ppm].	Satisfied
SYS-PAY-10	(Key) The remote sensing system shall be able to measure the presence of methane with an accuracy of ± 2 [ppb].	Satisfied
SYS-PAY-11	(Key) The remote sensing system shall be able to measure the presence of ozone with an accuracy of 0.150 [ppm].	Satisfied
SYS-PAY-12	(Key) The remote sensing system shall be able to measure the presence of atomic oxygen with an accuracy of 3 [ppmv].	Satisfied
SYS-PAY-13	The remote sensing system shall be able to measure the presence of argon with an accuracy of ± 1 [ppb].	Satisfied
SYS-PAY-14	(Key) The remote sensing system shall be able to detect shallow ground ice deposits up to a 10 [m] depth.	Satisfied
SYS-PAY-15	(Key) The remote sensing system shall be able to detect shallow ground ice deposits at a 17 [cm] ground resolution.	Satisfied
SYS-PAY-16	(Key, driving) The soil collection system shall have an instrument to collect subsurface samples at a depth of at least 1 [cm].	Satisfied
SYS-PAY-17	(Key, driving) The soil collection system shall be able to collect soil samples up to 500 [g].	Satisfied
SYS-PAY-18	The soil collection container(s) shall be able to survive all flight loads without damage.	Satisfied
SYS-PAY-19	The soil collection system shall seal the sample container(s) after retrieval.	Satisfied
SYS-PAY-20	The soil collection system shall provide the capability for the operators to replace soil container(s).	Satisfied
SYS-PAY-21	The soil collection system shall be able to exert a force of at least 100 [N].	Satisfied
SYS-STN-08	It shall be possible for the operators on Mars to disassemble the drone to access reusable components after end-of-life.	Satisfied
SYS-STN-09	The instruments and sensors used on the drone shall have expected minimum lifetimes of 2 years.	Satisfied

7.2 Model and Analysis

In this section the models made for different parts of the payload suite are presented. These models ensure that the specifications of each instrument is carefully chosen ensuring that the requirement can be completed.

7.2.1 Collect and Return

The requirements state that the drone should be able to collect and return 100 [g] soil samples autonomously and collecting and returning 500 [g] of soil samples when human controlled. The instrument should be capable of collecting a wide range of samples to accurately reflect the large range of geological specimens that are present on Mars. Many of these specimens could hold clues to the presence of life on Mars [165]. These specimens range from hard basalt rock to softer formations such as evaporites which are a sedimentary rock often found in marine basins [64]. To fulfill this requirement, a robotic arm with a hammer drill coring tool at its end is designed, sample containers are designed and the process of transferring samples from the drill to the container is shown. A coring tool is a hollow cylindrical drill bit that is filled with sample material and then deposited into the container.

The model made for the drilling itself is based on a variety of inputs related to the constraints of drilling on Mars. The inputs can be summarized in three parts which are the drill bit design, the process of drilling and properties of the material being drilled into [64]. The formula for the rate of penetration is Equation 7.1. In addition, the formula for the total drilling time is also shown.

$$ROP = G_2 \times (WOB)^{\frac{9}{8}} (S) \times \left(\frac{S_a^{\frac{1}{4}}}{C_a^{\frac{1}{12}} D_{avg}^{\frac{1}{8}}} \right) \times \left(\frac{E^{\frac{7}{8}}}{H_v^{\frac{3}{2}} K_{IC}^{\frac{3}{2}} (1-v^2)^{\frac{1}{4}}} \right) \quad (7.1)$$

$$Time = \frac{m_{sample}}{\rho_{sample} \pi r_{drill}^2 ROP} \quad (7.2)$$

Where ROP is the rate of penetration [m/s], WOB is the weight on bit [N], S is the speed of the drill bit [1/s], S_a is the abrasive particle size [m], C_a is the abrasive particle concentration, D_{avg} is the average diameter of the coring bit [m], E is the Young's modulus of the material being drilled into [Pa], H_v is the Vickers hardness of the material being drilled into, K_{IC} is the fracture toughness of the work piece and lastly v is the Poisson ratio. The final output of the model is the amount of time it takes to drill the samples taking in a to account the variables in the formulas above. The assumptions made are that the times shown are a worst case scenario in which samples of the hardest rock on Mars are taken. This is Basalt rock with a H_v of 1.5×10^9 , a K_{IC} of 1.2×10^6 and an E-modulus of 74×10^6 . There are two types of samples which are 5x20 [g] for the autonomous mission or 25x20[g] for the human controlled missions. It is chosen to drill 20 [g] samples at a time to balance the time required to drill and the mass of sample required to do a proper analysis of the material [64].

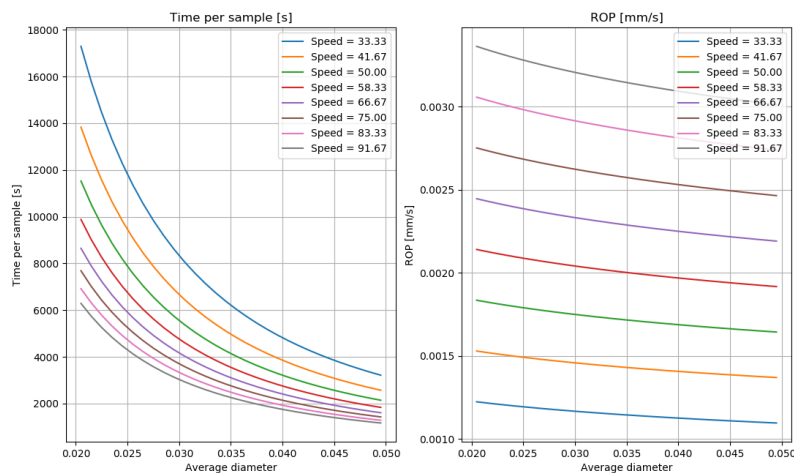


Figure 7.1: Drill performance based on parameters in Equation 7.1

As can be seen on the graph the value that needs to be maximized is rate of penetration. Primarily using diameter of the coring tool and the rotational speed of the tool. The boundaries for these values are taken based on limitations of the Martian environment. The reason this is an important part of the model is because there are two scenarios on Mars where excessive heat production could lead to failure of the drill system. This is when drilling into saturated materials at pressures below the triple point, the heat due to friction evaporates water which may freeze again thus trapping the drill. The second critical scenario is when the pressure is above the triple point. In this scenario liquid water could get into the drill and freeze again leading to the coring mechanism failing [165]. By keeping the drilling speeds within the boundaries shown this risk is mitigated as discussed in Section 7.4.

The result of this model is shown in Figure 7.1. It can be seen in a worst case scenario with the highest realistic drill speed, highest drill diameter and a weight on bit of 130 [N] completing **SYS-PAY-21** which is the maximum load the arm can handle it would take 30 minutes per sample. A sample is seen as a filling a soil container with 20 [g] of material with a volume of at most 400 [cm^3] thus ensuring low density samples can be collected. This amount of material per sample is chosen because it is sufficient to do a geological analysis and multiple samples provide a much higher chance of making accurate geological conclusions about an area [64]. For a 100 [g] missions this would mean 150 minutes of drilling and for 500 [g] missions this would mean 750 minutes of drilling complying with **SYS-PAY-17**. This is a long time however, it is for the absolute worst case scenario. It is interesting to note that although the rate of penetration increases with decreasing diameter this effect is trumped by having to drill less deep. The drill depth in this worst case scenario is 1 [cm] complying with **SYS-PAY-16**. This is an acceptable lower boundary for all drilling depths and fulfills the requirement set for the collection of subsurface samples. Furthermore, in all other materials the drilling depth would be higher and the diameter of the drill bit smaller.

The next step in the collect and return process is to design the robotic arm that the drill is connected to. This is necessary because the drill components needs to be manoeuvred and oriented so that it can effectively collect samples. The drill arm designed is based on designs that have been used or will be used on Mars in the near future [10] [53] [109] [27]. The dimensions the drill arm fits into are a cuboid of 70×45×15 [cm] when stored, its power usage is 52 [W] and the final mass of the arm is 9.5 [kg]. The layout which is discussed in Section 7.3 shows how the arm is able to maneuver a cylindrical sample of material into the containers. Lastly, the sections of the drill arm are sized based on a WOB of 130 [N] for which it results that a radius of 0.09 [m], a thickness of 0.007 [m] and a length of 0.4 [m]. A model of the arm is shown below in its folded and extended positions without the drill bit attachment.

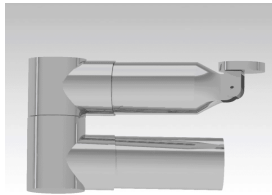


Figure 7.2: Top view of folded robotic arm

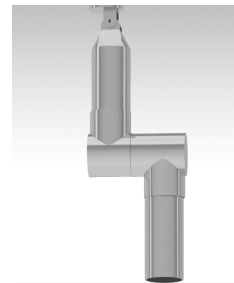


Figure 7.3: Extended robotic arm

The last part of the collect-and-return instrument is the soil containers. These are assumed to be very similar to those on the Perseverance rover, meaning they are capable of sustaining large loads and also sustaining radiation [27], thereby satisfying requirement **SYS-PAY-18**. To comply with requirement **SYS-PAY-19**, the tubes get hermetically sealed once the coring tool deposits its cylindrical sample into the container. Once the drone returns to base the door present for the drill arm is opened and the operator can easily dismount the 21 containers and do an analysis of the material at the base.

7.2.2 Visual Imaging

The requirements for the visual imaging were that a minimum swath width of 100 [m] is required and the resolution should be better than 10 [cm]. Currently satellites have provided images of the whole of Mars with a resolution of 2 [km] per pixel and around 2% of the surface with a resolution of 100 [m] per pixel [112]. This shows that the drone provides a resolution 1000 times better than current satellite imagery. To complete this requirement, a camera is placed in the underbelly of the aircraft to film in the remote sensing region. A consumer grade camera often used for drone video recording was found called the RunCam 5 Orange. It has a 12 megapixel camera sensor with a 4:3 aspect ratio, corresponding to a resolution of 4000×3000 pixels with a frame rate of 60 frames per second. The original field of view of this camera is 145° which can be adjusted by using different lenses and adjusted for different altitudes of flight [124]. Based on these specifications, the camera can provide the required resolution up to 208 [m] in height and a better resolution than required anywhere under this in accordance with requirements **SYS-PAY-01** and **SYS-PAY-02**. This assumed a standard FOV of 72° to prevent distortion at the edges of the feed. This camera weighs 56 [g], uses 3.1 [W] of power, and measures 3.8×3.8×3.6 [cm] [124].

No specific models were made for the visual imaging instrument. Instead, a mission profile from a top and side view can be seen below detailing exactly how the data is collected, what it looks like and how it is processed. This demonstrates the capability of the visual imaging camera to fulfill the resolution and range requirement as it is described. The turn radius of the drone due to its high cruising speeds is approximately 700-800 [m]. This means the approximately 200 [m] wide visual swats can not be done in order. Instead the drone effectively flies in spirals around the area skipping a number of swats and then coming back to cover them. The minimum turn radius is used in the bottom turns and the top turns are larger than the minimum turn radius. This is shown in Figure 7.4 below. Lastly, to ensure there are no gaps left in the imaging the swats are made to overlap increasing the range minutely but ensuring effective data collection.

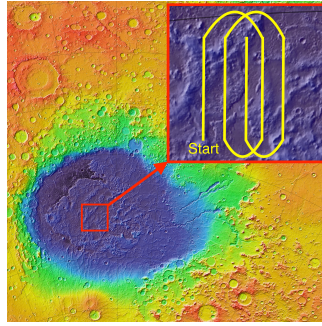


Figure 7.4: Route map for remote sensing mission (unedited original image from [156])

7.2.3 Height Mapping

It is stipulated by the customer that the aircraft should be able to perform height mapping at 10 [cm] ground resolution at a swath width of 100 [m]. The camera system can be used for height mapping as well, through the use of photogrammetry. This works by taking multiple photos of a target from different angles and then based on this determining the height of the target. As a result of the high number of images this method has inherent redundancy in its measurements [2]. No specific models are made for this requirement as qualitatively it is clear that it can be completed. The route taken is specified in Figure 7.4. The resolution requirement of 10 [cm] on the ground and in height is met by cameras of 8 megapixel resolution or higher, meaning that a camera subsystem equivalent to the RunCam 5 Orange meets these requirements [2]. This completes SYS-PAY-03 and SYS-PAY-04. It would even enable a swath width of up to 500 [m] at the same height mapping resolution completing SYS-PAY-05.

Choosing photogrammetry as a height mapping solution does have implications for height mapping under certain light conditions. Shadows cast on the ground can have adverse effects on the accuracy of collected height mapping data. A way to remedy this would be to fly over affected areas once before and once after noon [116]. This would have a significant impact on the range and power requirements. An alternative would be to use a light detection and radar system which uses laser pulses to measure distance of the terrain to the aircraft for example as this does not depend on visible light. It is decided based on these arguments that adding the extra power and mass of a LiDAR system is not worth it. The added scientific benefit of night time height mapping flights is deemed insignificant when considering the mission objective as a whole.

7.2.4 Underground Mapping

The requirement for underground mapping states that shallow ground ice deposits up to a depth of 10 [m] should be visible to the radar with a 10 [cm] resolution. The technology chosen to fulfill this requirement is a ground penetrating radar consisting of a transmitter, a receiver, and a signal processing unit. A simple mathematical model is made based on the functioning of a radar to determine the specifications of the radar that are required to collect data up to the standards set by the requirements. The model is based on the physical limitations of ground penetrating radar which is a balance between resolution and depth [24]. The inputs for the model are a range of the permittivities of the Martian surface, a range of conductivity's of the Martian surface and a fixed length for the local variability in the material. The outputs are the achievable resolution of the scan, the centre frequency of the radar and a sanity check to ensure the penetration depth is realistic for the frequency chosen based on the scattering of the signal [15].

$$Frequency_c = \frac{75\beta}{d^{0.25} * \sqrt{(K)}} \quad (7.3)$$

$$Resolution = \frac{d^{0.25}}{\beta} \quad (7.4)$$

Where β is the frequency limit factor for scattering, d is the depth of exploration and K is the permittivity. The model yields a central frequency of 458 [MHz] which is capable of a resolution of 17 [cm] and up to a depth of 10 [m] in line with **SYS-PAY-14** and **SYS-PAY-15**, working in permittivities ranging from 1-12 [9] which is representative for the Martian surface and conductivity's between 0.1-1.0 [mS/m] which are also representative of the Martian surface. The local variability of the surface is set to 0.1 [m] as this is the minimum size of ice that originally needed to be detected.

The transmitter and receiver are two antennas that are sized based on the wavelength of the radar. This results in two antennas of approximately 32.5 [cm] in width which is exactly one half of a wavelength based on the previously mentioned frequency of 458 [MHz] [4]. In addition to the antennas a control unit is present that acts as the coordinator for transmitting and receiving pulses. It is important to note as part of the control system that balancing the signal to noise ratio is critical to the resolution of the data. Based on the attenuation in different Martian surfaces up to a depth of 10 [m] it is selected that 50 [W] is the required power usage by the transmitter to have resolvable scans.

7.2.5 Gas Measuring

The aircraft should be able to measure trace gas emissions of methane, carbon dioxide, atomic oxygen, ozone and argon at a 500 [m] horizontal resolution. This horizontal resolution corresponds to the distance that the aircraft flies

whilst the cavity containing the gas fills up. The instrument chosen to fulfill this requirement is the greenhouse gas analyzer designed by Berman et al, which was designed and constructed for operation aboard NASA's SIERRA aircraft, an unmanned aircraft system for remote sensing and atmospheric sampling missions [26].

The instrument is already capable of measuring methane to an accuracy of ± 2 [ppb] in line with **SYS-PAY-10**, carbon dioxide to an accuracy of ± 0.6 [ppm] in line with **SYS-PAY-09** and measure argon to an accuracy of ± 1 [ppb] in line with **SYS-PAY-13** [26]. Ozone can also be measured in the sampling container. Although the specific reference instrument does not have this capability the technology to do so without significant impact on the mass, power or sizing is present [77]. This can be done to an accuracy of ± 0.150 [ppm] in line with **SYS-PAY-11**. The final gas measurement to be made is that of atomic oxygen. Once again, this specific instrument does not have this capability however based on the method of measuring atomic oxygen using UV light in the chamber. The measurement accuracy of this method is approximately ± 1 [ppmv] thus in line with **SYS-PAY-12** [38].

A simple model is made to show which specifications the instrument needs to fulfill the requirement. The inputs of this model are the pump rate of the instrument, the velocity the drone is flying at and the volume of the measurement container. The output is the resolution. It is known for the SIERRA aircraft that it flies at 28 [m/s], has a 400cc sample container and takes 9 seconds to fill up with the pump attached to the instrument [26]. This leads to a resolution of 250 [m]. The cruise speed of the drone being designed is 80 [m/s]. With the same pump this would mean a resolution of 714 [m] however it is assumed that by the time the missions takes place a pump will be available within the same constraints capable of inhaling 1.5 times more gas per second. This estimate is made based on the improvements in trace gas analyzing equipment that has taken place over the past 15 years [16].

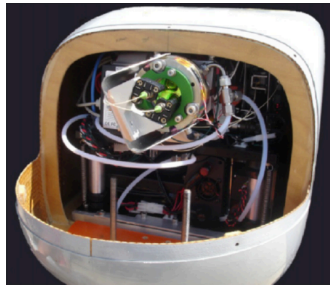


Figure 7.5: Trace gas analyzer in casing designed for NASA SIERRA drone [26]

7.2.6 Dust Composition

The last requirement states that dust composition and particle size distribution in the lower atmosphere need to be collected for analysis in a $50 [km^2]$ area and that dust particles sized in the range of 1-40 [μm] need to be collected. To do this, magnets are used which are capable of collecting dust in this size range [85]. The mechanisms functions as follows. During a remote sensing missions the drone flies to an area of interest and starts its route to fully image the area. At each point in the diagram a sliding door exposes one magnet to the environment. After this, the sliding door is actuated further thus covering the previous magnet and exposing a new magnet to the environment. Using this mechanism, the difference in dust particles within the remote sensing area can also be identified. Each magnet capture and filter magnet is used in $5 [km^2]$ areas of the remote sensing region leading to an effective resolution of $5 [km^2]$ for the dust collection at whatever height the drone is flying at completing **SYS-PAY-06**.

There are two types of magnets on board the drone. These are filter magnets and capture magnets [85]. The main difference between the two is the strength of the magnetic field they produce. The capture magnetic has a much stronger magnetic field than the filter magnet. The result is that the filter magnet only attracts particles that are highly magnetic and the capture magnetic attracts all particles. Based on these two types of magnets it is determined that **SYS-PAY-07** can be complete for dust collection and a simple sizing is done for the instrument. Magnets for space are often made out of Samarium Cobalt. The size of the magnets on the Mars rover are 4.5 [cm] in diameter and 1 [cm] thick. [85]. Based on the density of the magnets of $8.2 [g/cm^3]$ it is concluded that each magnet weigh 130 [g] and thus 20 magnets with a mass of 2.6 [kg] [31]. Two small motors are taken into account for the sliding door mechanism which have a mass 66 [g] each. The total mass of the instrument is thus 2.73 [kg]. The power usage based on the motors is 16 [W] and the dimensions of the mechanism are estimated to be $25 \times 1 \times 4.5$ [mm].

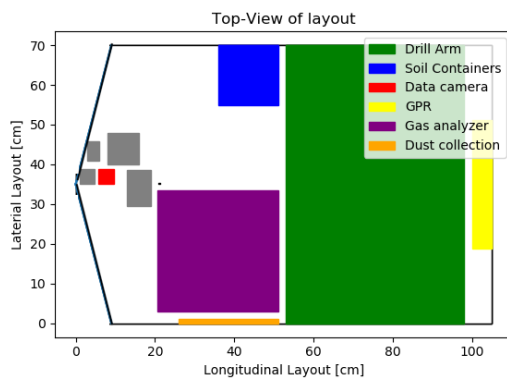
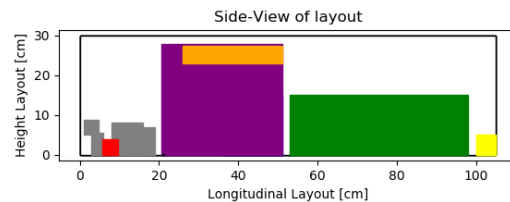
7.3 Layout

In terms of the layout of payload, it is fitted into the aerodynamic shell in the body of the aircraft. The table below summarizes the dimensions of each instrument that is present and the figure below that displays how they are placed. The placement of the instruments has a significant impact on the centre of gravity of the drone which is why the instruments are placed as aft as possible.

Table 7.2: Dimensions of all scientific payload present in the body of the drone

Instrument	Dimensions ($x \times y \times z$ [mm])	Mass [kg]	Power [W]
Collect and Return Arm	450×700×150	9.5	50
Collect and Return Containers	150×150×150	2.2	0
Visual imaging camera	38×38×38	0.056	3.1
Height mapping camera	-	-	0
Ground penetrating radar	5×32.5×5	3.3	8.25
Trace gas analyzer	305×305×280	16	70
Dust composition magnets	25×1×4.5	2.7	16

In Figure 7.6, green refers to the collect and return arm, blue refers to the collect and return containers, red is the visual imaging and height mapping cameras, yellow is the ground penetrating, purple is the trace gas analyzer which is the largest and also heaviest piece of equipment and lastly orange is the dust composition collection mechanism. The items in grey refer to the navigation and control payload and are not considered in this chapter.

**Figure 7.6:** Top view of layout with different colours referring to different instruments**Figure 7.7:** Side view of layout with different colours referring to different instruments

7.4 Risk Analysis

There are a number of risks related to the payload subsystem and more specifically per instrument. These can be seen in the bullet points below. Many of the risks listed as part of this subsystem do not have large consequences for the mission. The reason for this is that failure of a part of the payload only has consequences for the collection of data and not for the drone as a whole. To amend this, often the instrument can be repaired or replaced and the drone can be sent on the same mission again to collect the data that was missing.

- **PL-1: Collect and return system gets trapped by ice**
 - **Effect:** Can lead to the drone getting stuck at a drilling location
 - **Probability:** This risk is classified as **Probable** as it has occurred in past missions
 - **Severity:** **Catastrophic** as if the drill bit gets stuck there is a chance the drone will tip over or not be able to take off again
 - **Mitigation:** Carefully measure the electrical resistivity of the formation being drilled into to determine whether ice is melting [165]
 - **Effect of Mitigation:** Using this mitigation strategy the severity of the risk is not decreased however the probability of it occurring is significantly decreased. As soon as ice starts melting the drill can be put in idle. The result is an **Improbable** risk
- **PL-2: Drill bit breaks or is worn down to unusable extent**
 - **Effect:** The drill can no longer penetrate the Martian surface and thus can not collect subsurface samples
 - **Probability:** **Probable** as drill bits will eventually wear down when they are extensively used
 - **Severity:** **Critical**, as the drone would no longer be able to perform a large part of its scientific mission.
 - **Mitigation:** Take many spare drill bits to the base.
 - **Effect of Mitigation:** By taking multiple drill bits to the Martian base they can be frequently replaced unlike on a rover mission. Returning then to the same location to continue soil collection is not an issue only a minor inconvenience. After implementing this mitigation strategy the risk remains **Negligible** however the frequency is not decreased.
- **PL-3: Dust gets into payload subsystem**
 - **Effect:** Sufficient remote sensing data can not be collected during the mission
 - **Probability:** **Rare** as the payload is relatively well sealed off from the environment

- **Severity: Marginal**
- **Mitigation:** The design is made in such a way that the relevant parts of the instruments are exposed to the environment but sealed around the edges of the openings
- **Effect of Mitigation:** The probability is reduced from rare to **Improbable**
- **PL-5: Magnets are unable to collect dust due to the high air speed**
 - **Effect:** No data about the Martian dust composition can be obtained
 - **Probability: Occasional** as the boundary layer on the aircraft may be too strong to allow for dust to settle on the magnet at times
 - **Severity: Marginal** as missing a small amount of data although inconvenient does not have any impact on the mission as a whole
 - **Mitigation:** Maximizing the time the magnets are exposed to the environment
 - **Effect of Mitigation:** The probability is reduced to **Improbable** but the severity is not affected
- **PL-6: Lighting conditions are too dark**
 - **Effect:** Accurate photogrammetry, height mapping and navigation can not be done
 - **Probability: Probable** however it is determined that the drone's manoeuvrability as a whole would be more limiting when it comes to analyzing areas that are not well lit. This is because it would not fit in deep canyons or valleys.
 - **Severity: Critical** as a large amount of scientific data would be mission from the expedition
 - **Mitigation:** The drone will not be flown during night time or in bad lighting conditions
 - **Effect of Mitigation:** The probability of the event is reduced to **Improbable** as instead of being the result of a lack of light it may occur by chance due to shadows. These shadows would likely reduced visibility for a very limited amount of time reducing the severity of the risk to **Negligible**

7.5 Verification and Validation

For each model made a number of verification tests are carried out to ensure the model is coded correctly. There are 3 pieces of code that need to be verified and these are the model for the drilling speed, the model for the drill arm structure and the model for determining the ground penetrating radar frequency. In addition, a framework is set up for how the models could be validated however these are not carried out as this is beyond the scope of this report.

7.5.1 Unit Tests

Collect and Return Speed Model

For the drilling speed code a number of unit tests are done based on the formula for the rate of penetration of the drill. The concept for the tests is to double, half or zero variables in the governing equations of the rate or penetration and drilling time formulas. It is important to note that some tests specifically influence one of the two formulas ensuring thus ensuring a lack of change in the result is also a test.

Table 7.3: Unit tests carried out on drilling speed model

Unit test	Expected output	Test Result
Doubling the WOB	Double the ROP and half the drilling time	Successful
Halving the WOB	Half the ROP and double the drilling time	Successful
Zeroing the WOB	Zero ROP and infinity error for drilling time	Successful
Doubling drill speed	Double ROP and half the drilling time	Successful
Halving drill speed	Half the ROP and double the drilling time	Successful
Zeroing the drill speed	Zero ROP and infinity error for time	Successful
Doubling the drill diameter	$2^{-\frac{1}{8}}$ change in ROP and quartered drilling time	Successful
Halving the drill diameter	$2^{\frac{1}{8}}$ change in ROP and 4x the drilling time	Successful
Doubling the sample mass	Doubling the drilling time and no effect on ROP	Successful
Halving the sample mass	Halving the drilling time and no effect on ROP	Successful
Zeroing the sample mass	Zero drilling time and no effect on ROP	Successful

Collect and Return Arm Structure Model

For the drilling structure code a similar logic is applied. Different parameters in the code are adjusted and the expected resultant output based on the formulas used is determined. This is checked for whether it is in line with the original equations. The results for this code are displayed below:

Table 7.4: Unit tests carried out on drill arm structural model

Unit test	Expected output	Test Result
Double density	Mass gets doubled	Successful
Half the density	Mass gets halved	Successful
Zero the density	Mass goes to zero	Successful
Double WOB	Total sigma doubles and Tau doubles	Successful
Half the WOB	Total sigma halves and Tau halves	Successful
Zero the WOB	Sigma and Tau reduce to zero	Successful
Double radius	$\frac{1}{4}$ bending stress and $\frac{1}{2}$ normal stress	Successful
Half radius	Double bending stress and double normal stress	Successful
Double thickness	$\frac{1}{2}$ bending stress and $\frac{1}{2}$ normal stress	Successful
Half thickness	4x bending stress and 2x normal stress	Successful
Double length	2x bending stress and no impact on normal stress	Successful
Half length	$\frac{1}{2}$ bending stress and no impact on normal stress	Successful

GPR Model

For the ground penetrating radar a simple model based on two simple formulas for the frequency and resolution are used. As the formulas are relatively simple verifying the code is not that interesting however validating the code with an eye on the assumptions is of more importance here.

Table 7.5: Unit tests carried out on GPR model

Unit test	Expected output	Test Result
Halving Depth	$2^{0.25}$ times frequency and $\frac{1}{2}^{0.25}$ resolution	Successful
Doubling Depth	$\frac{1}{2}^{0.25}$ times frequency and times $2^{0.25}$ resolution	Successful
Zeroing Depth	Error to infinity in code	Successful
Doubling beta	Double the frequency and half the resolution	Successful
Halving beta	Half the frequency and double the resolution	Successful
Zeroing beta	Error to infinity in code	Successful
Doubling K	$\frac{1}{\sqrt{2}}$ times the frequency and no effect on resolution	Successful
Halving K	$\sqrt{2}$ times the frequency and no effect on resolution	Successful
Zeroing K	Error to infinity in code	Successful

7.5.2 System Tests

Systems tests aid in finding errors in the connections between different parts of a model or piece of code. In this chapter, almost all the code written was based on a handful of formulas and most of the code did not contain many input or output functions. Based on this, it is decided that units tests are sufficient in verifying the code and that systems tests do not provide any added value.

7.5.3 Validation

The last step in ensuring the quality of the models built is validating the code. This means the outputs of the code are compared with experimental data to ensure the model is an accurate reflection of the real world. To do this a number tests are devised.

For the collect and return arm two models need to be validated. First of all, the drilling time calculated needs to be validated. This can be done by setting up a testing rig with the selected coring tool and relevant specifications. The drilling times from this test should be in line with those from the model. Secondly, the structure of the drill arm needs to be validated to ensure it is strong enough to withstand the drilling loads. To do this, the most realistic method would be to separately structurally test the parts of the drill arm for their critical loads. By separately testing each component the specific mistake in the model can be found rather than testing whether the model as a whole is right or wrong.

For the visual imaging, height mapping and ground penetrating radar the most effective method of validating whether the instruments are capable of making measurements as expected. The most effective way of doing these tests would be at Earth locations that have similar landscapes to that of Mars. A similar narrative applies to the gas measuring instrument and the dust composition magnets however, as it is difficult to replicate Martian environments for these instruments tests in a wind tunnel or laboratory would be more suitable.

8 Flight Operations Analysis

Flight operations covers many onboard aspects of the expeditions: the navigation system, the autonomy system, the human flight control methods, and the procedures surrounding emergency and abort situations are all covered in this chapter. These aspects of the design are vital for the proper functioning of the aircraft and the success of the mission, as together they help to guide the drone to the right locations and they ensure that the astronauts and the drone are safe. The flight control system, which uses many of the same sensory inputs as the autonomy and navigation systems, is covered in Chapter 12. After presenting the requirements and their compliance in Section 8.1, the details of the autonomy system are given in Section 8.2, including navigation, guidance, weather monitoring, and the hardware needed to carry out these tasks. The remote piloting methods are described in Section 8.3. The software required for the onboard computer and how it functions is presented in Section 8.4. Section 8.5 shows the layout of the hardware components. The in-flight emergency and safety procedures are listed in Section 8.6, and Section 8.7 details the risks associated with flight operations and their mitigation strategies. There is no verification and validation section in this chapter because no computer models were used to assist the decisions and designs made. The selected off-the-shelf components will be validated as described in Chapter 19.

8.1 Requirements

The requirements of this mission which are directly related to flight operations are listed in Table 8.1. Throughout the chapter, it is explained how each requirement meets its indicated compliance (given in the table's rightmost column).

Table 8.1: Requirements related to flight operations and their expected compliance

Index: DME-REQ-	Requirement	Compliance
SYS-AUT-01	The autonomy system shall be able to assess weather conditions.	Satisfied
SYS-AUT-02	The design shall be able to assess the state of all subsystems in flight.	Satisfied
SYS-AUT-03	The autonomy system shall be able to assess whether there are obstacles on the flight path.	Satisfied
SYS-AUT-04	The autonomy system shall be capable of determining the system's position with an accuracy of ± 0.15 [m].	Satisfied
SYS-AUT-05	The autonomy system shall be able to fly to a target point with an accuracy of ± 0.50 [m].	Satisfied
SYS-AUT-06	The autonomy system shall be able to fly at a target height with an accuracy of ± 0.15 [m].	Satisfied
SYS-AUT-07	The autonomy system shall assess wind velocities with an accuracy of ± 1 [m/s].	Satisfied
SYS-AUT-08	The autonomy system shall assess visibility with an accuracy of ± 50 [m].	Satisfied
SYS-AUT-09	The autonomy system shall provide flight path planning to the target location(s).	Satisfied
SYS-AUT-10	The autonomy system shall be capable of determining the system's attitude with an accuracy of ± 0.1 [deg].	Satisfied
STN-09	The instruments and sensors used on the UAV shall have expected minimum lifetimes of 2 years.	Satisfied

8.2 Autonomy System

The top-level requirements specify that the drone must be capable of semi-autonomy. A semi-autonomous flight mode alleviates the burden of constantly controlling the drone from the astronauts, and frees them to work on other tasks. Semi-autonomy does however require some input from the astronauts in terms of choosing the expedition type and target location(s). Once these are given, the autonomy system of the drone then handles flight path planning, obstacle avoidance, determination of the UAV's position and orientation, assessment of danger, and whether to abort the flight. The methods for how the drone will perform these duties are described in sections 8.2.1 to 8.2.3, and the relevant hardware and sensors selected for reference are given in Section 8.2.4.

8.2.1 Positioning and Attitude Determination

Determining the position of a drone on Mars is not as straightforward as on Earth. There is no global navigation satellite system (GNSS) available on Mars and it is not assumed that one will be available by the time this mission is taking place. Mars' magnetic field is very weak and unreliable, making magnetometers or compasses ineffective. Inferring height from a barometer's pressure measurements is also not feasible due to how thin the atmosphere is [13]. For these reasons, the drone will have to determine its location by making observations about its surroundings. The methods explained in this section, along with the hardware detailed in Section 8.2.4 satisfies requirement **SYS-AUT-04** and partially satisfies requirements **SYS-AUT-05** and **SYS-AUT-06** (which are fully satisfied together with the methods explained below in Section 8.2.2).

The primary method of state-estimation to be used by the drone is a visual-inertial odometry (VIO) algorithm, a type of sensor fusion. This algorithm uses visual information from at least one camera and inertial measurements

from an inertial measurement unit (IMU) to assess the movement of the drone and to infer the drone's position. In particular, the algorithm assesses a stream of images from the camera and identifies how objects track across in the field of view. By combining the camera data and the IMU data, the drone can estimate its pose (both its position and its orientation in 3D space). This is already possible and has been implemented [13], and the algorithms and image processing are certain to improve over the coming years before this mission begins. Each aspect of the positioning and attitude determination is described in the following paragraphs. Because Mars is a challenging environment for flight and in order to ensure redundancy (and possibly improved accuracy), the drone will often make use of more than one method to complete the same task. Vision measurements alone from a single camera have been shown to provide extremely accurate assessments of orientation (down to 0.01°) [168], so it is reasonable to assume that the suite of techniques explained below will be able to meet the accuracy requirements for determining position, orientation, and height.

Vision

The drone will need multiple cameras for a number of reasons. First, multiple cameras positioned in various places and pointing in various directions allow for a very wide total field of view, giving the autonomy system good overview of the drone's surroundings and reducing blind spots. This is beneficial for terrain recognition and weather observation conditions. Second, multiple cameras ensure redundancy: even if one or two cameras fail unexpectedly, the autonomy system should still have enough visual information to perform its tasks successfully, although with larger blind spots than usual (as identified in the risk analysis, see Section 8.7). Third, more than one camera pointing in the same direction allows for binocular vision, which can help to make the VIO algorithm more accurate and efficient [79].

The visual part of the VIO algorithm takes in the camera data and applies image processing and/or correction to reduce blurring or distortion. It then searches for features in the images and tracks them by checking subsequent frames of input and correlating them to find differences and to determine how the features move across the images. After searching for and eliminating outliers, the visual data is ready to be combined with the inertial data. It is then linearized and solved, and an updated state estimation is made [169]. This algorithm should be designed to work for normal flight, where features move across the frame according to the ground velocity of the drone, and during vertical take-off and landing, where features scale and appear/disappear from view as the drone rises/descends.

There are a number of potential problems and limitations with the visual side of VIO. First, take-off and landing are challenging because of the small distance between the downward-pointing cameras and the ground (see Section 8.5). This causes problems since most of the field of view will be filled with only a small area of ground, likely in shadow from the wings and body of the aircraft, so little useful visual information can be parsed [13]. Second, the VIO algorithm tends to need relatively high contrast in the images in order to correctly identify and track surface features. This means that certain ground textures (stony areas) provide easier tracking than others (rolling sand dunes). The time of day also plays a role, as the Sun casts larger and more defined shadows in the morning and evening than it does around midday. The midday Sun lights the ground quite evenly, making features harder to detect for downward-pointing cameras [13]. However, the wide total field of view of the cameras should mitigate this effect, as features can be identified from many different directions. Third, the positioning of the cameras has been chosen to give an almost full view of the ground below and past the horizon during normal steady flight (see Section 8.5). During turns, the cameras will be angled differently, covering less of the ground and more of the sky. However, as long as this is properly accounted for in the autonomy systems' programming, this should not be a significant problem. Fourth and finally, the bending from the aerodynamic loading on the wings will cause the cameras located at the wing tips to move during flight. Camera shaking effects can be reduced by using image stabilization software to provide a smoother video feed. Slower movements (due to the relatively constant bending in the wing) are less problematic for the VIO software and these deflections can be estimated based on testing of the wing structure before the mission.

Accelerations

An integral part of VIO is, of course, the inertial measurement unit (IMU). This unit contains sensors for measuring linear and angular accelerations. The acceleration data from these sensors is integrated to give (angular) velocity, position, and orientation information. All of this data is used by the VIO algorithm as an input to help to determine the drone's current pose and how it is changing over time. It can also be used to help the algorithm to understand the changes seen in the images when the drone is performing a turn, for example. Since IMUs are prone to drift (a small sensor error which grows over time), IMUs in drones on Earth often include magnetometers to allow for in-flight calibration [35]. Since Mars' magnetic field is not suitable for this [13], this design will instead calibrate the IMU with a different method. Here, the visual side of VIO can help out: if, for example, the IMU is giving a reading which indicates that the drone is rolling slowly to the left, but the camera feeds indicate that the drone is level and steady (by observing the horizon), the IMU's roll axis sensor can be calibrated back to zero.

Positioning

The autonomy system must be able to accurately determine the drone's position in 3D space in order to fly to the correct target location and to ensure that the scientific data collected is useful. Positioning will take place using a combination of techniques. As explained, 10 cameras will be placed on the drone to give it a good overview its surroundings. Since the VIO algorithm traces objects across the field of view of the cameras and changes in acceleration are measured by the IMU, the drone's change in position can be inferred as a result. Since this method alone is susceptible to drift because of the IMU however, terrain recognition can also be used to increase accuracy.

At the beginning of the mission, the drone would have a low-resolution 3D topographic map of the area surrounding the base. By analyzing the terrain seen from the onboard cameras, including the features on the ground below and larger features such as hills on the horizon, the drone could verify its position in 3D space with respect to the value found through the VIO algorithm.

Because of the severity of a scenario in which the VIO algorithm fails, it is important to include a back-up/secondary positioning method, as identified in Section 8.7. For this mission, an appropriate choice is positioning using multilateration. This is similar to how GNSS systems work, only in this situation the drone would be using the communications beacons instead of orbiting satellites. If the drone has line of sight with all three beacons, the guidance system sends a signal antenna out to the three communication beacons on the ground (see Chapter 9 for more detail on these) and measures the time taken to receive a signal from each beacon. Since the speed of light in Martian air is known and the locations of the beacons are known, the signal's return journey time can be used to calculate the distance to each beacon. However, since there are only three beacons in total, this method alone would result in two solutions for location (since the general intersection of three spheres is a set of two distinct points). Therefore, understanding of the surroundings through terrain recognition is needed in tandem with multilateration to determine the position of the drone for certain. Since height above the ground is also measured separately (see next paragraph), this information can also be included to help to distinguish which of the two solutions from the multilateration is the correct one. This method is an appropriate back-up for positioning in case the IMU becomes faulty or not functional.

Height Measurement Method

During any kind of flight, it is important to know the distance between the vehicle and the ground, as it will affect flight path planning, maneuvers, aerodynamic performance, and communications. While this can be determined to a degree from positioning, it is beneficial to have a dedicated instrument for height measurement for accuracy and redundancy. Given the accuracy problems of measuring height using barometric pressure [13], it has been decided to use a laser altimeter to measure the distance between the drone and the ground using the time of flight principle. This will be placed on the underside of the drone in the payload module, pointing directly down. The Ingenuity helicopter also uses laser altimetry to measure its distance from the ground [58]. However, Ingenuity's laser altimeter has a range of only 40 [m] (its expected maximum altitude was only 10 [m] [22]), and these kinds of compact altimeters typically have ranges only up to a couple hundreds of meters unless special reflective surfaces are used. Therefore, an alternative method of determining the drone's height must be used for higher-altitude activities and for use as a back-up: multilateration using the communication beacons on the ground.

As explained above, multilateration (in combination with terrain recognition) can be used to determine the drone's position in 3D space as long as the antenna has line of sight with all three beacons. This can therefore be used as a back-up method of height measurement. The altitude from this method would likely be calculated relative to the Mars vertical datum. This could then be converted to height above the ground through the use of a topographical map. Note that this brings two sources of uncertainty into this measurement: the inherent uncertainty from positioning using multilateration and the error in the topographic map.

Velocity

Knowing the aircraft's ground velocity is important for flight control and performance (some velocities are more energy efficient than others) and for expedition reasons (estimating time until arrival at a location, which is also useful information for power/energy management). The VIO software is capable of determining accelerations, velocities, and positions by combining visual data with (integrated) inertial data. This will be the primary velocity measurement method for the drone. In the same way that multilateration is an alternate method for positioning (which can act as a back-up or just as extra information for improved accuracy), it is also an alternate method of velocity measurement. The ground velocity of the drone can be calculated by measuring the time between subsequent position readings.

Measuring airspeed is also important for flight control and performance, and can be used as part of the weather monitoring system (see Section 8.2.3). While pitot-static tubes are the standard method for determining airspeed on Earth, they come with a number of problems, which are worsened when considering flight on Mars. Pitot-static tubes calculate airspeed from the measurement of a pressure differential (between total and static pressure), but they can be inaccurate if the pressure differential is small (when flying at low velocities) [104]. With an atmosphere as thin as Mars', pressure differentials would always be very small and thus pitot-static systems would not be appropriate on Mars. Furthermore, a pitot-static tube needs to stick out of the aircraft into the airflow, where it causes additional drag and where it is susceptible to damage [111]. An alternative is to use a newer technology: a laser airspeed sensor. These instruments send ultraviolet lasers into the air in front of the aircraft and measure the scattering of the light. Based on the observed wavelength change due to the Doppler effect, the airspeed can be calculated. These sensors work equally well at low or even negative airspeeds [111], making them highly appropriate for a VTOL drone.

8.2.2 Flight Path Planning

Given a target location, the autonomy system must be able to plan and follow an appropriate flight path to that location. This will be possible with the use of an algorithm combined with data about the terrain surrounding the base. 3D topographic maps of Mars are already available thanks to Mars-orbiting satellites, though the resolution is not as high as is achievable in this mission through height mapping. As the mission progresses, the height map information collected by the drone can be used to update the satellite-measured topography to give higher fidelity.

These maps will be essential to successful flight path planning. The implementation of an algorithm like the one described here would satisfy requirements **SYS-AUT-03** and **SYS-AUT-09**, and partially satisfy requirements **SYS-AUT-05** and **SYS-AUT-06** (which are fully satisfied together with the methods explained above in Section 8.2.1 and the hardware explained below in Section 8.2.4)

The essential inputs and processes of the algorithm can be seen in the flow diagram in Figure 8.1. In general, the algorithm will be designed to minimize the energy usage of getting to the target location. Thus, it chooses a straight flight path if possible, with an energy-optimal climb path, cruise altitude, and descent path. These will vary depending on the distance to the target location, as there is a balance between spending energy to climb higher, saving energy by reducing drag, and aerodynamic effects of lower Reynolds numbers at higher altitudes. There are then a series of checks and corrections to make the route feasible in the real world, including checking the topographic map and weather information for obstacles along the flight path (hills, cliffs, dust storms/devils). If any such obstacles come within a predefined safety radius, the flight path will be amended with a wide berth around the obstacle(s). Finally, an energy estimate is made for the entire expedition, and the batteries are checked for their charge.

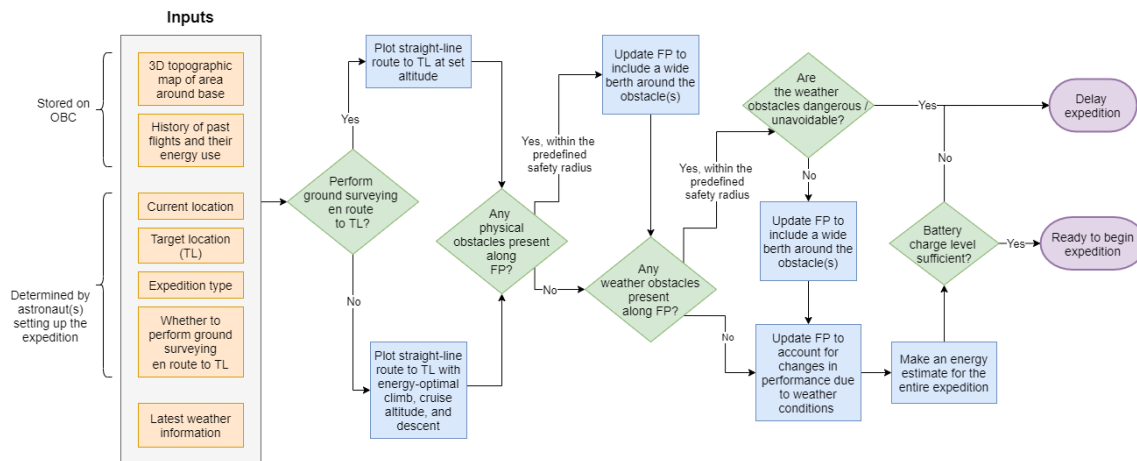


Figure 8.1: Flow chart showing the inputs and processes of the flight path planning algorithm

During the flight, the autonomy system will continually monitor the flight path to check that it is followed properly. The flight path may be updated in-flight, in any of the following cases: 1) new updated commands are received from the base which include alterations to the expedition type or target location; 2) updated weather information is received from the base which indicates the presence of dust storms/devils in the flight path, the target area, or between the drone and the base; 3) the autonomy system identifies dust storms/devils or other weather changes through its own observations which may affect the expedition (see Section 8.2.3); 4) the autonomy system notices discrepancies between the observed terrain and the expected terrain from the topographic map; and 5) an abort command is received from the base. For cases 1 to 4, the autonomy system must make a decision itself on what to do, which in many cases will be to simply update or plan a new flight path with regard to the new information. The drone may also decide to abort the expedition and depending on the identified severity of the new situation, it will follow one or more of the procedures explained in Section 8.6. In case 5, the drone immediately aborts the expedition and plots a route for the base.

8.2.3 Weather Monitoring

Monitoring weather conditions during expeditions is important for ensuring the safe return of the drone to the base. While weather updates from orbiting satellites can provide useful updates, they may not be comprehensive and they may miss smaller weather developments such as dust devils. Requirements **SYS-AUT-01**, **SYS-AUT-07**, and **SYS-AUT-08** state that the autonomy system must be capable of assessing wind velocities, visibility, and general weather conditions. These requirements can be satisfied by using the techniques described in this section.

Low visibility can make flying difficult on Earth, but on a Mars drone which relies heavily on visuals for navigating, it may be detrimental. Although the thin atmosphere may lead to better visibility than on Earth in ideal conditions, suspended dust can often cause the atmosphere to be hazy and results in worse than visibility on Earth [114, 32]. Therefore, it is important that the drone can assess visibility. It will do this primarily through image processing software: by utilizing techniques such as edge detection, filtering, comparison with images of known visibility, uniformity segmentation, and contrast ratios, it is feasible that software processes could accurately determine atmospheric visibility [118]. The accuracy such software can also be expected to increase as the image processing algorithms improve and more (Mars-specific) data becomes available for training these algorithms, and thus it is reasonable to assume that this will be able to comply with requirement **SYS-AUT-08**.

Dust storms are a danger to the drone due to the large amounts of suspended fine dust and because they provide extremely low visibility. These can again be detected through image processing and object detection software. This (machine learning) software would likely use similar techniques to the visibility determination software, to de-

tect local patches of sky with lower visibility. It would also be trained with datasets of images of dust storms so that it can understand and recognise typical shapes or formations caused by dust storms. Similarly, object recognition can be applied to dust devils, which have distinct shapes and movements.

In order to guarantee stability, it is useful for the flight control system to understand wind conditions. While wind speed cannot be directly measured on an aircraft, it can be inferred by comparing ground speed to airspeed. Both ground speed and airspeed can be calculated as described in Section 8.2.1, using VIO/multilateration and a laser airspeed sensor, respectively. Wind speed can then be calculated simply by taking the vector difference of these measurements.

Air temperature is another environmental characteristic which has an effect on the Mach number, thermal control system, and the scientific results of the mission (as it would give context to atmospheric readings). Therefore, a simple thermometer should be placed on the outside of the drone, outside of the drone's thermal boundary layer which can regularly measure the air temperature.

8.2.4 Hardware

This section will present the sensors and instruments selected for carrying out the tasks of the autonomy system, all of which are off-the-shelf components. The make and model of each piece of hardware is given, as well as some of the most important specifications. Note that all of these items are selected for reference to show that the described design would be possible. Since this mission takes place in the future, different models which perform similar functions will likely be available at the time of production. These models are likely to have even better performance than what is available on today's market. Alternatively, hardware such as the onboard computer could be built to specification with this exact mission in mind. Since the selected instruments are high-grade consumer products, it is expected that each of them will withstand at least two years of operational use without failing, assuming that proper inspection and maintenance procedures are followed. This therefore satisfies requirement **STN-09**.

Cameras (Vision)

The camera model to be used as reference is the RunCam 5 Orange. This camera is designed for first-person view (FPV) drones on Earth, so it has a high resolution and a wide field of view. Its resolution is 4000×3000 (12 megapixels, 4:3 aspect ratio) with a frame rate of up to 60 frames per second and has a built-in image stabilization chip. The entire camera weighs only 56 [g], uses 3.1 [W] of power, and measures $3.8 \times 3.8 \times 3.6$ [cm]. The standard lens gives a field of view of 145° [124], which is quite a wide viewing angle. This camera is also used for reference for the payload tasks of performing visual imaging and height mapping (see Chapter 7). Since there are 10 cameras placed around the drone for the autonomy system, their total mass is 0.56 [kg] (excluding wiring and thermal control) and their power usage is 31 [W] (also excluding thermal considerations). These cameras will be used by the autonomy system for VIO, flight path planning, terrain recognition, and weather assessment, and will be used to provide a video feed for the human remote control mode (see Section 8.3 and Chapter 9).

The RunCam camera is used for reference in this design, but it is possible that omnidirectional (360°) cameras may become the more desirable option in the future. These would generally require lenses that stick out from the aerodynamic surface in order to make full use of their wide field of view, but as the technology improves, this may become more feasible. The feasibility for this design will also depend on the camera quality and resolution, as well as the achievable data transmission rate. For now, the drone will be designed with the previously described 10 RunCam cameras in mind.

IMU (Accelerations)

The IMU to be used on the drone is the Bosch BMI088, which combines a high-accuracy accelerometer and gyroscope into a unit designed specifically for drones and robots. The detectable linear acceleration range can be selected, with the options being $\pm 3 g$, $\pm 6 g$, $\pm 12 g$, and $\pm 24 g$, as can the detectable gyroscopic range, with five options between ± 125 [°/s] and 2000 ± 125 [°/s] [132]. Both have 16-bit resolution, dividing the detectable range into 2^{16} increments. Depending on the selected ranges, this gives resolutions between 0.09 and 0.73 *mg* (accelerometer) and between 3.81×10^{-3} and 3.05×10^{-2} [°/s] (gyroscope). This unit is a small chip with dimension of only $3.0 \times 4.5 \times 0.95$ [mm] and has a mass of just 0.67 [g] [132]. It can provide data output at rates between 12.5 and 2,000 [Hz], it draws up to 0.019 [W], and it has an operating temperature range of -40 to 85°C . Since these units are important to the proper functioning of the VIO algorithm (as identified in the risk analysis, see Section 8.7), and because they are so small, light, and low power, two are included in the design for redundancy. This instrument allows the design to satisfy requirement **SYS-AUT-10**.

Laser Altimeter and Antenna (Positioning and Height Measurement)

The chosen laser altimeter sensor for low-altitude height measurement is the LightWare SF30/D LiDAR sensor. This infrared laser device has a mass of only 35 [g], dimensions of $30 \times 56.5 \times 50$ [mm], power usage of 0.55 [W], and can measure distances between 0.2 and 200 [m] to an accuracy of ± 10 [cm] at a rate of 49 to 20,000 readings per second [81]. It also features an alarm setting to send a signal if a distance is measured below a predefined value. While the listed operating temperature range is -10 to 50°C , it is not an unreasonable assumption that this may be widened to -25 to 50°C through further technological advancements over the coming years, especially when looking at other laser altimeters with similar optical ranges. As explained in Section 5.3.1, most of the surveying tasks of the UAV will take place at an altitude of approximately 100-200 [m] in order to achieve the desired ground

resolution for visual imaging and height mapping. Therefore, this sensor will be useful during take-off, landing, and for the duration of most ground surveying activities.

Multilateration will be carried out with the help of the onboard communications antenna. Details about this component can be found in Section 9.2.3.

Laser Airspeed Sensor (Airspeed)

While laser airspeed sensors have been developed and tested, they are not yet in regular use, and so off-the-shelf options are not available. Therefore, assumptions must be made about the characteristics of such a sensor. Based on the specifications of other products which use similar measuring principles (such as radar speed guns [50], optical speed sensors for measuring rotations [84], and non-contact optical sensors for road vehicle testing and racing [34]), it is reasonable to assume that a laser airspeed sensor would be approximately the size, shape, and weight of a medium handheld flashlight or microphone. Assumptions about this sensor include: a cylindrical shape with a 40 [mm] diameter and a length of 150 [mm]; a mass of 0.2 [kg]; a power consumption of 10 [W]; an operating temperature range of -25 to 50°C; an accuracy of <1 [m/s]. Two of these sensors would be required on the drone; one to measure airspeed in the direction of flight and one to measure airspeed in the cross wind direction (it was decided that the vertical airspeed is not important enough to include an additional sensor).

Thermometer (Air Temperature)

The type of sensor to be used to measure air temperature will be a Pt1000 sensor, which is a platinum resistance thermometer. Since the relationship between platinum's temperature and its electrical resistance is known, temperature can be calculated by measuring the resistance through the sensor. This type of sensor was used on the Curiosity and Perseverance rover missions for measuring air temperature, and typically has a wide temperature range (150 to 300 [K]) and high accuracy (better than 0.9 [K] "in the worst case" [122]). Perseverance's air temperature sensors were passive instruments [55], so the power usage can be expected to be negligible in this mission as well. The dimensions can also be expected to be similar, at around $5.7 \times 2.5 \times 6.9$ [cm] [102].

Computer Hardware

All of the tasks of the autonomy system and other subsystems on the drone will require a small and powerful on-board computer (OBC). The software and required programs for this computer are described in Section 8.4. Since computer technology typically changes and improves very quickly, the best available components for a drone's OBC will be quite different by the time this design is actually produced. For this reason, a representative product which is currently on the market will be used for reference for the OBC's hardware. This will be a combination of the DJI Manifold 2-G and the DJI Manifold 2-C. These computers are designed for autonomous drones, and each has different specialties: the 2-G features a powerful GPU (NVIDIA Jetson TX2) for performing object recognition, motion analysis, and image processing, while the 2-C houses a powerful CPU (Intel Core i7-8550U) and is appropriate for autonomous flight, data analysis, and communications. Together, they feature 16 GB of DDR4 RAM, 384 GB of SSD storage, and multiple USB and other ports. Their combined mass is around 450 [g], their maximum power usage is 85 [W], and they each have dimensions of $91 \times 61 \times 35$ [mm] and operating temperature ranges of -25 to 45°C [40]. Using two separate computers also allows for redundancy, thereby mitigating the risk identified in Section 8.7: each computer will have access to the most essential software needed to fly and land safely so that the failure of one computer will not cause the drone to crash.

8.3 Human Remote Control

The top-level requirements specify that the drone must be capable of being remotely controlled by humans on the ground. This means that astronauts at the base should be able to choose the trajectory and actions of the drone without needing to specify an expedition type or target location beforehand. The human controller will not be responsible for controlling every aspect of flight such as adjustments to the control surfaces to ensure stability or the precise thrusting of the propellers required for take-off or other maneuvers. The drone already includes a flight control system and an autonomy system which are capable of performing flights independently of human control, so it is logical to utilize these capabilities to simplify the experience for the astronaut. This also reduces the amount of training the astronauts require before they can remotely operate the drone.

At the base, the controller will conduct operations from a computer with a display and a control stick setup. A video feed will be continuously broadcast from the drone to the base. The controller has the choice of which camera feed to view and can switch between views to look around the environment to find points of interest. There will be an overlay on the display which shows the controller important flight information such as velocity, altitude, location, orientation, remaining charge in the batteries, weather conditions, and housekeeping information for various subsystems. This kind of data can be transmitted from the drone to the base almost instantaneously, but the video feed comes with a slight delay of around 0.3 seconds (see Chapter 9). This is another reason why the human controller only controls high-level functions of the drone.

In general, the human has control over the flight path, velocity, flight altitude, making turns, deciding where to land for soil sampling, and which instruments are operational. The autonomy and flight control systems are active throughout the flight are responsible for keeping the aircraft stable, controlling the rotor speed, tilting the rotors, staying within the flight envelope, providing information on positioning and velocity, providing weather informa-

tion, warning the controller about potential dangers (obstacles, dust storms, etc.), and taking over control from the controller if nothing is done to avoid the dangers.

Since the controls are quite simple, the astronauts responsible for operating the drone remotely would likely not need advanced pilot training on Earth. They would however require training on the drone, its purpose, its design, and its dynamics, as well as training with a simulator to practise the remote operation of the drone. This would be done on Earth before the astronauts' departure to Mars, and simulation practise could even continue during the transit to Mars. For more details on astronaut training, see Section 16.2.

8.4 Onboard Computer

The onboard computer (OBC) will be responsible for a host of data processing and decision making tasks. The computer hardware used for reference in this design is described in Section 8.2.4. Here, the software and programming side of the OBC will be described briefly.

In terms of general software, the OBC first needs an operating system for task scheduling and managing the systems resources, such as processing power and memory. The operating system is also the main hub for connecting different pieces of software or external devices. The OBC also needs system management software for monitoring all subsystems for problems (thereby satisfying requirement **SYS-AUT-02**) and scheduling long-term tasks (such as activating payload instruments, changing power configurations, or activating thermal control modes). Payload management software monitors the payload instruments and acts as the interface between the payload and the rest of the drone, helping to ensure that it is oriented correctly for observation, for example. It also handles the collection, compression, and storage of the scientific data. These responsibilities slightly overlap with the command and data handling (CD&H) software, which handles housekeeping and subsystem health data and prepares it for transmission to the base. Depending on the software setup, the CD&H software may also be responsible for the collection, compression, and storage of some data [160]. Communications software is also needed for handling the transmission of data back to the base through the antenna, and for decoding and processing commands received from the base.

Some of the more specific software functions have already been mentioned above. Guidance and navigation software is required as part of the autonomy system for determining the location of the drone (using VIO, terrain recognition, and multilateration as described in Section 8.2.1) and for plotting and monitoring flight paths (including obstacle avoidance, as explained in Section 8.2.2). Separate weather software would also be included specifically for analyzing atmospheric conditions and the visual data from the onboard cameras to calculate wind speed and visibility, and to detect dust storms and dust devils (as explained in Section 8.2.3). The autonomy system also needs programming and software for making high-level decisions, such as whether to change course to avoid a dust devil, or whether to abort an expedition. Flight control software is needed to determine how the drone can ensure its own stability through the movement control surfaces and controlling of velocity. Software is also needed to manage the human remote control mode, to interpret inputs from the base and to convert those into actions for the subsystems. Finally, simulation software is required so that astronauts can get a feel for remotely operating the drone and understanding its behavior during their training.

Much of this software will need to be developed for this mission, as most of it is very specific and would not be available in another format from a previous mission. This would occur in the 'Research Software Systems for Autonomy', 'Develop Software Systems for Autonomy', and 'Develop Procedure for System Integration' blocks of the Project Design & Development plan (see Figure 20.1). Much of the flight control and simulation software would need to be developed following preliminary production and testing of parts to ensure that the flight dynamics are properly understood.

8.5 Layout

All of the hardware selected needs to be placed on or in the drone in such a way that it is able to perform properly, without interfering with any other subsystems. This section describes the positions of all of the hardware components discussed above.

8.5.1 Camera Placement

The drone will make use of 10 cameras (including the camera used for the payload) to provide a wide view of the ground beneath. No cameras are oriented to look up into the sky because this would rarely provide any useful information for the autonomy system or for a human remote pilot. Each camera has a horizontal field of view of 145° and a vertical field of view of 108° , except the payload camera, which has a field of view of $72 \times 54^\circ$.

An overview of the camera locations and their respective fields of view from three different perspectives can be seen in Figures 8.2, 8.3, and 8.4. The naming of the cameras in the winglets follows from the direction they point and which winglet they are on. F, O, I, and B stand for Forward, Outward, Inward, and Backward, while L and R stand for Left and Right. The payload camera points directly downward from the fuselage of the drone. One camera is placed in the nose of the aircraft, pointing forward. Each winglet houses four cameras: one at the leading edge which points forward, one at the trailing edge which points back, and two in between with one pointing inward and the other pointing outward. The nine non-payload cameras all point slightly downward such that the vertical field of

view extends 18° above and 90° below the horizon. Placing cameras in the winglets mitigates the problem of dust being kicked into the air during take-off and landing, since they are placed relatively far from the propellers. Since the camera units will be larger than the thickness of the winglet airfoil (especially at the trailing edge), additional panelling will need to be manufactured which can accommodate the cameras.

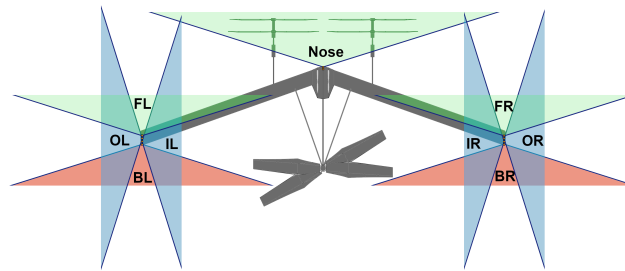


Figure 8.2: Top view of drone showing camera fields of view

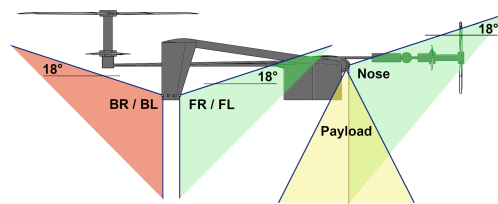


Figure 8.3: Side view of drone showing camera fields of view

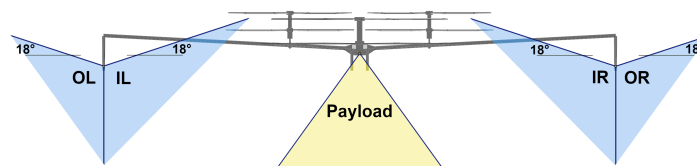


Figure 8.4: Back view of drone showing camera fields of view

8.5.2 Placement of Other Components

The IMUs, laser altimeter, and OBC will all be located in the payload module in the main fuselage of the drone, near the payload instruments. In order for the laser altimeter to point directly down toward the ground during cruise, it will need to be installed at a slight angle (equal to the cruise angle of attack plus the offset angle of the fuselage, or approximately 10°). When flying at other angles (during take-off or landing, for example), the reading from the altimeter will need to be adjusted appropriately using a simple trigonometric relation. This setup allows for the best accuracy during cruise, which is how the drone flies most of the time. The laser altimeter can be seen as the dark red block in Figures 8.5 and 8.6 (note that the small installation angle is not indicated). The IMUs will be placed on the inner walls of the payload module, with the primary IMU on the bottom (seen as a very small green rectangle dot in Figure 8.5) and the back-up IMU on the side wall (not pictured in the figures). The OBC is located near the front center of the payload module, such that it has access to other components through cabling. It is the black box in the figures below.

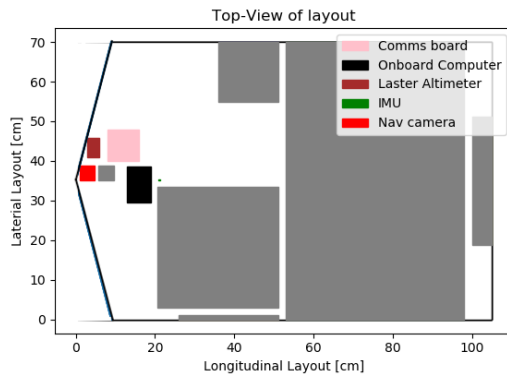


Figure 8.5: Top view of layout with different colours referring to different instruments

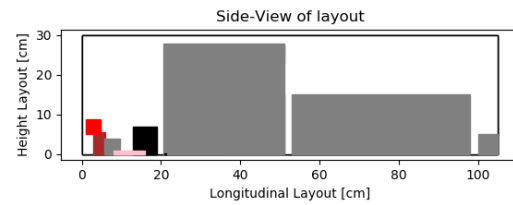


Figure 8.6: Side view of layout with different colours referring to different instruments

The two airspeed sensors will be integrated into the wing (see Figure 6.1). One will be oriented in the direction of flight, such that it can measure airspeed in that direction. The other will be oriented perpendicular to the first, such that it can measure crosswind speeds. Both will require small cut-outs in the wing structure so that they have access to the outside world.

The thermometer needs to be placed such that its readings are not affected by the thermal control system, ensuring that it is measuring the outside air temperature. It will therefore stick out from the underside of the fuselage. The appendage which holds the thermometer will also act as a thermal insulator, protecting the thermometer from the heated fuselage.

8.6 Procedures

This section explains some of the procedures which will occur if certain problems occur during flight. Problems may include the malfunctioning of an instrument or the detection of a dust storm. The drone's programmed response to these problems will depend on their severity. These procedures are put in place primarily to ensure the safety of the drone. Take-off and landing procedures are described in Chapter 12.

General Abort Sequence

The abort sequence may begin for a number of reasons: the autonomy system may detect a danger, a critical component may be malfunctioning, or the crew may send an abort command from the base. In any case, the abort sequence is the same. First, a notification is sent to the base to let the crew know that the drone is aborting its current expedition. The target location is then set to be the base, and a flight path is plotted. Depending on the severity of the situation which caused the abort, or depending on commands from the base, the drone may fly above its normal cruise speed to return more quickly. Throughout the flight back to the base, the base crew will be able to take over control of the drone if they feel it's necessary. They may also decide to cancel the abort, thereby continuing the previously set expedition.

Detection of Danger Procedures

The autonomy system has multiple methods for detecting dangers, and will also have the capability of categorizing these dangers as minor, mild, or serious. A minor danger may be wind speeds which are slightly higher than expected, or the failure of a non-critical instrument such as the thermometer. The autonomy system will typically be able to deal with these problems without any intervention from the crew. As opposed to a minor danger, a mild danger may negatively affect the scientific outcome of the expedition. It may be that a scientific instrument is malfunctioning, or that a dust storm has been identified along the flight path. A serious danger is something which is an immediate threat to the safety of the drone. This may be the failure of a critical function or piece of hardware, such as one of the OBCs.

If a mild or serious danger is detected, an abort request notification is sent to the base. The crew may respond by: 1) approving the abort request, thereby initiating the abort sequence, 2) entering human remote control mode, or 3) forcing the expedition to continue (if they determine that the danger is not actually dangerous). In the case of a mild danger, the drone will wait 60 seconds for a response, and in the case of a serious danger, it will wait only 10 seconds. If the drone does not receive a response within the time limit, it initiates the abort sequence by default.

Other Malfunctioning Procedures

If the drone is in human remote control mode, it is possible that a malfunction occurs which prevents the human from continuing to control the drone. This may be as a result of a problem with the onboard antenna or a communications beacon, for example. As identified in the risk analysis in Section 8.7, this could cause the loss of the drone if no procedures are in place. Therefore, the procedure will simply be to monitor incoming commands: if the connection

is lost or if commands cease, the autonomy system will take over again. A notification will be sent to the base that this has happened (if possible), and the autonomy system will execute a flight path back to the base. If the connection is re-established, the human remote controlled flight may continue as before. This procedure follows from the mitigation strategy for risk FLOR-5 (see Section 8.7).

If any part of the weather monitoring system fails, this will not be considered critical for flight safety. If any sensors or processes in this system are malfunctioning, a notification will be sent to the base containing details on the problem. The drone then will rely solely on the weather updates from the base weather system rather than on its own observations/measurements. Other weather sensors or processes that are still functioning normally will continue to do so. If the visibility or dust storm detection processes are affected, astronauts will be advised to check the video feed from the drone regularly to manually look for dust storms on the horizon or to assess visibility. This procedure follows from the mitigation strategy for risk FLOR-6 (see Section 8.7).

8.7 Risk Analysis

A number of risk have been identified related to flight operations. Often, these risks involve the failure of a certain component or system during an expedition where they cannot be directly solved by an astronaut at the base. This makes it important to include redundancy or back-up methods, as can be seen in the mitigation strategies listed below. These strategies have been taken into account in the descriptions given previously in this chapter. The code FLOR is used to denote a flight operations risk.

- **FLOR-1 - One of the onboard cameras fails during flight**
 - **Effect:** Reduced visual information is available to the autonomy system for guidance/positioning/weather monitoring, and more limited options for human remote controllers to view surroundings.
 - **Probability: Probable**, as it is likely that a connection will fail at the camera itself will malfunction at some point during the mission.
 - **Severity: Critical**, depending on which camera fails, the autonomy system may have a difficult time positioning itself or maintaining a flight path back to the base.
 - **Mitigation:** Include 10 cameras in total, together giving an (almost) full view of the ground below, up to and just past the horizon.
 - **Effect of Mitigation:** If one camera fails, there will still be plenty of visual information available to the autonomy system, so it can continue to function normally. Severity reduced to **Negligible**.
- **FLOR-2 - IMU fails or gives faulty readings**
 - **Effect:** VIO algorithm loses a significant input source or is provided with faulty information.
 - **Probability: Occasional**, at some point during the mission the IMU may become damaged or dislodged from its position.
 - **Severity: Critical**, depending on how exactly the VIO algorithm works, it could lead to severe problems with positioning and guidance. Chance of hard landing which may cause structural damage.
 - **Mitigation:** Include a spare IMU onboard and include code in the VIO algorithm which checks the validity of the readings based on the incoming visual information.
 - **Effect of Mitigation:** If the VIO algorithm identifies a problem from the primary IMU, it can switch to taking readings from the back-up IMU. Reduces severity to **Negligible**.
- **FLOR-3 - VIO algorithm fails**
 - **Effect:** Drone is no longer able to determine/measure its own position, speed, acceleration, or orientation.
 - **Probability: Rare**, since this algorithm would be very well tested before the mission.
 - **Severity: Catastrophic**, would almost certainly lead to an uncontrolled crash since the drone is effectively blind.
 - **Mitigation:** Include a back-up positioning method: multilateration. By sending signals to the communications beacons and measuring the times to receive responses, the drone can narrow its location down to two points (since there are three beacons). It can then determine the exact position using terrain recognition or the laser altimeter or both.
 - **Effect of Mitigation:** Allows positioning in most areas (beacon coverage is not 100%), reduces severity to **Marginal**.
- **FLOR-4 - Onboard computer fails**
 - **Effect:** All scientific processes and all essential flight processes cannot continue.
 - **Probability: Occasional**, a malfunction at some point during the mission is possible, even though such a critical component would be well tested before the mission.
 - **Severity: Catastrophic**, would almost certainly lead to an uncontrolled crash.
 - **Mitigation:** Include 2 OBCs with shared functionality. Allow each to perform critical functions needed for carrying out an abort sequence flight back to the base.
 - **Effect of Mitigation:** If one OBC fails, the other can take over the essential functions while the processing of scientific and other data is put on hold. This allows the drone to fly back to the base safely. Reduces severity to **Marginal**.
- **FLOR-5 - A malfunction occurs preventing human remote control from continuing**

- **Effect:** The drone (in human remote control mode) stops receiving control commands from the base and continues in a straight line.
- **Probability: Probable**, due to the low technology readiness of the communications subsystem and the less than 100% coverage in the region surrounding the base. Other malfunctions may also cause this risk.
- **Severity: Catastrophic**, the drone would continue to fly away until its batteries run out and would either crash or become lost or both.
- **Mitigation:** If no commands are received for a set amount of time, the drone automatically returns to semi-autonomous mode and flies back to the base. It continues to look out for signals from the base to continue the remote controlled expedition.
- **Effect of Mitigation:** Remote control malfunctions will not lead to crashes or the loss of the drone. Reduces the severity to **Negligible**.
- **FLOR-6 - Weather monitoring systems fail**
 - **Effect:** Can no longer detect wind speeds, air temperature, visibility, dust storms, etc.
 - **Probability: Occasional**.
 - **Severity: Marginal**, as these systems are useful but not critical for flight. Flight performance and thus energy efficiency may decrease. Dust storms may not be avoided as quickly as they should be (but external weather systems would eventually notify the base, leading to commands to avoid the dust storm or return to base).
 - **Mitigation:** Notify base if any readings from weather instruments are malfunctioning. If applicable, astronauts will then be advised to check the video feed from the drone regularly to manually look for dust storms on the horizon.
 - **Effect of Mitigation:** Reduces severity to **Negligible**.

9 Communications Analysis

Regardless of the expedition type, the communications subsystem is a significant component that enables the drone to communicate with the base in order to provide control and/or manage the transfer of data. In this chapter the communication subsystem of the UAV is presented. A simulation is run to size the beacon network. After the analyses are performed, the overall communication architecture is presented with a flow diagram. To ensure that the communication links are supported, a link budget is calculated. Finally, verification and validation is performed to ensure that the numerical model complies with the specifications and requirements.

9.1 Requirements

In Table 9.1 the requirements that should be fulfilled by the communications subsystem and their compliance is presented.

Table 9.1: Requirements related to communications and their expected compliance

Index: DME-REQ-	Requirement	Compliance
SYS-COM-01	<i>(Driving)</i> The communication subsystem shall transfer live video feed for entirety of the expeditions.	Satisfied
SYS-COM-02	The communication subsystem shall have at most 3 seconds of delay for imaging data.	Satisfied
SYS-COM-03	The communication subsystem shall have at most 0.5 seconds of delay for command data.	Satisfied
SYS-COM-04	<i>(Key)</i> The communication subsystem shall be single point failure free.	Satisfied
SYS-COM-05	The communication strategy shall comply with the rules and regulations set by the International Telecommunication Union.	Satisfied
SYS-COM-06	The communication subsystem shall transfer at least 0.0025 [kBps] for entirety of the mission.	Satisfied

9.2 Model and Analysis

Based on the requirements that were presented in Section 9.1, three communication strategies with two different means were identified to be feasible for the mission. The first two were by use of beacons. A network of beacons or a single beacon at the base were identified as feasible options along with usage of satellites. In this section all these options are analyzed in depth.

9.2.1 Required Data Rates

Before elaborating on the communication strategies and choosing a feasible option, the required data rates are calculated. Considering the requirements on payload and commanding, it was established that there were various types of data that needs to be transmitted and received. The uplink data is that which goes from the base or controller to the UAV, also called the commanding data. The downlink data is that which goes from UAV to the base, and consists of imaging data, a live video feed, ice detection data, control data, and navigation data. All data rates, except the ones for commanding data and live video feed, were supplied by the payload providers. As a result, the values in Table 9.2 are obtained.

Table 9.2: Required Data Rates

Data Type	Data Rate [kBps]
Imaging Data	12.50
Live Video Feed	27468
Ice Detection Data	10.00
Control Data	0.9296
Navigation Data	0.1392
Commanding Data	0.0025

In order to calculate the data rate of the live video footage, resolution is taken as 1280×720 pixels with 30 frames per second and a bit depth of 8 bits per pixel. This resulted with a data rate of 27.648 [MBps]. Note that this is the amount of raw data. Hence, it is possible to perform image compression. If ICER compression is used this value can be decreased to 3.46 [MBps] [74]. Meanwhile in order to calculate the commanding data, a simple data packet format is assumed. The data packet consists of a start statement, includes acknowledgments and the message bit and ends with an end statement [28].

9.2.2 Beacon Analysis

Using beacons to provide contact with the base during semi-autonomous flight or in human controlled flight provides an efficient communication strategy. It is especially advantageous due to its dual purpose for position estimation.

It is important to consider that the performance of the beacon network is closely related a combination of various factors. These factors are include the height and locations of the beacons. Hence, before performing an analysis on the beacon network and beginning optimization, a preliminary decision was taken in order to simplify the beacon network and ensure that construction of the model can be carried out in an straightforward manner.

- The optimum height of the beacon is 10 [m]. Therefore by transporting the beacons in a disassembled state, they can comply with the launcher dimension requirements while obtaining the highest amount of coverage.
- It was assumed that a maximum of two beacons, apart from the one in base, can be placed by astronauts. This assumption limits the amount of manual work that has to be performed by the astronauts outside of the base.
- The beacons operate at S-band with a frequency of 2.4 [GHz]. This is a common band for Earth based beacons.
- Each beacon within the network includes a solar panel for power generation and batteries for power storage.

Numerical Model

Having obtained the set of decisions that describe the characteristics of the communication strategy, a model can be created to simulate the efficiency of the beacons and analyze it to an even further extent. This is mainly performed by considering the coverage of the beacons. The coverage is highly related to the placement of beacons, thus the line of sight, and height of beacons. Therefore, a numerical model is constructed considering all these relations.

The model begins running with constructing the elevation map of the site around the base, and places the first beacon at the base. Depending on the first placed beacon, which is the base for this scenario, the area of 50 [km] radius is constructed and identified with a red circle, as can be seen in Figure 9.1. Every time a beacon is placed, first the code calculates the distance between the UAV and that beacon. Then the code goes through every point in this distance and interpolates the data set to obtain the height that UAV has to fly in order to be in line-of-sight of the beacon. If the data set contains a zero this indicates that when UAV is at 0 [km] altitude, therefore on the ground, it can be in contact with the beacon. Using the number of zeros in the data set and size of the data set, the coverage of a beacon at the ground level is calculated as a percentage.

From the preliminary analysis it was determined that a beacon network of three beacons (including the base beacon) is an optimum setup. This was due to logistic reasons as well as technical reasons. Therefore, in order to verify this analysis and find the most optimum location for the two non-base beacons, a Monte Carlo method is used.

It should be noted that the image is downsized and the model runs with iterations. In order to output more accurate results, these two values can be altered. Therefore, if different downsizes run for the same iteration number, it is expected to see a higher output, thus coverage, for the code with a lower downsize. This is due to the fact that as downsizing increases, the pixel information is altered as any unneeded pixel is discarded during image processing. Therefore, in order to get more accurate results, the downsizing should be kept as small as possible.

Note that as downsize is decreased, it requires more time to process the image, because of the higher resolution. Therefore, if the iteration is set to be a high value, the code could run for weeks before outputting a result.

Beacon Placement

Initially, the simulation is run to evaluate the height required by a single beacon to cover the entire circular area. Having only one beacon at the base is not a feasible option. In Figure 9.1, it can be seen that with downsizing of 20, a 1000 [m] high beacon only gives around 95.7% coverage, while a beacon of 10 [m] height gives a coverage of 32.2%. Having a beacon of 1000 [m] tall is not possible due to the height restrictions that are imposed by the launcher. Furthermore, astronauts have to manually place the beacons around the base, in the indicated locations. Therefore, it would be enormous amount of laboring to carry the infrastructure to build a beacon structure of 1000 [m] tall. Note that, although the beacon could be placed on top of a balloon that is tethered to the base and suspended 1000 [m] above the ground, dust storms are significant threat for such balloons. Although the turbulence reduces at such high altitudes, the abrasive properties of the dust are still a threat. Especially for such a mission that requires high durability for a long lifetime.

Therefore, using a network of beacons is the most suitable strategy. Usage of one beacon of 10 [m], additional to base, yields a coverage around 50-60%, however this value is increased to 65-75% when the number of beacons outside of the base is set to be two. As literature suggests, with increasing height, the line-of-sight improves [99]. Hence, off the ground, it is expected to see even higher values of coverage. Indeed, once the code is run for UAV that is flying at 100 [m] altitude, the coverage for a beacon network of 2 beacons with 10 [m] height is 92%. This satisfies the requirement **SYS-COM-01**.

Below in Table 9.3 coverage and most optimum beacon placement that is obtained for different iterations and downsize values are presented. As it can be seen from the table there are multiple locations that output the best location for the optimum coverage. Meaning that there might be more than one set of locations that outputs 74.5% coverage when downsize is 3 and iteration number is 1000. Hence, out of these set of locations, the one that is not on top of the hill and closer to the base will be preferred. This is decision is taken manually, in order to reduce the laboring that has to be performed by astronauts while planting the beacons around the base.

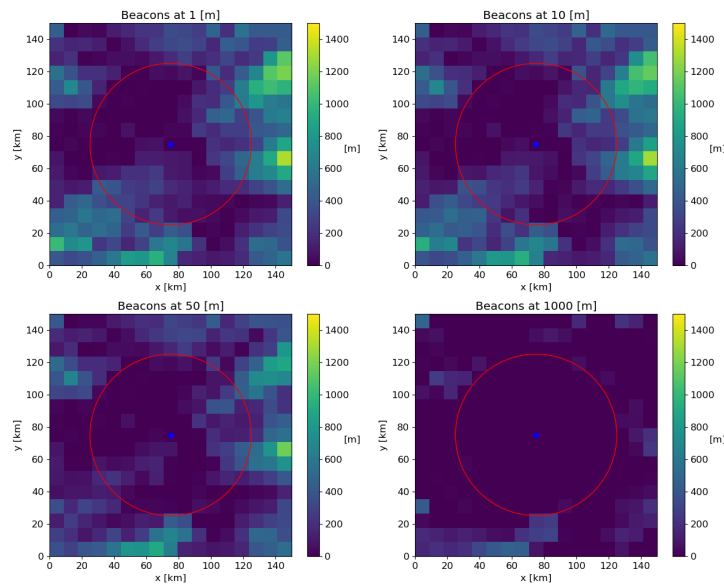


Figure 9.1: Coverage for only one beacon at the base

Table 9.3: Coverage and most optimum beacon placement for different iterations

Downsize	Iteration	Placement	Coverage
20	100	(75.0, 75.0), (65.02, 37.15), (65.02, 111.46)	67.7%
20	1000	(75.0, 75.0), (83.60, 111.46), (65.02, 46.44)	70.7%
3	1000	(75.0,75.0), (86.38,26.47), (66.88,101.71)	74.5%

Power Sizing

Once all the architecture of the beacon network is constructed, battery and solar power sizing is carried out. This is primarily performed in order to ensure that the whole beacon structure complies with the launcher requirements on the size. From the preliminary analysis it was obtained that the power required by each beacon would be around 2 [W]. Regarding a mission of 2 hours it was possible to obtain various characteristics for batteries and solar panels on board of beacon system. The sizing of the battery is achieved by following the procedures on Section 14.2.2 and the sizing of solar panels is performed by following the steps in Section 14.2.1. As a result Table 9.4 and Table 9.5 is constructed.

Table 9.4: Sizing of Batteries

Characteristics	Value
Minimal Battery Capacity [Ah]	1.96
Battery Energy stored [Wh]	6.49
Battery Volume [L]	0.0168
Battery Mass [kg]	0.023

Table 9.5: Sizing of Solar Panels

Characteristics	Value
Area of Solar Panels [m ²]	0.0054
Mass of Solar Panels [kg]	0.0027
Capacity [Ah]	1.45
Energy Produced [Wh]	4.785

Beacon Architecture

Once it was identified the power supply system of the beacons and height of the beacons are decided on, the beacon structure is constructed. It was previously elaborated that, having a balloon attached to a beacon, gain the required height, is not a favorable structure. Therefore, in order to raise the beacon to 10 [m], a simple pole is chosen. Although pole structures are not too advantageous in terms of load carrying, this is the scenario for Earth conditions. On Mars, gravity is around one third of gravity on Earth, therefore regarding this and low density of the wind, 20 [kg] of an initial estimate is made for the beacon structure. The estimation followed the same steps that were taken in Chapter 10. In Figure 9.2a the beacon structure is presented. The red box represents the beacon while two dark grey boxes represent the solar panels. Meanwhile, in Figure 9.2b the placement of beacon on top of the tower, along with placement of solar panels and with battery is visualized.

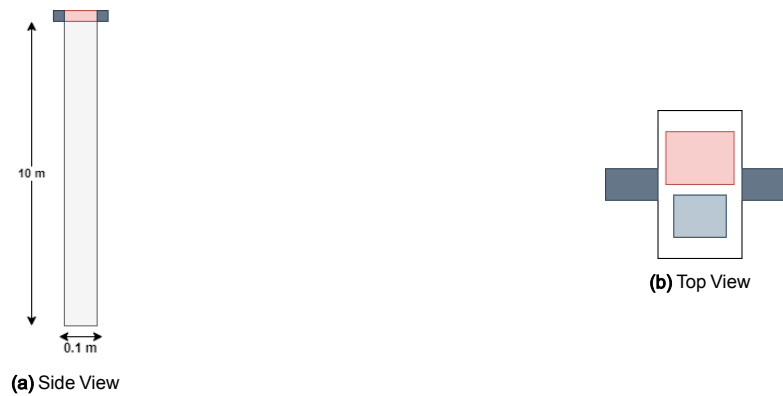


Figure 9.2: Beacon tower

9.2.3 Satellite Analysis

Antenna Choice

A type of antenna that is considered for space missions is omnidirectional antennas. This type of antenna receives and transmits signals equally from all directions, thus the antenna does not require pointing. Therefore, the UAV does not need to alter its position to receive or transfer data. This is a large advantage over a pointed antenna, however it results with lower received power.

The communication between the UAV and an orbiter around Mars is short range communication, since the signals are not reaching to a ground station on Earth. Therefore, it is feasible to use an omnidirectional UHF antenna system. This type of antenna is used mostly in CubeSats and a few NASA missions, including the Perseverance rover [101]. Regarding the specifications of the UAV and the data that has to be transferred from payload, taking the Perseverance rover as a model for sizing would result with a more accurate antenna size than taking a CubeSat as a model. Looking at previous missions, preliminary estimates for the communication subsystem are given below:

- Ultra-high frequency (UHF) transceiver on board of UAV.
- Mass of the antenna is around 2 [kg] [7].
- Power required by UHF antenna is around 20 [W] [139].

Delay Calculations

As it was mentioned previously, communication in this mission does not require contact with Earth. Therefore, even though this Mars to Mars communication is considered as a short range communication, there is still a chance of delay being present when transmitting or receiving data from the base.

It is highly possible that a transmission delay, which is the delay due to time taken for data to be transmitted across a link, and a propagation delay, which is the delay due to time taken by first part of the signal to be transferred from sender to receiver, are present. Hence, in order to obtain the delay and perform the calculations accurately, few points have to be taken under consideration.

- All payload data is not transferred with the communication link. Only images, video footage, telemetry data and commands require transmission via the communication link, as the data provided by other scientific payload is transferred once the UAV is landed back at the base. Among all these, imaging data requires the highest data rates, see Figure 9.3. Therefore the delay calculations were going to be performed regarding the imaging data.
- In order to fulfil the height mapping requirements, a camera of 8 megapixel resolution is used.
- When satellite is at the closest point to surface of Mars, the distance between the UAV and the satellite is 400 [km]. This value is obtained regarding operational orbiters, such as Mars Reconnaissance or 2001 Mars Odyssey, closest points to surface of the planet and the height that can be reached by the UAV [45].
- It was defined that the maximum data rate that can be carried by the orbiter is 6 [Mbps] [69]. This value defines the maximum amount of data that can be transferred per second and it is used to calculate the delay of the downlink, from orbiter to base on Mars surface.
- It was defined that the maximum data rate that can be carried by the UAV is 256 [kbps] [138], which is used for calculating the delay of the uplink, from UAV to orbiter.

Once all these considerations were made, it was elaborated that transferring images that has 8 megapixel, (3840×2160 p), is not efficient. Since the requirements on imaging suggests that much information is going to be redundant, down-scaling and compressing the imaging data before transfer became a feasible option. Compression technique is chosen to be ICER compression, of decreasing the bit depth down to 0.25 bits per pixel. Furthermore, since it does not interfere with compliance with the requirements, the bit depth is decreased from 8 bits per pixel, which is the amount provided by the camera, to 1 bit per pixel [74]. Meanwhile, down-scaling allowed images to be 1080×720 pixels.

Therefore when the bit depth is taken as 1 bit per pixel and the resolution is dropped to 1080×720 pixels, the total amount of pixels that need to be transferred by the UAV is 777600 pixels. Since one pixel corresponds to one bit, the image also consists of 777600 bits. Therefore the transmission delay of the link is calculated as:

$$t_{\text{trans}} = \frac{L}{B} \quad (9.1)$$

in which L refers to length of the package and B refers to bandwidth of the link. Therefore, adapting Equation 9.1, the transmission delay from UAV to orbiter is calculated as:

$$t_{\text{trans}} = \frac{777600}{256 * 10^3} = 3.0375[s] \quad (9.2)$$

Following the same procedure the transmission delay from orbiter to base is calculated to be 0.0162 [s]. Meanwhile, the propagation delay is calculated regarding the location of the satellite in the orbit. Since it was assumed that the satellite is 400 [km] above the UAV, the propagation delay is calculated as:

$$t_{\text{prop}} = \frac{d}{s} \quad (9.3)$$

where d is the distance and s is the propagation speed. Since the communication link is carried through radio waves, propagation speed is equal to speed of light. Therefore propagation delay is calculated to be 0.00133 [s]. Finally, all these added up to calculate the total delay, which is the overall time that take to transmit data between UAV and base, of 3.055 [s]. This value can be decreased further to 0.777 [s] by keeping number of pixels same and decreasing the bit depth.

Looking at other missions on Mars that contact with an Earth ground station, it expect to encounter with a delay between 3 to 22 minutes [96]. In order to avoid catastrophic results that could be associated with these large values, commands are predefined and sent in advance considering the last image that is received from the rover, or in this scenario drone, and map of Mars [68]. Same procedure is also followed for the drone, decreasing the probability of failure. Therefore, it is feasible to assume that delay of 3.055 [s] is an upper bound that is acceptable by the mission to be used as an emergency link but not as a primary link, since it still poses a risk of failure.

9.2.4 Link Budget

Having the communication architecture obtained, a link budget can be constructed. It is significant to calculate the link budget as it determines whether or not the data can be received with adequate signal to noise ratio. Since the communication architecture in the mission consists of two links, primary and emergency, two link budgets are calculated, as it can be seen in Table 9.6 and Table 9.7. Throughout these calculations, various design choices were made, these are presented below.

- Any antenna characteristic that are related to pointing, such as pointing offset angle or pointing loss, were set to be zero, since an omnidirectional antenna is chosen for both links.
- System noise temperature for the emergency link budget is estimated to be 1000 [K]. The value is obtained considering the galactic noise and the physical temperature of Mars.
- The system noise temperature for the primary link budget is estimated to be 135 [K].
- A swath width angle of 10 degrees is assumed. Depending on the area that want to be imaged this value can be altered. Note that up until swath width of 70 degrees the link margin is closed.
- The modulation type is estimated to be 8FSK for both link budgets. This effects the required signal to noise ratio and resulted with a value of 10 dB.

Table 9.6: Primary Link Budget: UAV to Beacon

	Unit	Value
Received SNR	dB	14.63
Required SNR	dB	10
Margin		4.63

Table 9.7: Emergency Link Budget: UAV to Orbiter

	Unit	Value
Received SNR	dB	18.63
Required SNR	dB	10
Margin		8.63

Note that if the signal to noise ratio is low, meaning if there is more noise power than signal power, the link budget can be altered by changing the efficiency of components in the transmitter and receiver chain. Moreover, in the further iterations, the modulation type can be altered to save power within the system. This power is called the coding gain and if it is high enough, the transmitter power or antenna sizes can be altered, to adjust the link margin.

9.3 Risk Analysis

Either in autonomous or human-controlled state, the drone is being operated without an on board operator. Therefore, it is significant to maintain contact with the base, in order to assess the state of the drone at any given time. Therefore, the main risk related to the communication subsystem is loss of contact with Mars base. In order to comprehend the consequences of this risk, below the in depth elaboration of such risk is presented.

- **CR-1/Communication subsystem Risk - Loss of communication with Mars base**
 - **Effect:** Could lead to a crash or missing the target
 - **Probability:** Loss of communication is thought to be **Occasional** due to the untested nature of such a system on another planet.
 - **Severity: Catastrophic**, could lead to a crash.
 - **Mitigation:** UAV needs to enter a predefined abort sequence to be performed if loss of communication persists, that applies for both the human-controlled and semi-autonomous flight modes.
 - **Effect of Mitigation:** The procedures serve to reduce the severity of the event, but have no effect on the probability. This is due to the fact that the reliability of the communication system stays the same. The severity will be reduced to **Marginal** due to the UAV initializing abort procedures.

9.4 Communication Flow Diagram

Since communication subsystem include components that are also operating outside of the UAV, the layout of the communication subsystem can be visualized with the overall communication architecture. This architecture is presented in Figure 9.3, along with the communication flow diagram which visualizes the flow of data through the whole communication architecture. Two different arrow types are used to represent different links. The continuous arrows represent the primary communication link, in which the communication between UAV and the base is supported by a network of beacons. This link is the primary preference for the communication and it is valid as long as UAV is in the coverage range of beacons. In any case the beacon network is out of reach the secondary link will be activated. This link is acting as an emergency link and fulfilling the single point failure free requirement for the communication subsystem. In the diagram secondary link is represented with noncontinuous arrows.

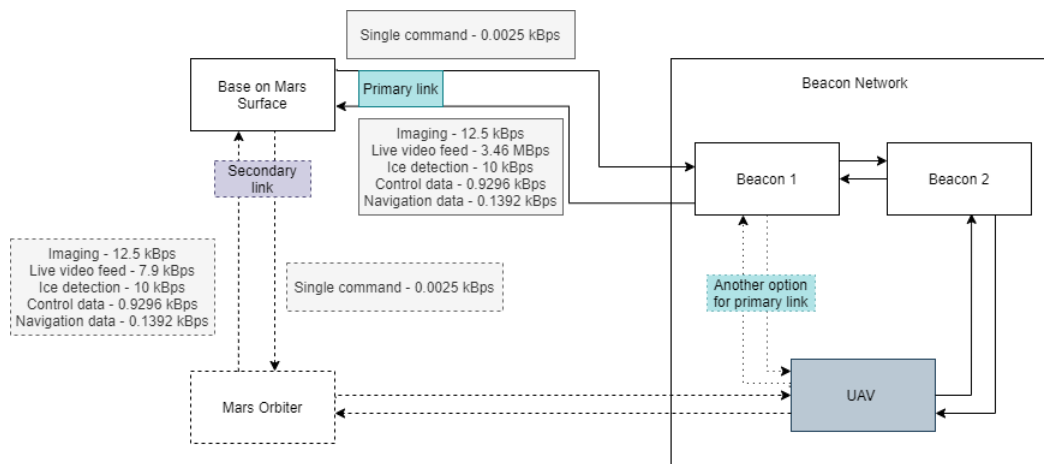


Figure 9.3: Communication flow diagram

9.5 Verification and Validation

9.5.1 Unit Tests

Unit tests are performed in order to test the smallest individual components within the big blocks of code. By doing so it is verified that each unit of the code performs as anticipated.

Circle Unit Test

The area, which needs to be discovered, around the base is defined with a circle of 50 [km] radius in the code. In order to check whether or not this area is defined correctly, the first unit test is performed by changing the location of the base. It was expected to observe a shift in the circular area, since the base is located at the center of the circle. Indeed, once the alteration is performed the results were as expected. As it can be seen in Figure 9.4 if the location of the base is shifted from (75,75) to (100,100), the whole area shifts to right.

9.5.2 System Tests

In order to ensure that the integration between these individual components are correct and complete, system tests are performed on larger sections of the code. Regarding the characteristics of the model, the system tests are performed in a similar manner. It was decided to alter various components and observe the output coverage. The tests that are performed are presented below.

Data Size Test

Currently, the model is obtaining the coverage for only the circular area around the base, since that is the area to be explored by the UAV. However, while maintaining the amount of beacons, if the data size is increased from only the circular area to the square area that is visible on the graphs, as it can be seen from Figure 9.4, it is anticipated to observe a decrease in the coverage. This is due to the fact that now the same amount of beacons at the same

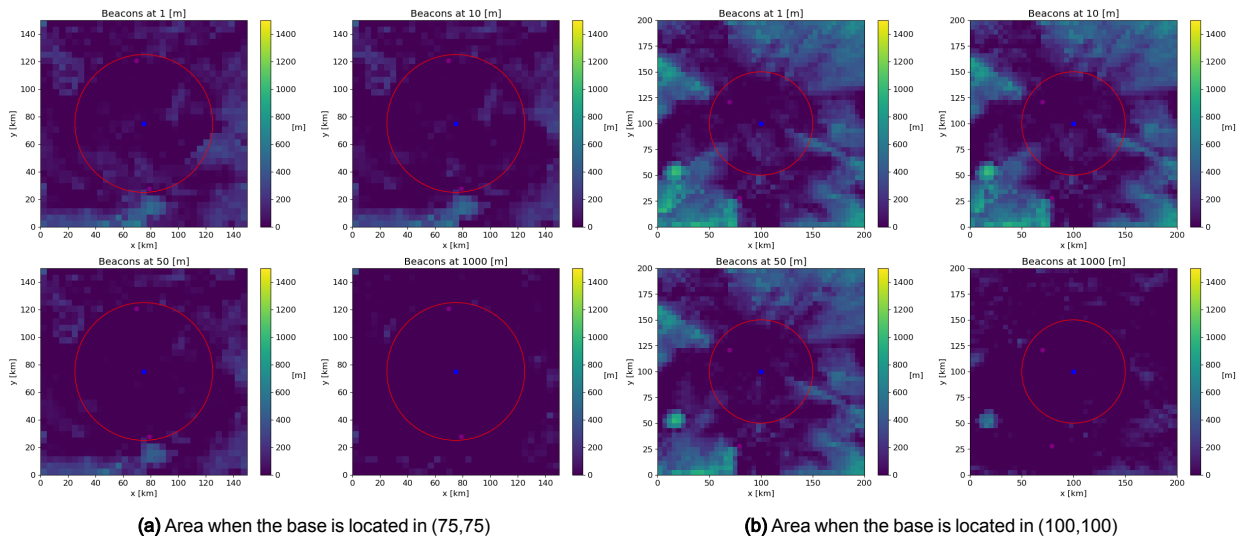


Figure 9.4: Shift in base

location have to cover a larger area. In fact, once both the downscaling and iteration is set to be 10, and the locations of the beacons are (75.0, 75.0), (97.54, 32.52), (78.95, 106.82) the coverage for the circular area is 68.69%, while the coverage of the square area is 37.56%.

Beacon Height Test

Height and coverage of a beacon are directly related, this is due to the fact that in order to have a line of sight that is clear from obstacles, it is significant to add height to the beacon or placement should be on a high point. Therefore in order to ensure this relationship is captured accurately in the model, the height of the beacon is decreased from 10 [m] to 2 [m] for the beacons that are placed at the same location. As it was expected, this resulted the coverage to drop from 52.90% to 39.61%.

Radius Test

Simple beacons that are generally used on Earth, 2.4 GHz, usually cover 10 [m] to 20 [m]. These beacons are also used to construct the model. Therefore, if the area around the central beacon is increased, while maintaining the amount of beacons and the placement of beacons, the coverage must be decreased. Therefore, in the model the radius is increased from 50 [km] to 80 [km], as it can be seen from Figure 9.5. As it was anticipated, this resulted with a coverage drop from 60.94% to 36.80% for a beacon of 10 [m].

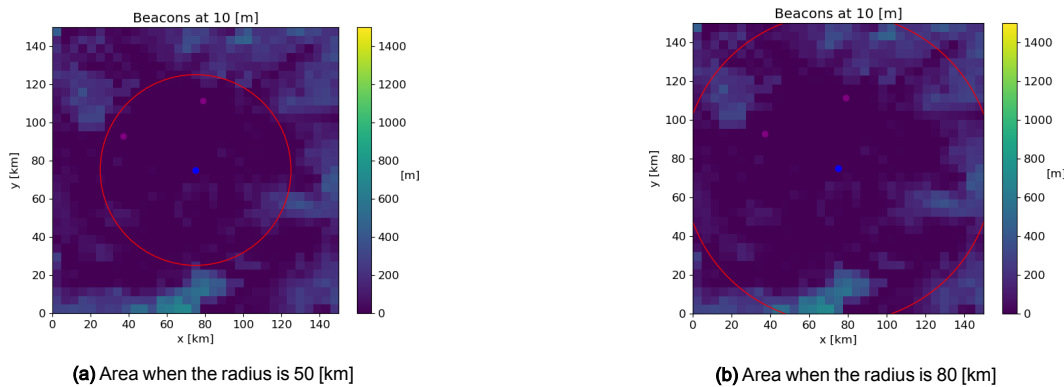


Figure 9.5: Increased area around the base

9.5.3 Validation

To ensure that model reflects the real life world it is significant to validate the results that is obtained from the numerical model. One way to perform validation is by comparing the numerical model response to an actual experiment. Laying the output of the numerical model along with the results of an actual experiment would give an indication whether or not the model output is similar to data measured.

However, it should be noted that in order to perform this validation, data from an actual experiment is missing. Therefore, a beacon network of three beacons with same area around the base should be constructed on Mars and the coverage of the network should be obtained. It is possible to perform the validation when the actual experiment is performed on Earth as well. However in that scenario, it should be noted that the majority of the discrepancies

will be due to different nature of the two distinctive atmospheres. Therefore for a more accurate validation the experiment should be performed in the Martian atmosphere.

It is reasonable to assume that discrepancies will be apparent when both data is obtained under same atmospheric conditions as well. First of all, there might be imperfections in the Martian atmosphere due to the harsh weather conditions. Furthermore, for simplification reasons the numerical model runs with assumptions, one example of this is the downsizing factor which scales 128 pixels per kilometer. This alters the resolution of the image thus effects the output. Finally, in the actual experiment it is more likely to experience external and internal interference with other components of the communication system. Eventually this will cause the data to be more noisy.

10 Structures and Materials Analysis

In order to make sure the UAV does not fail under the loads that it experiences during the mission, the structure of the system has to be carefully designed. Therefore, a number of structural requirements have to be satisfied. These requirements and their compliance are given in Section 10.1. In order to provide a better overview of the structure of the design, a layout is presented in Section 10.2. This is followed by a detailed description and analysis of the structural model Section 10.3. Then, an analysis on the possible risks of the structure is done in Section 10.4. Finally, verification and validation on the model is done and presented in Section 10.5.

10.1 Requirements

Table 10.1: Requirements related to structures and materials and their expected compliance

Index: DME-REQ-	Requirement	Compliance
TL-OPE-01	The design shall be able to be disassembled into sub-components.	Satisfied
TL-OPE-02	The design shall be able to be transported in its disassembled state.	Satisfied
SYS-GEN-06	The system shall be subjected to all the requirements that follow from the selected launcher.	Satisfied
SYS-GEN-07	The system shall be subjected to all the requirements that follow from the selected Mars landing module.	Satisfied
SYS-STR-01	The structural subsystem shall be capable of withstanding a maximum launch loads of $6g$ longitudinally [14].	Satisfied
SYS-STR-02	The structural subsystem shall be capable of withstanding a maximum re-entry load of $12g$ [159, 115].	Satisfied
SYS-STR-03	The structural subsystem shall be capable of withstanding the vibrational loads of 100 [Hz] both longitudinally and laterally [14].	Satisfied
SYS-STR-05	The structural subsystem shall be capable of withstanding the maximum loads during take-off and landing on Mars of 400 [N] in vertical direction.	Satisfied
SYS-STR-06	The structural subsystem shall be capable of withstanding the maximum loads during cruise flight on Mars with a limit load factor of $n = 2.5$.	Satisfied
SYS-STR-07	The structural subsystem shall be capable of withstanding the maximum loads due to its own weight of 400 [N] while at rest on Mars.	Satisfied
STN-08	It shall be possible for the operators on Mars to disassemble the UAV to access reusable components after end-of-life.	Satisfied

10.2 Layout

In this section the layout of the UAV is given, as well as a Free Body Diagram including the loads. As can be seen below, the structure is split up into three part: the VTOL propeller carrying structure (Figure 10.2a), the wing box (including forward propeller beams) (Figure 10.2b) and the main body (including landing gear) (Figure 10.2c). The UAV is assembled at the reaction forces and division lines that can be seen in Figure 10.1.

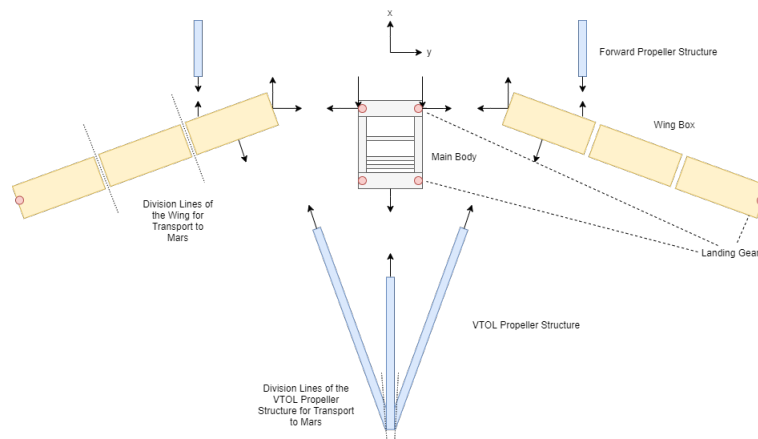


Figure 10.1: Free body diagram of the general layout containing the three analyzed components and the reaction forces between them. These are disassembled further for transport, where each wing is split in three and the VTOL propeller structure is split into the three separate beams.

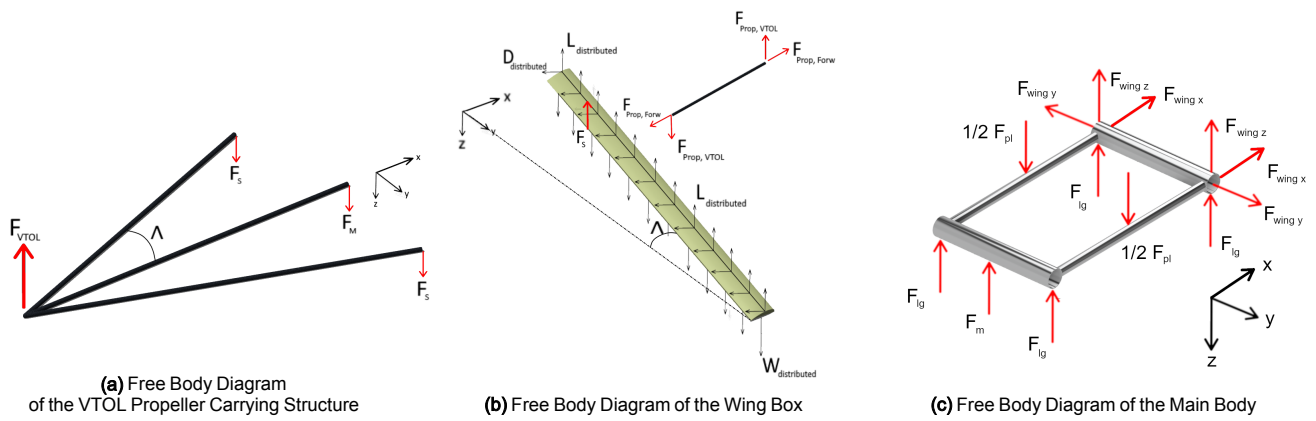


Figure 10.2: Free Body Diagram of the Different

Structural Components. It should be noted that reaction moments are not depicted for readability, but they are present and analyzed.

10.3 Model and Analysis

The design of the UAV’s structure is critical in supporting the other subsystems and components of the vehicle. The structural components should all be able to withstand the loads during operation on Mars, but also the loads during transportation to Mars. In this section, first, the load cases will be discussed and accounted for. This is followed by an analysis and description of the components described earlier during the mission on Mars.

10.3.1 Load Cases

To make sure the structure can survive all possible scenarios, several different load cases were identified. The method used to obtain them differs for the operational loads and the launch loads, both of which are described in this subsection. For evaluating the stresses a safety factor of 2 was used on all structural components as advised in [161], since the design is still in a phase that everything has been computed theoretically and no tests have been conducted. Every load case was then tested on every component, where the limiting load case was used as final sizing for the component.

Operational Loads

The loads were determined for four operational load cases: cruise; flight under limit load factor; the aerial part of landing and take-off under maximum thrust; and the touchdown part of landing, sized to drop the last 0.5 [m] from zero velocity to the ground. The loads were obtained by creating 3D free body diagrams of the three components and setting the sums of forces and moments to zero. By evaluating the propeller carrying structures first, the wing box second and the main body last, the reaction forces could be taken into account. The equations were derived and then put into a Python program to make sure the loads can be computed easily for different input parameters. The output of this program consists of a list containing the original input loads, the reaction forces and moments between the main structural components and the internal shear force and moment diagrams in the wing box. The most limiting loading diagram, the diagram for the wing box in z-direction under a maximum load factor of $n = 2.5$, is given as an example in Figure 10.3. Here it can be seen that the deflection is only approximately 8° , proving the small angle approximation is still valid satisfying **SYS-STR-06**.

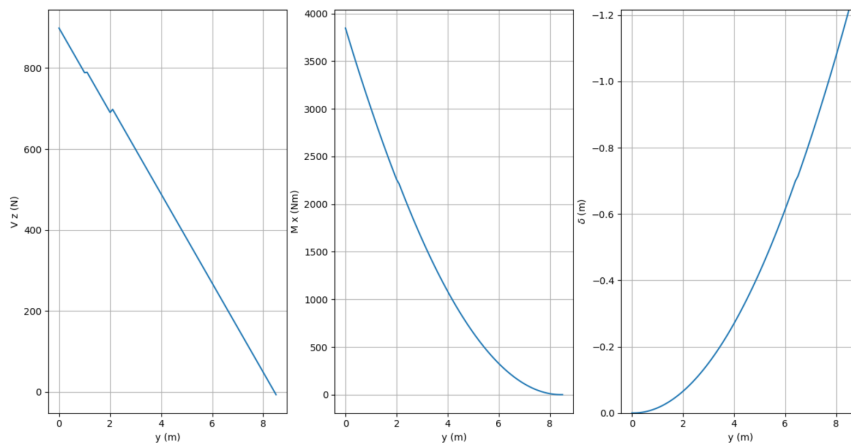


Figure 10.3: Loading diagram of internal shear force in the wing box in z-direction and internal moments about the x-axis and deflections in the z-direction (negative, since downwards is positive). The limiting load case is shown which is the case of the maximum load-factor of $n = 2.5$.

Launch Loads

During the transportation to Mars, the components of the design are exposed to certain launch and entry loads. In order to make sure that the design arrives in good condition, the structure has to be designed to withstand these extreme loads. During previous missions to Mars, the payload module has been designed to experience a peak deceleration of $12g$, satisfying **SYS-STR-01** and **SYS-STR-02** [159, 115]. Therefore, the launcher payload structure of this mission will also be designed to withstand this value.

Since the complete design is larger than the available dimensions in the launcher, it has to be split in different sub-assemblies such that it does fit, satisfying **TL-OPE-01** and **TL-OPE-02**. These components are disassembled on Earth, then transported to Mars, and finally will have to be assembled on Mars to complete the design. The decision was made to split up the design into the following separate components.

- Body of the UAV (including payload)
- Propeller carrying beams (2 forward with motor, 1 VTOL with motor, 2 VTOL without motor)
- All the propeller blades (split in the middle)
- Landing legs (6 in total)
- The wing split up in 6 parts

The landing structure will be a frame with the separate sub-assemblies attached under it as can be seen in Figure 10.4b. It is attached under the skycrane with explosive bolts to make separation possible for the landing maneuver. It features landing legs to be landed on from the skycrane, such that the components are not damaged by landing on them. The outer dimensions are $2.9 \times 2.7 \times 1.6$ [m], as specified as the maximum available according to requirement **SYS-GEN-12**. After landing, the frame can be disassembled to recover the beams used for sustainability, which satisfies **STN-08**.

During both the launch and the atmospheric entry a pushing force is applied to the bottom of the capsule, which is shown in Figure 10.4a along with the resultant load path into the payload. From this load path it was identified that the capsule pulls on the frame and in turn on the sub-assemblies, meaning that they are loaded in tension. The configuration of a preliminary frame and the sub-assemblies is shown in Figure 10.4b.

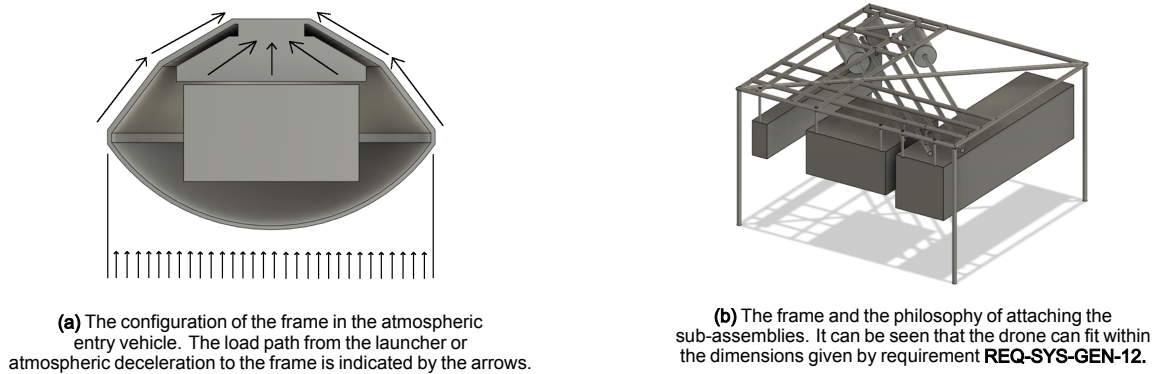


Figure 10.4: The launch configuration of the drone. The rectangle in figure (a) represents the outside dimensions of the frame in figure (b).

With the orientation, attachment points, and peak deceleration known, the loads on the sub-assemblies was computed and sized for. This load also acts on the rods connecting the sub-assemblies to the frame. Hence, the rods were sized to resist the tensile forces and to make the natural frequency of the suspended parts higher than the natural frequency of the launcher. This ensures that there is no resonance between launcher and payload. For this, it is assumed that the sub-assemblies are a point mass at the end of a beam. Equations for the minimum total cross-sectional area and moment of inertia of all rods attaching a certain sub-assembly to the frame were derived from [161]. Since the rods are pulled in tension, the minimum area could also depend on the allowable stress, hence the maximum of the two requirements should be used:

$$I \geq \frac{(2\pi f_{n_{lateral}})^2 mL^3}{3E} \quad (10.1)$$

$$A \geq \max\left(\frac{(2\pi f_{n_{longitudinal}})^2 mL}{E}, \frac{m g_{reentry}}{\sigma_{allow}}\right) \quad (10.2)$$

Where I is the moment of inertia of all rods attaching to a certain sub-assembly, A is the total area of those same rods, $f_{n_{lateral}}$ is the lowest natural frequency of the launcher in lateral direction, $f_{n_{longitudinal}}$ is the lowest natural frequency in launch direction, L is the distance between the point mass and the frame, and E and σ_{allow} refer to the Young's modulus and allowable stress of the frame material. Results for rods satisfying the launcher requirements given in **SYS-STR-03** in terms of vibrations are given in Table 10.2. Note that there may be additional struts between the parts to prevent them colliding with each other during launch. However, due to the current preliminary analysis of the frame, they are not added yet and should be investigated in the next phase. A preliminary mass estimate

for the frame is done by adding up the lengths of all beams currently present in the frame and computing the mass assuming it is entirely made up from the heaviest rods from Table 10.2, which are the connection rods to the propeller blades and have a diameter of 40 [mm] and a thickness of 4 [mm]. This gives an conservative initial mass of 56.6 [kg]. It can be concluded that in this phase, the launch structure will be able to support the drone during transportation to Mars, satisfying **SYS-GEN-06** and **SYS-GEN-07**.

Table 10.2: A possible configuration for connection rods from the frame to the various components. Note that it is not the final design since that depends on what the leftover space will be filled with. This is just a possible configuration to prove the feasibility of the frame design for transport.

Component	Amount	Length [m]	Diameter [mm]	Thickness [mm]	Material
Main Body	4	0.25	30	2	Aluminum
Propeller Beams (per beam, 5x)	4	0.2	30	3	Aluminum
Propeller Blades	4	0.4	40	4	Aluminum
Landing Legs (per beam, 6x)	2	0.1	20	2	Aluminum
Wing Parts (per beam, 6x)	10	0.25	40	3	Aluminum

10.3.2 Propeller Carrying Structure

As can be seen in Figure 10.1, the carrying structure of the propellers can be divided in two parts: the forward propeller beams attached to the wing box on the front and the VTOL propeller structure, attached to the main body and wing box at the back. First, an analysis is done on the carrying structure of the back propeller. This large VTOL propeller is carried by three beams. One of these beams is connected to the main body structure (the middle beam, B_m) and the other two side beams are connected to the wing box (the side beams, B_s). Here, the subscripts indicate the beam. Due to the fact that these beams are connected to each other in the centre of the propeller, some assumptions can be made:

- The beams are assumed to be clamped on the connecting structures
- The beams are made of the same material with the same cross-section, and thus have the same material properties and moment of inertia
- The deflection of the beam in the back structure is the same at the centre of the VTOL propeller
- The total VTOL propeller lifting force equals the forces over the three beams
- The angle between the beams is assumed to be the same as the sweep angle of the wing
- The failure mode is assumed to be bending stress, since the other loads are negligible compared to this

These assumptions lead to a more simplified model of the beam structure of the VTOL propeller. Since the beams are attached at the end, it can be said that this end deflection is the same for each beam: $v_m = v_s$. Due to the clamped beams and the propeller load acting on the end of the beams, the maximum deflection can be assumed to be [63]:

$$v_{max} = v_m = v_s = \frac{F_m L_m^3}{3EI} = \frac{F_s L_s^3}{3EI} \quad (10.3)$$

where F is the applied force, L is the length of the beam, E is the Young's modulus of the material and I is the moment of Inertia of the beam. Since the sweep angle, Λ , between the two beams is known, the lengths of the beams can be determined, leading to the following load equation:

$$F_{prop} = F_s + F_m + F_s = 2F_s + F_m = F_m(2 + \cos\Lambda^3) \quad (10.4)$$

Now that the forces and the lengths of the beams are known, the bending moment can be computed. The maximum bending stress of the beam is given to be:

$$\sigma_{bending} = \frac{M_{max} y_{max}}{I} \quad (10.5)$$

where M_{max} is the maximum bending moment and equals $P_{max} L$ and y_{max} is the maximum distance to the centre of the beam. Taking the moment of inertia as a parameter, the optimal beam can be constructed. In order to do this, an optimization program was written, taking a variable diameter and thickness for a hollow cylinder beam. This program outputs the geometry and mass of the beams that result in the minimum mass, such that it can withstand the loads without plastically deforming. Using the assumption that the beams are loaded in bending, a composite fibre reinforced polymer (CFRP) is used as material, since this has the most optimal mechanical properties regarding bending strength and density. Once the program is run, the diameter and thickness for the beams are chosen. Then, the forward propellers of the design are analyzed. These propellers are connected with beams to the wing box. Again, the assumption is made that these beams are clamped at the wing box. To size the beams, Equation 10.5 is used again. In addition an equation for the torque in a thin walled circular section is used for the torque the motors may provide, and the direct stress equation for the pulling force of the motors on the beam, as well as for the weight of the propellers and motors [63]:

$$\tau = \frac{T}{2A_m t} \quad (10.6)$$

$$\sigma_{norm} = \frac{F}{A} \quad (10.7)$$

where T is the torque, A_m is the total cross-sectional surface, t is the thickness of the beam, F is the applied force and A the cross-sectional area.

These equations are used in the optimization program to find the optimal thickness and diameter of the beams. However, in addition to these optimizations, now also the length of the beam is taken as a parameter input for optimization. This is due to the fact that an optimal length has to be chosen for stability and control during take-off. Since the large VTOL propeller in the back is already positioned, the position of the forward propellers can still be varied. Only when this program is run with regard to the stability and control constraints, the geometry and mass of the beams for the forward propellers are determined. For these beams, the material CFRP is chosen as well, since the shear strength of this material is able to withstand the torsion on the beams. Also, with Equation 10.3, the maximum deflection of the beams was analyzed for the different parameters. For the final values, this was found to be small enough to prevent the beams from failing.

By varying the beam diameter and skin thickness an optimal mass was found for all components while still being able to withstand the loads on the structure during the different mission operations, satisfying **SYS-STR-05**, **SYS-STR-06** and **SYS-STR-07**. In Table 10.3 below, the dimensions and masses of the total propeller structure are given:

Table 10.3: Propeller-carrying structure components

Beam	Amount	Length [m]	Diameter [mm]	Thickness [mm]	Material	Mass [kg]
VTOL Propeller to Wing	2	3.30	30	0.5	CFRP	0.49
VTOL Propeller to Body	1	2.76	31	0.5	CFRP	0.21
Forward Propeller to Wing	2	2.0	34	0.5	CFRP	0.34

10.3.3 Main Body Structure

The main body structure of the UAV is designed to carry and transfer the loading of the wing, propellers and landing structure. Next to that, it needs to have the ability to support the payload. Therefore, this is a crucial part of the structure of the UAV. Due to the fact that this structure has to take up a lot of loads in different directions, aluminum is chosen for this design. This choice is made based on the isotropic property of metals and the fact that aluminum has one of the highest strength over density ratios [63]. This will result in the lightest design for the main body structure. The body structure consists of a few components:

- Two longitudinal beams to which the payload is attached
- Two lateral beams carrying the wing box and propeller structure
- Four vertical beams with two skis, acting as the landing gear structure of the UAV
- Two vertical beams at the end of the wingbox hidden in the winglets acting as both the rear landing gears and the winglet wing box.

For the design of these different components of the body structure, some assumptions are made. These assumptions are:

- The longitudinal beams are assumed to carry the payload components
- The payload components are assumed to be one point mass at the center of the longitudinal beams.
- The longitudinal and lateral beams are assumed to fail at touchdown due to impulse
- The forward lateral beam is assumed to be a connecting beam between the two wing components
- The wing loading is assumed to be transferred to the forward lateral beam ends
- The landing gear beams are assumed to be loaded in pure normal stress
- The touchdown condition is based on the load being transferred into the aft landing gear on the main body and the landing gear on the wing. The forward main body landing gear is then given the same dimensions as the aft.
- The whole main body structure is made of aluminum

First, the landing gear is designed. This should be able to withstand the loads caused by the weight of the UAV during touchdown. Next to that, it should provide enough stability to prevent the UAV from tipping over. In order to obtain the dimensions of these beams, two different failure modes are checked. One is the normal stress on the area of the beams calculated using Equation 10.7. The other failure mode is the Euler critical load, which takes into account the load at which the landing gear will suddenly buckle:

$$P_{cr} = \frac{\pi^2 EI}{(KL)^2} \quad (10.8)$$

where E is the Young's modulus, I is the moment of Inertia, L is the length of the beam and K is the column effective length factor, which is determined by the column shape. In case of the landing gear geometry, normally a factor of 1 is chosen. However, the recommended design value for K for this case is 1.2, so the beam is designed for this value [78]. Due to the center of gravity not being exactly in between the wing landing gear and the main body landing gear, resulting in that they do not have the same dimensions. Next to the vertical landing gear beams, the four landing gear beams at the body are connected pairwise with two 'skis'. These two longitudinal beams carry a uniform load,

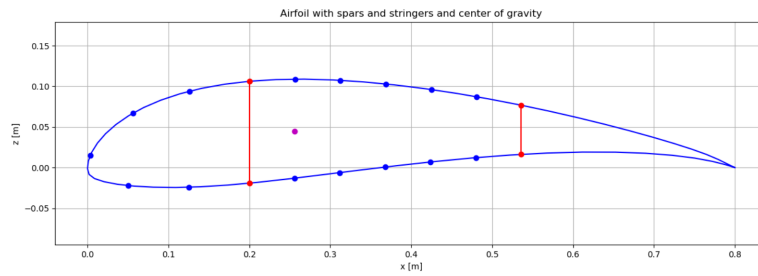


Figure 10.5: Airfoil cross section including spars and dots on the possible stringer locations.

and thus to prevent large deflections a hollow cylinder shape was used for this part as well. However, the design of this landing gear prevents it from being able to land on really steep slopes. The wing tip landing struts allow for this, although the slope is limited. Therefore, it is assumed that the drone will land on relatively flat terrain. For future recommendations, the landing gear could be designed to be flexible in length, allowing it to land on steeper slopes, but this is beyond the scope of this process.

Again by varying beam diameter and thickness, the optimal geometry was found. The landing gear structure beams are given in Table 10.4:

Table 10.4: Landing gear structure components

Beam	Amount	Length [m]	Diameter [mm]	Thickness [mm]	Material	Mass [kg]
Main Body Vertical Beams	4	0.6	18	0.5	Aluminum	0.18
Wing Tip Vertical Beams	2	1.0	17	0.5	Aluminum	0.14
Longitudinal Skis	2	0.8	18	0.5	Aluminum	0.12

Furthermore, the main body structure has to be designed. This main body structure consists of a rectangular shape made up by two lateral cylindrical beams and two longitudinal cylindrical beams. For the forward beam, the wing boxes exert forces and moments on the ends, putting the beam in bending using Equation 10.5. The torque in pitch direction causes the entire beam to rotate and thus causes no shear stress. For the rear beam, since the VTOL system exerts a vertical force on the center of the beam, and the landing gear or longitudinal beams on the ends of the beam, Equation 10.5 is used again to find the stresses due to bending. The torque due to the VTOL system is assumed to be transferred to the longitudinal beams and thus is assumed to cause no twist or shear stress.

By varying beam diameter and thickness, the masses of the beams were optimized while still being able to withstand the loads on the structure during the different mission operations, satisfying **SYS-STR-05**, **SYS-STR-06** and **SYS-STR-07**. The resulting geometry and masses of the lateral and longitudinal beams can be seen in Table 10.5.

Table 10.5: Main body structure components

Beam	Amount	Length [m]	Diameter [mm]	Thickness [mm]	Material	Mass [kg]
Longitudinal Body Beams	2	1	48	1.2	Aluminum	0.96
Lateral Body Beams	2	0.7	101	3.1	Aluminum	3.6

10.3.4 Wing Box Structure

The wing box is the most critical component of the structural analysis. Since the design is practically a flying wing, the wing box mass is the major contribution to the total structural mass. Furthermore, the shape of the desired airfoil and attachments of the VTOL and forward rotor structures complicate the analysis. A program was created to estimate the wing mass based on the following inputs: loads, material, and wing parameters such as airfoil shape, sweep, chord length and wing span.

The following design decisions were made for the wing box structure. Firstly, the wing box is the airfoil shape split into three parts by placing two spars as can be seen in Figure 10.5. This is in contrast to the Helios prototype which had an internal central cylinder with ribs, around which a covering skin was placed [148]. This decision was made to be able to place the batteries in the wing, which was desired to keep the main body size limited to keep drag low and to make sure the center of gravity was in the right location. Furthermore the decision was made to place the front spar at the location of maximum thickness, for ease of manufacturing. The rear spar was placed at a location of 66% of the chord to allow for control surfaces to be placed. Moreover, the material was chosen to be CFRP, due to its high specific characteristics and to keep it equal to the material used for preliminary sizing. Additionally the following assumptions were made to simplify the calculation.

- It was assumed that the rods from the forward and VTOL propeller structures are attached to the front and rear spar respectively at the same height as the shear center to prevent a twisting torque. It was deemed an

assumption with little consequence since the wing box is a closed box and most selected airfoils did not have enough camber to place the shear center above the spars.

- It was assumed that the third cell takes no load due to the cutouts required for the control surfaces. As a result a lower thickness was used, which is to be supported by ribs, to save on mass.
- A structural idealization using booms was used to find stresses within the wing box. This idealization assumes that the skin and spars only carry shear loads and no direct loads. The booms on the other hand only carry direct loads and no shear loads. To minimize the effect of neglecting the skin the booms are computed from the stringer areas and contributions from adjacent skin sections. The moment of inertia's are then computed using only the boom areas with the parallel axis theorem. Since these booms are also used to compute shear stresses, a consequence of this assumption is that only the average shear stress will be computed, and thus the maximum will be underestimated. However, due to the safety factor of 2 already in place, this consequence was deemed mitigated.
- It was assumed that the bending around the x-axis is significantly more than bending around the z-axis. This has an effect on computing the moment of inertia's from the boom areas, since the stress ratio is changed. The consequence is that normal stresses are underestimated in certain booms and overestimated in the others.
- Angles of twist and deflection are assumed to be small and are thus neglected, meaning that the internal forces and moments are applied to the original non-deflected wing. The consequence is mainly that angles of deflection and twist are inaccurate.

The program used the following method to estimate the mass of the wing box. First airfoil data was used to find the shape of the wing box, after which the two spars were placed to split the box into the three cells. The third cell was discarded as assumed above, which yielded three sections to place stringers on: the top skin section, bottom skin section and leading edge skin section. Based on these sections and the amount of stringers entered as input, the stringer locations were determined, stringers were also placed at the four spar attachment points. With the stringer and skin locations known the center of gravity is determined. Next structural idealization is performed to find boom areas at all stringer locations, using Equation 10.9:

$$B_i = A_{stringer_i} + \sum_{n=1}^{adj} \frac{t_{D_n} b_n}{6} \left(2 + \frac{\sigma_n}{\sigma_i} \right) \quad (10.9)$$

With B_i the boom area, $A_{stringer_i}$ the stringer area, adj the number of adjacent skin sections, t_D the skin thickness, b the skin length and $\frac{\sigma_n}{\sigma_i}$ the ratio of direct stresses computed using the distance to the neutral axis. It should be noted that in case the wing box was too strong, certain stringer area contributions were set to zero. This resulted in no loss of accuracy, since the boom was still considered, but the mass could be minimized further. The moment of inertia's follow straightforwardly.

With the cross sectional characteristics known and the fact that the wing has no taper, the stresses in the box can be determined. Normal stress was found by adding up stress due to axial load in the wing box using Equation 10.7 and stress obtained from the complete general bending equation, which resulted in Equation 10.10:

$$\sigma_{normal} = \frac{F_y}{\sum B} + \frac{M_x I_{zz} - M_z I_{xz}}{I_{xx} I_{zz} - I_{xz}^2} z + \frac{M_z I_{xx} - M_x I_{xz}}{I_{xx} I_{zz} - I_{xz}^2} x \quad (10.10)$$

Shear stress was then found by using the shear flow in each wall due to torsion and shear forces. Due to the two cell design of the wing box, the multi-cell approach had to be used. For shear flow this meant calculating shear flow contributions due to booms using Equation 10.11 and adding the base shear flow per cell by evaluating Equation 10.12 in combination with setting Equation 10.13 equal for both cells:

$$q_{ij} = \frac{-V_z I_{zz} - V_x I_{xz}}{I_{xx} I_{zz} - I_{xz}^2} \left(\sum_{i=1}^n B_i y \right) + \frac{-V_x I_{xx} - V_z I_{xz}}{I_{xx} I_{zz} - I_{xz}^2} \left(\sum_{i=1}^n B_i x \right) + q_i \quad (10.11)$$

$$\sum M_i + 2A_{m,1} q_{0,1} + 2A_{m,2} q_{0,2} = 0 \quad (10.12)$$

$$\left(G \frac{d\theta}{dy} \right)_i = \frac{1}{2A_{m,i}} \int \frac{q_{ij} ds}{t_{D_i}} \quad (10.13)$$

Where q is the shear flow between two booms, and V is shear force. For shear flow due to torque, Equation 10.14 was used in combination with setting Equation 10.13 equal for both cells:

$$T = 2A_{m,1} q_1 + 2A_{m,2} q_2 \quad (10.14)$$

By adding the separate shear flows and using $q = \tau t$, the shear stresses were obtained.

At several points on the wing, the section was tested for failure, where every section was evaluated at the stringer locations. The Tsai-Hill failure criterion was used to determine whether the box will fail, since it is able to evaluate

the anisotropic CFRP. Ply rupture and thus failure occurs under the following condition [106]:

$$\left(\frac{\sigma_{11}}{\sigma_{allow11}}\right)^2 - \left(\frac{\sigma_{11}\sigma_{22}}{\sigma_{allow11}^2}\right) + \left(\frac{\sigma_{22}}{\sigma_{allow22}}\right)^2 + \left(\frac{\tau_{12}}{\tau_{allow12}}\right)^2 \geq 1 \quad (10.15)$$

Finally a skin buckling check was performed to ensure the chosen stringer spacing was small enough as to prevent buckling. For this the plate buckling equation was used as shown by Equation 10.16 [110]:

$$\sigma_{cr} = k_{cr} \frac{\pi^2 E}{12(1-\nu^2)} \left(\frac{t}{b}\right)^2 \quad (10.16)$$

Where σ_{cr} is the critical buckling stress, which has to be higher than the normal stress times the safety factor. k_{cr} was set to be 6.98, since both edges are clamped to the spars [110]. Furthermore, ν is the Poisson's ratio and b the distance between stringers.

By iterating over increasing skin thickness and stringer areas the minimum mass could be found to withstand the loads on the structure during the different mission operations, satisfying **SYS-STR-05**, **SYS-STR-06** and **SYS-STR-07**. This iteration was done many times in the main program to find the optimal design. The final sizing results can be seen in Table 10.6.

Table 10.6: Wing box structure parameters

	t_{top} [mm]	t_{bottom} [mm]	t_{LE} [mm]	t_{rear} [mm]	$A_{stringer}$ [mm ²]	Material	Mass [kg]
Wing Box	0.5	0.35	0.5	0.2	4	CFRP	12.86

10.3.5 Tilting Mechanism

For the tilting mechanism of the forward propellers, it is decided to use a servo motor in combination with a rod. To give a better understanding of this tilt mechanism, Figure 10.6 is included below. The forward propellers including motor have a mass of 5.2 [kg] each, resulting in a weight of 19.35 [N]. In order to make sure that enough torque is provided by the servo motor itself, it is decided to implement a servo motor that is able to provide a torque of 100 [kg cm]. In this way, the attached rod can be at approximately 20 [cm] distance from the centre of rotation of the propeller. The selected servo for this is the K-Power Hb150t [71]. The servo motor is capable of rotating 180 [degrees], which is necessary, since the propeller should be able to rotate 96 [degrees] clockwise to compensate for the angle of attack. In this way, the propeller should be able to be tilted automatically from VTOL to forward propulsion positions.

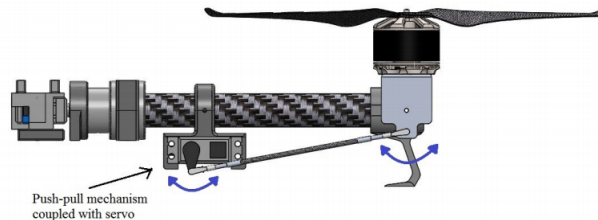


Figure 10.6: Tilting mechanism of the forward propellers [70]

10.4 Risk Analysis

The structure of the UAV is designed to make sure that it prevents all the components from failing. However, there are some risks introduced in the operation and design of the structure. These risks, including their probability, severity and mitigation method are presented below.

- **SR-1/Structural risk - Materials not able to withstand Martian environment**
 - **Effect:** Can lead to structural damage which could cause systems to malfunction.
 - **Probability:** Mars has highly abrasive and fine dust suspended in its atmosphere [89], so this is characterized as **Probable**.
 - **Severity:** **Critical**, Would damage components leading to large loss of performance.
 - **Mitigation:** Choose suitable materials that have been tested to withstand the harsh environment on Mars. Assess the suitability of weather conditions before performing flight too.
 - **Effect of Mitigation:** The mitigation procedure is thought to only have an effect on the probability, lowering it from **Probable** to **Occasional**. The severity is not affected since structural damage is still as severe.
- **SR-2/Structural risk - The internal structure fails due to manufacturing mistakes**
 - **Effect:** Can lead to failure of the whole design.
 - **Probability:** Manufacturing processes mostly happen very carefully, so this is characterized as **Rare**.

- **Severity: Critical**, it would lead to a failed mission.
- **Mitigation:** Test the materials beforehand to make sure that they do not fail at the critical loading. Include a safety factor to account for possible manufacturing mistakes. Next to that, supply additional replacement components in case a component fails.
- **Effect of Mitigation:** The effect is that the materials are less likely to fail, due to the fact that they are tested with a safety margin, so the probability decreases to **Rare**, but the severity stays the same.
- **SR-3/Structural risk - The wing box fails when something drops on it or when picked up at the wing tips**
 - **Effect:** Can lead to structural damage which could cause the wing box to fail.
 - **Probability:** It can be that during assembly, a tool drops on the wing box. Also when it has to be moved, the drone gets picked up, so this is characterized as **Probable**.
 - **Severity: Critical**, since a wing box failure will lead to loss of performance.
 - **Mitigation:** The wing box is ultimately designed for loads far from the root. Next to that, the design has a safety factor of 2, to make sure that when such a risk occurs, the wing box will not fail immediately.
 - **Effect of Mitigation:** The mitigation procedure is thought to only have an effect on the severity, lowering it from **Critical** to **Marginal**. The probability is not affected since this still might happen as probable..

10.5 Verification and Validation

Once the design of the structure is obtained, it has to be checked whether the methodology behind the design and results are correct. This is done in the verification and validation process. First, the verification of the model and code is discussed, followed by a validation of the results of the model.

10.5.1 Unit Tests

Unit tests were utilized to ensure that certain code modules were returning correct results. Since the model uses many input parameters to determine things such as loads and cross-sectional properties, most modules were verified by manually computing a simpler test case, and comparing results. In this way the following modules were verified.

Loads Calculator

The method to obtain the loads was already derived in order to be able to create the code module. Hence, by inputting a certain load case, the results could be compared to the sketch to check for the correct sign and the magnitudes could be checked by checking with a calculator. The loads and signs were deemed correct and thus the module was verified.

Moment of Inertia

A simplified wing box with a specified amount of stringers and a constant skin thickness was evaluated for verification. By evaluating the boom areas by hand and computing the moment of inertia's it could be verified that the automated version of the code works properly.

Stress Module

Continuing with the same manual calculation as for the moment of inertia, the direct and shear stresses could be evaluated for the simplified wing box. These were then compared to the stresses the program was reporting. Since the stresses were similar and the loads at which the wing box should fail were also approximately similar, the stress module was also considered verified.

10.5.2 System Tests

In order to verify the model of the body structure, a similar model is created in CATIA. The different beams are created and analyzed in terms of stress and load cases. Since CATIA has a pretty detailed simulation, this can be used to verify the model on system level due to the following reason. The geometry of the beams are outputs of the Python program and thus should be valid designs for the load cases. By then running the geometries through the same code applying a known force and applying the same force in CATIA, interactions of the code are evaluated. It should be noted that the material taken for verification is aluminum in each case due to complications that arose while trying to use the an-isotropic CFRP. However, this does verify the code used for the model, since the inputs are the same. In order to make sure that this is also the case for CFRP, validation has to be performed.

Bending Stress

The beams that are loaded in bending are analyzed in terms of bending stress. This is done by assuming one side of the beam is clamped and applying a load and possible bending moment at the other end of each beam. As can be seen in Figure 10.7, the highest stress concentrations occur at the largest distance from the neutral axis of the beam. Subjecting a vertical thrust of 100 [N] to the beam with a length of 3 [m], this results in a maximum bending stress of approximately 70 [MPa]. Using CATIA to model this, the same force is applied. As can be seen in Figure 10.8, the maximum bending moment is approximately the same. Therefore, the code module computing bending loads is verified.

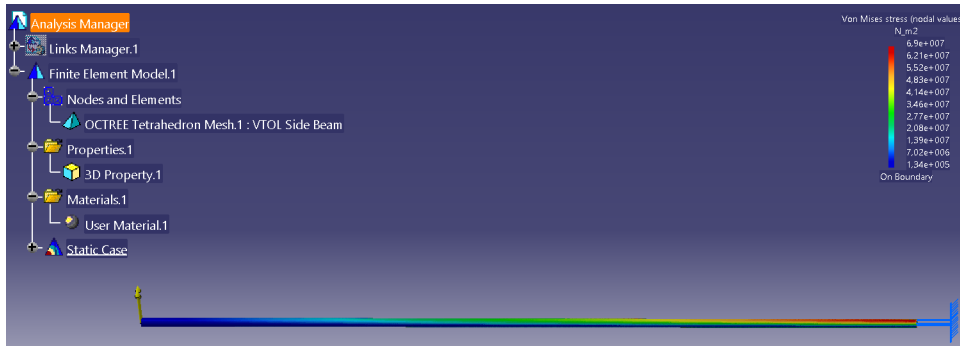


Figure 10.7: Finite element analysis of the VTOL propulsion beam to wing box

Normal Stress

For the pure normal stress, the landing gear beams are tested. This is due to the fact that at the moment of impact, the landing gear gets exposed to the biggest load, making it the best case for testing. This is tested in CATIA with a load of 400 [N], evenly divided over the four front landing gear beams. As can be seen in Figure 10.8, the result for the landing gear beam is that it has a maximum normal stress of 11 [MPa]. The maximum stress that was calculated by the stress model of the UAV was approximately 9 [MPa]. As can be seen, the value obtained in CATIA is about 25% higher, which is likely caused by using the standard stress calculation on a thin-walled beam in compression.

However, the model is still considered verified due to the following two reasons. First, Euler buckling load for a column in compression was already accounted for, meaning that even though the normal stress is a bit higher, it is still not causing failure due to exceeding critical load. Secondly, the safety factor was already set at 2, since the CATIA stress did not exceed twice the stress computed by the model, there will not be failure yet.

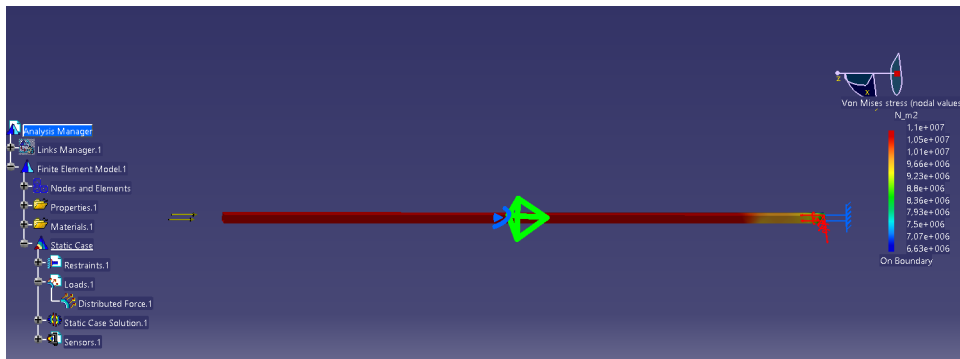


Figure 10.8: Finite element analysis of the landing gear beam

10.6 Validation Strategy

In order to validate the model of the structure of the UAV, a complete and detailed model of the structure can be made in CATIA. Once this model is created, it can be analyzed in terms of displacement, principal stress and Von Mises stress using a Finite Element Analysis method. This complete model will be subjected to the different loads acting on the structure during the various mission scenarios. This leads to a detailed overview of the stresses on the structure of the UAV. Next to that, it can be easily seen where the highest stress concentrations are. In this way, a detailed analysis of the structure can be done. However, it was decided that the validation plan will not be executed completely. Therefore, in this case, only a few separate beams with different loading cases were modelled and analyzed, which gives a simplified analysis which is still useful to verify that the Python program works as intended. A safety factor of 2 was already applied to the full structure in order to be certain that the structure will not fail in its operational lifetime and to compensate for not having a full FEM model yet at this phase.

11 Aerodynamic Analysis

The aerodynamics subsystem ensures that the drone can generate sufficient lift during flight while minimizing drag in order to ensure the drone is able to fly with minimal thrust. Additionally, it produces an aerodynamic model which can be used to evaluate the flight performance of the drone. This section covers the drag reduction measures taken as well as the design of the wing from an aerodynamics perspective. Section 11.1 presents the requirements specific to the aerodynamics subsystem. Section 11.2 gives an overview of how the parasite drag was estimated and mitigated. Following this Section 11.3 describes the software used to model the lifting surfaces of the drone. Then Section 11.4 describes the functions created for the final sizing of the design. Based on this the aerodynamic characteristics of the final drone are presented in Section 11.5. Finally, the risk analysis and verification and validation procedures are covered in Section 11.6 and Section 11.7.

11.1 Requirements

Table 11.1: Requirements related to aerodynamics and their expected compliance

Index: DME-REQ-	Requirement	Compliance
SYS-AERO-01	The wing shall produce 410 [N] of lift under particle accumulation conditions.	Satisfied
SYS-AERO-02	The wing shall produce sufficient lift during cruising flight to fully counteract the aircraft's weight.	Satisfied

11.2 Drag

Drag at cruise should be reduced to increase range and limit the required thrust (and thereby the power required from the battery). There are a number of components which must be considered as contributing towards the drag experienced by the UAV. The following components are expected to have a large impact on the drag during cruise:

- Wing
- Landing Gear
- Vertical rotor
- Vertical rotor structure
- Forward propulsion structure

In general there is a trade-off between reducing drag and optimizing other subsystems. For example, increasing the VTOL rotor radius will increase the efficiency of that subsystem but it will also increase parasite drag caused by the rotor blades during cruise. Hence, the goal is to accurately estimate the drag such that an optimum can be determined.

11.2.1 Reducing Strut Drag

Some measures can be taken in order to minimize the drag of structural components. For the struts an airfoil shape can be placed around the structural element which greatly decreases the parasite drag compared to a cylinder. However, for all struts, a trade off must be made between minimizing the mass of a strut and the parasite drag induced during cruise. A strut with a larger radius will be lighter but it will create a larger amount of parasite drag. Therefore, a number of symmetrical airfoils were selected in order to determine the optimal airfoil for a given radius. The selection contains airfoils with a wide range of maximum thickness to chord ratios as this was found to be the most influential parameter. The results are presented in Figure 11.1. The advantage to reducing thickness to chord ratio is that an airfoil will have a largest chord for a given strut radius; this increases the Reynolds number. However, a larger chord also leads to a greater surface area which leads to higher drag as can be seen by the HT05 and NACA 0006. These factors result in the RAF MOD 30 airfoil (with a maximum thickness to chord ratio of 7.6 %) providing the lowest drag area per meter for a given strut radius.

For some struts, such as those which attach to the vertical rotor, the surface area should also be minimized as a large area will negatively impact the thrust of the vertical rotor. Meaning the airfoil options for these struts are limited to options with a high thickness to chord ratio. On the other hand around the main landing gear and the winglets thin airfoils can be used to minimize the drag for a given radius.

11.2.2 Modelling VTOL Rotor Drag

The VTOL rotor is heavily optimized to provide the best performance during the take-off and hovering phase as these are the most energy intensive parts of the mission. The drag induced by the VTOL rotor can be estimated based on the wetted area, skin friction coefficient and form factor. The wetted area is simply calculated based on the geometry of the VTOL rotor which is provided by the propulsion department. The skin friction coefficient is heavily dependent on the Reynolds number which is calculated based on Equation 11.4. During cruise, to estimate the drag, each blade of the vertical rotor is treated separately with a characteristic length equal to the rotor radius, as the VTOL rotor blades are aligned with the flow during cruise. The skin friction coefficient is calculated based on

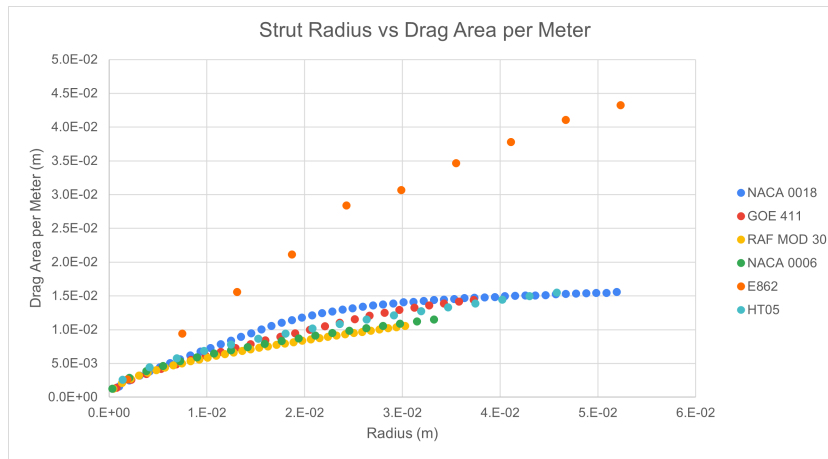


Figure 11.1: Plot displaying the Drag area and the radius for the considered airfoil options

the logarithmic fit by von Karman [113]:

$$c_f = \frac{0.455}{(\log Re)^{2.58}} \quad (11.1)$$

Finally the drag area per blade is calculated as:

$$f = k c_f S_{wet} \quad (11.2)$$

11.2.3 Crosswind Drag

An approximation of the crosswind drag is determined by estimating the drag of the wing and body based on Equation 11.1 and by modelling the winglets and landing gear as a flat plate. This is later used during the flight performance analysis of the drone.

11.3 Aerodynamic Model

The full 3D design including internal subsystems of the drone has been created in CATIA V5. However, a full scale CFD analysis of this model is beyond the scope of this report. Hence, an equivalent aerodynamic model is created in XFLR5 to model the aerodynamic characteristics during take-off, landing and cruise. This model is also used to evaluate the stability characteristics and eigenmotions which is elaborated upon further in Chapter 12. It is important to note that XFLR has limitations in modelling the stall characteristics which is why angle of attacks close to the stall angle are avoided in the flight envelope, this could be further improved upon with more accurate CFD simulations at a later point in the design process.

11.3.1 NCrit

As the modelling software (XFLR5) uses e^N transition theory it is crucial to determine an achievable NCrit value for the operating environment. NCrit is a measure of free flow turbulence as well as the effect of airfoil roughness and can have a large impact on aerodynamic performance. While in theory a wing could be designed which relies on a smooth surface (which corresponds to a higher NCrit of 12-13), the simulations show that at these Reynolds numbers there is limited aerodynamic benefit to this design decision. In fact, at very low Reynolds numbers a lower NCrit can improve aerodynamic performance. The risk caused by designing for a smooth surface is quite large as it is likely that the wing will get dirty during operation and dust suspended in the martian atmosphere will further reduce NCrit of the wing. Hence, as it makes the design resistant to external environmental factors, the choice has been made to design for a low NCrit of 5 which can certainly be achieved by making the surface of the wing slightly rough such that the roughness of the surface is not affected by the martian dust. This choice removes the risk of dust accumulation on the wing (from an aerodynamics perspective) which results in a more reliable design.

11.3.2 Aspect Ratio Correction

For the sizing methodology in Section 6.2, a large airfoil selection has been presented. For the optimization of the design the airfoil aerodynamic characteristics must be translated to those of a wing. In order to achieve this an XFLR5 model of a representative wing is generated for each of the airfoil options. It was not deemed reasonable to generate and simulate a wing for a large number of aspect ratios for each airfoil option. Therefore, an aspect ratio of 21 is chosen for the reference wing, as initial calculations showed this would be close to the optimal. In the sizing function aspect ratio is varied based on the weight and lift coefficient of a given design. As a larger aspect ratio causes a decrease in the lift induced drag of a wing a correction must be put in place to accommodate this. The drag of a wing can modeled by the equation:

$$C_D = C_{D,0} + \frac{C_L^2}{\pi A R e_0} \quad (11.3)$$

Where $C_{D,0}$ is the zero lift drag coefficient and e_0 the Oswald efficiency factor. The AR correction is performed by subtracting the right most term in Equation 11.3 from the wing drag coefficient and adding an equivalent term with the correct aspect ratio. It is important to note that this correction is only used in the sizing code (in order to find an optimal solution with variable aspect ratio) and not in the analysis of the aerodynamic characteristics of the final design.

11.4 Wing Sizing

The wing sizing process is quite complex as it must be optimized for; aerodynamics, structures and stability. There are quite a large number of options and parameters to be optimized over, such as; airfoil selection, cruise speed, sweep angle etc. Therefore, the wing sizing is performed by using an iterative process to determine the mass. The wing sizing function takes total mass, velocity, selected airfoil and the desired Reynolds number as an input. The function outputs the wing geometry (chord, wingspan, wing area and aspect ratio). Finally, wing twist and dihedral are determined based on stability analysis.

11.4.1 Aspect Ratio

The drone be must designed to operate at low Reynolds numbers. This presents difficulties as generally the aerodynamic performance of airfoils becomes negatively affected at these operating conditions and it becomes difficult to achieve a favourable lift to drag ratio, boundary layer stability is also negatively impacted by low Reynolds numbers. A minimum Reynolds number of 50,000 is selected for the worst case cruise condition during the sizing of the wing. For given atmospheric conditions the Reynolds number can be increased by increasing the chord of the wing or the free stream velocity of the flow. However, for a high lift to drag ratio a high aspect ratio (small chord) wing is desired. Therefore an optimal point must be found which balances these two effects. The Reynolds number for a wing is defined as:

$$Re = \frac{\rho V c}{\mu} \quad (11.4)$$

where ρ is the fluid density, V the flow velocity, c the chord of the wing and μ the dynamic viscosity. The cruise velocity of the drone is given by

$$V_{cr} = \sqrt{\frac{2W}{C_{L_{cr}} \rho S}} \quad (11.5)$$

Combining Equation 11.5 and Equation 11.4 shows that the Reynolds Number experienced at cruise will increase with increasing ρ :

$$Re = \frac{\rho V c}{\mu} = \frac{\rho \sqrt{\frac{2W}{C_{L_{cr}} \rho S}} c}{\mu} = \frac{\sqrt{2\rho W} c}{\sqrt{C_{L_{cr}} S} \mu} \quad (11.6)$$

As a larger Reynolds Number is preferred this leads to the conclusion that the critical case for the Reynolds Number design of the wing is at the maximum altitude.

When Equation 11.6 is combined with the wing geometry of $S = bc$ and the aspect ratio $AR = \frac{b}{c}$ the following relation can be obtained:

$$Re = \frac{\sqrt{2\rho W} c}{\sqrt{C_{L_{cr}} S} \mu} = \frac{\sqrt{2\rho W} c}{\sqrt{C_{L_{cr}} bc} \mu} \Rightarrow \sqrt{\frac{b}{c}} = \frac{\sqrt{2\rho W}}{\sqrt{C_{L_{cr}} \mu Re}} \Rightarrow AR = \frac{2\rho W}{C_{L_{cr}} (\mu Re)^2} \quad (11.7)$$

As can be seen, the required aspect ratio can directly be determined based on the weight, cruise lift coefficient, some atmospheric constants and the desired Reynolds number. In general, the goal is to maximize the aspect ratio in order to reduce drag. Equation 11.7 shows the maximum aspect ratio that can be achieved while still obtaining the required Reynolds number. As a minimum Reynolds number of 50,000 is chosen as the design goal. This means that in the sizing process the aspect ratio can be determined based on the cruise lift coefficient and service ceiling.

11.4.2 Surface Area

The wing surface area is calculated based on the required force balance at cruise. That is, the lift generated by the wing must equal the weight of the system. As the velocity is one of the parameters which is optimized over, this is given as an input to the wing sizing function. The lift coefficient is also an input which depends on the chosen airfoil, which is determined based on the simulation of a representative wing with the given airfoil. Using the following formulas, wing area, span and chord can be calculated:

$$S = \frac{2W}{\rho C_L V^2} \quad (11.8)$$

$$c = \frac{b}{AR} \quad (11.9)$$

$$b = \sqrt{AR \cdot S} \quad (11.10)$$

11.4.3 Twist

Twisting the wing downward at the tips has two main benefits; it counters the negative C_m of the airfoil (therefore it helps to trim the drone during cruise) and it delays stall at the tip to ensure that the control surfaces are the last to stall. The delay of tip stall is especially important due to the swept wing design as the sweep increases the effective angle of attack along the span which means that without twist the wing tip will naturally have a higher angle of attack than the rest of the wing. A disadvantage of this negative twist is that (since it reduces the angle of attack) it reduces the lift coefficient of the wing. The wing twist is determined to sufficiently trim the wing during cruise with minimal elevon deflection.

11.4.4 Dihedral

The dihedral increases the stability of the drone during various eigenmotions in flight. Due to the sweep the design already has some effective dihedral, therefore a relatively small additional angle is required. It is desired that the eigenmotions are naturally damped to increase reliability and reduce wear on the control surfaces. The dihedral is chosen to achieve the desired damping based on the analysis performed in Chapter 12.

11.5 Layout

The layout of the aerodynamics subsystem can be summarised as the final wing geometry. The airfoil is based on the airfoil selection and the sweep is determined based on the stability requirements. The dimensional parameters are determined based on the process described in Section 11.4. The winglets have been chosen as downward facing such that they can act as landing gear to avoid tip over. Twist is used at the wingtips to ensure the drone can be trimmed during cruise and to ensure the control surfaces are the last to stall. Finally, the wing dihedral is determined such that there is sufficient damping in the eigenmotions of the drone based on the stability analysis. The dimensions and geometry of the final design is presented in Chapter 17 as it is greatly influenced by the subsystems to be discussed in the following chapters. The aerodynamic polars of the final design are presented in Figure 11.2 and they show that the requirements **SYS-AERO-01** and **SYS-AERO-02** are met.

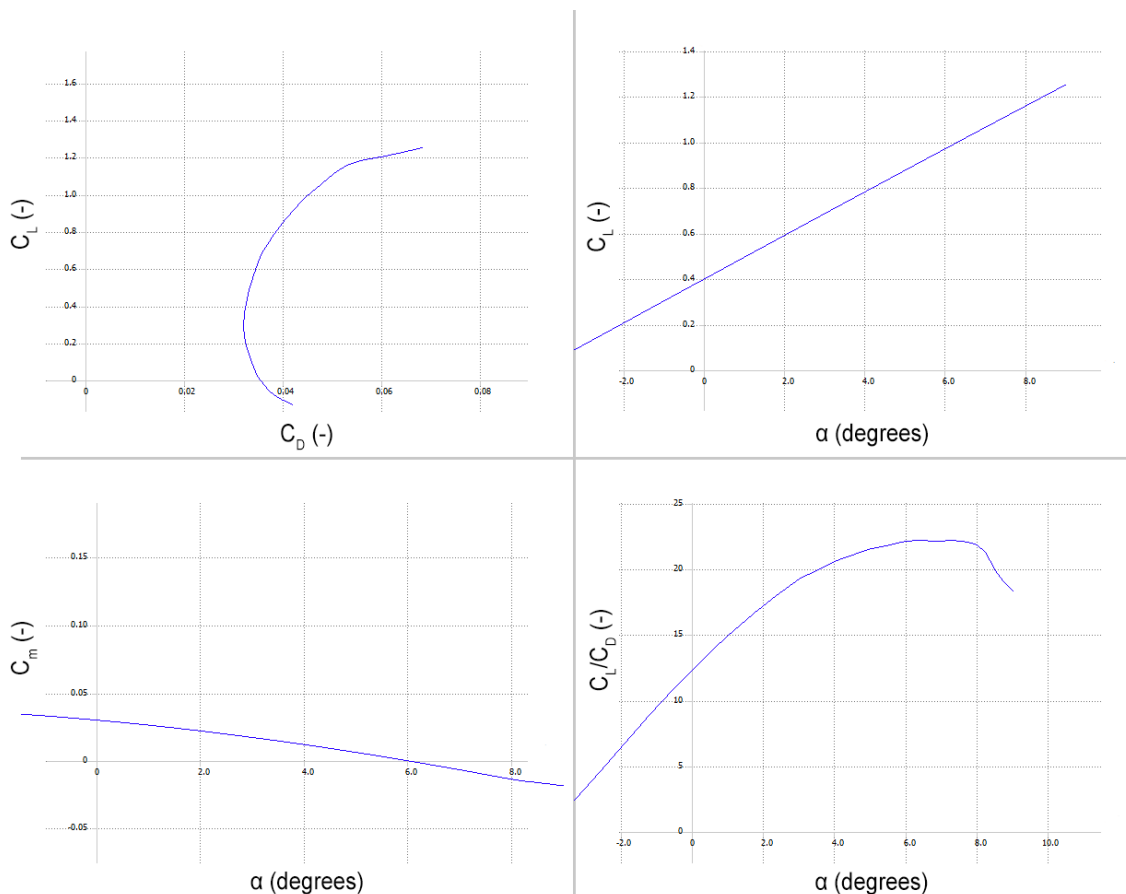


Figure 11.2: Aerodynamic polars of the final design

11.6 Risk Analysis

- AER-1/Aerodynamics subsystem Risk - Loss of lift due to stall
 - Effect: Could lead to a crash due to loss of lift.

- **Probability:** The probability of this can be considered **Occasional** due to limited knowledge of the wind conditions in the martian atmosphere.
- **Severity:** This risk is seen as **Catastrophic**. Since the drone flies at a height of 200 [m] off the ground most of the time it is possible it will not recover from a stall, which would result in a complete mission failure.
- **Mitigation:** The drone should fly at an angle below the stall angle and it should be designed to have favourable and predictable stall characteristics. The bottom right of Figure 11.2 presents the lift to drag ratio vs alpha for the aerodynamic model in XFLR, the drone is designed to be trimmed at an angle of 6 degrees during cruise, this gives the design at least 3 degrees of margin before the onset of stall. For a more precise prediction of the stall characteristics a CFD simulation or wind tunnel test must be performed. Another mitigation for the stall risk is the twist of the fuselage and wing tips. The fuselage is twisted upwards by 4 degrees and the tip of the wings (as well as the elevator section) is twisted downward by 3.31 degrees. This means the first section to stall is the fuselage, this reduces the lift generated in front of the center of gravity which in turn causes a pitch down moment on the drone.
- **Effect of Mitigation:** The first mitigation reduces probability of a stall from **Occasional** to **Improbable** occurring as it means a larger wind gust is required to increase the angle of attack above the stall angle. The second mitigation reduces the severity of the risk from **Catastrophic** to **Critical** as it increases the chance of recovering from a stall by ensuring the control surfaces will keep operating.

11.7 Verification and Validation

This section presents verification and validation procedures taken to ensure the model is running as expected and producing the required outputs. A number of unit tests are performed to test small components of the aerodynamics code for the sizing function. This is done to verify that the equations are coded correctly and outputting realistic values. Some larger (system) tests have been performed on the aerodynamics code in order to verify that the individual components work in conjunction in the desired way.

11.7.1 Unit Tests

Parasite Drag

The parasitic drag equations are verified by hand and the results of the hand calculations are compared to those given by the code. The results are expected to differ by a maximum of 0.1% due to differences in rounding. This is achieved which verifies the unit test for the parasitic drag equations.

Reynolds Number and Aspect Ratio

Similarly the Reynolds number and aspect ratio are verified using hand calculations. They are tested for a variety of values and the results are shown to differ less than 0.1% which is deemed acceptable to verify the equations.

11.7.2 System Tests

Aspect Ratio Correction

The aspect ratio correction described in Section 11.3.2 is tested to ensure that the assumption (and equation used to model the relation between AR and lift induced drag) is accurate. The reference wing has an aspect ratio of 21, the correction is tested for wings with aspect ratios between 10 and 30. The test results in a maximum difference of 5% between the induced drag predicted by the correction and the value obtained when the wing is simulated. This is seen as sufficient accuracy considering the AR correction is only used to help determine an optimal design.

Wing Surface Area

The wing surface area is sized based on the cruise condition. However, it is determined based on the computed lift coefficient which has been determined for the reference wing. The wing sizing must be verified through the use of an XFLR5 model of the final wing. The final wing is modeled, including the fuselage and winglets, using XFLR5. The lift generated at cruise conditions by the final aerodynamic model is 4% larger than that predicted by the sizing function which is deemed an acceptable margin of error based on the aerodynamic assumptions made for the sizing function.

11.7.3 Validation

The used methods must be validated to ensure that they correspond to real life behaviour. XFLR5 has been used to plot the aerodynamic characteristics of the final wing. XFLR5 has been validated for low angles of attack, however it is known the model is not reliable for modelling conditions close to and past stall. In order to properly validate the aerodynamic characteristics of the final design experimental or CFD data must be used. Unfortunately these validation methods go beyond the scope of this report. At a later stage in the design process, wind tunnel tests should be performed at the correct Reynolds numbers in order to validate the drone.

12 Flight Control, Stability, and Performance Analysis

The flight control and stability subsystem ensures controllability- and stability of the drone. This section covers the design of hardware components relevant for the flight control system as well as flight control and stability considerations in the design of the wing.

12.1 Requirements

Table 12.1: Requirements related to flight control, stability, and performance and their expected compliance

Index: DME-REQ-	Requirement	Compliance
SYS-ADC-02	The flight control system shall ensure stable flight of the UAV.	Satisfied
SYS-ADC-04	The flight control system shall control the system with an accuracy of 0.1 [deg] at flight velocities up to 90 [m/s].	Satisfied
SYS-ADC-05	The flight control system shall control the system with an accuracy of 0.2 [deg] at climb gradients up to 12%.	Satisfied

12.2 Model and Analysis

First, a general concept description of the control and stability subsystem is given in Section 12.2.1. After which longitudinal and VTOL stability and control aspects and their influence on the design is discussed in Section 12.2.2. Lateral stability and control aspects and their influence on the design are discussed in Section 12.2.3. More detailed actuator sizing for pitch, roll and yaw control is performed in Section 12.2.4. After which a final evaluation of the mass and power budgets for the actuators is given in Section 12.2.5 and finally a control and stability analysis of the final design is presented in Section 12.2.6, including an evaluation of the eigenmotions of the wing.

With regards to flight control: a flight performance simulation that accurately models landing, take-off, and cruise maneuvers, including the power used during each of these phases, is presented in Section 12.2.7, together with results relating to the mission profile and the system's flight performance. The integration of this model within the sizing routine is elaborated on in Section 12.2.7.

12.2.1 General Concept Description Control and Stability

Although reasoning and analysis behind design choices is given in more detail in the subsections below, there are certain decisions that play a role in each of these analysis. These will be shortly explained here for clarity.

First of all, it is found early on that passive stability is possible longitudinally, directionally, and laterally. From a reliability point of view a passively stable aircraft is highly preferable as that simplifies the electronic flight controls of the system a lot. Furthermore, the drone will need less constant modifications to the control surfaces and will be significantly easier to model and analyse.

The largest from a control and stability standpoint is the exclusion of a horizontal tail. This decision was made for 2 main reasons: (1) the power and energy requirements are heavily dominated by the VTOL phases of flight, a small increase in efficiency of the wing thus does not stack up against the added weight of a tail (as will be discussed below) and (2) the arm of the tail would be extra space in the launcher and during landing and take-off phases (as discussed in Chapter 8). In terms of control surfaces, there will be outboard elevons that provide pitch and roll control. Yaw control is provided by rudders on the winglets and differential thrust from the two tilt rotors. Further details on sizing and reasoning is given in Section 12.2.4.

12.2.2 Longitudinal and VTOL Stability and Control Aspects

This section will present control and stability considerations for longitudinal motion and the VTOL phase. As explained in Chapter 6 the general design of the system will follow from an optimization routine around an iterative sizing model. This sizing model includes constraints such that the system is stable in pitch, these constraints follow from the analysis below.

Longitudinal Stability

A simplified overview of the different forces on the system and the position of the center of gravity and the aerodynamic center is given in Figure 12.1. Note that this drawing serves as a visual aid, it is not an exact representation of the final design, but it serves to illustrate the different forces and lengths relevant for longitudinal and VTOL stability.

The moment equation for a flying wing without elevons is given in Equation 12.1. For the wing to be stable in pitch, the aircraft would need to have pitch-down response to a positive angle of attack disturbance; i.e. $\frac{dC_m}{d\alpha} = C_{m\alpha} < 0$. Taking the derivative of the equation below with respect to α gives that $\frac{x_{cg} - x_{ac}}{\bar{c}} < 0$; or the aerodynamic center of the wing (x_{ac}) has to be behind the center of gravity (x_{cg}). This relation is called the *stability margin*.

$$C_m = C_{m_{ac}} + C_{N_w} \cdot \frac{x_{cg} - x_{ac}}{\bar{c}} \quad (12.1)$$

Longitudinal Eigenmodes

The two longitudinal eigenmodes are the short period and the phugoid. Both of which will be discussed in more detail in Section 12.2.6. But it serves for this design section to note that both of these modes will be stable with a negative C_{m_α} .

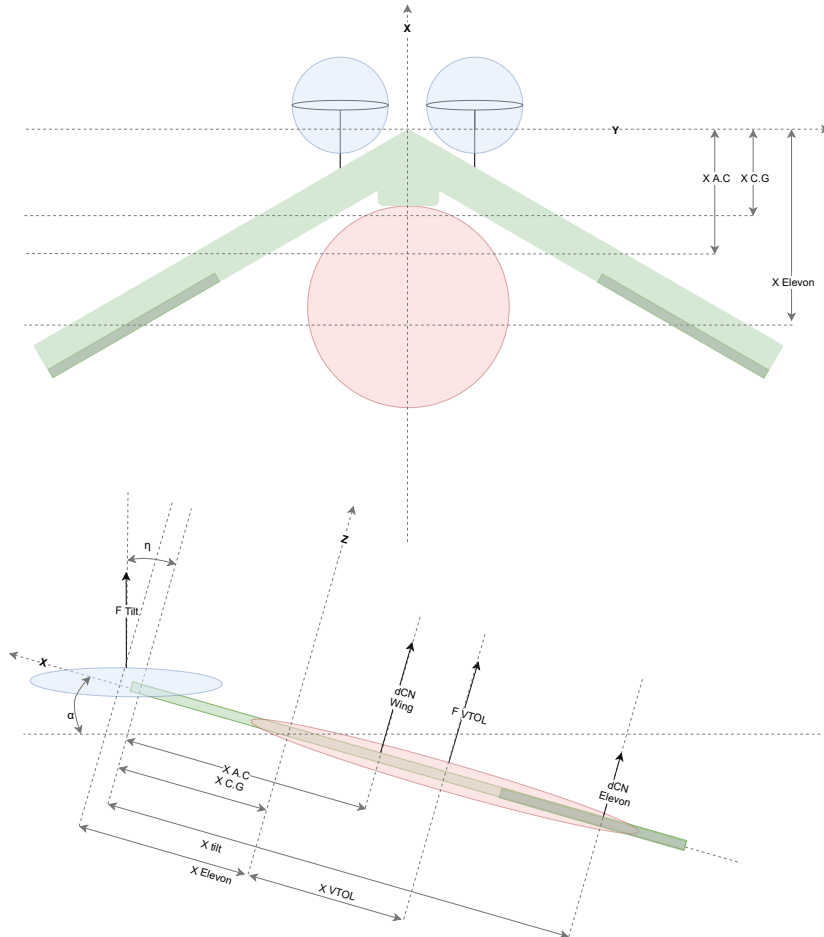


Figure 12.1: Free-body diagram of the flying wing

VTOL Stability

The center of gravity is constrained (with respect to the aerodynamic center) by the pitch stability requirement explained above. In this case, the center of gravity is also constrained by the placement of the VTOL rotor with respect to the tilt rotors. The total upward force (see Equation 12.2) has to be larger than 0 ($F_z > 0$) for the system to be able to lift off, however, the moments will need to be in balance (see Equation 12.3) ($M = 0$).

$$F_z = \cos(\epsilon - \alpha) \cdot F_{tilt} + \cos(-\alpha) F_{VTOL} - F_g \quad (12.2)$$

$$M = \cos(\epsilon - \alpha) \cdot F_{tilt} \cdot x_{tilt} - \cos(-\alpha) F_{VTOL} \cdot x_{VTOL} \quad (12.3)$$

The center of gravity is thus constrained by the position of the tilt and VTOL rotors as well as the amount of thrust produced by each.

Aerodynamic Center Position

The aerodynamic center is a property of the wing. It is the point on the wing (span- and chord-wise) where the moment coefficient is independent of the angle of attack ($\frac{dC_{m_{ac}}}{d\alpha} = 0$) and thus the point through which changes in lift coefficient will act.

The position of the aerodynamic center follows from the planform of the wing and the chosen airfoil. The chord-wise aerodynamic center is taken to be at the quarter-chord point and span-wise at the mean aerodynamic chord position; and is thus heavily dependent on the span (b), mean aerodynamic chord length (\bar{c}), taper ratio (λ) and sweep angle (θ). With a taper ratio of 1 (i.e. tip chord length is the same as root chord length), this results in:

$$x_{ac} = \frac{\bar{c}}{4} + \tan(\theta) \cdot \frac{b}{4} \quad (12.4)$$

It was verified using XFLR5 that the aerodynamic center is indeed at this position.

Stability Margin as a Function of VTOL Rotor Positioning

As explained in Chapter 6, the forward thrust-to-drag ratio is an input to the sizing loop. The VTOL thrust is computed such that the device is able to lift off with a specific maximum acceleration (a_z). There is a careful balance as to what the optimal a_z is, given the increase in mass due to the higher thrust required on the one hand and the increased VTOL take-off speed on the other. This gives a relation between the total tilt rotor VTOL thrust and the VTOL rotor thrust; coupled with an estimate for the wing planform and the position/size of the tilt and VTOL rotors (with the VTOL rotor constrained by the sweep angle of the wing, see Figure 12.1), this results in a relation between wing sweep and the c.g. and a.c. position, see Figure 12.2.

Note the different constraints for the VTOL rotor, it is constrained by (1) the sweep angle of the wing; (2) the length that the body protrudes from the wing itself and (3) the radius of the VTOL rotor. We can see that adding body lengths requires an increase in sweep angle, as does an increase in rear VTOL radius. With regards to the rear VTOL radius, note that increasing radius results in increasing efficiency of the rotor, there is thus again a careful balance here.

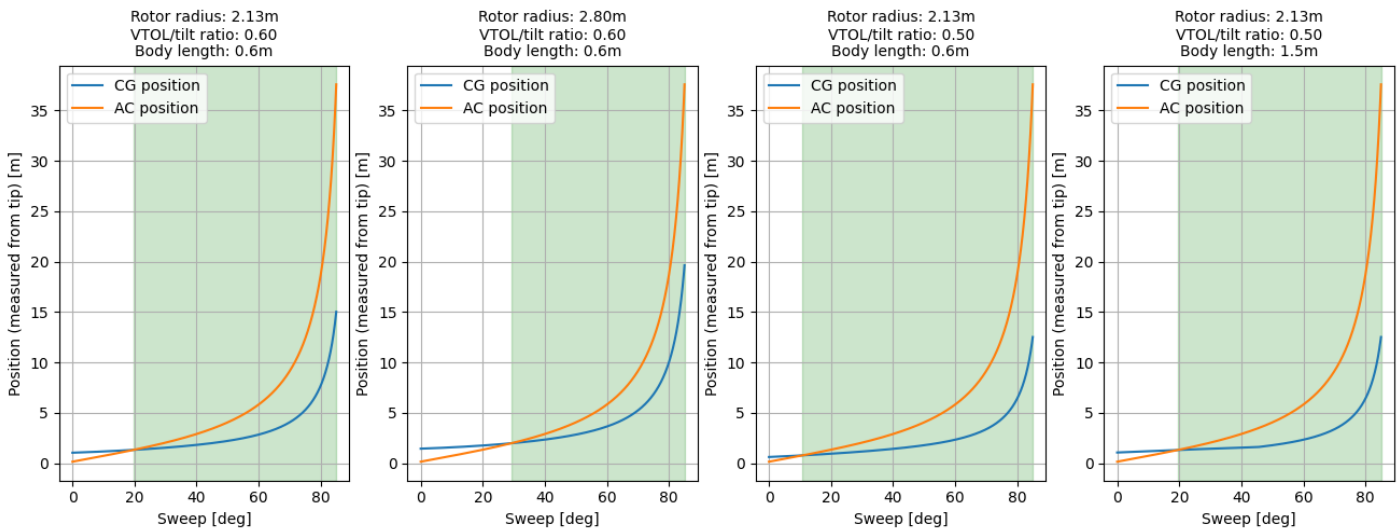


Figure 12.2: Wing sweep influence on stability margin

The above figures serve as an example, in the actual sizing process, an iterative solver is used to solve for the lowest possible sweep angle that delivers the desired stability margin for a given set of inputs. Note that this solver solves for the lowest sweep angle to achieve a desired stability margin (there are two solutions, as is evident from the above plot). An overview of the main effects of adding sweep angle is given in Section 12.2.2, but given the downsides of large sweep angles from a structural and aerodynamic point of view we wish to minimize it.

Influence of Elevons

One downside of a flying wing is that there is a small arm between the elevator and the center of gravity (dependent on the sweep angle of course). With a longer tail arm, as in a conventional aircraft, the tail will need to create a smaller amount of lift to balance the moment produced by the wing. If there is a large moment to balance (i.e. high C_m), this means that a relatively large elevon deflection might be required on the main wing, reducing efficiency. Furthermore, if the elevators need to provide a pitch-up moment and are behind the center of gravity (as we will see they need to be), they subtract from the total lift of the design. Thus decreasing both $\frac{L}{D}$ and C_L .

The moment balance for the wing including elevons is given in Equation 12.5. In this equation, the e subscript denotes variables relevant to the elevon.

$$0 = C_{m_{ac}} + C_{N_w} \cdot \frac{x_{cg} - x_{ac}}{\bar{c}} + dC_{N_e} \cdot \frac{S_e}{S} \cdot \frac{x_{cg} - x_e}{\bar{c}} \quad (12.5)$$

This equation leads us to conclude that a low total pitching moment is preferable to reduce the amount of dC_{N_e} that is required to balance the aircraft. However, consider that this is not the only characteristic of a good selected airfoil,

hence why this effect needs to be included in the sizing model such that we can actually quantify the relative importance of $C_{m_{ac}}$ with respect to other airfoil quantities (i.e. C_L , maximum $\frac{L}{D}$, etc.). For methodology and conclusions on the final airfoil selection process, review Section 6.2.2.

In the sizing model, the negative effect on the cruise lift-over-drag ($\frac{L}{D}$) follows from sizing the elevons for the given wing at each iteration and computing the added lift and drag based on relations from XFLR5, normalized to the new elevon's surface area compared to the reference surface area. This sizing process is explained in more detail in Section 12.2.4. Including elevon sizing in the sizing model like this means that the whole sizing process is as holistic as possible, as the trim deflection angle required by the elevons has a non-negligible effect on $\frac{L}{D}$ and total drag C_D .

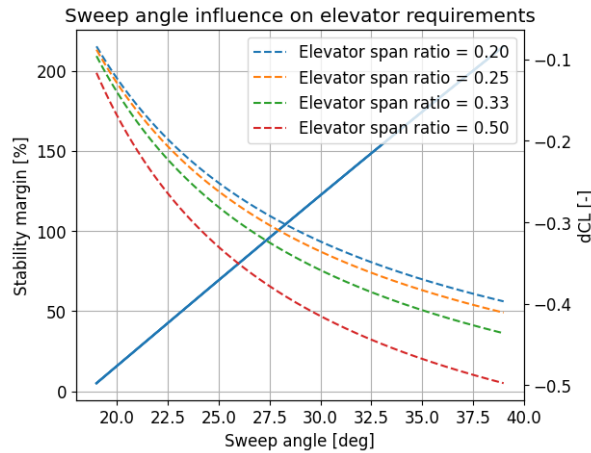


Figure 12.3: Influence on sweep angle and required elevon dC_L for a representative wing with $b = 17$ [m], $c = 0.61$ [m] and the C_L and $C_{m_{ac}}$ for the selected airfoil

Note that increasing the sweep angle will result in a larger moment arm for the elevon; thus decreasing the amount of $dC_{L\delta}$ for a given required C_m and subsequently increasing the efficiency of the wing. There is a trade-off here though, as increasing sweep above the minimum required sweep angle to achieve the desired negative C_{m_α} also increases the second term in the moment equation above - as the aerodynamic center will move backward in relation to the center of gravity (Equation 12.5) - and thus increases the pitching moment that needs to be supplied by the elevon in the first place. This effect is visualized in Figure 12.3 and we can conclude that lower sweep is always the best decision as the dC_L required from the elevon still increases with increasing θ .

Center of Gravity Margins and Component Layouts

At this point, we have considered the desired center of gravity position from a longitudinal and VTOL stability point of view. Component placement should be such that this center of gravity position is achieved. The total mass and center of mass of eight subsystems is considered:

1. **Scientific payload:** Refer to Chapter 7. From a stability and control point of view, the payload configuration is such that the center of mass is as far backward as possible.
2. **Rear VTOL propulsion system:** Follows directly from the sizing model.
3. **Forward propulsion system:** Follows directly from the sizing model.
4. **Wing structure:** Follows from the wing structure sizing code and the wing planform, refer to Chapter 10.
5. **Body structure:** Follows from the body structure sizing code, refer to Chapter 10.
6. **Communications system:** Assumed to be at the payload center of gravity. Refer to Chapter 9 for details on mass sizing.
7. **Miscellaneous mass fraction:** As explained, there is a 10% miscellaneous mass fraction. The center of mass is assumed to be at the battery center of mass.
8. **Battery:** The battery mass follows directly from the sizing model. The batteries are placed inside the wing (as was also taken into account when selecting a relatively high $\frac{L}{c}$ airfoil, see Section 6.2.2) and their center of mass is adjusted until the center of gravity of the design is at the desired location.

The only variation in mass during a sortie is the added mass from the soil sample, a maximum of 500 [g]. This is taken into account during energy calculations as well (see Section 12.2.7). In terms of center of gravity shift; assuming a worst case location fully at the nose (as the soil collection containers are close to the drill) and a wing relatively close to the final design (85 [kg], 20° sweep, 14 [m] span), this amounts to a forward shift of ~1 [% of MAC]. Given that this is a forward shift, this will only increase the stability margin of the aircraft, albeit at the cost of decreased efficiency of the wing due to the elevons (as explained above). It follows from the data in Chapter 13 that both the forward and VTOL rotors are able to provide more vertical thrust if required, albeit at the cost of efficiency. This allows compensation for small shifts in the center of gravity.

In terms of a stability margin used as a sizing target, we wish to minimize it to achieve the most efficient design while maintaining passive stability (see Figure 12.3). *It is decided to size the design for a stability margin of 5% with an extra 5% margin added as a safety factor for the elevon design.*

Longitudinal and VTOL Stability in the Sizing Model

All in all, there are two core stability and control related aspects that are implemented in the sizing model:

1. VTOL stability and the calculation of the wing sweep angle based on a desired stability margin. This is a constraint.
2. The detrimental effect of the trimmed elevons on the wing's aerodynamic performance.

Sweep angle is the most important parameter here from a control and stability point of view but it is important to keep in mind the downsides of excessive sweep, most importantly the ramifications from a structures and an aerodynamic point of view. Structurally, increased sweep adds moment and makes the wing heavier (see Section 10.3.4) and aerodynamically, sweep reduces lift by a factor of $\cos(\theta)$ (see Chapter 11). All these considerations are implemented in the sizing model such that their relative importance is implicitly traded off.

Wing Twist

Wing twist is used to locally increase or reduce the angle of attack. This means that: (1) the angle-of-attack independent moment coefficient changes due to the sweep angle; and (2) the tip of the wing stalls after the root, meaning the outboard control surfaces retain effectiveness during onset of stall. This comes at the cost of reducing the maximum $\frac{L}{D}$ and $C_{L_{max}}$. These effects will be discussed in more detail in Chapter 11, wing twist for longitudinal control and stability will be further discussed when sizing the elevons in Section 12.2.4.

12.2.3 Lateral and Directional Stability and Control Aspects

Several important lateral stability derivatives dictating stability in the lateral modes will be discussed in this section, including how they are influenced by wing parameters; most importantly the sweep angle and the dihedral angle.

On tailless flying wings, directional stability is often achieved using either high sweep or electronic augmentation. The winglets in this design helps significantly with lateral stability. This is covered below as well.

The three lateral modes that are considered are the periodic dutch roll, the aperiodic roll and the aperiodic spiral. These will be covered in more detail in Section 12.2.6. The most important stability derivatives are identified in the list below.

1. $C_{l_\beta} < 0$ The rolling moment due to sideslip. Having negative roll due to sideslip is advantageous as that translates to roll into the wind. Dihedral has a positive effect and is the main contributing factor. As does increased sweep and span, as that means a larger area straight into the flow on the inboard wing. Lower negative C_{l_β} leads to increased spiral stability but decreased dutch roll stability. The spiral stability follows from the asymmetric equations of motion, see Equation 12.6. Spiral stability thus increasing with increasingly negative C_{l_β} as C_{n_r} should also be negative.
2. $C_{n_\beta} > 0$ The yawing moment of the drone due to sideslip, also referred to as weather vane stability. For the same reasons as above, a high sweep and span helps as that increases the drag of the wing facing the flow. In conventional aircraft, this stability derivative is dominated by the vertical tail; i.e. a vertical surface behind the center of gravity. The winglets serve a second purpose as weather vanes in this regard. Their length is based on the distance to ground, as explained in Chapter 10. These add a significant positive contribution.
3. $C_{l_p} < 0$ The rolling moment due to roll. A negative value means the rolling motion is damped, as there is a negative moment response to a positive disturbance. This is the main contributing factor to the aperiodic roll response. The main influences are dihedral (which will be covered below in more detail) and sweep.
4. $C_{l_r} > 0$ The rolling moment due to a yawing motion. Similar to C_{l_β} ; a high sweep and span wing has a positive effect as the wing with the incoming flow has more chord-wise velocity.
5. $C_{n_r} < 0$ The yawing moment due to a yawing motion. Similar to the weather vane stability C_{n_β} ; the winglets play a large role in ensuring this is negative.

$$E = C_{l_\beta} C_{n_r} - C_{n_\beta} C_{l_r} > 0 \quad (12.6)$$

Influence of Dihedral on Stability Derivatives

Using a representative model in XFLR5, we can evaluate the influence on dihedral on the lateral stability derivatives. The primary effect of dihedral is on C_{l_β} . Several stability derivatives are plotted against the dihedral angle Γ in Section 12.2.3. Notice that indeed C_{l_β} appears to be influenced most. All derivatives are normalized to their maximum value. The spiral stability (see Equation 12.6 is highest at $\Gamma = 3^\circ$. There are some negative effects to dihedral as well, most notably: (1) reduction of lift by a factor $\cos(\Gamma)$ and (2) ineffectiveness of the elevons for the same reason as well as the fact that the moment arm gets shorter. Both of these effects are very minimal at such low dihedral angles: at 3° dihedral there is a lift reduction of $\sim 0.15\%$.

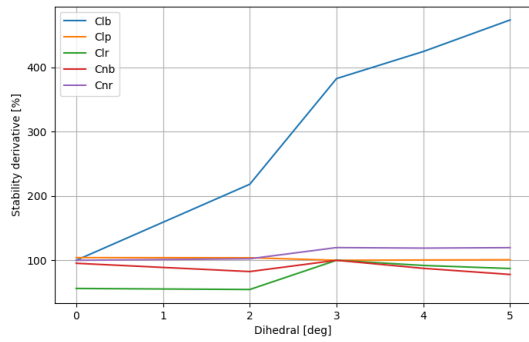


Figure 12.4: Dihedral effect on several stability derivatives

	With winglet	Without winglet
C_{l_r}	0.2406	0.3025
C_{n_r}	-0.01063	-0.007533
C_{Y_r}	0.06125	0.02010
C_{l_β}	-0.1527	-0.2016
C_{n_β}	0.04128	0.004536
C_{Y_β}	-0.3217	-0.01427
C_{l_p}	-0.8096	-0.7956
C_{n_p}	-0.1228	-0.1238
C_{Y_p}	0.1903	0.1052

Table 12.2: Winglet effect on lateral and directional stability derivatives

Influence of Winglets on Stability Derivatives

As explained, the winglets help with the directional stability derivatives. From a simple analysis, we find the results in Figure 12.2.3. Note that the downward angle of the winglets - which helps them serve a dual purpose as landing legs - causes a negative rolling moment due to yaw, so C_{l_r} actually goes down.

Note that especially the weather vane stability C_{n_β} is significantly better with winglets. Given the large decrease in C_{n_β} , we can deduce from Equation 12.6 and the lateral stability diagram that without winglets the spiral stability will go up significantly and the dutch roll stability will go down and possibly become unstable.

Conclusions on Lateral Stability During the Design Phase

With winglets and a 3° dihedral angle Γ , all lateral stability derivatives have the desired sign. For this combination of lateral and directional derivatives, the drone will be just unstable in spiral (from Equation 12.6: $E = -0.0083$ [-]) and stable in dutch roll (from XFLR-5 a negative eigenvalue of -0.00458 [-] is found). Increasing C_{l_β} further by increasing dihedral would result in increased spiral stability, but come at the cost of decreased dutch roll stability, unless the weather vane stability could similarly be increased.

From a control perspective, a slightly unstable spiral is relatively common and can easily be resolved using active yaw control. Yaw control will be covered in Section 12.2.4 below. More detailed analysis of the eigenmotions of the aircraft will be given in Section 12.2.6, however, for now, relaxed stability in the spiral mode is deemed acceptable.

Finally, note that drag and lift from the landing gear is not included in this analysis. Although these have a small moment arm, they are expected to add a positive contribution to the directional stability derivatives.

12.2.4 Control Surface Sizing

Pitch and Roll Control

As explained in Section 12.2.1, outboard elevons are used for both pitch and roll control. Elevons are hardware-wise the same as an aileron, however they are designed to provide the functionality both of an aileron and an elevator. There are two main reasons for this:

1. For both pitch and roll control, an outboard elevon provides the maximum moment with the least flap deflection. For roll control the moment arm along the longitudinal axis is largest that way. For pitch control the arm is similarly maximized due to the sweep angle (see Figure 12.1).
2. The complexity of the design is reduced as just a single control surface is used on either side of the wing, as opposed to two.

The largest drawback of the coupled control is that the elevator deflection might need to be relatively large when climbing and turning at the same time, as essentially the aileron deflection is superimposed on top of the elevator deflection.

There are several design parameters for the elevon control surface, most importantly the chord-ratio ($\frac{c_e}{c}$), the span-ratio ($\frac{b_e}{b}$) and the minimum and maximum deflection ($\delta_{e_{max}}$ and $\delta_{e_{min}}$). The surface area (S_e) of the elevon is dictated by the chord and span ratios. The design methodology used here starts with an upper limit for the chord-ratio and maximum and minimum deflections for the elevon.

There is a 20 [cm] margin between the edge of the elevon and the edge of the wing, where the winglet is mounted. This is because of downwash or upwash due to the elevon near the winglet, reducing efficiency of the wing significantly. This margin is referred to as b_{margin} .

Elevon Chord Ratio

As mentioned, there are downsides to increasing the elevon chord ratio both from a structures and an aerodynamic perspective. Purely from an elevon design perspective, the chord ratio should be as high as possible to maximize the moment arm for the same surface area.

Based on research on separation and non-linear behaviour for control surfaces in low-Reynolds number with high $\frac{t}{c}$, a chord ratio of $\frac{1}{3}$ is deemed the maximum possible.

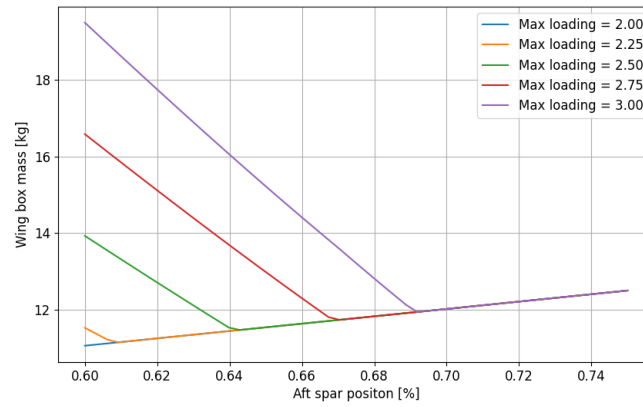


Figure 12.5: Aft spar position as a fraction of the chord versus the total wing box mass

Using the wing box mass estimation model (see Section 10.3.4), it is found that moving the spar to 67% is not critical as long as the maximum wing loading stays below ~ 2.75 [-], see Figure 12.5. The effect of wing loading on turn radius will be discussed below. The two effects causing this are (1) moving the spar forward decreases the wing box mass by decreasing the amount of relatively thick skin and (2) moving the spar forward decreases shear, torsion, and bending resistance of the wing box, thus requiring extra thickness at high wing loading.

Maximum and Minimum Elevon Deflection

Based on this same research, the maximum feasible elevon deflection in this low-Reynolds number environment is determined to be $\pm 15^\circ$.

Control Surface Gap

Based on this same research, it is found that as long as the gap between the wing and the control surface is kept below x [mm], there is no noticeable effect on control surface effectiveness, even at such low Reynolds numbers. This assumption is used throughout this section.

Requirements For Pitch

Pitch requirements follow from requirements on controllability: the aircraft should be trimmable in all relevant flight cases. The limiting cases are the minimum and maximum required lift coefficients. The stall angle of attack is taken as the positive limiting case, which gives $\alpha_{max} = 9^\circ$. Refer to Chapter 11 for lift and drag curves.

Requirements For Roll

The roll requirements follow from two factors: (1) the amount of aileron deflection needed in steady, non-sideslipping turns, and; (2) the amount of aileron deflection needed to satisfy the roll rate requirement. The roll requirement is given as a maximum amount of C_l (rolling moment coefficient) the drone should provide. It should be able to provide this amount of C_l at every trim angle. With $C_l = C_{l_{\delta_a}} \cdot \delta_a$, we can find for a certain elevon design how much extra δ_a is needed to get the required C_l . This iterative process is further explained below.

Based on an initial reference design we can compute the amount of roll (ϕ) needed for a steady, non-sideslipping turn with a certain turn rate. The maximum turn radius follows from Equation 12.7, where n ($n = \frac{L}{W}$) is the maximum loading. Based on Figure 12.5, this max loading was set to 2.5 [-], to have a small safety factor.

$$R = \frac{v^2}{g \cdot \sqrt{n^2 - 1}} \quad (12.7)$$

Based on the equations of motion for horizontal, steady asymmetric flight, we can derive the amount of roll (ϕ), aileron deflection (δ_a) and rudder deflection (δ_r). For steady, non-sideslipping flight ($\beta = 0$) - which is the most efficient - this results in the following required roll angle:

$$\phi = \sin^{-1} \left(4\mu_b \frac{rb}{2v} \right) \quad (12.8)$$

Where the roll rate r follows directly from the turn radius via:

$$r = \frac{v}{R\pi^2} \quad (12.9)$$

Note that the velocity v drops out here. Although the minimum turn radius is dependent on v , the required ϕ for a given turn radius is not. Taking a mass of 95 [kg], a C_L of 1 [-] and the worst-case density, we find a maximum ϕ of $\sim 25^\circ$. With an estimate for C_{l_r} of 0.24, this means that in a coordinated turn the C_l requirement is $\pm \sim 0.00061$ [-].

As for the roll rate requirement, this is dependent on the C_{l_p} of the aircraft:

$$p = -\frac{C_{l_{\delta_a}}}{C_{l_p}} \delta_a \cdot \frac{2v}{b} \quad (12.10)$$

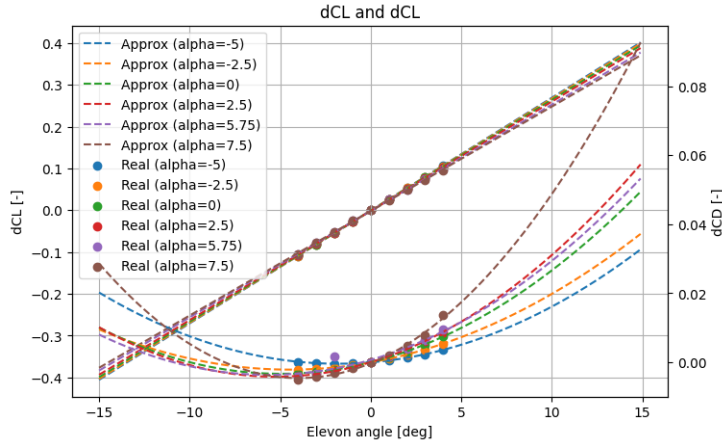


Figure 12.6: Elevon effectiveness as a function of δ for different α

With $C_l = C_{l_{\delta_a}} \cdot \delta_a$, the C_l requirement for a certain roll rate can be computed. For pilots, 15 - 20 [$^{\circ}/s$] is deemed acceptable. This means that we can roll to the desired maximum ϕ of $\sim 25^{\circ}$ in under 2 seconds. Although this is an unmanned system, this minimum acceptable limit for human pilots is considered a decent benchmark for a controllable design. The worst-case velocity is taken to be the velocity at low density at $C_{L_{max}}$. Taking a mass of 95 [kg], a density of 0.0228 [kg/m 3], a surface area of 9.5 [m 2] and a $C_{L_{max}}$ of ~ 1.3 [-], this results in a worst-case velocity $v = \sqrt{\frac{mg_{mars}}{\rho C_{L_{max}} S}} = 52$ [m/s]. This gives for a roll rate requirement of 20 [$^{\circ}/s$], a required C_l of ± 0.04 [-], with an estimate of -0.8 for C_{l_p} (see Figure 12.2.3). As mentioned, these stability derivatives will be further refined in Section 12.2.6. All in all, the C_l requirement is set to ± 0.04 [-].

Elevon Effectiveness

The moment coefficient of the elevon ($C_{m_{\delta}}$) is given as:

$$C_{m_{\delta}} = C_{L_{\delta}} \frac{l_h}{\bar{c}} = C_{L_{\alpha}} \tau \frac{S_e l_e}{S \bar{c}} \quad (12.11)$$

Where τ is a measure of the elevon's efficiency in relation to $C_{L_{\alpha}}$ and follows from the chord ratio and l_h is the moment arm of the elevon. This moment arm follows from the span and chord of the elevon:

$$l_e = \tan(\theta) \cdot \left(\frac{b}{2} - \frac{b_e}{4}\right) + \left(1 - \frac{3c_e}{4\bar{c}}\right) \cdot \bar{c} - x_{cg} - \tan(\theta) \cdot b_{margin} \quad (12.12)$$

Similarly, the aileron effectiveness $C_{l_{\delta_a}}$ follows from:

$$C_{l_{\delta}} = 2 \cdot C_{L_{\delta}} \frac{l_a}{b} \quad (12.13)$$

Where l_a is the moment arm for the aileron, which similarly follows from the planform of the wing::

$$l_a = \cos(\theta) \cdot \left(\frac{1}{2} - \frac{b_e}{4b}\right) - \tan(\theta) \cdot b_{margin} \quad (12.14)$$

Using data from XFLR5 with a wing close to the final wing design with known parameters, we can fit Equation 12.11 to find τ for an elevator with a chord ratio of $\frac{1}{3}$. The data is presented in Figure 12.6. Note that $C_{L_{\delta}}$ does not change much for differing α , meaning that we can use the same τ for all angles of attack.

From this data, we obtain for a chord ratio of $\frac{1}{3}$ a τ value of 0.541. This matches closely with the empirical relation of τ found in literature (see Equation 12.15), which gives a τ value of 0.547.

$$\tau = 1.129 \cdot \frac{c_e}{\bar{c}}^{0.4044} - 0.1772 \quad (12.15)$$

For the wing sweep θ in the final design of 20° and a stability margin of 10% (note the added margin as explained in Section 12.2.2 above) and the pitch and roll requirements as given above, we obtain the following relation for the minimum and maximum required elevon angle against the span ratio $\frac{b_e}{b}$.

Wing Twist

As noted, twisting the tip down comes with several benefits. Quantitatively; (1) it causes an upward pitching moment and (2) it adds an offset to the required elevon angle. In the elevon sizing process, an optimal twist is determined for the part of the wing where the elevon is. This twist distribution is further refined in XFLR5, as will be discussed in Chapter 11. Twist is denoted by β , downward twist (so the angle of incidence becomes lower) is positive.

An approximation of the effect on the constant C_m of the wing is given by:

$$C_{m_{twist}} = C_{L_{twist}} \cdot \frac{(l_h - \frac{1}{4}\bar{c})}{\bar{c}} = \frac{b_e + b_{margin}}{b} C_{L_\alpha} \beta \cdot \frac{(l_h - \frac{1}{4}\bar{c})}{\bar{c}} \tag{12.16}$$

In effect, this means that $C_{m_{ac,wing}} = C_{m_{ac}} + C_{m_{twist}}$.

Elevon Sizing

All in all, these requirements and relations lead to the results in Figure 12.7. The twist and span ratio is determined by evaluating at what twist the minimum elevon span ratio is required to comply with the elevon requirements within the predetermined minimum and maximum deflection of the elevon.

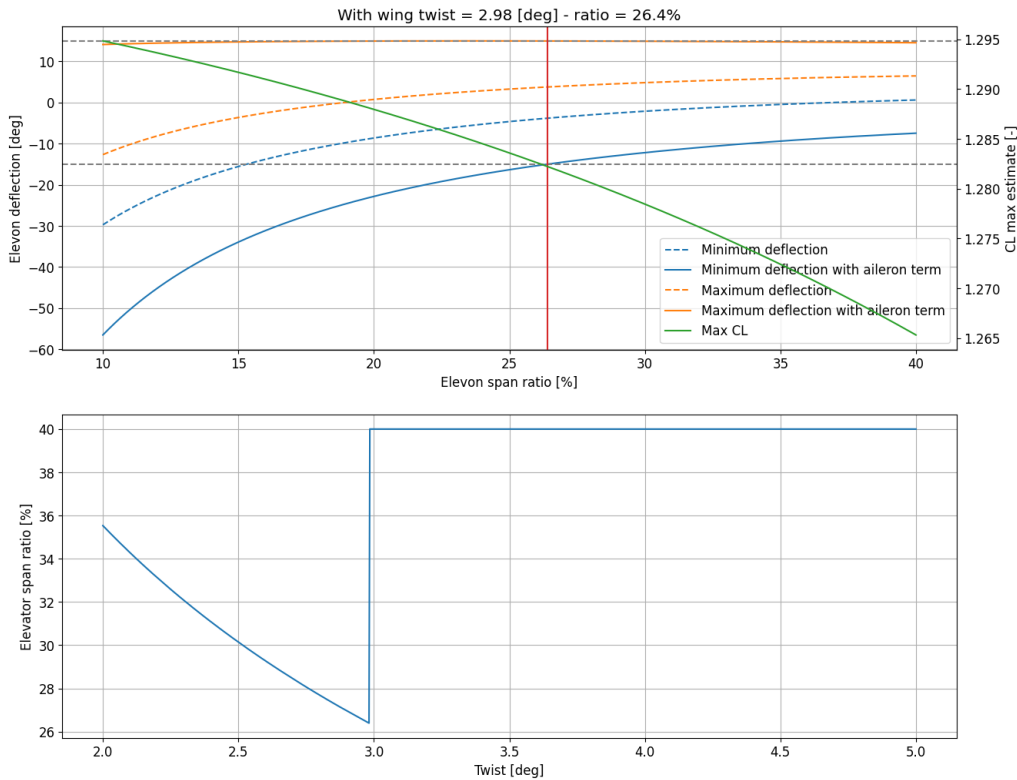


Figure 12.7: Elevon sizing curves for different wing twists β and elevon span ratios

This finally results in an elevon with a chord ratio of $\frac{1}{3}$ and a span ratio of 29%. With the wing twisted 3.3° downwards for the segment with the elevon.

These calculations do not include the contribution from the small fuselage in the middle. Given that this fuselage is not included in any of the sizing, the total lift of the wing will go up slightly. Furthermore, the pitching moment will go down ever so slightly due to the (small) positive contribution to lift at the front. More detailed wing twisting including this fuselage section is analyzed in the aerodynamics section (see Chapter 11) where an XFLR-5 model is used for more detailed analysis.

Yaw Control

There are two ways to achieve yaw control on this design: (1) differential thrust from the front rotors and (2) rudders. The critical requirements follow from (1) front rotor failure, (2) cross-wind flying and (3) rudder requirements in coordinated turns (see also the paragraph on roll requirements). The yaw requirement will be expressed as a maximum desired C_n , with $C_n = \delta_r \cdot C_{n_{\delta_r}}$. The rudders are sized to handle each of these three requirements such that the design can remain operable with one side failed during flight.

Rudder effectiveness computations are the same as for the elevons. The winglets are angled backwards and have a taper ratio λ of two. With a maximum achievable chord ratio of $\frac{1}{3}$, this results in an elevator chord of 0.1 [m] at the tip of the winglet and a chord ratio that changes over the span of the winglet. In terms of span, a 5 [cm] margin is included at the top and bottom of the winglet for mounting clearance and to ensure that the drone does not land

on the control surface. Calculating the average τ over the rudder then gives $\tau = 0.44$. The surface area ratio ($\frac{S_r}{S}$) is ~ 0.2 [-]. From XFLR5-data, it was found the selected airfoil has a C_{L_α} of 0.056 [1/deg] at a Reynold's number of 50,000, see Chapter 11 for more information.

The moment arm of the rudder is given by:

$$l_r = \tan(\theta) \frac{b}{2} + 0.9c - x_{cg} \quad (12.17)$$

This results in a rudder effectiveness of:

$$dC_n = 2 \cdot dC_y \frac{l_r}{b} = 2 \cdot C_{L_\alpha} \tau \delta_r \frac{S_r l_r}{S b} \quad (12.18)$$

With a maximum deflection of $\pm 15^\circ$ and a span of 15 [m], this means these rudders are able to produce a maximum dC_n of 0.0181 [-].

Coordinated Turn Requirement

For coordinated turns, the same relations are used as for the roll requirements. From the lateral equations of motion, we arrive at Equation 12.19 for the yaw rate. The same worst-case scenario is used.

$$r = -\frac{C_{n\delta_r}}{C_{n_r}} \delta_r \cdot \frac{2v}{b} \quad (12.19)$$

Which results in a desired C_n of -2.7×10^{-5} [-], with $C_{n_r} = -0.0106$ [-] (see Figure 12.2.3).

Crosswind Requirement

The crosswind rudder requirement follows from a set of two equations describing the force and moment balance across the lateral axis of the design. The moment balance is Equation 12.20 and the force balance is Equation 12.21. The moment due to the center of drag along the longitudinal axis is neglected as this distance is assumed to be relatively small, given that the center of gravity is roughly in the middle of the wing and the rudder, fuselage, rotors, and landing gear (the main lateral drag producing components) are all placed around this point. The crosswind velocity is given as v_w and the forward velocity as v_f . The total velocity is given as $v_t = \sqrt{v_f^2 + v_w^2}$.

The crosswind velocity is assumed to be 10 [m/s] and is based on typical near-surface wind measurements [58]. With a low estimate for the cruise speed of 52 [m/s], this means that the side-slip angle $\beta = \tan^{-1}(\frac{v_w}{v_f}) = 10.9^\circ$.

$$\frac{1}{2} \rho v_t^2 S b (C_{n_\beta} (\beta - \sigma) + 2dC_y l_r) = 0 \quad (12.20)$$

$$D_y - \frac{1}{2} \rho v_t^2 S (C_{y_\beta} (\beta - \sigma) + dC_y) = 0 \quad (12.21)$$

The total lateral drag $D_y = \frac{1}{2} \rho v_w^2 S_s C_{D_y}$ is computed in Chapter 11 and found to be 3.9 [N].

Solving these equations results in a crab angle σ of 13° with a required C_n of 0.0015 [-]. Significantly lower than the maximum capabilities of the rudders.

Note that it is possible to fly in cross-wind with less rudder, but this requires a roll angle which would result in the instruments no longer pointing downwards, reducing the scientific value of the flight.

Forward Rotor Failure

Although forward rotor failure will surely lead to an emergency landing, as explained in Chapter 13, this is still taken into account in rudder sizing to allow controlled flight to the best possible site for an emergency landing. The cruise drag is given as 36 [N] (see Chapter 11), with an arm of 2.1 [m] (x_{rot}). The required dC_n follows from:

$$dC_n = \frac{2T x_{rot}}{\rho v^2 S b} \quad (12.22)$$

In the worst-case scenario, at $v = 52$ [m/s], this results in a required dC_n of 0.01635 [-], within the limits of the rudder.

Conclusions Regarding Yaw Control

In conclusion, 0.9×0.1 [m] rudders on both winglets alone should be sufficient for yaw control for each of these three scenarios superimposed, within the $\pm 15^\circ$ limit.

In the general case, with two working forward rotors, the rotors can supply differential thrust as well. Albeit at the cost of efficiency (see Chapter 13). Given the VTOL requirement these rotors are heavily oversized for cruise, with a total forward rotor thrust of about 90 [N] at an arm of 2.1 [m], this amounts to a total moment of ~ 113 [Nm], or a dC_n of 0.014 [-] at a cruise speed of 80 [m/s].

12.2.5 Mass, Power, and Cost Budgets

Other than software, the only hardware components on the flight control side are the actuators for the control surfaces. The front tilt rotor actuators are discussed in Chapter 10. The rate requirements follow from the performance model and the required tilting rate during the acceleration and deceleration sequences, see Section 12.2.7.

Elevon Actuators

The total hinge moment for the elevators was found to be ~ 1.5 [Nm] at $v = 80$ [m/s], maximum angle of attack α (9.5°) and maximum elevator deflection δ (15°). With a safety factor of 2, this amounts to a torque requirement of 3 [Nm]. Servos providing such torque are relatively expensive and heavy. The other two options are electro-hydraulic actuators (EHA) and electro-mechanic actuators (EMA). For low hinge moments, an EMA is suitable, which consists of an electric motor and a high-ratio reduction gearbox.

Given that the drone does not fly with relaxed stability and only needs to cover a total of 30° elevon range, the requirements on actuator rate are not very stringent. With 60 [$^\circ$ /s] as a baseline - based on commonly used values - this results in a total motor power requirement of $2\pi \cdot \frac{60}{360} \cdot 3 = 3.14W$. Selecting an existing brushless motor with roughly such a power output and using an estimate of the motor being 36% of the mass of an EMA actuator, this amounts to a total actuator mass of ~ 300 [g].

A decision is made to use redundant actuators on both control surfaces, one on either side, the 20 [cm] margin to the winglet allows for enough space to fit one actuator. The rate of failure is considered negligible with two actuators. The other actuator will need maintenance at base. In total the elevon actuators thus weigh 1.2 [kg] and consume a maximum power of 6.2 [W].

Rudder Actuators

Given the reduction in surface area for the rudder ($\frac{S_r}{S_w} > 10$), as well as the use of a symmetric airfoil, the estimated required torque is significantly lower, in the order of 0.5 [Nm] at 1 [W]. Using a direct-drive servo here reduces complexity, maintenance requirements and weight. An example of such a servo is the [], which amounts to an estimated actuator mass of 200 [g]. Again, redundant actuators are included on both control surfaces, resulting in a total rudder actuator mass of 0.8 [kg] and a maximum power usage of 2 [W].

Conclusions on Mass, Power, and Cost budget

In total, the actuator mass is estimated to be around 2 [kg], with a total power usage of 8.2 [W].

12.2.6 Dynamic Stability Analysis

Dynamic stability analysis is performed using XFLR-5. The process is the same as the process used in Section 12.2.3. The eigenmodes are given in Table 12.3.

Table 12.3: Dynamic eigenmodes of the drone

Eigenmode	Eigenvalue
Phugoid	$-1.247 \pm 2.674i$
Short period	$-1.089 \times 10^{-5} \pm 0.1840i$
Aperiodic roll	-3.575
Dutch roll	$-0.0046 \pm 1.558i$
Aperiodic spiral	0.020

We can distinguish among the symmetric (or longitudinal) eigenmodes: the two conjugate phugoid modes and the two conjugate short period modes. Both of which have negative real values (as expected given that $C_{m_\alpha} < 0$) and are thus stable.

Among the asymmetric (or lateral) eigenmodes we can distinguish the two conjugate Dutch roll modes, the heavily damped aperiodic roll (given that $C_{l_p} \ll 0$) and the slightly unstable aperiodic spiral. As explained in Section 12.2.3, relaxed stability in the spiral mode is not considered a significant issue since the electronic flight control system can be made to cope with this.

12.2.7 Flight Performance Simulation

In terms of flight performance analysis, it is most important to assess what kind of mission profiles the design is capable of. In terms of scientific value the limit to the design's capabilities is largely dictated by the amount of energy used during a certain mission profile. A model was made to assess different mission profiles in detail. This model works by actually controlling the thrust of the two rotors, the tilt angle of the front rotors and the angle of attack. The environment and the design are thus modeled completely separately. This allows for much deeper analysis of the design's capabilities, especially during the complicated and hard to analyze (VTOL) ascent and descent phases. Another major advantage of this approach is that the feasibility of controlling the design in these complicated phases within its limits is proven during this early design phase as well.

A general overview of the model is given in the first section below, after which the complicated landing and take-off maneuvers are explained in more detail. Energy and power usage for different mission profiles is evaluated in

Section 12.2.7.

Flight Performance Model Overview

As explained, the UAV and environment are modelled separately from the drone control. In a broad sense, this amounts to the schematic in Figure 12.8. A Δ_t of 0.01 [s] is used.

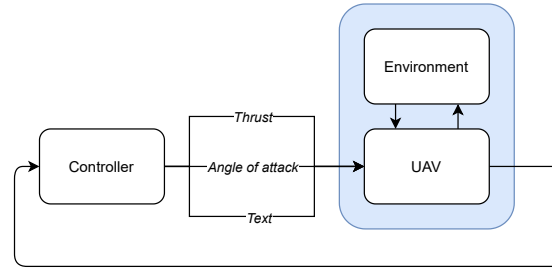


Figure 12.8: Simple overview of the flight performance analysis model

There are a number of different flight phases in the model, which can be chained together to model every possible mission profile. A distinction is made between four different flight phases:

1. **VTOL ascent and descent:** Purely vertical flight until a specified height with a given maximum upward velocity and acceleration.
2. **Horizontal acceleration:** Build speed horizontally and slowly twist the tilt rotors as aerodynamic lift starts to take over from vertical thrust.
3. **Height and airspeed controlled flight:** Controlled flight at a given height with a given speed.
4. **Deceleration:** Reduce speed horizontally, tilt the forward rotors upward and decelerate using the VTOL rotors.

In each of these flight phases, the total thrust (given as a ratio between 0 and 1, x_T), tilt angle (η) and angle of attack (α) is controlled to a target. The total thrust is coupled given that (as explained in Section 12.2.2) the two VTOL rotors need to be in balance to ensure there's no moment about the center of gravity. The total F_x and F_z then follow from Equation 12.23 and Equation 12.24. The acceleration in x and z follow ($a_x = \frac{F_x}{m}$) and $v_x(t)$, $v_z(t)$ and $x(t)$ and $h(t)$ follow from integration. The power ($P(t)$) is similarly computed from the thrust, energy ($E(t)$) follows from integration.

$$F_x = F_{x_{thrust}} + F_{x_{aero}} = \sin(\eta - \alpha) \cdot x_T T_{forward} - \sin(\alpha) \cdot x_T T_{VTOL} - \frac{1}{2} v_{total}^2 \rho S C_D \quad (12.23)$$

$$F_z = F_{z_{thrust}} + F_{z_{aero}} - W = \cos(\eta - \alpha) \cdot x_T T_{forward} + \cos(\eta - \alpha) \cdot x_T T_{VTOL} + \frac{1}{2} v_{total}^2 \rho S C_L - m g_{mars} \quad (12.24)$$

The model for forward and VTOL rotor thrust and power usage at given conditions is further explained in Chapter 13 and Chapter 13. The lift and drag coefficients (C_L and C_D) follow from the lift curves for the airfoil and parasitic drag computations, as explained in Chapter 11. Furthermore, there is a contribution from the required elevator trim (see the lift and drag curves in Figure 12.6) that follows from the required trim at that angle of attack. The total velocity v_{total} follows from v_x and v_z : $v_{total} = \sqrt{v_x^2 + v_z^2}$. Constant power usage from instruments and other devices during the different mission phases is covered in Chapter 14. Power usage due to thermal is covered in Chapter 15. Constant power input from the solar panels can also be included and is similarly covered in more detail in Chapter 14.

VTOL Maneuver

The VTOL maneuver is relatively simple. A P-controller determines a velocity target in the upward direction ($v_{z_{target}}$) and the thrust is controlled to this target via another P-controller. This kind of cascaded control loop works well given the second-order relation between thrust and height. Following analysis from the propulsion subsystem, a 1.5 [m/s] limit is included on upward v_z to combat decreased thrust at high incoming velocity, see Chapter 13. A 0.5 [m/s] limit is included on downward v_z for landing safety.

The VTOL ascent and descent phases require almost full power from all three rotors.

Parameter Optimization VTOL Phase

The maximum upward and downward acceleration (a_z) as well as the target VTOL height (h_{VTOL}) are sensitive parameters to the energy usage in this phase. As noted in Chapter 8, the minimum height with regard to safety and obstacles is 3 [m]. From this analysis we can conclude that h_{VTOL} should be minimized for optimal energy usage, and a_z maximized. Note though that maximizing a_z further would mean increased mass on the front and rear VTOL rotors. In terms of general design sizing, the optimum is found to be around 0.25 [m/s²] at an ascent and descent height of 5 [m].

Acceleration and Deceleration Maneuvers

The acceleration and deceleration maneuvers are the most complicated maneuvers in the mission profile, as they include the tilting of the rotors. The tilt rotors have fixed pitch and - also given non-linearities when spinning back-

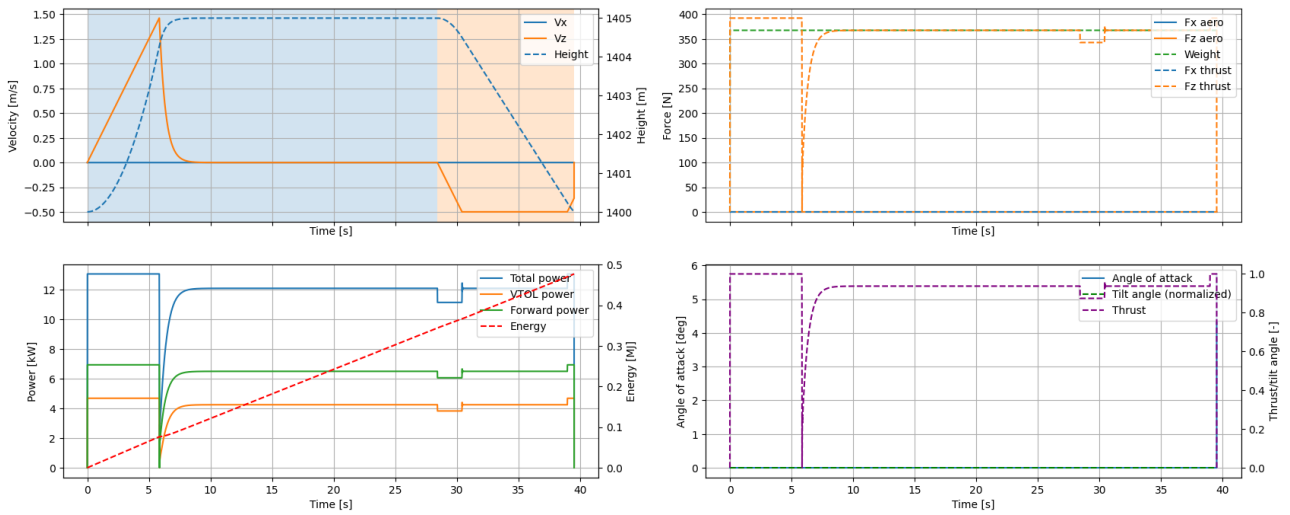


Figure 12.9: VTOL ascent and descent phases control outputs

wards - are thus incapable of producing reverse thrust, see also Chapter 13. The only effect taken into account is the reduced incoming velocity in the propeller, this is further explained in Chapter 13.

During the acceleration phase, the angle of the tilt rotors is computed such that there is no upward resultant force:

$$\eta = \cos^{-1}\left(-\frac{F_{z_{aero}}}{T_{VTOL}}\right) \quad (12.25)$$

The angle of attack is set to the maximum angle of attack, to make the tilting phase as quick as possible, as that means that $F_{z_{aero}}$ will get larger faster. Once the tilting phase is completed, the drone switches to the normal flight phase: the thrust is regulated to the optimal velocity (which follows from the C_L at the optimal $\frac{L}{D}$) and the angle of attack is regulated to a certain v_z target, which follows from a controller to a height target. This is a similar cascaded control loop as used for the VTOL ascent and descent stages. An overview of the control outputs and the velocities and heights during this phase is given in Figure 12.10.

The deceleration phase is slightly different. There are two separate parts: (1) deceleration to the stall velocity and (2) tilting the rotors and applying vertical thrust as the drone decelerates. This first phase is the same as the normal flight phase described above, just with a lower velocity and height setpoint. The second part of the deceleration phase starts with the tilt rotors tilting up again quickly. As there is no reverse thrust available, it's more efficient to tilt them immediately and start decelerating while applying enough VTOL thrust to have a net-zero upward resultant force. The angle of attack stays at the maximum angle of attack to achieve maximum drag and maximum lift. Note that due to the angle of attack there is some negative thrust (see Figure 12.1), which helps slow down significantly.

The acceleration and deceleration phase - with a small cruise phase in the middle - are shown in Figure 12.10 below.

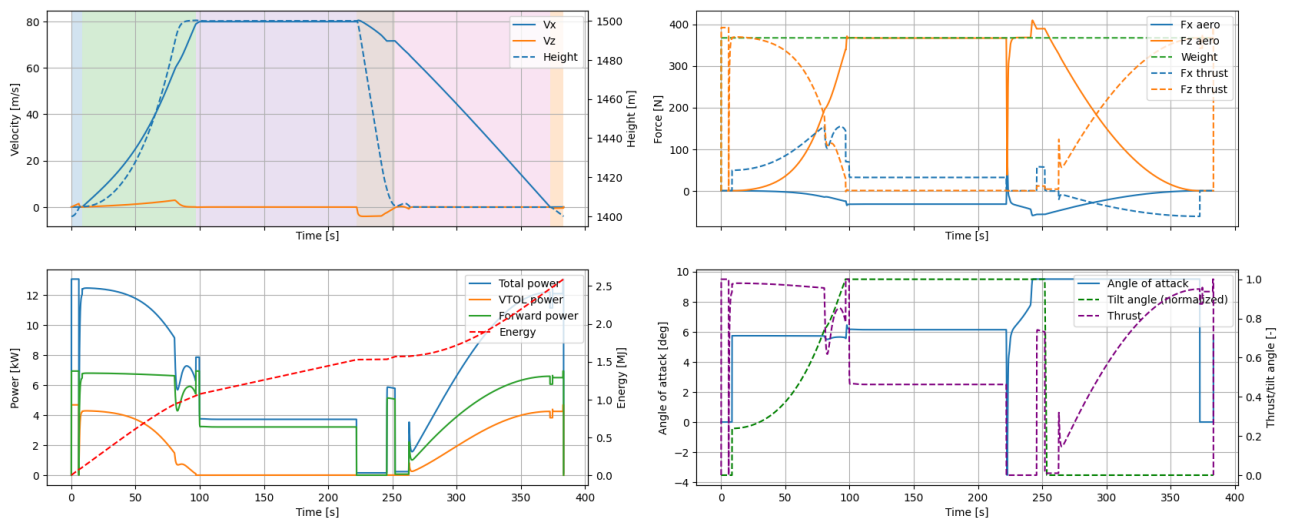


Figure 12.10: Acceleration and deceleration sequences

Note that for the acceleration sequence, the design can already start to climb as the tilt rotors angle down. This is found to be more efficient than first tilting the rotors down while flying horizontally (requiring a significant reduction

in thrust just to stay horizontal) and only then starting to climb. The climb gradient is set to 5% here. On such small height increases the climb gradient is negligible for energy usage.

The top-right graph with the aerodynamic and thrust forces in the x - and z -direction explain the concept of the acceleration and deceleration sequences a bit better. Note the balance between $F_{z_{thrust}}$ and $F_{z_{aero}}$. Note also how increased stall angle of attack would be beneficial as that allows the tilt and VTOL rotors to produce more negative thrust and slow down faster. Slowing down at angles of attack beyond the stall angle of attack has been considered but not implemented at the moment due to unknown non-linear aerodynamic effects and uncertain structural loads. Even if higher rotation angles are allowed only at lower v_x , this could be a major source of energy saving during the mission.

Compared with the small cruise phase in between, it is clear that the landing and take-off phase of the flight are significantly more power intensive.

Integration in Sizing Model

This performance profiling code is included in the sizing model. It is found quickly that the VTOL ascent and descent phases are the most energy intensive, so Section 5.3.2 is used as the worst-case mission profile in terms of energy usage. This total energy usage over a mission is used to size the batteries, as explained in Chapter 14.

Mission Profiles

With the selected design, we can now evaluate to what extent the drone is able to perform the required mission profiles. As well as explore the limits of its capabilities. The two mission profiles as given in Chapter 5 will be used as a baseline. Note again that the UAV is sized to be able to exactly perform the soil collection mission (Section 5.3.2).

Soil Collection

A reference soil collection mission profile is presented in Figure 12.11. The red line indicates the energy used at a given point in the mission. It is clear that for soil collection missions the majority of the power is consumed by the landing and take-off sequences. However, the majority of the time is taken up by the drilling operation.

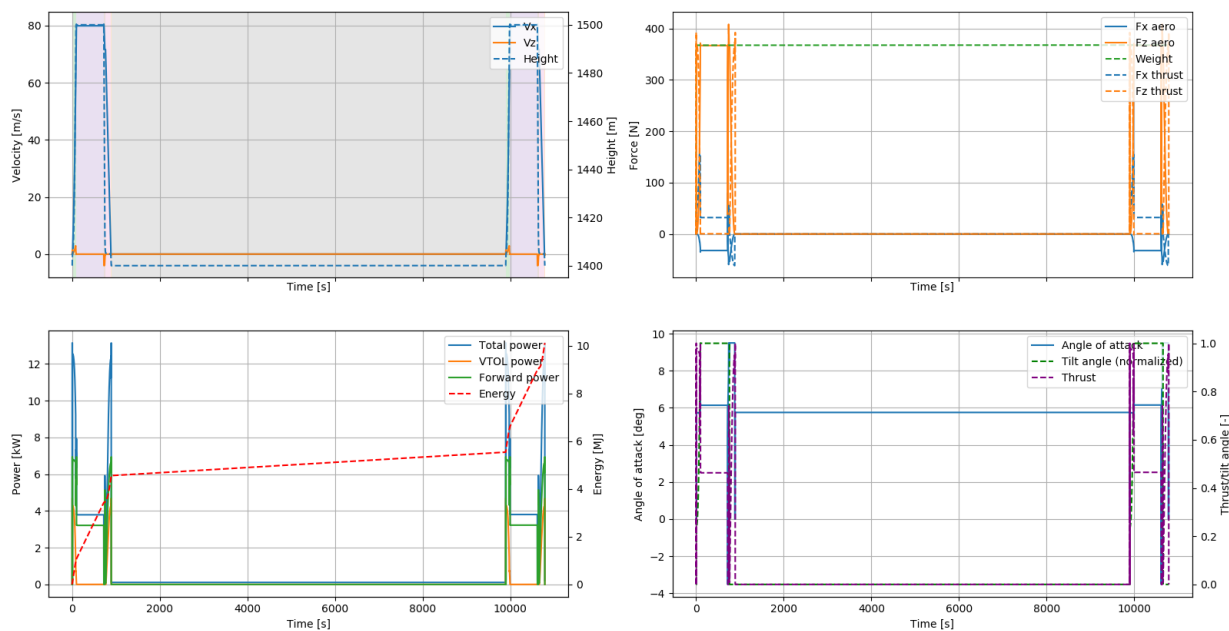


Figure 12.11: Soil collection expedition profile

Long-Range Flight

The long range surveying flight mission profile is presented in Figure 12.12. In this case the majority of the energy is consumed by the cruise phase of the design. And even though the flight time is significantly longer than the soil collection time the overall mission length is reduced by a factor of two due to the lack of drilling time.

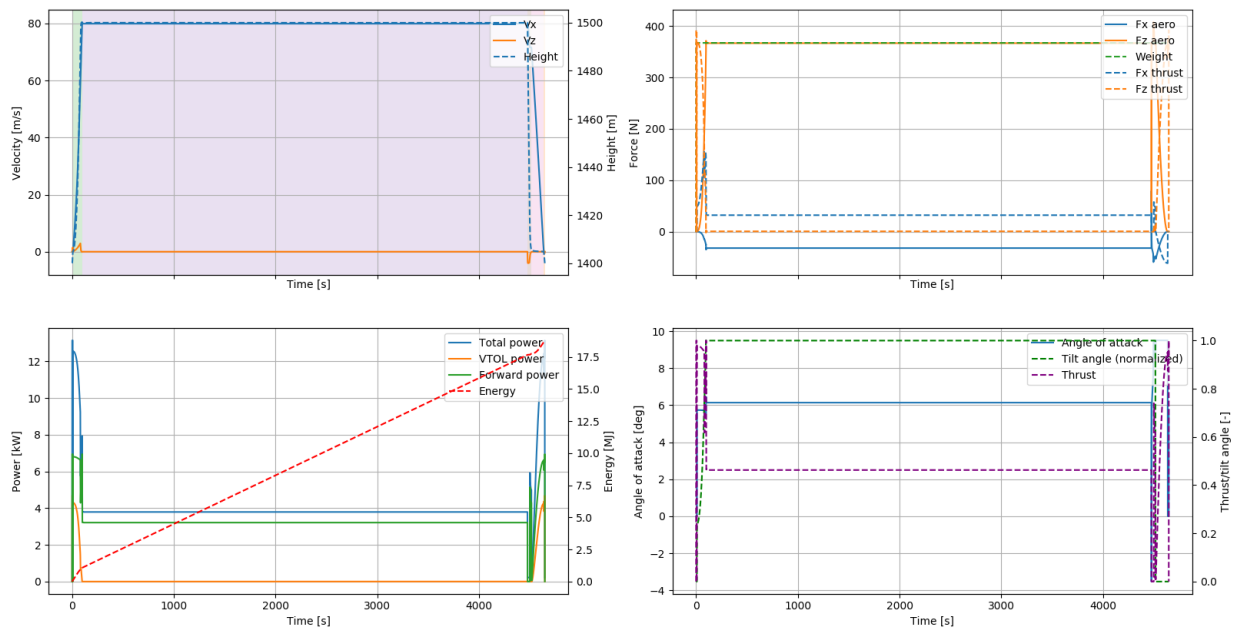


Figure 12.12: Remote sensing expedition profile

12.3 Risk Analysis

- **CL-1: Elevon actuator failure**
 - **Effect:** Loss of pitch control and partial loss of roll control (with failure on a single side). Unable to trim the aircraft in pitch
 - **Probability:** This risk is classified as **Rare**.
 - **Severity:** This risk is classified as **Catastrophic** as there is a large chance of total mission failure and the need for an emergency landing.
 - **Mitigation:** Two mitigation procedures are in place: (1) the tilt rotors have freedom to move up and down slightly to trim the aircraft (as explained in Section 12.2.7) at the cost of efficiency and (2) there are redundant actuators for both elevons.
 - **Effect of Mitigation:** The probability of elevon actuator failure is not decreased, the severity is significantly decreased to **Marginal**. The UAV would be able to fly on, but such a failure would warrant an immediate return to base and thus have a negative effect on mission performance.
- **CL-2: Elevon actuator stuck**
 - **Effect:** Unable to properly trim the aircraft and partial loss of roll control.
 - **Probability:** This risk is classified as **Rare**.
 - **Severity:** This risk is classified as **Catastrophic** as there is a large chance of total mission failure and the need for an emergency landing.
 - **Mitigation:** Two mitigation procedures are in place: (1) the tilt rotors can provide the required trim moment coefficient by tilting up and down and (2) there are two actuators, with the two actuators together possibly being able to provide enough torque to get the actuator unstuck. With regards to the first option, especially during landing and deceleration, this is a relatively unknown flight state and the design's capability to properly decelerate without being able to trim the angle of attack is uncertain.
 - **Effect of Mitigation:** The probability is not decreased, the severity is slightly decreased to **Critical** if the second mitigation procedure does not work. The severity is decreased to **Marginal** if the second actuator is able to get the actuator unstuck for the same reasons as risk **CTRL-1**.
- **CL-3: Rudder actuator failure**
 - **Effect:** Unable to provide yaw control when one of the front rotors fails as well (refer to Section 12.2.4).
 - **Probability:** This risk is classified as **Rare**.
 - **Severity:** This risk is classified as **Critical**.
 - **Mitigation:** The other rudder should be able to provide the required rudder deflection for all cases except rotor failure. In any case, the differential thrust from the front rotors also provides yaw control. This effect is mitigated by adding a redundant rudder actuator. This is deemed worth it given the only small increase in mass (see Section 12.2.4).
 - **Effect of Mitigation:** The probability is not decreased, the severity is slightly decreased to **Marginal**, for

the same reasons as risk 1L-1.

- **CL-4: Rudder actuator stuck**
 - **Effect:** Possibly unable to provide yaw control when one of the front rotors fails (refer to Section 12.2.4).
 - **Probability:** This risk is classified as **Rare**.
 - **Severity:** This risk is classified as **Critical**.
 - **Mitigation:** Two mitigation procedures are in place: (1) the tilt rotors and remaining rudder can provide the required compensation and yaw control and (2) there are two actuators, with the two actuators together possibly being able to provide enough torque to get the rudder unstuck.
 - **Effect of Mitigation:** The probability is not decreased, the severity is slightly decreased to **Marginal**, for the same reasons as risk CTRL-1.

12.4 Verification and Validation

12.4.1 Unit Tests

The analysis was mostly performed by deriving equations and using a Python program to plot the graphs in order to make a decision.

Needed Center of Gravity Position

The required center of gravity is determined based on the take-off and hover simulation. This states that the resulting thrust vector of all 3 rotors must act through the center of gravity for the system to be stable. As the locations of the front and back rotors are known this can simply be verified using a hand calculation.

Returned Center of Gravity

The needed center of gravity position is then used by the code to determine the location the batteries have to be at in order to ensure that the center of gravity is at the required location. Since the center of gravity for all other components, such as the payload, motors and structures, are known, determining the center of gravity location is rather straightforward. Nevertheless, it is still important to check the result with a simple manual calculation, which was thus subsequently performed and verified the center of gravity location calculator.

Stability Margin

The stability margin can simply be verified using hand calculations based on the locations for the aerodynamic center and the center of gravity. Additionally, this was used to verify that the code outputs a design with the desired stability margin (for 5, 10 and 15%).

12.4.2 System Tests

Energy Module

The code module to calculate required energy to perform a mission profile is integral for computing the battery mass and thus has a large influence on the final mass of the drone. Due to the importance and large extent of the code, two system tests were performed as verification. Firstly, the same mission profile as used for initial sizing was put into the program and the result was compared to the result of the initial sizing code. Secondly, if it is assumed that there is no power generation from the solar panels and the efficiencies are ignored, the sum of kinetic energy, potential energy and work done against drag should equal the amount of energy used from the battery. Using these two tests the energy module was verified.

Lift Module

Phase 2 of the take-off and landing operations require that the design produces sufficient lift to counter the weight of the drone. All of the parameters (such as velocity, angle of attack, rotor tilt angle, thrust setting etc.) which influence the forces in the free body diagram are stored in lists with time steps of 0.1 seconds. This can be used to verify that at any moment on the sequence the sum of the vertical components of the lift generated by the wing, vertical rotor and tilt rotor is equal to the weight of the drone.

12.4.3 Validation

The aerodynamic center position was validated using the XFLR-5 model. As XFLR is a validated software and has been shown to provide accurate results for the aerodynamic center position it can be used to validate the ac estimate given in Equation 12.4.

The exact aerodynamic characteristics and interactions between propulsion system and the wing must be modelled using CFD simulations or wind tunnel data to validate the stability conditions during take-off and landing.

Additionally, the assumption (based on literature) that the elevons can be deflected by an angle of 15 degrees must be validated using CFD or wind tunnel testing. This validation was not performed in this report and should be done at a later stage in order to validate the design

The planned maneuvers also need to be validated. In the current phase, gyroscopic effects on rotating the forward rotors were not taken into account yet. Furthermore, spin-up or spin-down of the rotors was not given a limit. For future validation of the sizing program, the currently used rotation rates of the forward rotors and the spin-up and spin-down of the rotors should be further analyzed and tested in a wind tunnel.

13 Propulsion Analysis

The propulsion subsystem is tasked with providing enough thrust for VTOL as well as forward flight, which will be achieved by rotating the forward rotors up and down for VTOL and forward flight respectively. This chapter will go into more depth about the performance analysis of both the tilt rotors and the fixed vertical rotors. Starting with the requirements in Section 13.1, continuing with a performance analysis in Section 13.2. After which the layout of the system will be discussed in Section 13.4. Following will be a subsystem specific risk analysis in Section 13.5, in which propulsion specific risks will be discussed and mitigation procedures presented. Finally verification and validation will be performed for the software used to analyse the rotor performance in Section 13.6.

13.1 Requirements

In this section a quick overview of all the propulsion subsystem requirements and their compliance can be found in Table 13.1. The compliance of these requirements will be elaborated on in Section 13.2.

Table 13.1: Requirements related to propulsion and their expected compliance

Index: DME-REQ-	Requirement	Compliance
SYS-PROP-01	The propulsion system shall be able to provide 424.44 [N] of thrust during VTOL.	Satisfied
SYS-PROP-02	One rotor inoperative shall not lead directly to mission failure.	Satisfied
SYS-PROP-03	The forward propulsion system shall have VTOL capabilities.	Satisfied
SYS-PROP-04	Propeller tip speed shall not exceed 0.8 Mach.	Satisfied
SYS-PROP-05	The forward propulsion system shall be able to provide 200.59 [N] of vertical thrust during VTOL.	Satisfied
SYS-PROP-06	The vertical rotors shall provide 115.73 [N] of vertical thrust with only one vertical rotor functioning.	Satisfied
SYS-PROP-07	The forward propulsion system shall provide 36 [N] of horizontal thrust with only one forward propeller inoperative.	Satisfied

13.2 Model and Analysis

In order to determine an efficient layout for the propulsion system the factors that influence rotor performance first has to be analyzed. This is be done by means of a literature study from which the important design parameters are identified. Afterwards different designs are generated and iterated in the blade element and momentum theory software JBlade, which is an adaptation of the QBlade software designed to work for propellers. First some background about blade element and momentum theory is given, after which the vertical propulsion is analysed and the results presented. Finally the tilt rotors are analysed as these combine concepts from vertical rotors and conventional propellers.

13.2.1 Blade Element Momentum Theory

Blade element momentum theory works by dividing the rotor blade up into small segments which can be evaluated 2 dimensionally so that the problem can be divided up into four forces. These being lift, drag, thrust, and torque, a sketch of such a blade segment can be seen in Figure 13.1. All the forces are calculated incrementally and their components summed in order to obtain the entire radial distribution along the blade. Additional equations are used in order to solve for certain variables which are obtained from momentum theory which treats the blade in a macroscopic sense instead of small segments.

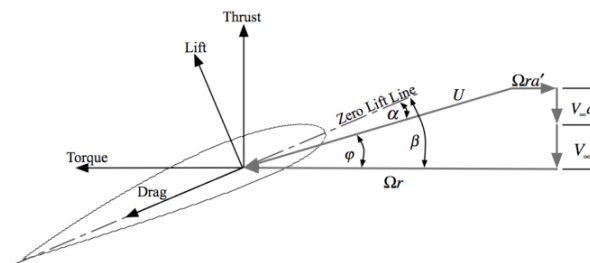


Figure 13.1: Blade segment with relevant angles and force vectors [126]

In Figure 13.1 several angles can be seen, these are the inflow angle φ , the angle of attack α , and the twist angle β which simply is a combination of the previous two. The flight path angle can be calculated by taking the arc tangent of the free stream velocity V_∞ and the free stream plus the free stream velocity times the axial induction factor a_i divided by the radial velocity Ωr minus the radial velocity times the tangential induction factor a_i' . Here Ω is the

rotors radial velocity in rad/s and r the segment's radial position in m. Thus in order to obtain the twist angle the flight path angle has to be calculated. In order to do this the induction factors will have to be calculated first. An expression for these induction factors can be obtained by combining expressions two different expressions for the torque and thrust. Yielding the following two expressions Equation 13.1 and Equation 13.2, more information on how these were obtained can be found in [67]. These induction factors together with the inflow angle can be solved iteratively until convergence is reached for the blade segment being treated. From these the torque and thrust can be calculated and thus the performance can be analyzed.

$$\frac{a_i}{a_i - 1} = \frac{\sigma_\lambda}{4\sin^2\varphi} (C_L(\alpha)\cos\varphi + C_D(\alpha)\sin\varphi) \quad (13.1) \quad \frac{a'_i}{a_i - 1} = \frac{\sigma_\lambda}{4\lambda\sin^2\varphi} (C_L(\alpha)\sin\varphi + C_D(\alpha)\cos\varphi) \quad (13.2)$$

Here σ_λ is the local solidity of the blade, and λ the ratio between radial velocity and velocity far down stream of the blade U_∞ . The lift and drag coefficients, $C_L(a)$ and $C_D(a)$ respectively, as a function of angle of attack also have to be known. How these are obtained will be elaborated on in Section 13.2.2.

$$\sigma_\lambda = \frac{Bc_\lambda}{2\pi r} \quad (13.3) \quad \lambda = \frac{\Omega r}{U_\infty} \quad (13.4)$$

Here B is the number of blades, and c_λ the local chord. It should be mentioned that Equation 13.1 and Equation 13.2 do not account for the fact that circulation of the flow has to be zero at the tip [67]. In order to account for this the Prandtl tip correction is applied to the induction factors. This correction however does not suffice when the axial induction reaches a value higher than 0.4, in order to still obtain valid results a hub loss factor is also introduced. The equation for the correction factors(F) and the equations for the induction factors with the corrections applied can be found below.

$$F = \frac{4}{\pi^2} \arccos\left(e^{-\frac{B(R-r)}{2r\sin\varphi}}\right) \cdot \arccos\left(e^{-\frac{B(r-r_{hub})}{2r\sin(\varphi)}}\right) \quad (13.5)$$

$$\frac{a_i}{a_i - 1} = \frac{\sigma_\lambda}{4F\sin^2\varphi} (C_L(\alpha)\cos\varphi + C_D(\alpha)\sin\varphi) \quad (13.6) \quad \frac{a'_i}{a_i - 1} = \frac{\sigma_\lambda}{4F\lambda\sin^2\varphi} (C_L(\alpha)\sin\varphi + C_D(\alpha)\cos\varphi) \quad (13.7)$$

These modifications already greatly increase the accuracy of the obtained values using BEM analysis, however to obtain even more accurate values 3D corrections can be applied in order to account for change in lift due to the rotation of the flow around the blade, for more information on these corrections the reader is referred to C. Lindenburg's paper [82]. An important assumption made by BEM theory is that the wake does not expand due to the vortices being shed by the tips. Which can reduce the validity of the results for lightly loaded rotors [43].

From these equations and the aforementioned assumptions the shortcomings of BEM theory start to become clearer, as BEM theory can't by nature deal with 3D effects and can only apply 3D corrections. With all the aforementioned corrections applied however BEM analysis can yield very accurate results and can be a great aid for designing a rotor when applied correctly.

13.2.2 Post-Stall Lift and Drag Model

In order for BEM theory to yield accurate results the post stall characteristics of the treated airfoil have to be known, preferably by means of wind-tunnel test obtained data. However for the low Reynolds number range experienced by the rotors, on the order of 10,000 - 100,000, post stall data simply doesn't exist. Meaning the post stall C_L and C_D will have to be evaluated by means of empirical model. Such an empirical model has been developed by B. Montgomerrie [95], which works by approximating the airfoil as a thin flat plate and applying corrections to make it better fit the existing pre-stall polar. An example of such a post stall polar can be seen in Figure 13.2. Polars such as these are able to give quite good results when they are fine tuned to fit with the existing low angle of attack polar.

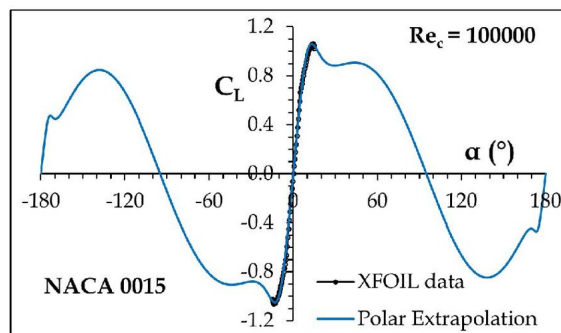


Figure 13.2: 360° C_L polar [123]

13.2.3 Ducted Vertical Rotor

Some research was done to evaluate the possibility of using a ducted propeller. Theoretical estimates conclude that using a ducted propeller can improve the efficiency of the vertical propulsion system by up to 30% [93]. However, some realistic estimates (for what is achievable in real life) expect an increase in performance of up to 10%. This makes it possible to use a smaller rotor for the VTOL system which is beneficial for the layout and size of the UAV. An initial analysis showed that an exposed duct would induce up to 90 [N] of additional parasite drag during cruise, this is quite extreme as the expected drag induced by the wing is 25 [N] during cruise. Integrating the duct with the body behind the wing could lead to some reduction in the drag. Initial estimates of the drag induced by the wing-integrated duct configuration lead to a parasite drag of 60 [N]. While this is a large improvement compared to the exposed configuration, it is clear that adding additional wetted area at these low Reynolds numbers quickly causes a large increase in the drag at cruise.

13.2.4 Rotor Performance

Performance of tilt rotors can be difficult to optimize, since one has to consider the performance of the rotor during hover as well as the performance during forward flight. During hover the power required for the rotor to lift the vehicle of the ground is dictated by Equation 13.8. Where P_i is the induced power, and P_o is the profile power. The parasite power (P_p) has been left out since during hover the vehicle's velocity is zero.

$$P = P_i + P_o \quad (13.8)$$

Equation 13.8 is displayed in its non-dimensionalized form in Equation 13.9 for ease of use during calculations. Which relates back to the required power according to Equation 13.10.

$$C_P = C_{P_i} + C_{P_o} \quad (13.9) \quad P = C_P * \rho * A (R\Omega)^3 \quad (13.10)$$

Induced Power

The induced power coefficient can be related to the thrust coefficient (C_T) by use of equation Equation 13.12, where k is an empirical factor which covers the effects of non-uniform flow and tip loss, which is typically set to be 1.15 [75], and λ_i is the induced velocity.

$$C_T = \frac{T}{0.5\rho(R\Omega)^2 A} \quad (13.11) \quad C_{P_i} = k * \lambda_i * C_T \quad (13.12)$$

Thus for given rotor thrust, the only parameter that has to be calculated to obtain the induced power coefficient is the induced velocity. Which can be calculated iteratively using Equation 13.13 and Equation 13.14. Where μ is the forward velocity, and λ the in-flow ratio.

$$\lambda_i = \frac{C_T}{2\sqrt{\mu^2 + \lambda^2}} \quad (13.13) \quad \lambda_i = \lambda - \mu * \tan(a_s) \quad (13.14)$$

During hover, when forward velocity is zero, these equations simply reduce to Equation 13.15.

$$\lambda_i = \sqrt{\frac{C_T}{2}} \quad (13.15)$$

Now it has become evident based on Equation 13.12 that the induced power can be directly related to the thrust coefficient and the empirical factor k .

Profile Power

Profile power is the power required to spin the rotor, i.e. the drag of the rotor during rotation. To estimate the profile power some blade characteristics like the drag coefficient have to be known in advance. Since rotors operate at high angles of attack, even post stall at some sections of the blade, it is required estimate the airfoils post stall behaviour. This does not mean that the blade will be operating post stall, as this is not desired, but it is required to perform the analysis. These estimations will be performed with the help of the Jblade software, which uses XFOIL in order to estimate the airfoil's pre stall characteristics and then uses the Montgomerie method to extrapolate the airfoil characteristics post stall, as described in Section 13.2.2. From this data the blade mean drag coefficient (C_{d0}) can be estimated. The profile power coefficient itself can be calculated using Equation 13.17, where σ is the rotor solidity which is calculated using Equation 13.16. Here B is the number of blades, c the mean blade chord in [m], and R the blade radius in [m].

$$\sigma = \frac{Bc}{R\pi} \quad (13.16) \quad C_{P_o} = \frac{C_{d0}\sigma}{8} (1 + 4.6\mu^2) \quad (13.17)$$

It should be noted that this method of calculating the induced power is very limited and will only be used for preliminary sizing, as it does not take into account stall and compressibility effects. A more accurate way to calculate profile power can be obtained when more is known about the blade profile.

13.2.5 Improving Rotor Efficiency

From Equation 13.10 it becomes evident that the required power can be reduced by reducing the tip speed and thus the rotational velocity of the blade. By using Equation 13.11 and Equation 13.10 it also becomes clear that power scales with rotational velocity cubed and thrust scales with the rotational velocity squared. Thus providing further incentive to reduce the rotational velocity required as much as possible. This can be achieved by using an airfoil with a high lift coefficient and preferably a low mean drag coefficient. Operating a rotor at low tip speeds and high lift coefficient relates to a high rotor solidity, which for a given diameter and number of blades yields the mean blade chord. A high solidity together with low tip speed leads to low disk loading, which in turn leads to a better hover efficiency. However due to the low Reynolds numbers found on Mars there exists a lower limit on the tip speed, this is due to the fact that even for airfoils optimized for low Reynolds numbers the lift decreases dramatically when the Reynolds number falls below 50,000. Together with an increase in drag this leads to low L/D and thus to more torque produced for less thrust, which in turn leads to a worse efficiency.

Tip Effects

Rotors suffer from the same adverse tip effects as normal fixed wings, namely tip vortices which are caused by the high pressure air flowing into the low pressure region of the blade. These tip effects should be taken into account as they can severely reduce lift generated at the tip and thus reduce efficiency. Ways to reduce tip effects would be to reduce the lift produced near the tip, which would lead to a weaker vortex at the tip. This however is undesirable as this section of the blade would no longer contribute optimally to producing thrust. Another way to reduce the strength of the tip vortex is to include taper at the blade tip [6], which would reduce the lift at outboard sections, but would still allow them to operate at optimal angles of attack and thus not unnecessarily increase drag. It should also be mentioned that reducing the number of blades is beneficial for reducing tip effects, this has the added benefit of reducing wake interaction between the blades. Which is especially important at the low operating Reynolds numbers found on Mars, as the boundary layer becomes more sensitive to disturbances at low Reynolds numbers. Thus the optimal number of blades is 2, as this still leads to a balanced propeller while reducing wake interaction and tip effects. This may sound contradictory given the previous comment about high solidity being better, however a higher blade number would mean more wake interaction between the blades. Another consequence is a shorter chord for the same solidity which reduces Reynolds number and thus an increase in drag and reduction in lift. Due to the aforementioned tip effects, relying on the tip to generate most lift can lead to bad physical performance. Therefore it was decided to include taper in order to reduce the strength of tip effects.

13.2.6 Coaxial Bi-Rotor Analysis

Due to size and center of gravity range constraints it was not possible to have two separate vertical rotors. It was therefore necessary to use a coaxial bi-rotor for the vertical propulsion system. While the performance of coaxial bi-rotors is harder to estimate with the methods that will be used in this report there exist some clear benefits. While coaxial bi-rotors have a 22% higher induced power their actual power required is 10% lower when compared to an equal solidity single rotor due to swirl recovery [117].

13.2.7 Airfoil Selection

As previously mentioned a high lift coefficient is beneficial to hover efficiency, since the rotational velocity of the rotor can be decreased. When performing the airfoil selection two parameters are key, namely a high lift to drag ratio, and good performance at low Reynolds numbers, in the 10,000 - 100,000 range. Due to structural reasons airfoils with a thickness to chord ratio lower than 8% were not considered, at least not for the root of the rotor. As lower thickness to chord ratios would make it difficult for the rotor to provide sufficient bending stiffness. The same airfoils which were selected for the wing airfoil trade off were considered for the vertical rotor, since many of the same parameters were important. These being a high C_L and a high C_L/C_D , selecting for these parameters presented two clear winners, the E63 and the S1223. But due to the E63 having a thickness to chord ratio of 4.30% it was also eliminated. Thus the S1223 was chosen for the vertical rotor as well as for the forward rotor as these also require a good hover performance.

13.3 Performance Analysis and Sizing

Both the vertical rotor and the forward rotor performance were analysed with help of the Jblade software, so that an optimal configuration could be reached. How this analysis was performed as well as the results of this analysis will be presented in this subsection.

In order to evaluate rotor performance XFOIL polars first had to be generated for the S1223 airfoil. This was performed for a range of Reynolds numbers from 10,000 to 120,000 in increments of 10,000 and with an NCrit value of 5. This NCrit value was chosen as it is believed that a smooth surface can not be ensured due to the abundance of dust suspended in Mars' atmosphere. These polars were then extended to their 360 degree form with Jblade's built in 360 polar extrapolation. The 360 polars were fine tuned by hand in order to ensure a gradual transition between the existing polar and the extrapolated parts, an example of a generated a polar can be seen in Figure 13.3. This polar has much more difference between the positive side and the negative side. This is likely due to the heavy camber of the airfoil, the 360° extrapolation is meant to predict airfoil behavior at positive stall angles. Meaning it may not be as accurate for negative stall angles, this however is not a problem as such angles are not experienced by the blades.

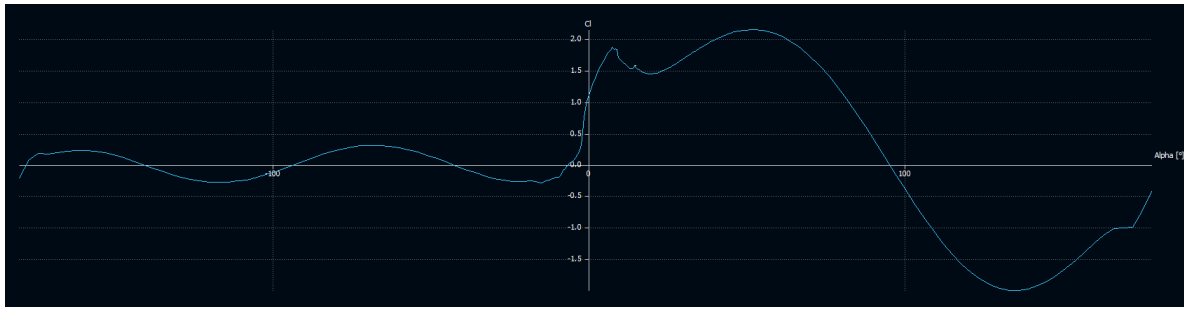


Figure 13.3: 360° polar for C_L evaluated at 70,000 Re for the S1223 airfoil

13.3.1 Tilt Rotor Performance Analysis and Sizing

With these polars blades could be generated. The analysis of the forward propulsion will be discussed first and afterwards the vertical propulsion analysis. First several blades of varying radius were generated but with a constant chord of 0.3 [m]. All analyzed blades used a root cut out of 10% radius. The blades themselves were split up into multiple sections in order to account for the changing Reynolds number across the blade’s radius. A total of 17 segments were used as this was deemed to give a high enough resolution for the Reynolds number. Because of the high thrust required from the forward propulsion system a large radius was required as a small radius was found to be unable to produce enough thrust in VTOL at reasonable efficiencies. This however has some impact on the cruise efficiency, as to produce a low enough thrust the rotor needs to spin slowly and thus reducing the Reynolds number. The effect of radius on the thrust and efficiency can be seen in Figure 13.4. All simulations were run with Martian conditions for the density and kinematic viscosity at 1500 [m], as this corresponds to the surface ceiling. It should also be mentioned that all calculations were performed without 3D corrections, unless stated otherwise. This lack of 3D corrections was caused by instabilities in the program for certain geometries. In order to account for this lack of correction a 10% margin was used for the thrust the rotor is required to produce. The plots ranging from 0 to 30 [m/s] were evaluated at 30° pitch angle, and the plots ranging from 55 to 80 [m/s] were evaluated at 50° pitch angle. These correspond to VTOL and cruise respectively.

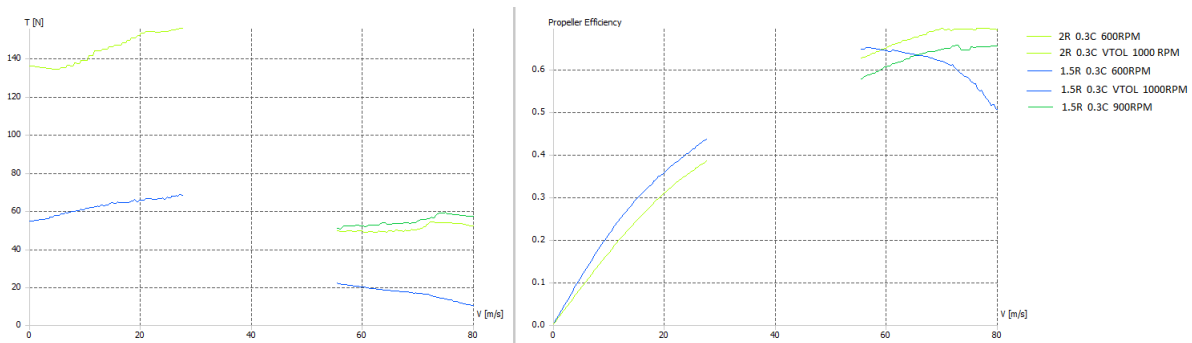


Figure 13.4: Jblade plots showing the effects of radius on efficiency and thrust

As is visible in Figure 13.4 in order for a propeller with a 1.5 meter radius to produce the same amount of thrust as a 2 meter propeller the RPM has to be increased by 50%. From Figure 13.4 it is also evident that a larger radius is capable of producing much more thrust when evaluated at the same RPM. For this reason it was decided that the upper bound of 2 meters for the forward propulsion system would be used. The aforementioned upper bound was set as otherwise the propellers would have to be placed too far span wise and stability during VTOL would become problematic. It was decided to optimize the forward rotors for the cruise phase, since the cruise phase makes up the largest part of the mission. This however does not mean that VTOL efficiency can be neglected, as the VTOL phase is very energy intensive good efficiency is still required. In order to reduce the strength of tip vortices different taper ratios were evaluated. It was decided to taper the final 80% of the blade, as this is usually where a sudden drop in lift can be found [82]. Several blades with linear taper ratios were used to evaluate the effects of taper. The plots for these blades can be found below in Figure 13.5, where the trailing number represents the chord at the tip.

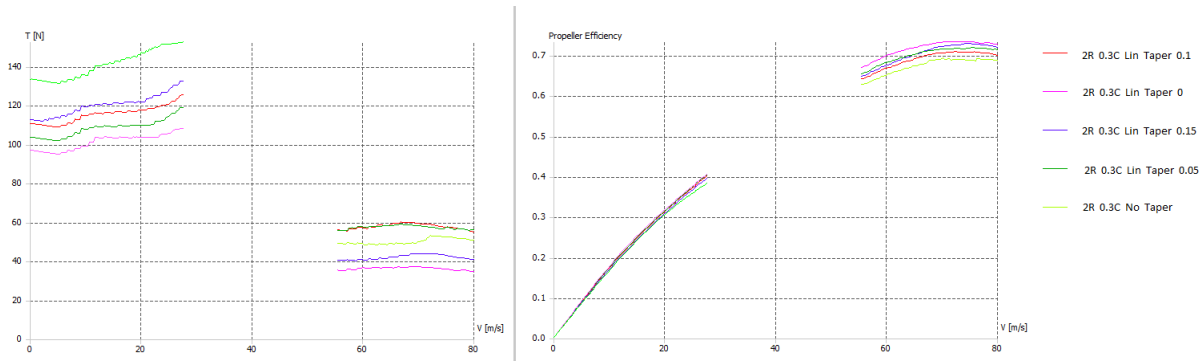


Figure 13.5: Jblade plots showing the effects of linear taper on efficiency and thrust

As can be seen in Figure 13.5 a linear taper with 0.1 [m] chord at the tip provided the most benefits to the cruise thrust and efficiency, whilst only having a moderate impact on the VTOL thrust. While one may argue that not including any taper is better for VTOL thrust and thus better overall, one must consider that the program could not be run with 3D corrections. It is therefore very likely that the performance without taper is overestimated more so than the performance of the tapered blades. In order to improve efficiency, one would like to reduce the profile power. This can be done by reducing the RPM, as it directly scales with RPM. Doing so however will lead to a decrease in Reynolds number, which will lead to a large decrease in lift and a large increase in drag. To counteract this the chord could be increased to increase the Reynolds number. The effects of increasing chord and decreasing RPM can be seen in Figure 13.6

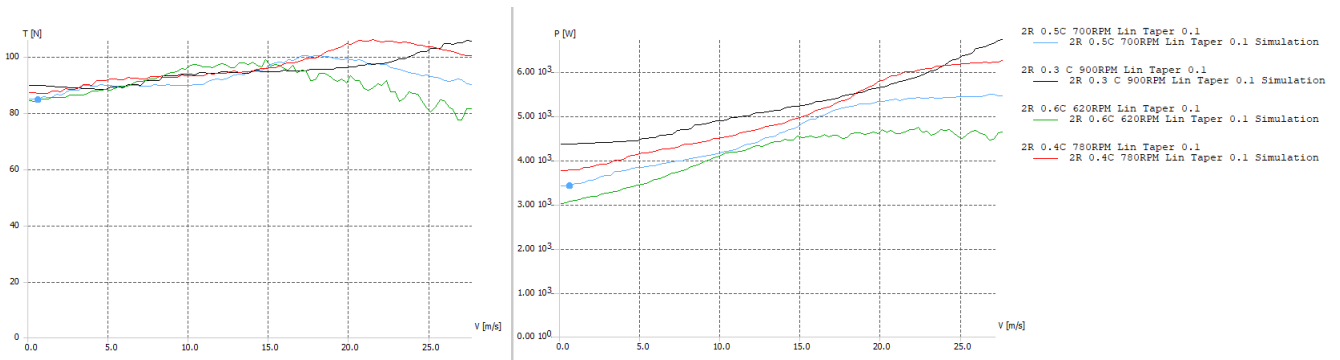


Figure 13.6: Jblade plots showing the effects of chord and RPM on profile power and thrust

From Figure 13.6 it becomes clear that increasing chord and decreasing RPM has a positive effect on the power required to spin the rotor. It should also be mentioned that increasing chord is beneficial to low RPM performance due to the increase in Reynolds number and thus C_L/C_D . In order to increase rotor efficiency even more it was decided that the effects of using a coaxial bi-rotor for the forward propulsion should be analyzed as well. In order to analyze these effects the coaxial rotor was analyzed as two single rotors with a ten percent margin on the thrust a single rotor should produce in order to account for interaction between the rotors [117]. The generated plots for this analysis can be found in Figure 13.7. In this plot the bottom line represents one of the rotors of the coaxial bi-rotor, thus multiplying the power and thrust by a factor 2 will give the total performance.

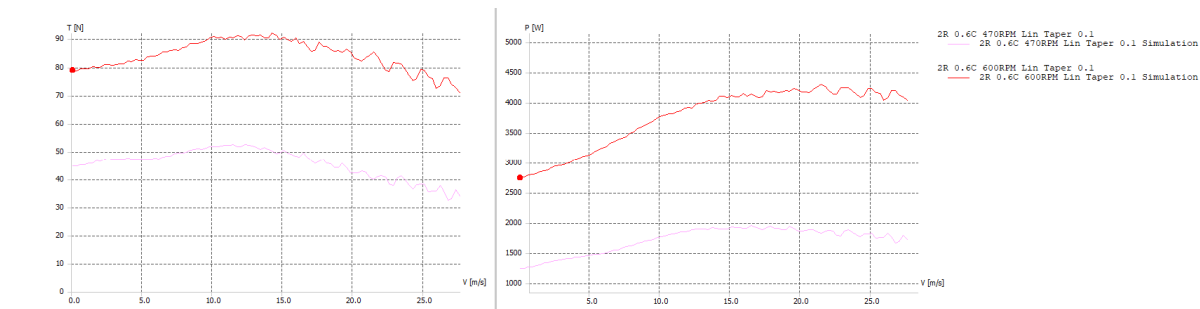


Figure 13.7: Jblade plots showing the effects of single rotor versus coaxial bi-rotor on required power

As can be seen Figure 13.7 turning the forward rotor into a coaxial bi-rotor does not have a huge effect on the required power, only reducing it by approximately 300 [W], since one has to take into account that the figure in the

graph should be doubled. However since the twist distribution will be optimized for cruise, where RPM will have to be low and incoming velocity high the twist will have to be quite aggressive in order to give good performance. Since the RPM can be lowered for a coaxial bi-rotor this means that the optimal cruise twist distribution will more closely match the optimal VTOL twist distribution for the coaxial bi-rotor case. Together with this and the added redundancy a coaxial bi-rotor can provide it was decided that the forward propulsion system would also have coaxial bi-rotors. Now the planform had been finalized the twist distribution could be optimized, the twist was optimized by twisting each section of the blade until it was at its angle of attack for maximum C_L/C_D , which for the S1223 is at around 2-5° angle of attack depending on Reynolds number. It was later found that increasing the chord beyond 0.375 [m] lead to a performance decrease during cruise, due to the fact that the blade had to spin too slowly to produce the required thrust. Thus the maximum chord was reduced to 0.375 [m], keeping the linear taper ratio towards 0.1 [m] tip chord. It was decided to also include a linear taper near the root of the blade, since due to the twist of the blade required during cruise made the inner 35% of the blade contribute more to torque than to thrust. The optimal twist distribution can be approximated by a linear twist starting from 0° at the root to -32° at 96% of the blade, with a linear decrease to -25° at the tip. The chord distribution is characterized by a 0.2 [m] chord at the root, which increases linearly to 0.375 [m]. The chord stays constant until 80% of the blade and then decreases linearly to 0.1 [m] at the tip.

The performance plot for the final blade can be seen in Figure 13.8. Where the point indicates the induced velocity during hover for the forward propulsion, which can be calculated by use of Equation 13.18

$$v_i = \sqrt{\frac{T}{2R^2\pi\rho}} \tag{13.18}$$

The analysis yielded a final reported cruise efficiency of 74%, and a hover efficiency of 32%. It should also be mentioned that during cruise only one rotor has to spin, due to the fact that splitting the thrust over the two rotors would mean the blades spin at an even lower RPM, which leads to worse efficiencies. In order to do this one rotor on each side will be put into vane position. The drag the blades produce in their vaned position is thought to be negligible.

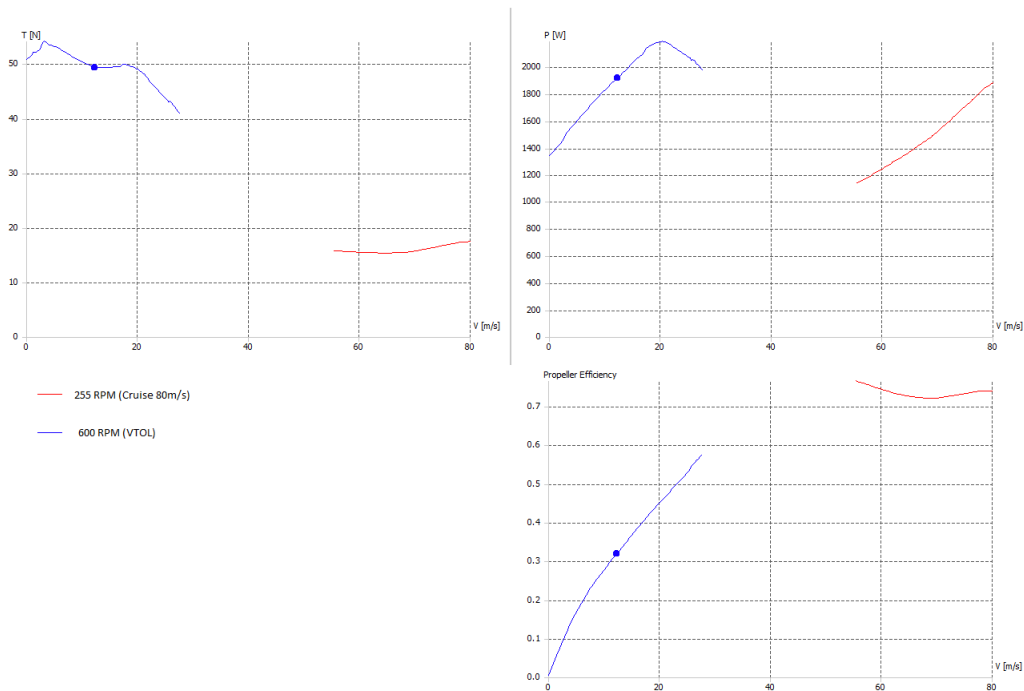


Figure 13.8: Jblade plots showing thrust power required and efficiency of a single forward rotor evaluated at 49°, and 91° root pitch for VTOL and cruise respectively

As can be seen in Figure 13.8 the thrust does not meet the required 20% imposed earlier due to rotor interaction losses and the lack of 3D correction. However this 10% margin is not required anymore for the tilt rotors as they do not seem to have a large effect on the thrust values in hover and in cruise, as can be seen in Figure 13.9. There only seems to be a large effect at velocities lower than 10, which are velocities that are not present during any stage of the flight. At higher velocities the effect of the 3D corrections is barely noticeable, meaning the tilt rotors and thus the forward propulsion system has been correctly sized.

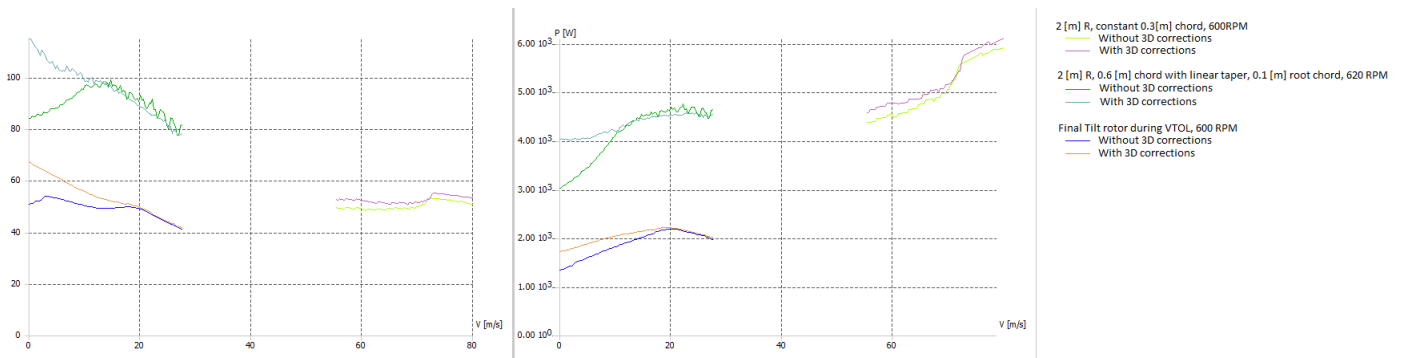


Figure 13.9: Jblade plots showing the effects of 3D corrections on the reported thrust and power values

13.3.2 Vertical Rotor Performance Analysis and Sizing

The performance analysis of the vertical rotors follows many of the same principles as the performance analysis of the VTOL phase for the tilt rotors. Thus many of the same optimization techniques can be applied. Due to the vertical rotors also being coaxial bi-rotors the same 10% will also be taken for the required thrust. The only difference of the optimization scheme for the vertical rotors will be a different twist and larger chord, as the vertical rotor does not suffer from the penalty to cruise efficiency. Since the vertical rotor is not as constrained as the tilt rotors in its diameter the blade radius was increased to 2.9 [m]. As a larger diameter gives better efficiency, due to the lower require RPM. The chord was increased beyond 0.375[m] in order to increase the Reynolds number while still allowing the rotor to operate at low RPM. First the effects of increasing chord were analyzed. The same taper ratios as those for the tilt rotors were initially used, as these yielded good results for larger chord and higher thrust as well. A plot which shows the effect of increasing chord on the hover efficiency can be seen in Figure 13.10. All rotors included no twist and were evaluated at the same pitch angle of 49°. The numbers in the legend indicate the chord at the root, which coupled with the taper ratios yield the chord at all different positions of the blade. These simulations were run without 3D effects, as doing so would crash the software due to diverging values for the thrust.

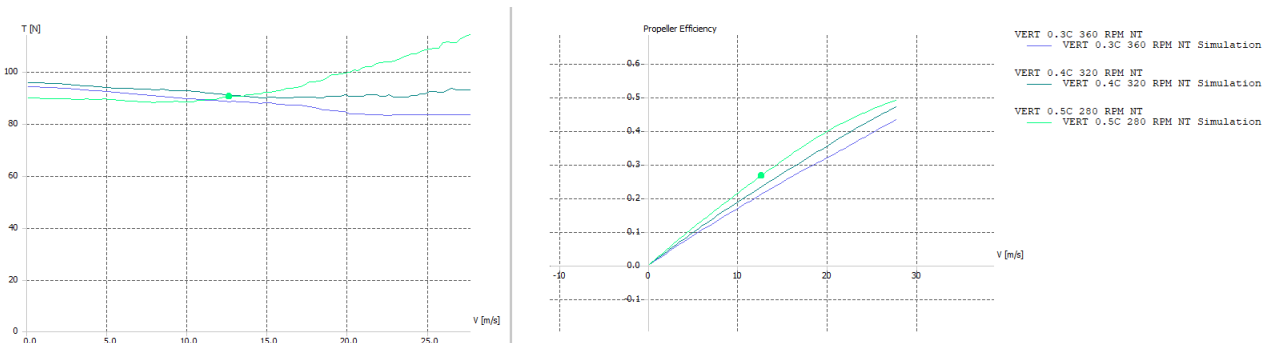


Figure 13.10: Jblade plots showing the effects of increasing chord on thrust and efficiency

From Figure 13.10, it becomes clear that increasing the chord and lowering the RPM will indefinitely lead to better hover performance. However doing so will lead to terrible forward flight and climbing performance, as indicated by the light green line in Figure 13.10, which quickly bottoms out at comparatively low speeds. Therefore the optimal root chord was decided to be 0.4[m] which yields a maximum chord of 0.75[m] and a tip chord of 0.2[m]. Increasing or decreasing taper were found to have a negligible effect due to the low RPM the rotor is already operating at. Thus the only factor left to optimize is the twist distribution. This was again performed by means of a highly iterative process to achieve the desired thrust and highest efficiency. The obtained twist distribution together with the chord distribution can be found in Figure 13.11, the vertical rotor performance can be found in Figure 13.12

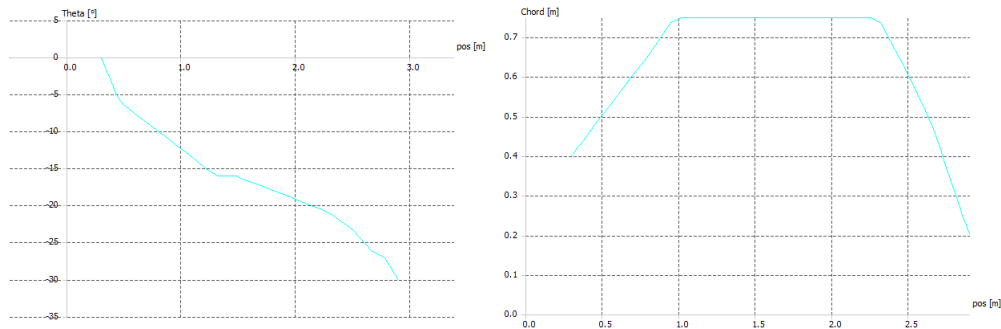


Figure 13.11: Twist and chord distributions of the vertical rotor blades

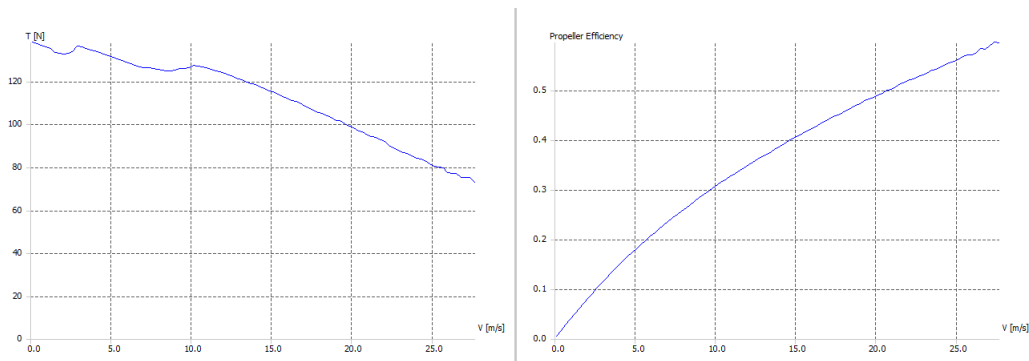


Figure 13.12: Jblade plot displaying vertical rotor thrust and efficiency evaluated at 330 RPM, and 51° pitch with 3D corrections applied

This blade planform yielded a thrust of 122[N], with a 10% margin to account for coaxial bi-rotor losses, at 330 RPM with a hover efficiency of 36%, this value for efficiency seems to be very low when comparing it with typical rotor efficiency. This can partly be attributed to the unfavorable conditions found on Mars, as low Reynolds number and low density reduce rotor performance drastically. An existing rotor design for a Mars helicopter for which the hover efficiency can be calculated was analyzed in Jblade [36]. This analysis was performed at 37° pitch angle, at 644 RPM, and with the described blade properties laid out in the MARV paper [36]. The results of this analysis can be seen in Figure 13.13, the power output of the MARV rotor was obtained by simply multiplying the induced velocity of the MARV rotor with the thrust require for hover. Dividing the output power by the required hover power for one rotor an efficiency of 53.8% is obtained.

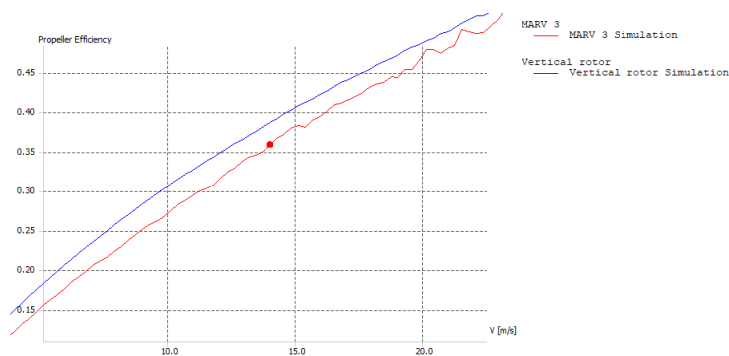


Figure 13.13: Jblade simulation of the designed vertical rotor and MARV rotor.

From Figure 13.13 it can be observed that the efficiency obtained by Jblade is 33% lower than the calculated efficiency. Meaning that a factor has to be applied to the efficiency to arrive at the correct result. A factor of 1.49 is applied to both efficiencies, yielding an efficiency of 53.8% for both the MARV and the vertical rotor. This correction is also applied to the hover efficiency of the tilt rotors, as Jblade reported similar values for these as well. The final values for the rotor thrust, efficiency and required power can be found in Table 13.2. Due to some changes in the design the required VTOL thrust required by the forward rotors went up by approximately 15 [N]. In order to accommodate for this the blade pitch was increased to 30°, this reduced the hover efficiency by approximately 0.2%.

Table 13.2: Rotor properties

Rotor	Thrust [N]	Efficiency [%]	Required power [W]
Tilt rotor cruise	17.5	74.0	1880
Tilt rotor hover	55.2	50.6	1406
Vertical rotor hover	122	53.8	2926
Total hover power	-	-	11474
Total cruise power	-	-	3760

From the values in Table 13.2 it can be concluded that all the requirements for the rotors regarding thrust output have been met. With regards to requirement **SYS-PROP-04**, the maximum operating tip speeds of the tilt rotors and the vertical rotors are 126 and 100 [m/s] respectively. These tip speeds are well below 192 [m/s], which corresponds to 0.8 Mach. It has also been ensured that one rotor inoperative does not lead to direct mission failure, as the drone can still cruise with one tilt rotor inoperative.

13.4 Layout

Having sized the propellers, motors and gearboxes can be selected for the front and rear propulsion systems. This section will describe the selection process of the type and model of motor, as well as the transmission system.

13.4.1 Motor Selection

Due to the electrical architecture of the UAV (the electrical power being supplied by a battery) DC electrical motors will be used for propulsion. There are two types of DC motor: brushed and brushless. Brushless DC motors have numerous advantages over brushed motors, including more precise speed control, better efficiency, longer life-time and lower temperatures [107]. Hence it has been decided to use brushless DC motors for propulsion. During VTOL, each forward propeller requires 1406 [W] of power and each rear propeller requires 2926 [W] of power. During cruise, one forward propeller on each side requires 1880 [W]. Hence, VTOL is the most power-intensive phase for both the front and rear motors. From this it follows that the front motors need to be able to supply 2812 [W] to the two front propellers on each side, plus a margin to take into account transmission efficiency. Assuming a transmission efficiency of 95%, the front motors need to be able to supply 2960 [W]. Assuming the same transmission efficiency for the rear rotor gives a power requirement of 6160 [W] for the rear motor. A lightweight brushless DC motor has been selected to fulfil this requirement, namely the Aveox UT-8023-32P/11. This electric motor weighs 2.09 [kg], has an outer diameter of 12 [cm] and is able to supply 7068 [kW] at 95% efficiency [18].

13.4.2 Transmission Selection

The UT-8023-32P/11 operates at optimum efficiency at a torque of 34.27 [Nm], and an RPM anywhere from 1500 to 3000 at this torque [18]. Since the torque required for the rear rotor in VTOL is 169.34 [Nm], a gear ratio of 5 is needed. The motor can then run at 1650 RPM to transfer the required 330 RPM to the rear rotors. The front rotors require a torque of 44.75 [Nm] at 600 RPM for VTOL, meaning a gear ratio of 2 can be used to convert a torque and RPM of 22.38 [Nm] and 1200 from the motor to the required values for the rotor. Although this operation point is removed a bit from the optimal condition for the motor, the loss in efficiency is negligible [18]. These reductions will be performed by planetary gearboxes. For all motors, after this gearbox, another gearbox will be needed to accommodate the use of two coaxial birotors. The three transmission systems (one for the rear, two for the front) will weigh approximately 1 [kg] each from comparison with similar systems [107] and it is conservatively assumed that the gearbox efficiency is 95%.

13.5 Risk Analysis

The functioning of the propulsion systems is of paramount importance to the functioning of the drone and thus the successful completion of the mission. During the design of the propulsion system a few risks were identified with regards to the propulsion system. These risks, including their probability, severity and mitigation method are presented below.

- **PR-1/Propulsion risk - One of the tilt rotors fails**
 - **Effect:** Would severely reduce the range if occurring during flight, would make VTOL take off impossible.
 - **Probability:** Due to the electrical nature of the propulsion system it does not contain many moving parts that are exposed to the martian elements **Occasional**.
 - **Severity: Catastrophic**, Could render the drone stuck at a remote location.
 - **Mitigation:** The tilt rotors were designed as a coaxial bi-rotor, making the design fully redundant during cruise. The parts of the propulsion system that are exposed to the elements should be inspected before every flight.
 - **Effect of Mitigation:** Due to changes in the design the severity this event decreased to **Critical**. Due to the pre-flight checks the probability was lowered to **Rare**.
- **PR-2/Propulsion risk - One of the vertical rotors fails during flight**
 - **Effect:** This would in the case of VTOL lead to a crash, or render the drone unable to take off if landed.

- **Probability:** Due to the electrical nature of the propulsion system it does not contain many moving parts that are exposed to the martian elements **Occasional**.
- **Severity: Catastrophic** Could lead to loss of the drone.
- **Mitigation:** As with risk PR-1, the vertical rotors will be inspected before every flight. In order to ensure that the drone can safely make an emergency landing requirement **SYS-PROP-06** was formulated.
- **Effect of Mitigation:** Due to the pre-flight checks the probability is lowered to **Rare**, due to requirement **SYS-PROP-06** the severity is reduced to **Critical**.
- **PR-3/Propulsion risk - One of the electrical components fails**
 - **Effect:** Can lead to total loss of thrust.
 - **Probability:** Since many of the components will be assembled on earth with the wiring in place this event is classified as **Rare**.
 - **Severity: Catastrophic**, since such an event could lead to partial or total loss of thrust. Leading to a crash when occurring during flight.
 - **Mitigation:** Extra wiring should be included for the electric motors in order to make the wiring fully redundant. Backup electric motors should be transported with the drone so these can be replaced when necessary.
 - **Effect of Mitigation:** The mitigation procedure only has an effect on the probability lowering it to **Improbable**.
- **PR-4/Propulsion risk - Tilting mechanism or gearbox fails**
 - **Effect:** Could render VTOL or general operation of the rotors impossible.
 - **Probability:** Since the systems do not contain many moving parts and are well protected from the environment in the case of the gearbox this event is characterized as **Rare**.
 - **Severity: Catastrophic**, since such this event could render the drone unable to land or take off. When occurring during flight it could even lead to a crash.
 - **Mitigation:** The tilting mechanism should be inspected before each flight and tests should be performed to check if the tilting mechanism works. The gearbox should be lubricated often and any dust should be removed every so often. Spare parts should also be transported with the drone.
 - **Effect of Mitigation:** The mitigation procedure only has an effect on the probability lowering it to **Improbable**.

13.6 Verification and Validation

In order to verify if the obtained thrust and power values were sufficient, the sizing code was run with the newly obtained values from Jblade. From this sizing new thrust and power requirements followed, which were then sized for. This process continued until the two converged in order to ensure that the rotor sizing was still sufficient. Any changes that were made to the design as a whole were also communicated so that these could be taken into account for the propulsion system sizing.

13.6.1 Validation

To validate the aerodynamic performance which were simulated by the models (and used for the sizing and power estimates of the propulsion subsystem) experimental or CFD data should be used. This is done to ensure that the required thrust will be able to be achieved during operations.

Vacuum chamber tests can be performed to validate the vertical propeller performance as that propeller should be tested without incoming flow. This test can also be used to validate the thermal performance of the electric motor to ensure it will not overheat during take off.

To validate the performance of the forward rotors in flight a wind tunnel test must be performed as an incoming flow must be used to simulate the drone velocity in flight. It should be noted that simulating the martian atmosphere in a wind tunnel on Earth is not a simple matter. A wind tunnel is not able to perfectly simulate the low density which will be experienced on Mars. The solution is to perform tests at a range of velocities and with multiple smaller scale models of the propeller blades in order to get data for the expected Reynolds number range. This data can be accompanied with CFD simulations in order to validate the final propulsive performance.

14 Power Analysis

The power subsystem provides the necessary electrical power for propulsion, command and data handling, communication and thermal subsystems, scientific instruments, soil collection mechanisms, and landing gear. It ensures the correct voltages enter the modules as needed. The requirements and constraints influencing the design are presented in Section 14.1. The models used and the resulting analyses are detailed in Section 14.2. The final layout showing the electrical block diagram is presented in Section 14.4. The risk analysis of the subsystem is discussed in Section 14.3 at the verification and validation of strategies are presented in Section 14.5. The values in this chapter are highly dependent on the final sizing iteration which could not be accessed in due time and will therefore change for the final version of this draft.

14.1 Requirements and Constraints

The goal is to size the battery module for the UAV to able to support a complete mission profile with an additional 15% margin on the energy required for battery reserve capacity in emergency situations. The batteries can be charged in two manners. The first is by making use of energy from the base. The second is through means of solar panels placed on the wings. This procedure takes place prior to the beginning of the mission. The solar panels can also be used during the mission itself to charge the battery during flight to perform an extended mission profile. The option of recharging at the base is selected such that it reduces the operational downtime of the UAV by allowing it to charge overnight as opposed to charging through the solar panels that can only be done during the day. The energy requirements necessary to support the most critical mission profile have been derived from the power used by the drone at all times throughout the mission. Therefore, satisfying the power requirements **SYS-POW-01** and **SYS-POW-02**. Several safety factors are added to this energy requirement, as further detailed in Section 14.2.1. The sizing of the solar panels is thus performed to reduce the strain on the power requirements that need to be provided by the base.

Table 14.1: Requirements related to the power subsystem and their expected compliance

Index: DME-REQ-	Requirement	Compliance
SYS-POW-01	(Driving) The power subsystem shall provide 3.760 [kW] nominally over the mission duration.	Satisfied
SYS-POW-02	The power subsystem shall be able to provide 11.474 [kW] peak power.	Satisfied
SYS-POW-03	The power subsystem shall provide energy storage with a capacity of 5687 [Wh].	Satisfied
SYS-POW-05	(Key) The power subsystem shall be single point failure free.	Satisfied
SYS-GEN-03	The design shall provide the capability of being recharged.	Satisfied

Analyzing the two different mission profiles results in the soil collection expedition profile being more critical in terms of peak power usage with 300 [s] necessary in contrast to 150 [s] for the remote sensing expedition profile. Thus the critical peak power energy requirement is 0.956 [kWh]. Analyzing the two different mission profiles results in the remote sensing expedition profile being more critical in terms of nominal power usage with 4350 [s] necessary in contrast to only 1250 [s] for the soil collection expedition. Thus the critical nominal power energy requirement is 4.543 [kWh].

14.2 Model and Analysis

The section is comprised of five parts. First, the power generation means are discussed in Section 14.2.1. Secondly, the approach for storing energy is presented in Section 14.2.2. Thirdly, the placement of the battery and solar panels is shown in Section 14.2.3. Lastly, the power management and distribution methods are detailed in Section 14.2.4 and an overview of the subsystem is offered in Section 14.2.5.

14.2.1 Power Generation

Solar Cell Selection

Solar cell efficiency has seen significant improvements in the last 20 years and is envisioned to increase even more in the years leading up to 2035. Solar cells are less effective on Mars' surface than they are on Earth, due to the greater distance from the Sun: the solar intensity is 590 [W/m²] [17], less than half of the value on Earth. Atmospheric dust, storms, and clouds further reduce this intensity and thus the performance of the solar panels on the surface of Mars. Low temperatures in the range of -100 [°C] to 0 [°C], wind, and electrostatic charging also affect material properties and solar cell performance of photovoltaic arrays [73]. For all these reasons, it is important to select cells that are space certified. The current practice for space application is to use multijunction solar cells, which are composed of layers that produce an electrical response at different wavelengths. This practice allows for the absorbance of a broader range of wavelengths and improving the efficiency of converting solar irradiance into electrical power.

Two manufacturers offer state-of-practice solar cells for space applications with an efficiency of around 32% respectively: Azur Space and Spectrolab. The cells from both manufacturers have the highest technology readiness

level possible of 9 according to NASA standards [105] meaning that the product has been flight tested. Therefore, two other criteria are important for selecting the best design, respectively: low mass as the design has to fly and high power density. The technical requirements used for comparison are summarized in Table 14.2. Although a higher voltage is desirable, the increase in mass will be considerable by 30% for the same design configuration. Therefore, XTE-LILT cells are selected for this power system.

Table 14.2:

Technical specifications of the most efficient solar cells for space photovoltaic applications currently available on the market [21] [134]

Manufacturer	Spectrolab	Azur Space
Type	XTE-LILT [135]	QJ 4G32C [20]
Composition	GaInP/GaAs/Ge	AlInGaP/AlInGaAs/InGaAs/Ge
Efficiency BOL	31.6%	31.8%
Minimum Cell thickness [μm]	80	110
Minimum Cell mass [mg/cm^2]	50	58
Voltage at max power [V]	2.459	3.025
Current at max power [A]	0.4887	0.4335

Availability of Solar Power on Mars

For sizing the amount of power generated through solar panels at a certain Mars location, it will be assumed that the solar irradiance that reaches the surface of Mars is available to the UAV both during flight and when the vehicle is stationary on the ground. This assumption does not influence the design greatly as the vehicle flies at relatively low altitude of 200[m].

Nasa has devised a procedure to approximate the solar variations of the solar flux [51]. The first aspect of interest is the solar radiation variation with respect to a standard location. Therefore it is interesting to analyse how the solar radiation varies for a certain latitude based on the aerocentric longitude. The aerocentric longitude represents the angle associated with the position of Mars in orbit around Mars, and it has been graphically represented in Figure 14.1. Every 30° of aerocentric longitude correspond to a new month on Mars. Another parameter that can influence the solar radiation variation is the optical depth which has values between 0 and 1. 0, meaning that the atmospheric haze is low and more solar radiation reaches the surface and one, meaning the atmospheric haze is maximum and barely any solar radiation reaches the surface through the atmosphere. For reference, the optical depth during a global dust storm is $\tau = 0.5$. Therefore in the figures plotted and the subsequent analysis a conservative value of $\tau = 0.35$ was selected. An example of how such a variation can be plotted for interpretation is shown in Figure 14.2. The second aspect of interest is to look into the hourly solar variation. In this manner, it can be determined what the most suitable operation or charging timeframe is based on the time of the year. An example of such a plot is shown in Figure 14.3.

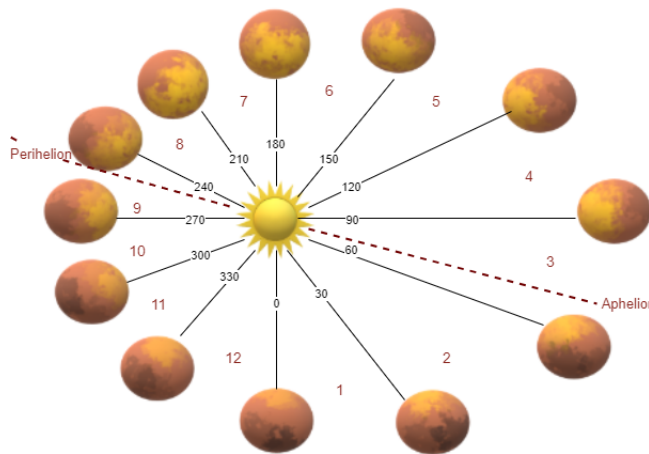


Figure 14.1: Visual representation of Mars proximity to the Sun at different aerocentric longitudes

The direct beam irradiance, G_b , on the Martian surface normal to the solar arrays is related to the global direct beam irradiance at the top of Mars atmosphere $G_{ob} = 590[\text{W}/\text{m}^2\text{K}]$, the optical depth τ and the zenith angle z through Equation 14.1. The cosine of the zenith angle can be computed with equation Equation 14.2 where ϕ is the latitude, ω is the hour angle measured from the true noon westward and δ is the declination angle computed with Equation 14.3. The declination angle varies with the aerocentric longitude L_s and is dependent on the obliquity of Mars rotation axis $\delta_0 = 24.936^\circ$ [51].

$$G_b = G_{ob} \exp\left(\frac{-\tau}{\cos(z)}\right) \quad (14.1)$$

$$\cos z = \sin \phi \sin \delta + \cos \phi \cos \delta \cos \omega \quad (14.2)$$

$$\sin \delta = \sin \delta_0 \sin L_s \quad (14.3)$$

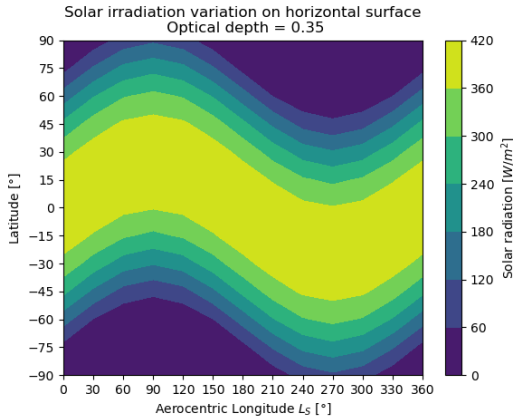


Figure 14.2: Variation of solar irradiance on horizontal surface of Mars (optical depth = 0.35)

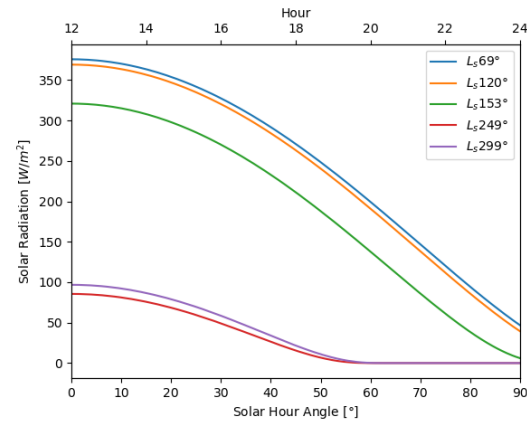


Figure 14.3: Hourly solar irradiance variance on the surface of Mars at 45° latitude for various aerocentric longitude (optical depth = 0.35)

Solar Array Configuration

Once the available resources for solar power generation have been analyzed, the design of the photovoltaic system can move on. The next step is to define the module configuration. Modules are a series configuration of cells that group to achieve the required voltage and powers compatible with the batteries [167]. The battery voltage needs to be around 24–25V to support the required voltages encountered in the system. Therefore, a slightly higher voltage has to be provided by the solar panels. Thus the solar cell modules are comprised of 12 XTE-LILT cells connected in series. The maximum power current of the module is equal to the maximum power current of one cell, as mentioned in Table 14.2. The maximum power voltage of the module is equal to the voltage is the product of the maximum power voltage of one cell times the total number of cells in series, 29.5V. The correct voltage that needs to enter the battery is achieved through a regulator, as further detailed in Section 14.2.4 on power management and distribution.

The second step is to determine the total load current and operational time. The total load current is derived by dividing the total energy requirement by the operational time of the solar panels. Thus the number of equivalent suns hours further detailed under step 4. The energy requirements are derived from the mission profile in [Wh] by accounting for the operation of all components required to sustain flight and perform the scientific mission. Now, an analysis has to be performed to investigate the current required by the system. All the components can be powered with direct current, DC. Therefore the power rating contributions are summed and divided by the nominal operational voltage to get the average operational time [Ah].

The third step is to account for system losses. Charge regulators and batteries use up energy to perform their functions. The energy required for the functioning of the PV system can be considered energy loss. Generally, a 20% margin can compensate for the losses [167] and is added to the energy requirement from step 2 to further be used for sizing.

The fourth step is to determine the solar irradiation in daily equivalent sun hours EHS. Local weather patterns and seasonal changes influence the power delivered by the PV module. These have been analyzed in Section 14.2.1. By analyzing the plots for hourly solar variation, such as the one displayed in Figure 14.3, it has been determined the solar radiation stays within a 20% margin of the peak value for roughly 12 hours a day in the timeframe 6:00–18:00. To add a safety margin, the EHS was found to be 8 hours. Thus, the ideal operation timeframe of the solar panels becomes 8:00–16:00.

The fifth step is to determine the entire solar array current requirements, including the additional safety margins added in the previous two steps. The solar array current is determined by dividing the total energy requirements, including losses, from step 3, by the equivalent sun hours on Mars selected in step 4.

The sixth and last step is to determine the optimum module arrangement. This stage aims to select the minimum number of modules to provide the previously computed solar array current. To determine the number of modules in parallel, the current required by the solar array is divided by the current generated by the module at peak power. The number of modules in series is determined by dividing the nominal PV system voltage with the nominal module voltage as computed in step 1. The total number of modules is the product of the number of modules required in parallel and the number needed in series.

Applying the sizing considerations for the PV system described in this section results in the following solar array configuration summarized in Table 14.3. The same approach has been used for sizing the beacons used for communication in Chapter 9 with the mention that given the low power requirement of only 2[W] per beacon and the low operational voltage of 3.3 [V], an additional module configuration is not necessary. Thus, the solar array for the beacon can be arranged with a 2 cells connected in series.

Table 14.3: Overview of the solar array configuration and sizing

	Energy [Wh]	Capacity [Ah]	Area [m ²]	Number modules	Number cells	Mass [kg]
UAV	4324.11	146.58	1.26	39	468	0.63
Beacon	4.785	1.45	0.0054	N/A	2	0.0027

14.2.2 Power Storage

Battery Requirements Sizing

To determine the battery size, the necessary reserve of 15% is added. The capacity of the batteries is computed by multiplying the total DC energy requirement for the mission profile used for sizing by the recommended reserve time in days. For extended battery life, it is recommended to only use 80% capacity of the battery; therefore, the minimum capacity of the battery is obtained by dividing the direct energy requirements by the operational battery capacity of 0.8.

Battery Cell Selection

Li-ion batteries make use of a polymer based electrolyte and have the advantage of being rechargeable. The company Saft produces batteries which are specially designed for the space market. As of 2021, an attractive product is available from Saft with an energy density up to 180 [Wh/kg] and a power range up to 1 [kW/kg]. Moreover, it is believed the current interest in lithium ion batteries for the automotive industry will drive further increases in performance over the coming years. Electrically powered vehicles are currently making use of lithium ion batteries with a specific energy density of 260 [Wh/kg]. Forecasts for this technology show that by 2025, a specific energy of around 580 [Wh/kg] can be achieved [39].

Due to all these recent advancements, the current space certified specific power density is deemed to be on the rather low side and will be outdated technology by the time the mission is performed. Saft batteries have been involved in powering previous space missions, and a timeline of the mission and the specific powers they used at this time was contoured. In 2003 batteries with a specific power higher than 100 W/kg and 250W/l have been used on the Mars Exploration Rovers, Spirit and Opportunity [11]. On the Phile Lander in 2014, batteries with a specific energy of 242Wh/kg have been used [128]. Therefore, it was considered acceptable to use technology with slightly higher performance than what is already available on the market with a battery energy density of 280Wh/kg. This decision was made as the overall design is highly sensitive to the mass of the batteries, and although higher-end technology is not currently available, the rate of development of the past show that this conservatory value which is slightly below the trend line, can be achieved in due time for performing this mission.

The battery cell used as a reference and deemed to be modified for the purpose of this mission is a VL51ES Li-Ion battery from Saft due to its high capacity storage per cell of 51[Ah]. An overview of its technical specification used for sizing is given in Table 14.4

Table 14.4: Technical specifications of the battery cell Saft VL51ES

Parameter	Unit	Value
Energy density	[Wh/kg]	280
Energy density	[Wh/L]	385
Cell Capacity	[Ah]	51
Cell Nominal Voltage	[V]	3.6

Battery Configuration

The battery configuration will be composed of cells coupled in series and parallel. Series configurations are necessary to achieve the operating voltage of the battery which is higher than that of the individual cell and parallel configurations add up to reach the total battery capacity [Ah]. Including all the safety margins due to losses, the battery is capable of storing 5.191[kWh] energy thus complying with **SYS-POW-03**. An overview of the sizing considerations of the battery is shown in Table 14.5

Table 14.5: Overview of the configuration and sizing of the battery

	Stored Energy [Wh]	Capacity [Ah]	Cells [-]	Parallel [-]	Series [-]	Mass [kg]	Volume [L]
UAV	5687	237	35	5	7	20.31	14.77
Beacon	6.49	1.96	1	1	1	0.023	0.0168

14.2.3 Battery and Solar Panel Placement

Due to their large combined mass, the placement of the batteries and the solar panels played a significant role in ensuring the longitudinal stability of the overall design. Therefore, they have been kept as a variable during design iteration. For the final design, the solar panels are divided into two arrays placed on either side of the wing, as shown in Figure 14.5. Due to the symmetry of the design, only one side is displayed. Similarly, the battery is split into two arrays at the extremities of the wing situated below the solar panels. The split is made such that on each side of the wing, there are 2 series modules and 4 other cells as part of the last series module. Given that the series module is composed of 7 series in parallel, an additional cell is placed on one side of the wing to provide symmetry along the longitudinal axis. The battery is positioned inside the wing box between the front, and rear spar, as shown in Figure 14.4, and the exact dimensions of the battery pack on each side are 222x972x54 [mm] (chord direction, span direction, wingbox height) such that the battery cell configuration fit at that specific cross-section in the wing. Thus, the spanwise length of the battery array on each side of the wing is 0.972 [m].

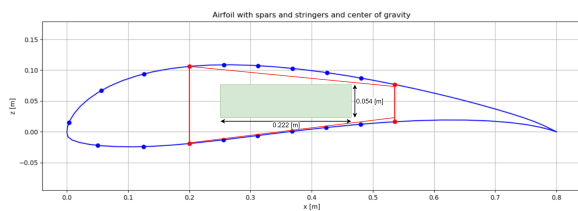


Figure 14.4: Cross sectional view of the battery placement, green rectangular box, inside the wingbox

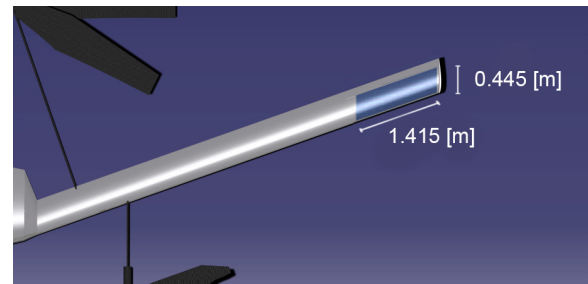


Figure 14.5: Placement of the solar panels on the surface of the wing. Inside the wing at the same location there is the placement of the battery with a similar rectangular shape of 0.222×0.972 [m]

14.2.4 Power Management and Distribution

The power management strategy comprises three main components, according to Brown et al. [30] First, the source control, regulating the power that comes from the solar arrays. Secondly, the storage control for which a battery charger regulator is necessary. And lastly, the output control that consists in the case of this design of DC-DC converters ensure the correct loads reach the different components.

Source Control

The mission is mainly designed that the solar panels charge the batteries and do not necessarily provide direct energy to the components. The latter only being true in the case of mission extensions. For the cases when the energy is directly being transferred to the components, no additional control is required. However, this design does not have direct energy transfer. Therefore, a peak power tracker PPT is necessary to operate in series with the solar array. The PPT extracts the load required for charging the batteries up to the peak power of the arrays and converts the output voltage to the operational battery voltage. The PPT is a small DC-DC converter that can be purchased from Texas Instruments for example model LM76005-Q1 [141]. The converter has small dimensions $4 \times 6 \times 1.8$ [mm]. Assuming the converter is made out of aluminium with a density of 2.7 [g/cm^3]. The mass of the PPT is 0.129 [g].

Storage Control

The battery charger regulator is a small component that the battery manufacturer can provide and has a marginal contribution to both mass and costs.

Output Control

The electrical profile load is of importance when it comes to selecting the output control method. The components have different operational voltages, and the power management approach needs to ensure that powerlines with the correct voltages and currents reach the individual components. An overview of all the different voltages and the corresponding regulators is shown in Table 14.6. The regulators will be organized in a centralized manner placing all the regulators together in the form of a power control unit. Three different regulators models are used all provided by Texas Instruments: Regulator 1 manufacturer model TPSM63603 [145], Regulator 2 manufacturer model TLVM13630 [143] and Regulator 3 manufacturer model TPS57140-Q1 [144]. The regulator blocks have relatively small dimensions of $4 \times 6 \times 1.8$ [mm], resulting in a 43.2 [mm^3] volume. Assuming the blocks are made out of aluminium with a density of 2.7 [g/cm^3]. The mass of one regulator is 0.116 [g]. For 27 regulators composing the power control unit, the total mass is 3.15 [g]. Relatively insignificant value compared to the rest of the components.

Table 14.6: Overview of the main power consumers and their associated voltage regulators

Component	No.	Voltage [V]	Reference	Type	Voltage [V]
Motor	3	40	Chapter 13	N/A	N/A
Electronic Speed Controller	3	12	Chapter 13	R1	1-16
On-board computer	2	15	Chapter 8	R1	1-16
Navigation Camera	9	5	Chapter 8	R2	1-6
IMU	1	3.3	Chapter 8	R2	1-6
Laser Altimeter	1	3.3	Chapter 8	R2	1-6
Li-ion Batteries	2	25	Chapter 14	R3	0.8-39
Communication Board	1	12	Chapter 9	R1	1-16
Robotic drill arm	1	12	Chapter 7	R1	1-16
Observation Camera	1	5	Chapter 7	R2	1-6
Gas Analyser	1	12	Chapter 7	R1	1-16
Ground Penetrating Radar	1	12	Chapter 7	R1	1-16
Magnetic Disks	1	5	Chapter 7	R2	1-6

Primary Power Distribution

The power distribution consists of cabling, fault protection and switching gear. This power system component is challenging to estimate in the incipient design stages, and its accurate mass estimation is generally determined when the prototype is being produced. Cabling can account for 10% to 25% of the electrical power system mass [161] and therefore a 15% margin has been selected for this purpose.

14.2.5 Power Subsystem Overview

A summary of all the masses comprising the power subsystem is shown in Table 14.7. The operational time of the drone without solar panels is obtained by dividing the stored energy in the battery at 80% battery capacity usage by the nominal power usage of 3.76 [kW], thus leading to an operational time of 1 hour 30 minutes. With a mission length of 1 hour 15 minutes, the battery provides 15 minutes of additional operational time.

Under normal circumstances, the drone will use the solar panels to charge for 8 hours per sol, receiving an average of 300 [W/m²] of solar flux. With the solar panel area of 1.26 [m²] at the given efficiency of 31.6%, the solar panels will be able to gather a total of 3.44 [MJ] in one sol. This is 16.8% of the full battery capacity. In the worst case scenario, the drone will need to charge the rest of the way up to 80% using base power. With a charging time of 16.6 hours (the remaining time in one sol), this would require a power draw of 216 [W] from the base. The two options for recharging the drone ensure compliance with requirement **SYS-GEN-03**.

Table 14.7: Overview of the total mass of the power subsystem

Power subsystem component	Mass [kg]	
	UAV	Beacon
Solar Array	0.63	0.0162
Battery	20.31	0.023
Power Conditioning	0.003	0.0001
Cabling	3.14	0.004
Total	24.08	0.043

14.3 Risk Analysis

- **PWR-1/Power Subsystem Risk - Li-ion Battery Explosion**
 - **Effect:** Li-ion batteries are inherently hazardous as they are made out of highly flammable solvents that pose a fire hazard.
 - **Probability:** Li-ion batteries have very low failure rates and therefore the probability is set to **Rare**
 - **Severity:** Explosion of a single cell may lead to a **Marginal** effect, however, if the explosion propagates to the rest of the module or the whole battery, the effect can become **Catastrophic**.
 - **Mitigation:** Thermal barriers must be set between the different battery modules to reduce the chance of propagation to the rest of the system
 - **Effect of Mitigation:** The mitigation strategy sets the probability to **Rare**
- **PWR-2/Power Subsystem Risk - Connector failure**
 - **Effect:** Inoperable subsystem or component, based on the nature of the component, the effect can be minimal assuming for example on scientific instrument fails, or lead to the mission failure in case the navigation system does not receive power.
 - **Probability:** This event is classified as **Rare** as space missions have very strict protocols with regard to the assembly of the final product.
 - **Severity:** The outcome of such a risk can be **Catastrophic**.
 - **Mitigation:** Fitting tests of the wiring have to be performed before the mission. The connections have to be checked using a multimeter to identify whether the correct voltage and current pass through the wires.

- **Effect of Mitigation:** With this mitigation the event is **Improbable**
- **PWR-3/Power Subsystem Risk - Diode failure**
 - **Effect:** Reverse current enters the solar panels that can damage their performance or render them unfunctional.
 - **Probability:** The probability of occurrence is set to **Occasional**. Diodes fail due to excessive forward currents or high reverse voltages.
 - **Severity:** The failure of the diode from the solar arrays to the batteries may be **Critical** and lead to the failure of the PV system.
 - **Mitigation:** Use of voltage regulators for the different components to prevent undesirable currents and voltages. Adding a bypass diode for the PV modules to prevent high reverse voltages.
 - **Effect of Mitigation:** The mitigation reduces the probability to **Rare**.
- **PWR-4/Power Subsystem Risk - No power flowing from the batteries**
 - **Effect:** Unable to perform the mission.
 - **Probability:** The probability of occurrence is **Occasional**
 - **Severity:** The severity of such an event is **Catastrophic** as the system relies fully on electrical power for operation.
 - **Mitigation:** The mitigation strategy is to add a backup power distribution network that ensures power can flow from the batteries to the safety-critical components. Another approach is to ensure direct energy transfer from the solar panels to the system however this method is reliant on the environmental conditions.
 - **Effect of Mitigation:** The probability of occurrence becomes **Rare**

14.4 Layout

The electrical subsystem’s layout configuration is shown through the means of an Electrical Block Diagram illustrated in Figure 14.6. Important to note that back-up power connection power lines have been added to the components required to maintain the aircraft in flight during operation in case of failure of the primary distribution network thus complying with requirement **SYS-POW-05**.

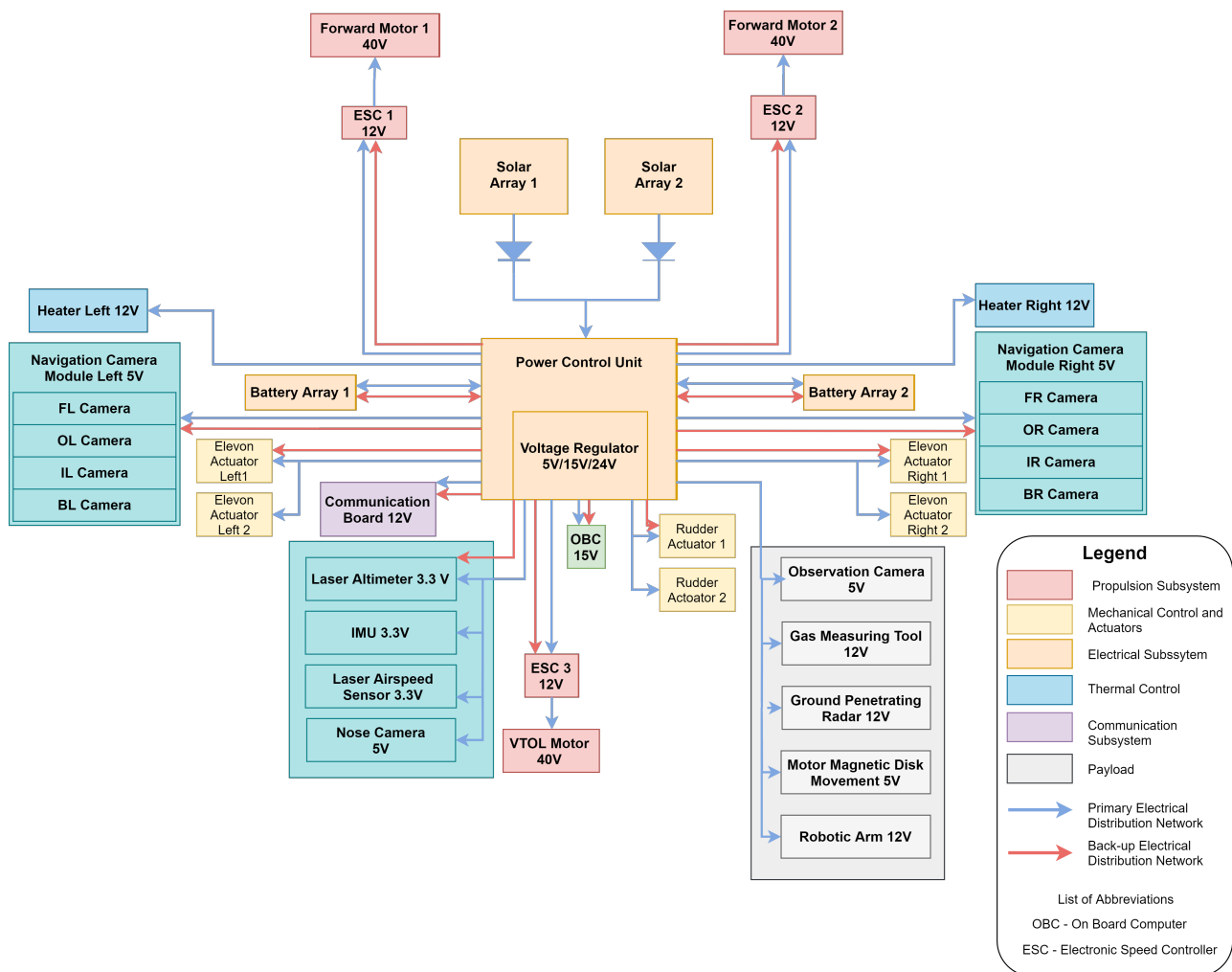


Figure 14.6: Electrical Block Diagram

14.5 Verification and Validation

The code implemented for sizing the power system is relatively simple. One class implemented the sizing and configuration for the solar panels and the battery based on the energy requirements coming from the latest sizing iteration.

14.5.1 Unit Tests

Total Energy Produced Test

By doubling the total energy requirement coming into the sizing function, the total energy produced by the solar panels has to double compared to the initial energy produced. Test was passed successfully.

Solar Modules in Series Test

The number of solar Modules in series is determined by dividing the nominal voltage of the system by the nominal voltage of the module of solar cells. If the nominal voltage of the system is doubled, it is expected that so will the number of modules grouped in series. Test was passed successfully.

Total Battery Capacity Test

By doubling the total energy requirement coming into the battery sizing function, the total battery capacity has to double as well. Test was passed successfully.

14.5.2 Validation

The first validation approach refers to the validation of the model. This can be done by using an actual mission, registering the energy requirements of that mission and running the code to investigate whether similar sizing values is used. It is essential to select missions where solar and battery cells with similar technical specifications are used. This validation method is not very accurate, but it should give a sense of the order of magnitude. The second validation step is for the results. For this, a prototype of the product would have to be built to obtain the subsystem's final mass, including the cabling. The system has to be tested ideally under Mars environmental conditions as designed for, and the requirements mentioned in the compliance matrix at the beginning of the chapter can be validated

15 Thermal Control Analysis

Keeping the aircraft and its subsystems within their operational or survival temperature range is an important part of the design that ensures the mission can be performed in the harsh Mars environment. The requirements the thermal control system has to comply with are presented in Section 15.1, and the Martian environmental conditions that drive the design are summarized in Section 15.2.1. The model used to analyze the thermal control needs and to size the required system is presented in Section 15.2. Lastly, the risks for this subsystem and the method used for verification and validation are presented in Section 15.3 and Section 15.4, respectively.

15.1 Requirements

The requirement for the thermal control subsystem is straightforward: to keep the temperature of each subsystem in its operational range. This is a requirement that can be verified through construction of the drone and simulation of the thermal Martian environment, as will be described in Section 15.4. The requirement is to be achieved through the use of thermal sensors and control, as will be described in this chapter.

Table 15.1: Requirements related to thermal control and their expected compliance

SYS-THE-01	(Driving) The thermal subsystem shall keep the temperature of the temperature-sensitive subsystems within their respective operational ranges during expeditions.	Satisfied
------------	---	-----------

15.2 Model and Analysis

This section outlines the method that was used to size the components of the thermal subsystems. Starting with exploring the Martian environment and components that need thermal control, the methodology is lined out and subsequently each thermal control element is described.

15.2.1 Martian Environment

The Martian environment is characterised by significant temperature variations based on the corresponding latitude and longitude positioning. This can easily be explained by the amount of available solar radiation that reaches the surface of the planet, with higher amounts near the equator, decreasing as we move to more extreme latitudes. The variation between a summer day at the equator and 45° latitude is approximately 100K.

Such a large temperature variation greatly impacts the design of the thermal control system. As expected, designing for the absolute worst-case scenario would lead to an oversized design. Thus, it was decided to size the thermal control unit for the most likely base locations and its surroundings: the Hellas Planitia. In this area, the minimum temperature on a cold winter night is -96°C, and the maximum on a summer day at noon is 0°C [158]. The sizing of the thermal control system for these conditions can be later evaluated for different base locations and thus temperatures to evaluate its efficiency and limitations.

Moreover, the amount of direct solar irradiance that reaches the ground surface is of importance as well. Using the method presented in Section 14.2.1, it has been determined that at 42° latitude (corresponding to the position of Hellas Basin), the lowest amount of incoming solar radiation is 25 [W/m²], corresponding to a cold winter evening on a day with high optical depth of 0.35. A non-zero value is selected for the sizing because the UAV does not operate at night; therefore, there is a small contribution from the sun at all times. The highest amount of solar radiation is 480 [W/m²], corresponding to a hot summer day at noon for a low optical depth of 0.1.

The type of environment also affects the types of heat contributions acting on the product and dictates the type of heat transfer between the components. For the Martian atmosphere, the following contributions are of importance:

1. Radiation
 - (a) Direct solar radiation
 - (b) Albedo radiation (the solar radiation reflected by the planet back to space)
 - (c) The infrared radiation of Mars
2. Conduction between components
3. Convection between the gases in the atmosphere and the components

15.2.2 Components Operating Range

The goal of thermal control is to ensure all components can operate within their operating temperature range despite the impact of the environment. An overview of the operational temperature ranges of the components is presented in Table 15.2. Noted that for sizing, these temperature ranges will be decreased by 5°C as a safety factor [161].

Table 15.2: Operational and critical temperature range overview of the UAV components and scientific instruments

Mission	Component	Operation Range [°C]		Survival Range [°C] [131]		Reference
		min	max	min	max	
2	Robotic drill arm	-135	70	-135	70	Chapter 7
1	Observation Camera	-25	20	-110	50	Chapter 7
1	Gas Analyser	-25	50	-25	50	Chapter 7
1	Ground Penetrating Radar	-25	50	-25	50	Chapter 7
1	Magnetic Disks	-20	85	-20	85	Chapter 7
All	Onboard computer	-25	45	-40	50	Chapter 8
All	Navigation Camera	-25	20	-110	50	Chapter 8
All	IMU	-40	85	-110	50	Chapter 8
All	Laser Altimeter	-10	50	-110	50	Chapter 8
All	Motor	-20	40	-77	44	Chapter 13
All	Solar Panels	-165	70	-165	70	Chapter 14
All	Li-ion Batteries	-20	60	-20	60	Chapter 14
All	Antenna	-55	125	-55	125	Chapter 9
All	Communication Board	-50	120	-50	120	Chapter 9

Before the thermal control system can be designed, the most extreme scenarios have to be defined. The environmental conditions dictate the harshest conditions the product may encounter, i.e. a cold winter evening or a hot summer day. The type of mission to be executed also has a large impact, as different instruments are active for different expedition profiles, generating different amounts of heat in different places. For example, during expedition profile 2 for collect and return, the drill will produce heat during operation. However, this is not the case during expedition profile 1 for remote sensing, when the drill is inactive. Given that the product is of rather large dimensions, the components that require thermal control can be divided into four different categories that do not influence each other: the main body section (consisting of all instruments required for navigation, communication, and scientific purposes), the motors, the batteries, and the additional navigation cameras present at the winglet tips. For each group, the coldest and hottest scenario will be further discussed.

15.2.3 Methodology

The approach used stemmed from the heat balance shown in Equation 15.1 and it was adjusted to account for the conditions present on the Martian environment. It is important to note that a steady-state equilibrium has been considered. Q_{absorbed} is composed of the solar radiation, albedo flux, and infrared radiation on Mars as shown in Equation 15.2. Thus, rewriting the heat balance equation yields Equation 15.3 which represents the equation used in the Python model. In this equation, C_{ij} , R_{ij} stands for a conductive or radiative link between node i and node j , respectively.

$$Q_{\text{in}} = Q_{\text{out}} = Q_{\text{absorbed}} + \sum P_{\text{dissipated}} = Q_{\text{emitted}} + Q_{\text{convected}} \quad (15.1)$$

$$Q_{\text{absorbed}} = Q_s + Q_a + Q_{IR} \quad (15.2)$$

$$Q_s + Q_a + Q_{IR} + \sum P_{\text{dissipated}} + \sum_0^{\text{no.nodes}} R_{ij}(T_i^4 - T_j^4) + \sum_0^{\text{no.nodes}} C_{ij}(T_i - T_j) + hA(T_i - T_j) = 0 \quad (15.3)$$

$$R_{ij} = \sigma \varepsilon A_{ij} \quad (15.4)$$

$$C = \frac{kA}{L} \quad (15.5)$$

In Equation 15.4, $\sigma = 5.68 \times 10^{-8}$ [W/m²K] as Stefan Boltzmann constant, ε is the emissivity of the radiative material, and A_{ij} is the radiation area. In Equation 15.5, k stands for conductivity constant in [W/(mK)], A is the area that is conducting, and L is the distance from the center of mass to the conducting surface. Conductance C is the opposite of resistance ($C = \frac{1}{R}$) and can be interpreted as a measure of how easy it is for current or heat to flow from one surface to another. If the surfaces are connected in series, the resulting resistance is $R_{ij} = R_i + R_j$. Therefore, the conductance can be computed as $\frac{1}{C_{ij}} = \frac{1}{C_i} + \frac{1}{C_j}$. The term R was used exclusively in this paragraph to explain the conductance notion better. All other references to the symbol R in the remainder of this chapter define radiation connections.

The components can be approximated to have a cuboid shape. Therefore, different surfaces have been taken into account for conduction and radiation links. For the latter, the surface area facing the ground from each instrument has been computed by investigating which surface of the cuboid is in contact with the environment. An example is shown in Figure 15.1b. For the former, only the contact area between two cuboids has been taken into account. Given that one cube has a smaller surface area, that is used to compute the conductivity between the two components. An example is illustrated in Figure 15.1a.

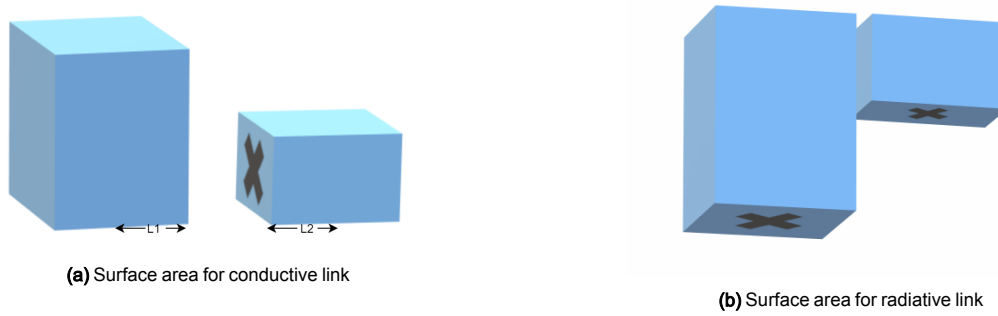


Figure 15.1: Surface areas used for computing the radiative and conductive links

The approach used is to write a heat balance equation for each node individually and combine all of the equations into a set. The nonlinear nature of the radiation formula raises a problem in the attempt to solving larger equations sets. Linearization is, therefore, necessary for the radiation term to reduce the computational time. The linearization method is shown in Equation 15.6. In this model, only radiative links with the Mars environment are considered. The radiation links between instruments are considered to be reduced to negligible impact through thermal finishes. An example of how linearization is applied for a radiation term with the environment is shown in Equation 15.7. This equation can be implemented in a Python code in a linear manner, with T_x being the only term that varies. T_1 , representing the temperature of the environment, is known and constant. The initial temperature T_{x_0} can be given an initial estimate and then iterated until the difference between the approximated heat resulting from the linearization and the real heat resulting from computing the 4th-degree polynomial with the temperature resulting from the equation sets is smaller than 1 [J].

$$L(x) \approx f(x) \approx f(x_0) + f'(x_0)(x - x_0) \quad (15.6)$$

$$R_{1x}(T_x^4 - T_1^4) \approx R_{1x}(-3T_{x_0}^4 - T_1^4 + 4T_{x_0}^3 T_x) \quad (15.7)$$

15.2.4 Thermal Analysis Body Structure

The body structure has the largest number of components and consists of the instruments required for communication and navigation and all the scientific payload. The thermal interaction between the components, the surrounding structure, and the environment have been analyzed by idealizing the components as nodes and defining the interaction type between them. To simplify the calculations, small components placed in close proximity to each other with similar operating temperature ranges were grouped together and were approximated as a cuboid shape of the resulting volume. This was the case for the two central cameras, which were grouped into a singular parallelogram and the elements required for navigation and communication. Thus, the communication, navigation boards, the laser altimeter, and the IMU have been grouped into a singular block and the most restrictive operational temperature range has been used for the group. Note that even in this situation, the resulting blocks had a smaller dimension than the surrounding components. The resulting nodal network is illustrated in Figure 15.2a and the name of the instruments composing each node can be found in Table 15.3.

The different types of interactions between the components are illustrated in Figure 15.2b as either conduction or radiation links. For example, Node 9 with temperature T_9 has conduction links with all other instruments that are in contact with it and a radiation link with the Mars environment, T_1 .

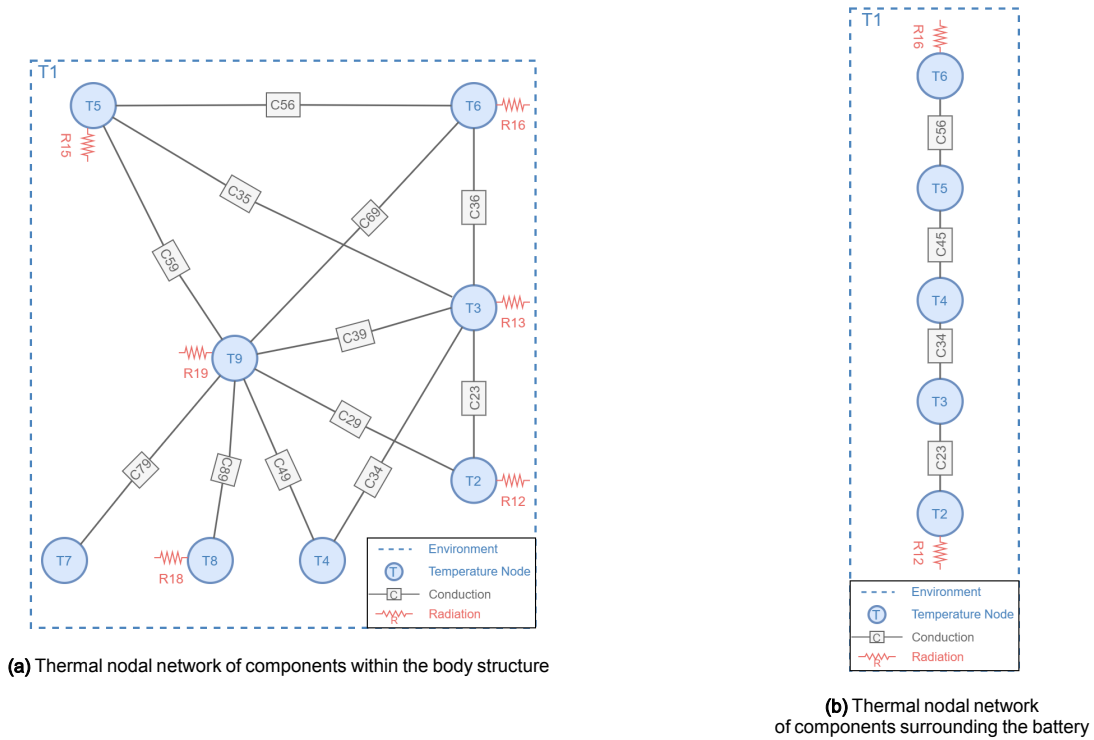


Figure 15.2: Thermal nodal networks

Table 15.3 shows the material properties of the different components. All components other than node T9 can be considered to be made out of aluminium, thus having emissivity $\epsilon = 0.1$, absorptivity $\alpha = 0.4$, and conductivity constant $k = 236 [W/(mK)]$. The top wall structure of the body is made out of carbon fibre, thus having emissivity $\epsilon = 0.77$, absorptivity $\alpha = 0.85$, and conductivity constant $k = 21 [W/(mK)]$ [155, 153, 154]. For better performance, thermal finishes are applied to the components. The top surface plate made out of carbon composite material is a flat absorber with both high absorptivity and emissivity. During a preliminary analysis, it has been noticed that a lower absorptivity is more desirable during hot scenarios. A white paint layer of PCBZ that reduces the absorptivity is applied on the top wall for these considerations. The navigation and communication module node T7 has been coated with vaporized deposited gold to bring the radiation of the electrical boards with the surrounding instruments. For the rest of the components, anodized aluminium was the coating of preference due to the extensive range of variation in terms of emissivity and absorptivity combinations [120, 161].

Table 15.3: Material properties of the components within the body structure

Node	Component	Thermal Finish	α	ϵ	$k [\frac{W}{mK}]$
1	Mars Environment	N/A	N/A	N/A	N/A
2	Ground Penetrating Radar	Aluminium with anodized aluminium coating	0.86	0.04	236
3	Robotic drill arm	Aluminium	0.4	0.1	236
4	Soil containers	Aluminium	0.4	0.1	236
5	Gas Analyser	Aluminium with anodized aluminium coating	0.86	0.04	236
6	Magnetic Disks	Aluminium with anodized aluminium coating	0.86	0.04	236
7	Onboard computer	Aluminium vaporized deposited gold coating	0.3	0.03	236
	IMU				
	Laser Altimeter				
	Communication Board				
8	Navigation Camera	Aluminium with anodized aluminium coating	0.03	0.8	236
	Observation Camera				
9	Top wall structure	Carbon Composite with white paint PCBZ	0.16	0.87	21

The nodal network of the body structure has been considered under both cold and operational conditions with a distinction between the two different expedition types. The product would have to perform ground observation during expedition profiles 1, and collect and return during expedition profile 2. Computing the steady-state temperatures from the nodal network revealed that the top wall plate acts as a very effective conductor that effectively brings all instruments to similar temperature with variations no more than 1-2 [K].

Coldest Case: Winter Night

During the cold operational scenarios, no additional active means of thermal control are necessary. The thermal finishes are applied to suffice for maintaining the instruments within operational range if they were active or survival range if they were not.

Hottest Case: Summer Day

Computing the steady-state temperatures from the nodal network revealed that additional heat dissipation is necessary under hot operational conditions with the most constraining conditions during expedition profile 1. Node 8 corresponds to the navigation and observation cameras representing the most constraining factor as their temperature needs to be reduced by at least 30.3 [K] to bring the instruments within operational range. The navigation and communication module, node 7, also required additional heat dissipation for a 5.8 [K] difference. These constraints translated into the necessity of adding a 150 [W] radiator during ground observation missions. High Performance Radiator technology from Airbus HiPeR [7] is used to dissipate excess heat. This is an ultralight, flexible radiator that can reject $370 \left[\frac{W}{m^2} \right]$ of heat and has a mass performance of approximately $3.5 \left[\frac{kg}{m^2} \right]$. Thus for 150W heat dissipation, the radiator area is 0.4 [m²] and the associated mass roughly 1.4kg. The radiator can be connected to the instruments through thermal links that can be disconnected during hot case scenarios to prevent overheating. An overview of the heat flows in and out of the system used to determine the required heat dissipation is shown in Table 15.4. A similar approach was used to analyse the system for expedition profile 2. The temperature differences in this case were not as significant as in the previous case and only 20 [W] of dissipated heat is necessary during drilling operations. Although essential for performance analysis and battery sizing, this consideration does not drive the design of the thermal control system and will not be detailed further.

Table 15.4: Overview of heat intake of the body structure

Node	Q_s [W]	Q_a [W]	Q_{IR} [W]	P [W]	Q [W]	Q_{in} [W]
1	N/A	N/A	N/A	N/A	N/A	N/A
2	0	0.66	0.04	2.48	0	3.18
3	0	9.68	3.41	0	0	13.09
4	0	0	0.25	0	0	0.25
5	0	6.14	0.4	2.6	0	9.14
6	0	0.2	0.01	4.8	0	5.01
7	0	0	0.02	25.85	0	25.87
8	0	0.2	0.01	2.79	-150	-147
9	53.76	0	65.88	0	0	119.65

15.2.5 Thermal Analysis Motors

The motors operate at an efficiency of 95%. At a maximum power consumption of 4865 [W] for the rear motor during VTOL, this means that the back motor dissipates 243.3 [W]. During cruise, the front motors use 2400 [W] which means that they dissipate 120 [W] continuously. The operational temperature range of the motors is given to be -80 to 315°C, however high temperatures will degrade the efficiency of the motors [18]. It should thus be ensured that the temperature of the motors is limited. This section describes the design of radiators for the front and back motors to make sure that their temperature remains within a desirable range.

Starting with the back motor, a finned cylindrical radiator has been sized to be put around the motor and the gearbox. This 20 [cm] high radiator is made out of aluminium and has a thickness of 1 [mm], a radius of 10 [cm] and 12 fins sticking out 7 [cm], spread around the perimeter of the cylinder. This results in a surface area of 0.4617 [m²], from which the radiator can radiate away heat from the motor.

For the front motors, a cylindrical radiator without fins has been designed to be put around the front motors inboard of the hinge controlling the front propeller orientation. This 50 [cm] long aluminium cylinder has a diameter of 15.56 [cm] and a thickness of 1 [mm]. The resulting surface area for radiation is 0.4889 [m²].

Coldest Case: Winter Night

The coldest situation that is considered in Hellas Planitia is -96°C. Examining the heat balance of the back motor:

$$P_{\text{dissipated}} = P_{\text{radiated}} \quad (15.8)$$

$$243.3 = \epsilon \sigma A (T_{\text{motor}}^4 - T_{\text{environment}}^4) \quad (15.9)$$

It is assumed here that the radiator always adopts the temperature of the motor, as it surrounds the motor completely. In this calculation, convection is neglected as it is very difficult to model for the geometry of the back motor. Filling in the radiator area and an emissivity of 0.96 for a painted surface, and solving for the motor temperature gives an equilibrium temperature of 48.2°C when the back motor is continuously running. Thus, it is not required to heat the back motor. Performing the same calculation for the front motors, with a dissipated heat of 120 [W] and a radiator area of 0.4889 [m²] results in an equilibrium temperature of -0.9°C. Hence, the front motors do not require any heating either, and the thermal requirement is met for the front and back motors.

Hottest Case: Summer Day

The warmest situation that is considered is 0°C on a summer day in Hellas Planitia. For the back motors, an equilibrium state is not considered here as the motors are only functioning during take-off and landing, in the order of tens of seconds. Rather, to simulate the thermal behavior of the back motor in these conditions, a Python program was written to calculate the change in temperature of the motor and radiator under influence of dissipated heat, absorbed albedo, and infrared radiation from Mars, and heat that the radiator radiates out. Using required motor power over time as an input, the following formula is used to calculate change in temperature every time step:

$$\Delta T = \frac{P_{\text{net}} \Delta T}{(m_{\text{motor}} + m_{\text{radiator}}) c_p} \quad (15.10)$$

Where the heat capacity of aluminium is used, and P_{net} is the sum of all incoming and outgoing heat:

$$P_{\text{net}} = P_{\text{dissipated}} + P_{\text{albedo}} + P_{\text{Mars IR}} - P_{\text{radiated out}} \quad (15.11)$$

Again, convection is conservatively ignored as the geometry does not lend itself to an approximation of convection effects. Simulating a take-off procedure, the mission segment that causes the largest rise in temperature, results in the figure below.

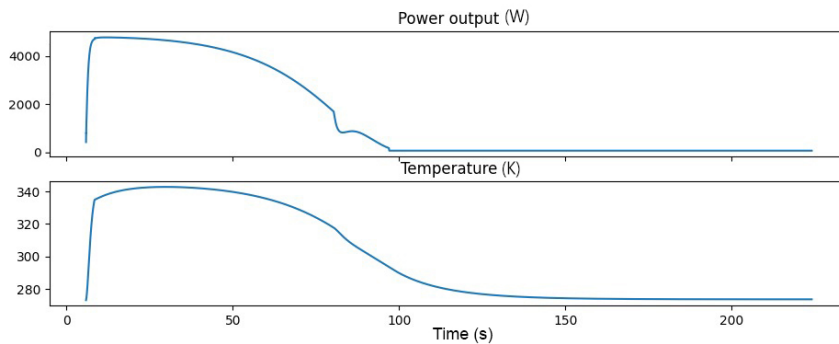


Figure 15.3: Power output and temperature response of a take-off procedure

As can be seen, using the radiator designed for the back motor, the temperature of the motor and radiator does not exceed 323 [K] or 50°C during take-off. Hence, the thermal requirement is met.

For the front motors, it is possible to find an expression for the effect of convection. First, the Reynolds number of the flow over the 0.5 [m] long cylinder is calculated:

$$Re = \frac{\rho V l}{\mu} \quad (15.12)$$

Where in these conditions, the dynamic viscosity μ is 1.464×10^{-5} [kg m⁻¹ s⁻¹] and the density is 1.4×10^{-2} [kg m⁻³] [23, 88]. Filling in a length of 0.5 [m] and a cruise velocity of 80 [m/s] gives a Reynolds number of 220729. The Prandtl number can be calculated with the following formula:

$$Pr = \frac{\mu c_p}{k} \quad (15.13)$$

Where the heat capacity c_p of CO₂ is taken to be 846 [J/K], and the thermal conductivity k of CO₂ is taken to be 0.015 [W/(mK)] at these conditions [152, 151]. This results in a Prandtl number of 0.748. With the Prandtl and Reynolds number, the following empirical relations can be used to approximate the Nusselt number of the flow over the cylinder, approximating it with flow over a flat plate [140]:

$$\overline{Nu}_{\text{tur}} = \frac{0.037 \cdot Re^{0.8} \cdot Pr}{1 + 2.443 \cdot Re^{-0.1} (Pr^{\frac{2}{3}} - 1)} \quad (15.14)$$

$$\overline{Nu}_{\text{lam}} = 0.664 \cdot \sqrt{Re} \cdot \sqrt[3]{Pr} \quad (15.15)$$

$$\overline{Nu} = \sqrt{\overline{Nu}_{\text{lam}}^2 + \overline{Nu}_{\text{tur}}^2} \quad (15.16)$$

Where $\overline{Nu}_{\text{tur}}$ is the average Nusselt number of a fully turbulent flow, $\overline{Nu}_{\text{lam}}$ is the average Nusselt number of a fully laminar flow, and \overline{Nu} is the estimate for the actual Nusselt number. This last formula is valid for Reynolds numbers between 10 and 10⁷ [140]. Filling in the Reynolds and Prandtl numbers gives an average Nusselt number of 660.16

for the flow over the cylinder. With the Nusselt number, the average convection heat transfer coefficient over the cylinder can be calculated as follows:

$$\bar{h} = \frac{\overline{Nuk}}{L} \quad (15.17)$$

Filling in the length of the cylinder and the thermal conductivity of CO₂ gives an average convection heat transfer coefficient \bar{h} of 6.602 [W/m²K]. For reference, a 2 [m/s] wind of Earth atmosphere corresponds to a heat coefficient of 26.2 [W/m²K]. Finally the heat balance of one of the front motors can be examined:

$$P_{\text{dissipated}} = P_{\text{radiated}} + P_{\text{convected}} \quad (15.18)$$

$$120 = \epsilon\sigma A(T_{\text{motor}}^4 - T_{\text{environment}}^4) + 0.8hA(T_{\text{motor}} - T_{\text{environment}}) \quad (15.19)$$

A factor 0.8 is applied to the convection effect to make sure that the estimate is conservative. Filling in the front motor radiator area of 0.4889 [m²] and outside temperature of 0°C gives an equilibrium temperature of 50°C for the front motors during cruise. Hence, the requirement is met.

15.2.6 Thermal Analysis Batteries

A visual representation of the nodal network used for analysing the temperatures of the batteries is present in Figure 15.2b. The batteries are placed in two different arrays, one on the left wing and one on the right wing. The thermal analysis is the same for both sides, and therefore only one side is shown in the schematic. The associated material properties are present in Table 15.5. The nodes considered for this analysis are the top and bottom wall structure, the top and bottom wing box structure, and the batteries. The battery is mounted within the wing box. Therefore only the vertical heat flow through the top and bottom plate, the top and bottom parts of the wing box structure, and the battery pack itself are of interest. Therefore, it is assumed that all components have the same conductive area of 0.05 [m²], and the same value of the area is used for radiation with the environment by the top and bottom plates.

Table 15.5: Material properties of the components surrounding the battery

Node	Component	Thermal Finish	α	ϵ	$k \left[\frac{W}{mK} \right]$
1	Mars Environment	N/A	N/A	N/A	N/A
2&6	Top& bottom wall structure	Carbon Composite with white paint PCBZ	0.16	0.87	21
3&5	Wing box wall	Aluminium	0.4	0.1	236
4	Li-ion battery	Li-ion	0.4	0.1	236

Coldest Case: Winter Night

Computing the steady-state temperature for the nodal network of the batteries revealed that the batteries would require additional heating during cold operational conditions as otherwise their temperature stabilizes at 247 [K], 8.6 [K] below their operating range. The temperature difference to bring the batteries within operational range can be achieved through means of graphene aerogel insulation of 1 [mm] between each node. This method brings the battery temperature to 262 [K]. With four interlayers of graphene aerogel of 1 [mm] thickness in between the top wall structure, the wing box and the battery, each with a surface area of 0.05 [m²], the necessary material volume is 50 [cm³]. With a material density of 12.5 [$\frac{mg}{cm^3}$], the total mass of insulation is 0.625[g], an insignificant mass contribution compared to the rest of the design.

Table 15.6: Overview of heat intake of the structure surrounding the batteries

Node	Q_s [W]	Q_a [W]	Q_{IR} [W]	P [W]	Q [W]	Q_{in} [W]
1	N/A	N/A	N/A	N/A	N/A	N/A
2	0	0.03	0	3.76	0	0
3	0	0	0	0.43	0	0
4	0	0	0.05	0.43	0	0
5	0	0	0	0.17	0	0
6	0.16	0	0	3.76	0	0

Hottest Case: Summer Day

Computing the steady-state temperature for the nodal network of the batteries revealed that the batteries reach a temperature equilibrium of 309K during hot operational conditions and require no other form of passive or thermal control. Moreover, the introduction of the insulation layer for cold operational conditions does not increase the temperature of the batteries, which maintain a steady 309 [K] operational temperature.

15.2.7 Thermal Analysis Wing Mounted Navigation Cameras

The navigational cameras are located at the bottom of the winglets. In each winglet, there is a set of 4 cameras measuring 3.8×3.8×3.6 [cm], spaced along the winglet chord with length [cm]. To approximate the heat behavior of this set of cameras, it is assumed that the cameras together form one node measuring 3.8×3.8×30 [cm] that

loses heat through the skin of the winglet, and that has an area twice that of the side of this cuboid on both sides of the winglet, totalling 0.0456 [m²], and gains heat through the power dissipated by the cameras, as well as a heater introducing 4 [W] of power into the system when functional. In each winglet, two of these heaters are included to ensure redundancy of the system. These heaters are controlled by temperature control units, of which there are also two corresponding to each winglet to ensure redundancy. The areas of the winglet that radiate out heat are covered in aluminium paint to lower the emissivity.

For the cold case, to see what the equilibrium temperature is of the cameras when functioning, the following heat balance is investigated:

$$P_{\text{dissipated}} + P_{\text{heater}} = \epsilon \sigma A (T_{\text{cameras}}^4 - T_{\text{environment}}^4) \quad (15.20)$$

Assuming the cameras have a 5% efficiency and all use 3.1 [W] of power, the dissipated heat is 0.62 [W]. Assuming the aluminium paint has an emissivity of 0.27 [153], solving for T_{cameras} with $T_{\text{environment}}$ being -96°C gives an equilibrium temperature of 22°C.

For the warm case, assuming the heaters to be off and an environment temperature of 0°C results in an equilibrium temperature of 10.3°C. Therefore, the thermal requirement is met.

15.2.8 Temperature Sensors

In order to control the heaters and generally keep track of the temperature of every subsystem, temperature sensors are included at several places in the drone. In each place, two sensors are included to ensure redundancy. The placement is as follows: two at the cameras in the left winglet, two at the cameras in the right winglet, two at the left battery array, two at the right battery array, two at the navigation-communication PCB module, two at each scientific instrument (totalling 10), two at the solar array on the left wing, two at the solar array on the right wing, and finally two at each motor (totalling 6), meaning in total there are 30 temperature sensors included onboard the drone. With the use of the thermal solutions previously described and the temperature sensors to ensure the temperatures are within recommended ranges, requirement **SYS-THE-01** is satisfied.

15.3 Risk Analysis

Based on the discussion of the thermal subsystem, a number of risks can be identified. These risks are based on aspects of the thermal subsystem that could fail or lead to performance issues. As a result of the thermal system being designed as a tool to mitigate the risk of temperature changes, the risks are focused on the subsystem components itself rather than the risks associated with temperature swings.

- **Ther-1: Radiator tube ruptures**
 - **Effect:** Radiator system no longer functions and components may overheat.
 - **Probability:** **Rare** and likely a result of faulty production
 - **Severity:** **Critical** as many subsystems only function within specific temperature ranges.
 - **Mitigation:** As the radiator is made up of many panels, the tubes can be separated meaning a single rupture does not lead to subsystem failure.
 - **Effect of Mitigation:** The severity is reduced to **Marginal** as the solution only provides the UAV with extra time to return to the base.
- **Ther-2: Broken thermal link to the body radiator**
 - **Effect:** The instruments overheat
 - **Probability:** **Improbable** as thermal links are space certified and flight tested.
 - **Severity:** **Critical** as the scientific objective of the mission cannot be met.
 - **Mitigation:** Check thermal sensors data to ensure the thermal link is used within the operational standards set by manufacturer.
 - **Effect of Mitigation:** The severity of the risk is reduced from critical to **Marginal**, as if a failure occurs it would be a random failure of a single pipe instead of a more serious systemic issue.
- **Ther-3: Launch/flight load damages the radiators rendering them unusable**
 - **Effect:** The thermal control system does not function and would need significant repairs
 - **Probability:** **Rare**
 - **Severity:** **Catastrophic**
 - **Mitigation:** The radiators are being tested for 18 years in GEO orbit and their design is being updated to account for these loads. This research is however ongoing
 - **Effect of Mitigation:** The results that arise from this research should reduce the probability of this occurrence down to **Improbable**

15.4 Verification and Validation

This section describes how the models and calculations used to size the thermal control system were verified and validated, and how the results from these calculations can be validated.

15.4.1 Unit Tests

Several unit tests can be performed to verify calculation steps in the models that are used.

Conduction Matrix Test

The code for the thermal control analysis is built in a linear manner. A matrix is built with all the nodes on the vertical and all the nodes on a horizontal axis. If there is a conduction link between the two nodes, the matrix entry is 1; else, it is a 0. The conduction connection matrix is given as input to the code. It is later populated with the correct conductive values. For a four-node network, T_1 being the environment and T_2 to T_4 regular nodes and conduction points between node two and three $C_{23}(T_2 - T_3)$ and node 2 and 4 $C_{24}(T_2 - T_4)$ the corresponding populated matrix will have the form shown in Equation 15.21. To check that the correct values enter the matrix at the correct location with the correct signs, a small 3×3 matrix has been verified both visually (by printing the entries as strings) and quantitatively (by computing the matrix entries by hand and verifying the output matrix with a 0.1 accuracy).

$$\begin{bmatrix} C_{23} + C_{24} & 0 & 0 \\ 0 & -C_{23} & 0 \\ 0 & 0 & -C_{24} \end{bmatrix} \cdot \begin{bmatrix} T_2 \\ T_3 \\ T_4 \end{bmatrix} \quad (15.21)$$

Radiation Matrix Test

A similar approach used for the conductive connection test was also used for the radiation connection, with the implementation differing slightly due to the nonlinear nature of the radiation formula. For this case, the linearization of the radiation formula has been implemented. The term that varied with the temperature has been added in the matrix, and the additional constant items have been stored in a separate vector, as shown in Equation 15.22. The separate vector of constants has been added in the end to the Q_{in} vector and used to compute the temperatures. Both the matrix and the additional vector have been verified through handwritten calculations that did not vary by more than 0.1 accuracy

$$\begin{bmatrix} C_{23} + C_{24} & 0 & 0 \\ 0 & -C_{23} & 0 \\ 0 & 0 & -C_{24} + 4R_{14}T_0^3 \end{bmatrix} \cdot \begin{bmatrix} T_2 \\ T_3 \\ T_4 \end{bmatrix} + \begin{bmatrix} 0 \\ 0 \\ -3R_{14}T_0^4 - R_{14}T_1^4 \end{bmatrix} \quad (15.22)$$

Heat Input Test

The five different heat inputs types (respectively: solar, albedo, IR, dissipated power and heater/radiation power), are specific for each node. And it is uniquely based on the type of nodes and interaction with the environment. This type of unit test needs to be performed every time the nodal network or the node type is modified and is a manual process of populating the vectors. This can be explained by the fact that not all components/nodes are exposed to solar radiation or albedo. Similarly, the correct power dissipation has to be verified as each instrument has a different power usage.

15.4.2 System tests

Considering the calculation of all the different contributions of heat input and output as units, a way to perform system tests for the thermal calculations in this chapter is to examine whether each heat balance does, in fact, equal zero. This is a way of ensuring that given that all the units are correct, there is no error in the system, and thus no error in the heat balance calculations. This can be done by calculating and summing each contribution by hand to check that the results correspond with the results generated by the Python programs.

15.4.3 Validation

Two different validation approaches are needed. The first is to validate the software. For example, the software created for determining the temperatures based on the conductive and radiative links can be validated by giving the same inputs to well verified and validated thermal analysis programs such as ThermXL or ESATAN.

The second validation method is that of the results. This can be done by creating a prototype of the product and testing it under environmental conditions and usage cases as described in the model. Through means of thermal sensors, the temperatures of each component are measured and can be used to validate the outcomes of the software. It is expected that in reality, the results will be different, as the model for the payload instruments does not take convection with air into account, and the conductivity between instruments is overestimated by assuming that all components are touching each other, although, in reality, there is a small slit between them for mounting ease. Next to the overestimation of heat transfer between instruments, neglecting convection means that the heat loss of instruments that directly touch the outside atmosphere is underestimated.

16 Ground Operations and Logistics Description

This chapter describes the procedures which occur on the ground to support the operation of the UAV, from before the launch to Mars until after the end of the mission. This includes the actions required of the base crew on Mars as well as the ground support team on Earth. The requirements to which the ground operations procedures must comply are given in Section 16.1. A number of assumptions have been made about the state of the Mars base at the time of arrival of the UAV on Mars, many of which directly relate to the various aspects of ground operations. These are listed and explained in Section 5.5. Sections 16.2 to 16.10 then describe all ground operations from the beginning to the end of the mission. Note that the structure of this chapter differs from the structure of the preceding subsystem chapters because it is a *description* of the ground operations, as opposed to a design analysis of one of the UAV's subsystems.

16.1 Requirements

The requirements of this mission which are directly related to the ground operations are listed in Table 16.1. Their compliance is given in the rightmost column; it is explained how each requirement achieves its indicated compliance in the following sections of this chapter.

Table 16.1: Requirements related to ground operations and their expected compliance

Index: DME-REQ-	Requirement	Compliance
TL-OPE-03	The design shall allow unloading and assembly by 3 astronauts within 24 hours.	Satisfied
SYS-GEN-02	The mission shall provide all tools necessary for assembly that are not already present at the base.	Satisfied
SYS-GEN-05	The launcher shall have a reliability of at least 95%.	Satisfied
SYS-GEN-20	The mission shall provide all tools necessary for inspection and maintenance that are not already present at the base.	Satisfied
SYS-GEN-22	The mission shall provide all necessary equipment for the communications system.	Satisfied
SYS-GEN-23	The base shall provide all necessary equipment for recharging the batteries.	Satisfied
SYS-THE-02	The thermal subsystem shall keep the temperature of the temperature-sensitive subsystems within their respective operational ranges during storage.	Satisfied
GO-01	It shall be possible to repair the UAV in case of minor damage/expected wear-and-tear.	Satisfied
GO-02	It shall be possible to perform routine maintenance operations on the UAV without extensive disassembly of the UAV.	Satisfied
GO-03	It shall be possible to update all onboard software.	Satisfied
GO-04	It shall be possible for the astronauts to calibrate the actuators before flight.	Satisfied
GO-07	The mission shall include a storage system at the base which can protect the UAV from dust when not in use.	Satisfied
GO-08	The mission shall include a storage system at the base which can assist with thermal control of the UAV when not in use.	Satisfied
GO-09	It shall be possible to transport the UAV on the ground with the assistance of a surface rover vehicle without disassembly of the UAV.	Satisfied
STN-05	The scientific data resulting from the mission shall be made available to scientists and scientific institutions for which this data is relevant to research.	Satisfied
STN-06	During the operational phase, components of the UAV relating to soil collection shall be sterilized at the base such that these components are restricted to a surface biological burden level of ≤ 30 spores before they are used for soil collection purposes.	Satisfied
STN-08	It shall be possible for the operators on Mars to disassemble the UAV to access reusable components after end-of-life.	Satisfied

Note that two of these requirements are satisfied as a result of the assumptions made about the base in Section 5.5. Following from the assumption that sterilization equipment will be present at the base, requirement **STN-06** will be satisfied. Following from the assumption that the base will generate its own power, some of which will be available for charging the drone, requirement **SYS-GEN-23** will be satisfied.

16.2 Earth Operations (Prior to Operational Life)

Context

The Mars base will be operated and controlled by a collaboration of governmental space agencies (likely led by NASA), referred to from here on collectively as the 'main party'. The authors of this report and the designers of the UAV are employed by a private company that has been subcontracted to provide a design for the given mission.

If approved by the main party, this private company will be responsible for producing and testing the design (in collaboration with the main party).

Astronaut Training

One advantage of the UAV being semi-autonomous is that it limits the workload of the astronauts. The astronauts living and working on Mars will have high pressure and risky jobs and will have to be well trained and knowledgeable in many areas. Therefore, it is not expected that they should be experts on the functioning of this design. They will, however, require training to understand how to perform basic procedures. Knowing these basics will ensure that the normal use of the drone is not dependent on constant communication with the design team on Earth.

The training course will be developed and carried out in the 'Train Personnel' block, as can be seen in Figure 20.1. Training will cover the purpose of this mission, an overview of the scientific instruments on board, the design of the aircraft, and safety precautions. The astronauts will also learn about all of the operations described in this chapter, including unloading and transport after arrival, assembly and setup, storage operations, transporting the aircraft on the ground, inspection, testing, routine maintenance, repair, and regular expedition procedures (such as setting up and monitoring expeditions). Finally, the astronauts would learn how to remotely operate the drone from the base using a simulator (see Section 8.3). The training would be most effective if it occurred in person before the astronauts left Earth using a mock-up drone for reference. Instruction books will be developed alongside the training programme which will provide all necessary information about the mission. These books will be sent digitally to the Mars base and physical copies will be sent along with the drone itself so that information can be accessed even in the event of computer failure or a power outage.

Pre-Launch, Launch, and Cruise

Part of the mission will be to choose how all of the components will be sent to Mars. Launch operations will be carried out by a private launcher company or by the main party (to be decided after the design process). Sizing of the design options was carried out using the Atlas V launch vehicle for reference, but a more suitable option may become available in the future. These operations will include constructing or refurbishing the launcher, loading the parts and components into the payload fairing, setting up the launch pad and all related systems, fuelling the launcher, carrying out the initial launch, performing orbit transfer burns, performing arrival and landing procedures, and monitoring systems throughout [49]. All of this must take place in accordance with regulations. Communication with this party will be important for ensuring that the UAV is launch-ready by the launch date. In any case, it will be ensured before this stage begins that the launch vehicle to be used will have a reliability of at least 95%, thereby satisfying requirement **SYS-GEN-05**.

16.3 Mars Operations (Prior to Operational Life)

Arrival

The UAV will arrive on Mars via an entry-and-landing system which will contain all the necessary components and peripheral equipment for the crew on Mars to operate the mission successfully. The entry-and-landing system will touch down within range of the SRV(s) such that the base crew can drive out to the landing point, unload the contents of the entry-and-landing system, and transport them back to the base. Once all components are at the base, they may be unpacked, organised, and inspected for any damage that may have occurred during the journey. In the event that no damage is detected, assembly can be then carried out.

Assembly

Assembly will take place as soon as weather conditions and the crew's work schedules allow. The astronauts will be outside the base modules for the duration of assembly, so they will be wearing protective suits. This limits dexterity in their hands and fingers, so small precise tasks will not be required during assembly.

The wings will be delivered as broken up into 6 separate components (as can be seen in Figure 10.1). Each will part will be pre-assembled on Earth, with the correct airfoil shape and part of the internal wing structure housed inside. They will also contain any parts which are designed to be housed within the wing, such as the batteries and the laser airspeed sensors. Each will have appropriate connection points at both ends for connecting to the next wing component, the fuselage, or the winglets, including physical joints, power connections, and data connections. The main fuselage will be delivered as a single pre-assembled piece. The propellers will each be divided into two pieces at their centre. Other components will include the winglets, landing gear, and the supporting beams for the rotors (three of which have motors attached).

The general assembly process will be as follows. The landing gear structures will be attached to the underside of the main fuselage. This component is then oriented upright on the ground. The left and right inner wing parts are attached to the fuselage, followed by the middle wing parts, and the outer wing parts. The winglets are then attached to the underside of the outer wings. The matching propellers parts are attached together and installed together onto the appropriate motors. The support beams are then installed onto the body structure. Most attachment of components will require electrical and data connections, which will be simplified for the astronauts through the pre-assembly process on Earth.

This entire process will be tested on Earth several times under conditions which are as close to the Martian surface as possible to ensure that everything is possible for 3 astronauts to complete within 24 hours. The assembly will

therefore satisfy requirement **TL-OPE-03**. That said, if the crew do encounter any problems during assembly, they will be able to contact the design and production team on Earth to ask for advice.

The astronauts will also need to set up and place the communications beacons at their appropriate locations. The inclusion of these components satisfies requirement **SYS-GEN-22**. The truss structures which support the beacons will be partially pre-assembled on Earth. This will be done with the help of an SRV. The pre-assembled truss pieces, the solar panels which will power the beacons, the batteries, and the beacons themselves will be loaded onto the SRV, along with any tools needed to complete the construction and set up the beacons. The astronauts will then drive to the specified beacon locations one at a time, and will unload and set up a beacon at each spot. For each beacon, this will involve stacking and connecting the truss pieces, fixing the beacon in place, and setting up the solar panel and battery.

The precise details of how the subassemblies will be joined together and which tools will be required for this task are not yet known, and neither are the precise tools that will already be available at the base. For this reason, a package of mass 10 [kg] is included in the total mission mass budget to account for the potential need to include additional specific tools. This include the tools needed for (dis)assembly, inspection, maintenance, and repair. This therefore satisfies requirements **SYS-GEN-02** and **SYS-GEN-20**.

16.4 Ground Equipment

The drone will require a certain amount of equipment to be present at the base to support the fulfilment of the mission. This will include the communication network beacons and tools for assembly and maintenance, as already mentioned, but a number of other components are necessary.

First is a number of physical manuals about the design. These will cover the design itself, the scientific mission, the assembly procedure, inspection and maintenance procedures, expedition procedures, and troubleshooting guides, as well as everything else covered by the training course and more. These manuals (which will also be available digitally) can be used for reference by the crew if ever they need a quick answer about the design without having to wait to communicate an issue with the team on Earth. The physical manuals may be useful in the event of computer failure or a power outage at the base. The mass estimate for these is 2 [kg].

Second, it is assumed that a number of computers are already present at the base which are capable of connecting to the beacon network and running the required software for setting up expeditions, monitoring expeditions, and operating the drone remotely. What will not be present at the base already is a flight control stick for plugging into the computer to operate the drone remotely. This equipment will therefore be included with the drone, at an estimated mass of 2 [kg].

Last is the storage and charging equipment. The storage system is combined with a landing pad for the drone, and will have dimensions at least as wide as the drone's wingspan and at least as long as the drone's length. The storage system also includes the upper tarpaulin and heating elements, as well as a cable to connect it to the base power network (see Section 16.5). The charging equipment will simply be a long durable cable with the appropriate connectors at each end to connect to the drone's charging port and the base power network.

16.5 Storage

In order to increase the lifespan of the drone, it is desirable to have some storage infrastructure in place at the base. This storage should assist in protecting the drone from dust (thereby reducing wear and maintenance) and provide some thermal insulation and heating to protect the battery during the colds nights on Mars. At the base, the drone lands on a rectangular landing pad which reduces the dust kicked up due to the landing and take-off sequences. This landing pad may have lines or patterns on it which can help calibrate the navigation cameras as the drone takes off and lands. Following this, the soil samples can be collected from the drone by the astronauts and any post flight checks can be performed. The astronauts connect the drone to the base power system to charge the batteries. The maximum expected power draw for the purpose of charging the drone is 216 [W] (see Section 14.2.5), or around the same as a desktop computer. The upper part of the storage system is a thin thermally insulated tarpaulin with heating lines. This is pulled over the drone and sealed, protecting it from dust. The storage system will also be connected to the base power system to provide energy to heat the inside of the storage envelope.

To size the storage system to a basic extent, the shape of the upper cover can be assumed to be a spherical cap, while the landing pad is the circular base of this cap. The diameter of the cap base is taken to be the drone's wingspan plus 15%, or 18.4 [m], and the height is taken to be 2 [m]. The total surface area of the upper cover and the landing pad are thus 550 [m²]. Assuming a tarpaulin-like material with a mass density of 0.1 [kg/m²], this gives a mass of 55 [kg].

For the thermal sizing, it is assumed that the inner surface of the landing pad and upper cover are coated with a heat reflective metallic material which has an assumed reflectivity of 0.97. The average emissivity ϵ and absorptivity α of the drone are taken to be 0.82 and 0.16 respectively. The radiating surface area A of the drone is taken to be 20 [m²], based on a 3D computer model. Assuming the drone is stored at temperature $T = -20^\circ\text{C}$, and it is sealed

inside the storage system which provides heating power flux of S , the thermal power balance can be written as:

$$Q_{out} = Q_{in} \epsilon A \sigma T^4 = 0.97 \epsilon A \sigma T^4 + S \alpha A S = \frac{0.03 \epsilon \sigma T^4}{\alpha} \quad (16.1)$$

So $S = 35.72 \text{ [W/m}^2\text{]}$. With a total area of $20 \text{ [m}^2\text{]}$, this leads to a thermal power requirements during storage of 714 [W] . This storage system complies with requirements **GO-07** and **GO-08**.

16.6 Ground Transportability

Ground transportability, or moving the drone to a location other than the base while on the ground, will be possible with the help of an SRV. This may be desired if the astronauts wish to conduct an expedition just past the drone's usual maximum range from the base.

As stated in the assumptions (Section 5.5), the SRV(s) at the Mars base is capable of transporting cargo. To transport the drone, the crew will need to lift the drone at the root of the wing and hoist it onto the cargo bed of the SRV. With a mass of approximately 100 [kg] and Mars' low gravitational acceleration, the drone should be easily lifted by two astronauts. The astronauts would then secure the drone down to the SRV using straps or other connectors. Then the SRV will be ready to transport the drone. The wings would of course stick out over the sides of the SRV cargo bay, so the crew would need to be careful during transportation in order to avoid collisions between the wings and stray rocks, and to avoid driving over very rough or uneven terrain, which may cause damage to the drone. This process satisfies requirement **GO-09**.

16.7 Expedition Procedures

Setting up a standard expedition will involve a number of steps for the crew. First, they will check the weather forecasts for the region surrounding the base. If there are any small local dust storms, they will make a note not to conduct any expeditions around that locality. Any larger dust storms may mean that no expedition can take place, depending on the exact size and progression of the dust storm. If the expedition is going ahead, they will open the appropriate software on a base computer and select the expedition type, the target location(s), and whether the expedition will be conducted semi-autonomously or with remote human control. The crew will check if any software updates for the drone have been received from Earth. If so, they will upload them to the drone's OBC and reboot it. This satisfies requirement **GO-03**. The drone's battery level will also be checked to ensure that it has enough energy to conduct the planned expedition. The drone will be removed from its storage system, and the charging cable will be unplugged. A standard program will be run for resetting and calibrating the sensors and actuators, thereby satisfying requirement **GO-04**. Before beginning the expedition, the drone will run its flight path algorithm and will make the planned route available to the astronauts to review.

Take-off and landing will always happen autonomously. See Section 8.6 for more technical details about this. More details about human remote controlled expeditions are given in Section 8.3. During take-off, landing, and indeed throughout the mission, the crew can monitor the expedition from the base computer which is connected to the beacon network. They will be able to see a (slightly delayed) live feed from one of the 10 onboard cameras, the drone's location, flight status (velocity, heading, etc.), subsystem status (whether everything is operational), battery charge level, and the autonomous system's decision logs. If they feel the need, the crew members can take over and begin to control the drone remotely. They can also send updated commands to the drone change the target location or expedition goal. Throughout the flight, the drone will be automatically provided with regular updates from the Mars weather system. The crew will be notified when: the drone arrives at its target location, it completes its expedition objective, a subsystem malfunctions, a mild danger is detected (so the drone is requesting a decision), or a serious danger is detected (so the drone has made the decision to abort).

16.8 Inspection, Maintenance, and Repair

After assembly, the drone will need to undergo a number of tests before it can become operational. Every attachment point will need to be inspected and tested, and all subsystems will need to be booted up and assessed. All sensors will need to be calibrated and tested, and the rotors will be spun up. It is also very important that the communication network is set up properly with the base network and that this is tested to ensure that the drone can communicate with the base.

Regular inspection and maintenance will be required throughout the operational life of the drone in order to find and fix any small problems. A certain amount of inspection will be carried out on Earth (see Section 16.9), mostly from analyzing subsystem data and checking for anything unexpected. Of course, it is important for the crew to inspect the drone physically as well. The estimated inspection schedule can be seen in Section 18.2, sorted by inspections that occur every flight, every 10 flights, and every 100 flights. If any (small) problems are identified as part of these inspections, maintenance will be carried out as needed. Of course, if a problem is identified sooner (for example, the power connection to an instrument is lost and it is no longer responding), maintenance will be carried out before any other flights take place. Because of the way in which the UAV is assembled, it will be relatively straightforward to remove the sub-assemblies which require maintenance. Therefore, the maintenance protocols satisfy requirements **GO-01** and **GO-02**.

Any required repairs which surpass what is expected for regular wear and tear should begin with contacting the ground support team on Earth and discussing the damage with them. This should result in a repair strategy that can be carried out using the available tools and materials at the base.

16.9 Earth Operations (During Operational Life)

As mentioned, a ground support team will be present on Earth throughout the mission to support the crew at the base with the operation of the drone. This team will be knowledgeable about the design of the drone, and in particular about the structures and software. They will be the first point of contact for the crew if any issues arise that cannot be answered by the instruction manuals. If problems do arise, they will communicate with the crew to understand the problem and to help arrive at a solution. They will have access to a mock-up/double of the drone which they can test and analyze to better understand the crew's issues. They will also have access to the software installed on the OBC and will be able to write and send updated code if any bugs are ever discovered or if the software is ever improved. They will regularly check the drone's logs, diagnostics data, and instrument data for any potential problems.

Since the purpose of this mission is scientific in nature, an important stakeholder in this mission is the scientific community. The scientific data collected during expeditions will regularly be sent back to Earth. This data will be organized and then made available to researchers upon request to the main party, via the mission website. It will be provided in a raw format with additional information on how, when, and where the data was collected on Mars. The data will include visual images, height map data, atmospheric gas measurements, underground ice deposit measurements, and the results from dust composition measurements and soil sample measurements. Planetary scientists working with the main party will also likely publish regular reports in which they analyze the data and summarize the most important scientific findings. This process satisfies requirement **STN-05**.

16.10 End of Life Operations

After it has been determined that the cost of continuing the mission outweighs the possible benefits of keeping the mission going, the mission will have reached its end. For more details on the post-mission operations, please refer to Chapter 20.

On Mars

It is likely that the end of the mission will be caused by the failure of one or more components of the drone; in this case the penalty of continuing the mission may be extensive repairs or a set of entirely new parts, which may be considered too high of a cost to continue the mission. However, it is also likely that several instruments or sensors may still be operational at end of life. Since Mars has very limited resources and because sending parts to Mars is costly and energy-intensive, the drone is designed to be dismantled after it retires. This will allow the crew to access instruments and other parts which may be useful for other applications. For example, the laser airspeed sensors may be installed at the base to help with monitoring and recording local weather conditions, or the propeller motors may be repurposed in any number of ways. Designing the mission in this way ensures that resources are used in the most sustainable way possible, thereby satisfying requirement **STN-08**.

On Earth

Some final steps will be taken by personnel on Earth to close out the mission. All of the data, scientific and otherwise, collected during the mission will be stored and archived. The entire mission will be reviewed, and the successes and shortcomings will be assessed. These will be published in one or more reports authored by personnel from the main party and from the design team.

17 System Description

This chapter presents a description of the final drone design. The outcome is based on the combination of the subsystems described previously. First the final configuration is presented followed by the hardware and software block diagrams and finally the technical drawings of the design.

17.1 Final Configuration

17.1.1 Internal

The internal layout of the final drone design is presented in Figure 17.1. It serves as an overview of which internal components are located where on the design.

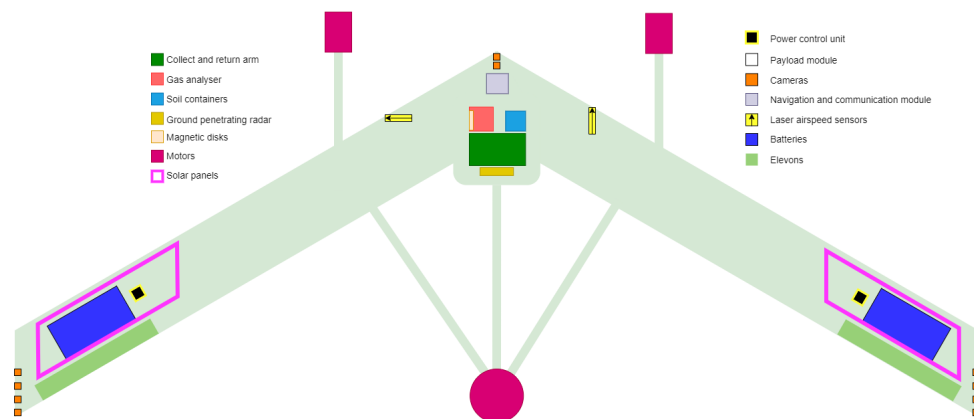


Figure 17.1: Internal layout overview

17.1.2 External

The external geometry and dimensions geometry of the final design are presented in Table 17.1. The mass of the final design contains a 5% margin in order to account for additional mass due to wiring as well as potential increase in mass of subsystems later in the design process.

Table 17.1: Overview of final system

Parameter	Value
Wing Airfoil	GOE 430
Wingspan (tip to tip)	16.08 [m]
Dihedral	3 (degrees)
Wing Chord	0.613 [m]
Sweep Angle	19.15°
VTOL Prop Radius	2.9 [m]
Forward Prop Radius	2.0 [m]
Fuselage Length	1.35 [m]
Total Drone Mass	106.2 [kg]
Launch Frame Mass	56.6 [kg]
Ground equipment	69 [kg]
Maintenance	43.3 [kg]
Beacons	60 [kg]

The table presents the outcome of the sizing code which contained the calculations done for subsystems as described in previous chapters.

17.1.3 Resource Budgets

In Table 17.2 the values from the mass and peak power budgets are compared to the values obtained in the subsystem analyses to check their compliance to the budgets set up in Chapter 4.

Table 17.2: Comparison of the mass and peak power budgets excluding margins with the values obtained from the analyses

Subsystem	Mass [kg]		Peak Power [W]	
	Budget	Analysis	Budget	Analysis
Structures	17.6	21.9	323	16.6
Propulsion	20.0	21.4	14368	11474
Power	17.7	24.08	323	229
Communications	1.7	1.0	17	20
Thermal Control	3.3	3.5	323	16
Payload	34.0	33.8	150	138.9
Onboard Data Handling	3.7	0.5	646	85
Total	98.0	106.18	16150	11979.5

It can be seen that there is non-compliance in the masses for the structures, propulsion, power and thermal control subsystems. However, of these, the masses for the propulsion and thermal control subsystems are still within their 20% margins. With regards to power, only the communications subsystem exceeds its budget, however, it is still within the 20% margin.

The structures subsystem has a mass of 21.9 [kg], whereas the budget allows it to use a maximum of 21.1 [kg], an increase of 4%. This exceedance is largely due to underestimation of the control surface mass during preliminary sizing. However, since the mass cannot be reduced further at this stage without further analysis, it is deemed acceptable since the design is still feasible.

The power subsystem is 36% heavier than the maximum value of the budget, which is more than the 20% margin. This is largely due to needing more energy for performing the mission than was expected during preliminary sizing. This is because for preliminary sizing only the motor power was sized for, since analysis on other required power for the payload and on-board computers was still ongoing. Exceeding the budget, however, did not cause the design to become infeasible and since there was no other option to reduce the mass it is deemed acceptable.

17.2 Hardware Block Diagram

The hardware diagram displayed below gives an overview of the main components of the UAV and the interrelation and interactions they have with other components. In combination with the 3-D model in the previous section a full picture of the design is obtained.

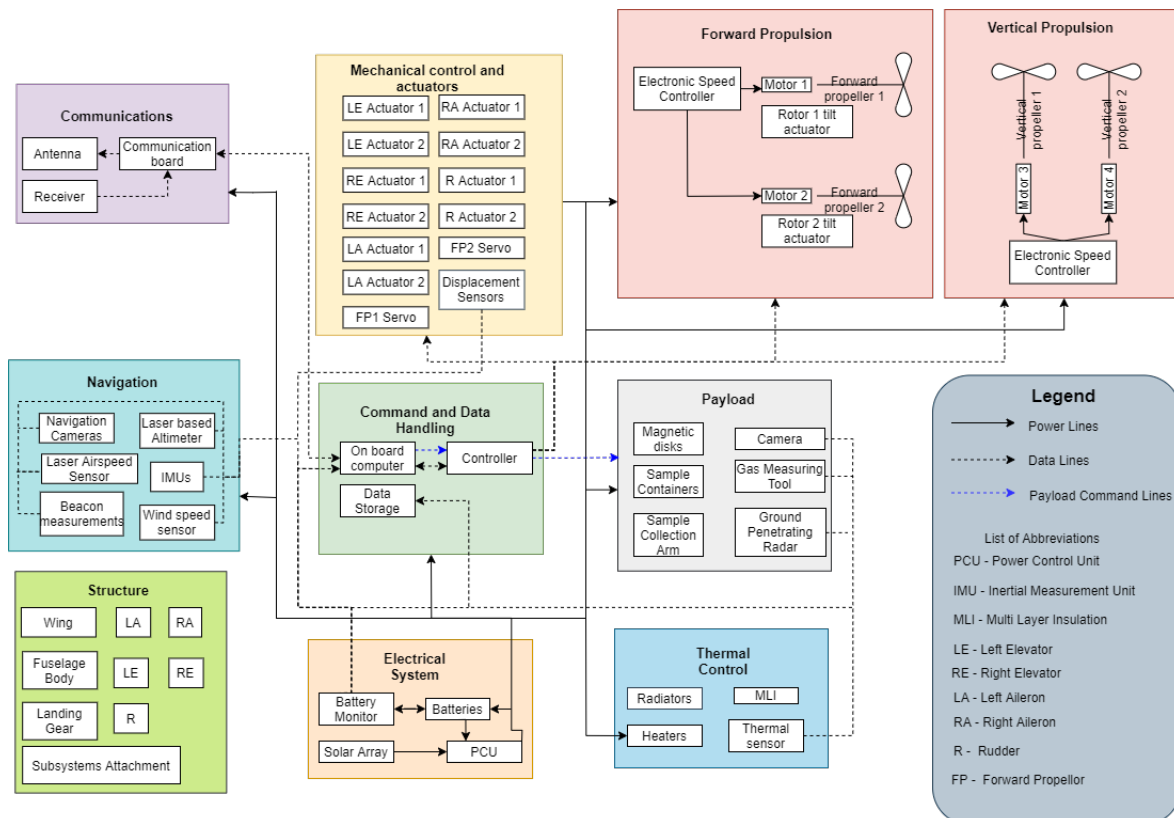


Figure 17.2: Hardware diagram

17.3 Software Block Diagram

The software block diagram visualizes interaction of all the software components that is installed within the drone. As it can be seen from Figure 17.3, on top of each arrow the type of data that is flowing from one software to another is identified. Command data is an input by the user and forwarded to the system via the communication software. Meanwhile navigation software inputs the command and images provided by the camera to identify a flight path for the drone. This information is fed to the control software, which determines the stability and control of the drone. Finally, all this information is sent to command and data handling so that feedback can be forwarded to subsystems, if needed, and communication software to be sent back to the user.

Note that this diagram could have been extended by adding blocks that represent data processing software, such as image mapping software. However, it was previously identified that all the data processing will be performed on the base, in order to reduce the power that is used.

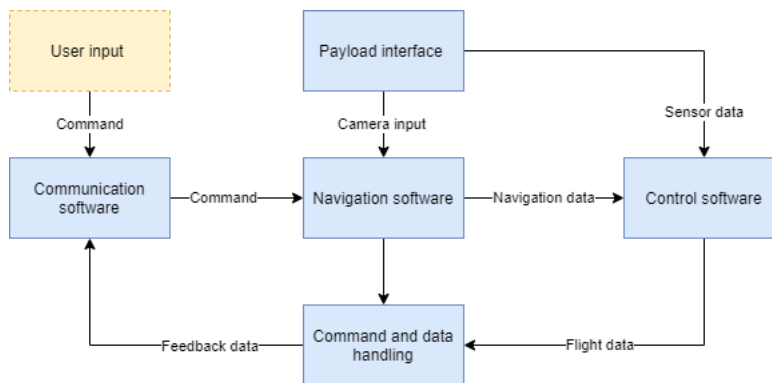


Figure 17.3: Software diagram

17.4 Technical Drawings

To best reflect the external layout of the design a number of technical drawings are made of the design. These show the design in its VTOL and cruise mode.

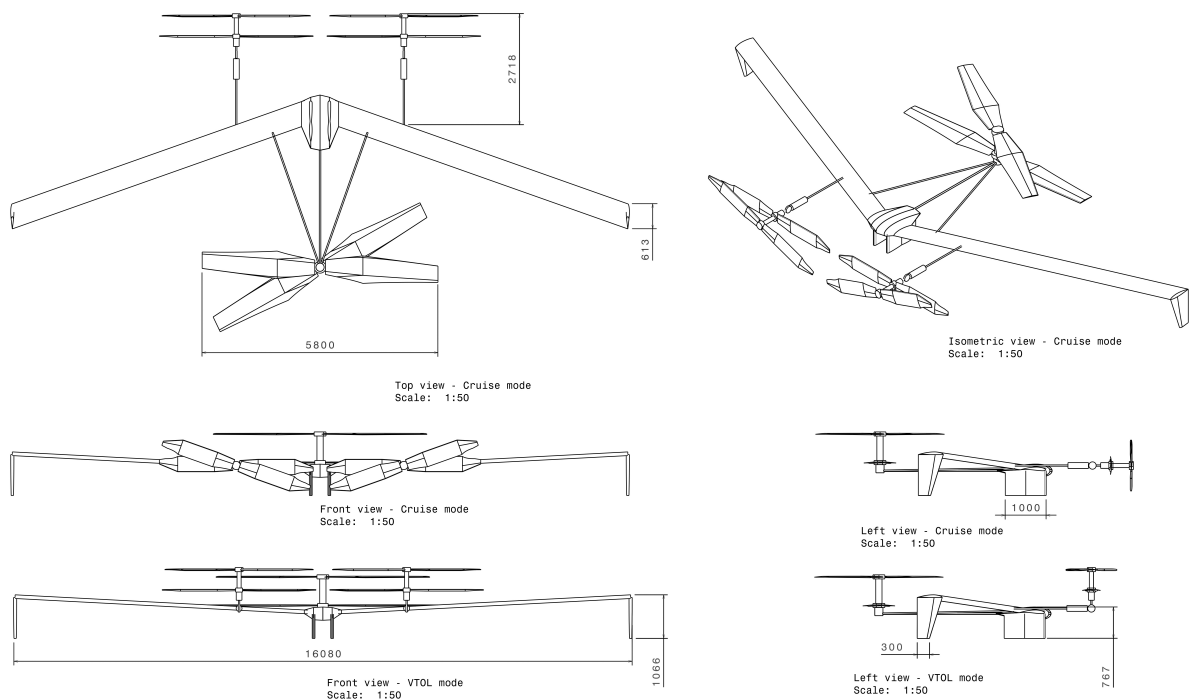


Figure 17.4: Multi-view technical drawings of external layout of design in VTOL and cruise mode (dimensions in millimeters)

17.5 Data Handling Block Diagram

Data handling block diagram is presented in Figure 17.5. This diagram visualizes the components of the data handling system and the interaction between these components. The content of the information that is flowing from one system to another system is identified over the arrows that are connecting the blocks. Furthermore, specifications of the hardware components are also presented within the diagram. The blocks of the diagram is color coded and refers to a specific subsystem, as it can be seen from the legend.

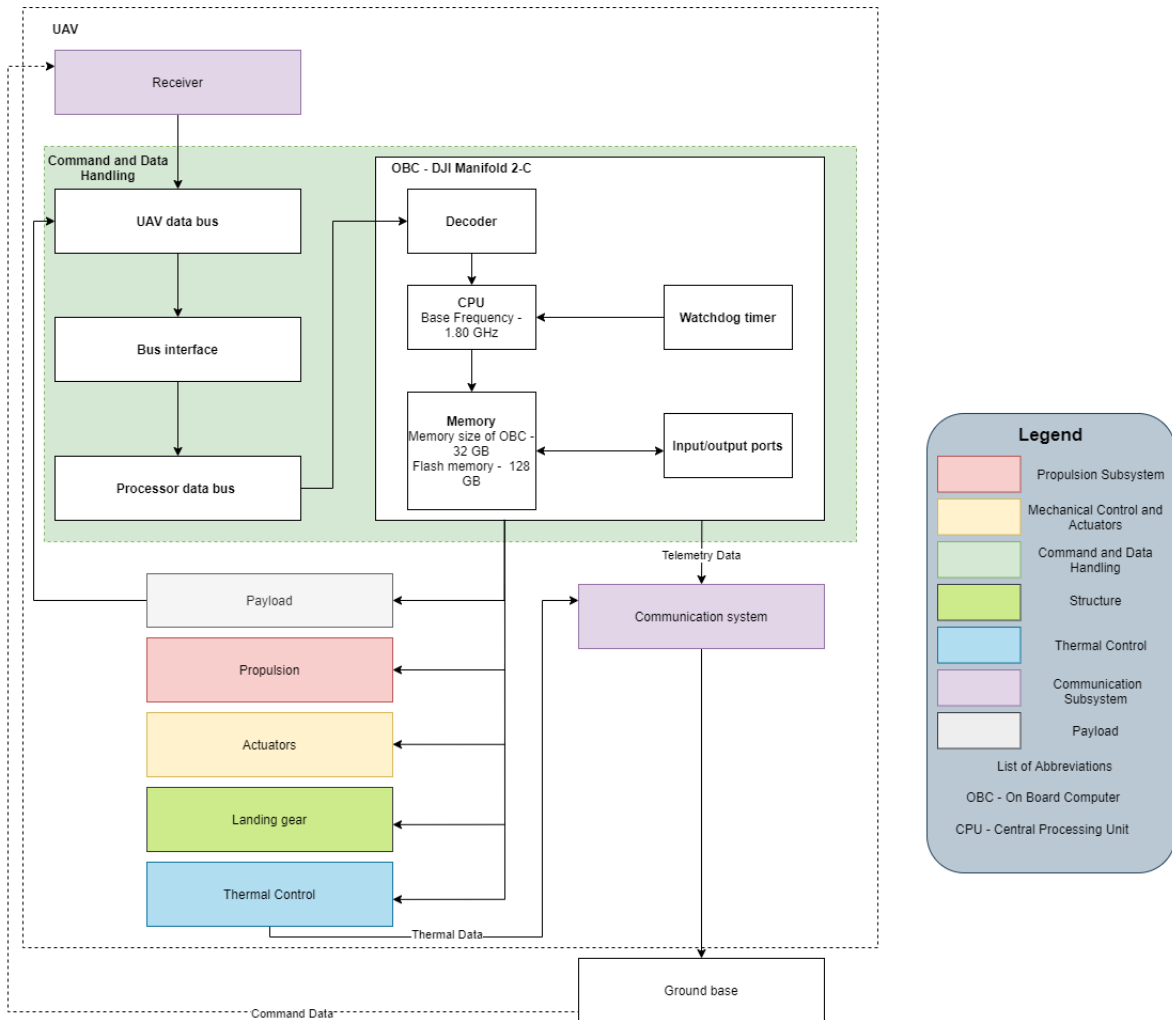


Figure 17.5: Data handling block diagram

18 Analysis of the Final Design

The final design obtained from the detailed design phase has to be evaluated to address some important aspects. Firstly, a sensitivity analysis is performed in Section 18.1 to check the design's sensitivity to the most important input parameters. Secondly, a RAMS analysis is done in Section 18.2 to evaluate the design on Reliability, Availability, Maintainability and Safety. Thirdly, a risk analysis regarding system wide risks is explained in Section 18.3. Finally, the sustainability of the design is evaluated in Section 18.4.

18.1 Sensitivity Analysis

The current version of the design is much more in depth compared to the preliminary sizing available at the start of this phase. However, due to the uncertainty regarding input parameters, a sensitivity analysis will be performed to identify the impact of changing those parameters.

The sensitivity analysis is performed by separately changing the input parameters to a range of inputs, for which the iterator is run for every entry. Since the drone mass has always been the primary output to compare different designs with, since this mass has to be transported to Mars, the mass is plotted versus the increase. The slope of these plots then is the measure of the sensitivity of the design to the changed parameter.

The following parameters were analysed. Firstly the payload mass as this is the main mass that is put into the system, hence, sensitivity to it is important to look at. Secondly the structural mass, due to small mistakes or oversights in subsystem sizing, the subsystem masses can still be a bit off at this phase. Hence, it is important to look at a subsystem and change its computed mass by a percentage. The system chosen for this analysis is the structural subsystem. Finally, the flight altitude should be looked at. The base is not yet built on Mars, hence, it could be that the base is at another location than currently assumed. Since this changes density, mass could be affected due to higher drag at lower altitudes and higher VTOL power requirements for higher altitudes and thus it should be considered.

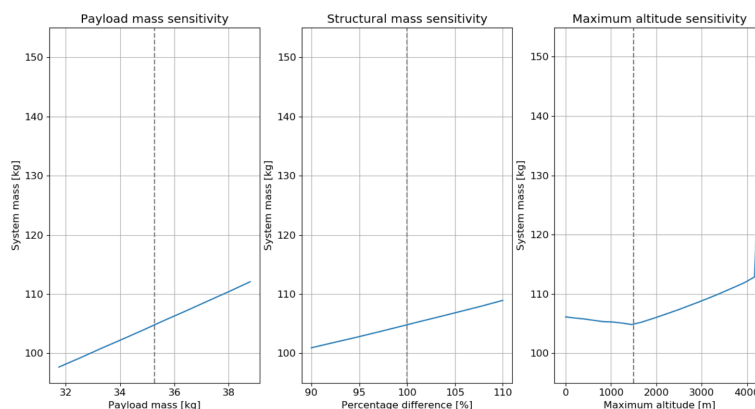


Figure 18.1: Sensitivity analysis of drone mass to the payload mass, structural mass, and flight altitude.

Payload Mass

The payload mass was analysed for a range of -10% to +10% since the payload still has a margin of 10% applied because most payload components were not analysed more in depth in this phase. It can be seen that the design becomes approximately 7% heavier or lighter for an increase or decrease of 10% payload mass. The mass of the design would thus definitely change based on a different payload mass, however, it is insensitive enough that it would not compromise the feasibility of the design.

Structural Mass

The structural mass was also given a range of -10% to +10%, at the start of this phase a margin of 20% was used, however, the analysis performed means the margin can be reduced to 10% [47]. The mass sensitivity to a percentage change in the structures subsystem is less than for the payload mass, approximately a 4% difference for a 10% difference in structural mass. Hence, it can be concluded that mistakes and oversights in the structural program would not cause the drone mass to change to unfeasible values. Since the other subsystems were analysed with the same amount of depth and have similar or lower masses compared to the structures subsystem, these yield approximately the same result.

Altitude

The altitude sensitivity analysis was performed to investigate the limitations for this type of drone design on Mars and evaluate at which base altitudes the design would be feasible. The analysis showed that the design quickly becomes unfeasible beyond an altitude of 4 [km] above the vertical datum. In fact, at these high altitudes the code stopped converging due to the fact that the vertical rotors were no longer able to produce sufficient thrust for take-off.

It is important to note that the shown masses for the lower altitudes are lower in reality as some of the Reynolds number improvements at low altitudes were not included in the sensitivity analysis.

18.2 RAMS Analysis

RAMS is an analysis that is performed in order to assess the reliability, availability, maintainability, and safety of the product. The main purpose of the analysis is to reflect whether or not the product requires improvement in terms of these points.

18.2.1 Reliability

Reliability of UAV depends on each subsystem and conditions they are operating in. In space missions, it is possible to expect a failure due to environmental conditions, design issues, quality of the components and operational problems. In Figure 18.2 reliability analysis of a satellite mission from 1985 is presented [62]. Looking at the characteristics of this mission and the development of space technology, a qualitative comparison between the satellite mission and the UAV can be performed. Since there is limited data, reliability due to environmental conditions and design is mainly considered for the comparison.

- **Navigation:** For the satellite mission navigation is performed using navigation satellites and the payload on board [62]. Meanwhile navigation of the UAV is dependent on various components, such as IMU, cameras, antenna and laser altimeter. Therefore, navigation is in series configuration with other subsystems. This indicates that failure of one subsystem results in failure of another [161]. For instance, if the antenna is lost due to dust storms, navigation cannot be performed as antenna has been in use for positioning. As a result the navigation subsystem becomes more sensitive. This would decrease the reliability even more than it is presented in Figure 18.2. In order to avoid significantly low reliability rate, redundancy philosophy is applied to these components. In Section 18.2.4 the actions that are taken to make these systems redundant is explained in more detail.
- **Power:** It is assumed that long lasting rechargeable lithium ion batteries were used in the reliability calculation of the satellite mission, since it is a commonly chosen battery for satellites [48]. However, since 1980's lithium ion batteries have been under development. With the enhancing technology everyday new methods to increase the health or efficiency of the batteries are being researched [33][136]. Furthermore, considering that the UAV will operate in the future and more advancements will be achieved by then, it is feasible to state that reliability of the power subsystem of the UAV will be higher.
- **Thermal:** Thermal subsystem is a very complex subsystem that is related to every component within the system. Therefore, it is expected to have a lower reliability compared to other subsystems, as it can be seen in Figure 18.2. Looking at the components used for the thermal subsystem it is feasible to state that same trend follows for the UAV mission as well. However, due to the complex nature of the subsystem, it would not be accurate to make an educative guess or comparison.
- **Communication:** The communication subsystem on board of the satellite consisted of a parabolic antenna [62]. Therefore, it requires accuracy for pointing. This reduces the reliability of the subsystem as if the accuracy is not provided the communication can malfunction. Since an omnidirectional antenna is in use the pointing is not a problem. However, it is expected for the antenna of the UAV to encounter harsh dust storms on the surface of the Mars.
- **Structures:** The UAV used a safety factor of 2 while sizing the structural components. This is an advised value for space missions; therefore, it is assumed that the satellite used the same value. However, while calculating the structural reliability of the satellite, separation mechanisms and deployment devices are regarded additional to primary structure [62]. When there are multiple stages present, the reliability tends to drop as the overall reliability is obtained by taking the product of the reliability of the individual stages [166]. Due to this structural complexity, it is expected to have a higher reliability than the satellite mission.

Note that it is possible to obtain more accurate results. In order to do so the failure rate of each subsystem must be known, along with the duration of operation. So that Weibull function can be used to obtain the reliability. Therefore, the failure rate can be obtained from the manufacturer or from a statistical data set, if that exact subsystem was used in previous mission.

18.2.2 Availability

Availability of the UAV indicates to what extent the UAV is operational throughout the mission duration. It is expected to have a reduced availability during various actions. For instance, while the maintenance checks or repairs are being performed. During maintenance checks of small components are taking place, such as the antenna, availability is not affected significantly. This is due to two main reasons. First, checking these components does not take as much time as inspection of bigger components. Secondly, since these components do not occupy much space during launch more than one can be launched. Therefore, in case of a serious maintenance issue the component can be replaced with a spare one and repaired separately. By doing so it will be aimed to increase the availability of the drone.

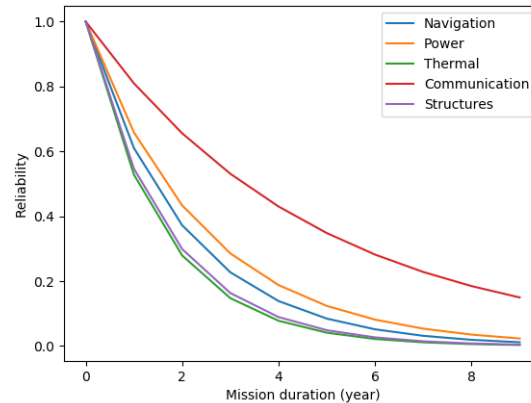


Figure 18.2: Reliability of a satellite mission [62]

18.2.3 Maintainability

Components within the UAV will require maintenance during its operational lifetime. These include both scheduled and non-scheduled maintenance. First the scheduled ones are performed as inspection. If the result of the inspection indicates that a component is malfunctioning, then non-scheduled maintenance is performed. While determining the frequency of scheduled maintenance, various considerations were made. First, it was identified how critical the component is for the functioning of the drone. For instance, if the batteries fails the mission cannot be carried out as the power distribution of the whole UAV is dependent on them. However, if the robotic arm fails only the collect and return mission profile fails, meanwhile the UAV is still operational for imaging. Secondly, the durability of the component was considered. Some components were built with a redundancy philosophy. For instance, a safety factor of 2 is applied to structural components. Therefore the structural components are built two times stronger than needed for carrying the applied forces. By doing so, unexpected loads are accounted for. Therefore, the main body and other structural components are durable and require less frequent maintenance. Below is a list of components sorted by how often they will be inspected; these numbers are approximate (order of magnitude) and may need to change depending on the results of testing the design.

- **Every flight:** Camera (height mapping and visual imaging), Antenna, Battery level, Dust composition magnets, Solar panels, Laser altimeter, Rotor blades, Electronic speed controller, Electric motors
- **Every 10 flights:** Coolant levels, Landing gear inspection, Wing surface inspection, Battery health, Thermal control sensors, On board navigation system, Power control unit, Weather sensors
- **Every 100 flights:** Robotic arm inspection, Wiring harness inspection, Wing structure inspection, Update drone firmware, Update control station software, Main body inspection

18.2.4 Safety

It should be ensured that when a system or function within the drone fails, the environment and people operating the drone do not get harmed. In order to guarantee safety, it is significant to identify the safety critical functions of the drone. These functions need to be treated with a redundancy philosophy so that the when failure occurs during operations, the outcome is not critical for the safety. As a result, for instance two on board computers are used. One being the master computer and the other one being the backup that is monitored by the watchdog timer to detect certain failures. In the list found below, safety critical functions are presented, along with the applied redundancy philosophy.

- **Vertical rotor:** (-)
- **Wing box:** During the design phase safety factor of 2 is used.
- **Main body:** During the design phase safety factor of 2 is used.
- **Landing gear:** During the design phase Euler buckling stress with a safety factor is taken into account.
- **Propeller carrying beams:** During the design phase safety factor of 2 is used.
- **On board computer:** 2-computer set up is designed, Therefore, if one fails during flight, all non-critical processes stop, the working computer takes over critical functions and aborts the expedition immediately. Both computers have access to software for critical functions.
- **On board antenna:** Two antenna are used, one on each wing.
- **Navigation camera:** Total of 10 cameras are included, counting the payload camera. They have bit of overlap in their fields of view. This indicates that losing 1 camera does not oppose a significant problem for autonomy, as remaining components can still be enough to operate.
- **Drill:** It is expected to observe As this tool will wear down much quicker than on a rover missions many spare drill bits are sent to Mars.
- **Thermal sensor:**
- **Power control unit:** Backup electrical distribution network for specific components.

- **Battery:** Reserve time of 2h is taken into account while designing with an 80% battery capacity in order to obtain an extended li-ion battery lifespan during operations.
- **Solar panel:** Conversion 20% losses are taken into account.

Note that the redundancy philosophy is not applied to vertical rotors. Making the vertical rotors redundant in common sense and adding extra vertical rotors would require a redesign of the whole structure since currently there is no place to put spare components. Furthermore, it would make the drone heavier and introduce more drag. However, the propulsion system is designed to be single point failure free. Such that, failure of one component does not result in loss of the UAV. More on this can be found in Chapter 13.

18.3 Risk Analysis

The technical risks applicable to the different subsystems have already been described in the relevant chapters. The risk analysis presented in this section will thus not repeat the subsystem risks and will include only the risks applicable on a system wide level. However, the risk map does include both the system wide risks and the subsystem risks, in order to ensure that all risks have sufficient mitigation strategies. Note that the definitions of the levels used is given in Chapter 10, where the first subsystem risks are already presented.

18.3.1 General Risks

- **GR-1 Materials not able to withstand Martian environment**
 - **Effect:** Can lead to structural damage which could cause systems to malfunction.
 - **Probability:** Mars has highly abrasive and fine dust suspended in its atmosphere [89], so this is characterized as **Probable**.
 - **Severity: Critical**, effects could lead to mission failure.
 - **Mitigation:** Choose suitable materials that have been tested to withstand the harsh environment on Mars. Assess the suitability of weather conditions before performing flight too.
 - **Effect of Mitigation:** The mitigation procedure is thought to only have an effect on the probability, lowering it from **Probable** to **Occasional**. The severity is not affected since structural damage is still as severe.
- **GR-2 Sudden increase in solar activity**
 - **Effect:** Can lead to a power surge damaging electrical components or lead to direct radiation damage.
 - **Probability:** Spikes in solar activity occur on a time frame of 154 days [121], which is closely monitored by satellites, meaning this risk item is characterized as **Occasional**.
 - **Severity: Critical**, effects could lead to mission failure, due to electrical components being broken or damaged.
 - **Mitigation:** Carry on board power surge protectors, and carefully monitor solar activity before and during the mission to decide whether flight abort is necessary.
 - **Effect of Mitigation:** The mitigation procedure only has an effect on the severity, decreasing it from **critical** to **Marginal**. Solar activity itself is not affected by the mitigation procedure.
- **GR-3 Dust storm occurring during flight**
 - **Effect:** Can reduce visibility greatly making navigation difficult or impossible, as well as potentially blow the UAV off course due to high wind speeds. Both of which could lead to a crash.
 - **Probability:** Large dust storms on Mars occur on an annual basis, especially in Mars' southern hemisphere [91]. This means that this risk item has an **Occasional** probability.
 - **Severity: Catastrophic**, as outlined in effects the event could lead to a crash.
 - **Mitigation:** UAV needs to be able to perform an emergency landing procedure or return to the base depending, where it can be stored for protection. The UAV also has to be able to assess weather conditions during flight, in order to perform the abort sequence in a timely manner.
 - **Effect of Mitigation:** The mitigation will have an effect on the probability as well as the severity, this is due to the UAV being grounded when a dust storm is detected. Thus reducing the probability of a dust storm occurring during flight to **Rare**. Due to the emergency landing or abort procedure the severity is reduced to **Marginal**.
- **GR-4 UAV contamination**
 - **Effect:** Can invalidate the obtained soil samples.
 - **Probability:** Spacecraft are thoroughly cleaned before they are launched, making contamination improbable, however astronauts could contaminate the UAV while performing maintenance. Thus this item is given a **Rare** probability.
 - **Severity: Marginal**, since the mission is not looking for signs of life the effects would only invalidate the soil samples partly.
 - **Mitigation:** Thoroughly clean the spacecraft before launch. Astronauts need to decontaminate when performing maintenance and extracting the ground samples.
 - **Effect of Mitigation:** Due to the decontamination performed before handling the UAV, or the soil samples the probability of contamination is reduced to **Improbable**.
- **GR-5 Incorrect Assembly**
 - **Effect:** Depending on what was assembled incorrectly effects can range from a minor inconvenience for example due to being unable to use a certain scientific instrument until it is fixed, to loss of the drone

- due for example the autonomy system being given incorrect information by a wrongly installed sensor.
- **Probability:** Incorrect assembly stems primarily from human error. Since human error was the cause of multiple failures in the past [86], the probability of this risk is **Probable**.
 - **Severity: Critical**, since the effects could lead to mission failure, but not necessarily.
 - **Mitigation:** Create and execute an in depth product validation and verification procedure. In phase 2 a start was already made on creating this plan and in this report the plan is expanded upon in Chapter 19.
 - **Effect of Mitigation:** The probability of a human error itself occurring is not changed by this mitigation strategy. However, by performing the product validation and verification mistakes can be corrected before launch, reducing the chance that a mistake possible of causing mission failure is still present at launch. Hence, probability is reduced to **Rare**.

- **GR-6 Drone Software Errors**

- **Effect:** Software errors or bugs in any of the on board software could cause the drone to not function properly. If the errors are in critical flight systems it could even lead to loss of the drone.
- **Probability:** Software errors stem primarily from human error and too little testing of the software. Since human error was the cause of multiple failures in the past [86] and since the project has a tight schedule, the probability of this risk is **Probable**.
- **Severity: Critical**, since the effects could lead to mission failure, but not necessarily.
- **Mitigation:** Create and execute an in depth product validation and verification procedure with respect to testing of software. A start on procedures to test software has been made in this report in Chapter 19.
- **Effect of Mitigation:** The severity is not changed. The probability is reduced to **Rare** due to the same reasoning as for GR-5.

18.3.2 Transportation Risks

- **TR-1 No sufficient launchers available**

- **Effect:** Would lead to the team having to design their own launch vehicle capable of transporting the UAV or wait for an applicable launcher to become available, which would lead to scheduling problems and cost overruns.
- **Probability:** The spacecraft is expected to be far below the maximum payload mass of all available launchers and is expected to fit in an existing Mars atmospheric entry module, so this item is given a **Improbable** probability.
- **Severity: Critical**, as lined out in effects this event would lead to major cost overruns and scheduling issues.
- **Mitigation:** Discuss with the customer about including time and cost contingency in the development plan for the case that no applicable launcher is available for the planned launch period.
- **Effect of Mitigation:** The mitigation procedure only serves to lessen the severity to **Marginal** due to the cost and time contingencies, it has no effect on the probability.

- **TR-2 UAV is damaged during transportation**

- **Effect:** Can lead to the UAV being unable to perform its mission due to broken components or inability to perform the final assembly on Mars.
- **Probability:** This item is given a **Occasional** probability based on the need of transporting and landing the drone in a disassembled state attached to a frame.
- **Severity: Catastrophic**, the event could damage vital components thus leading to possible mission failure.
- **Mitigation:** Make use of highly experienced personnel that ensures the UAV is secured when integrated with the launcher. Furthermore, create and perform product validation and verification procedures aimed at testing the frame and attached sub-assemblies under launch and Mars atmospheric entry and landing conditions.
- **Effect of Mitigation:** The mitigation procedure only affects the probability of the event, since securing the UAV does not decrease the damage done if it were to break loose. The probability is reduced to **Improbable**

- **TR-3 Explosion of the launcher**

- **Effect:** Direct mission failure.
- **Probability:** Launcher explosions are **Rare** occurrences, due to the high reliability of launch vehicles [59].
- **Severity: Catastrophic**, would lead to direct mission failure.
- **Mitigation:** Pick a launcher with a success rate of at least 90%. Furthermore the UAV could also be insured by an entrusted insurance company.
- **Effect of Mitigation:** A reliable launch vehicle will reduce the probability to **Improbable**, and the insurance will lessen the financial blow of a failed launch reducing the severity to **Critical**.

18.3.3 Risk Map

The system wide risks and subsystem risks are presented in a risk map in Figure 20.2, where the risks under initial probability and severity are shown in Figure 18.3a and the risks under mitigated circumstances in Figure 18.3b. It can indeed be seen that there are no dangerous risks left after mitigation.

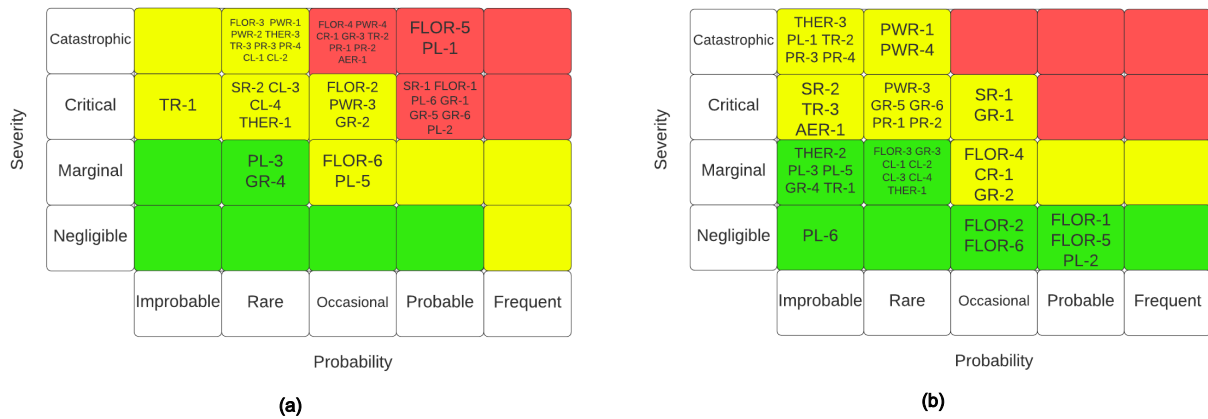


Figure 18.3: Initial risk map displaying all technical risk items (a), and risk map displaying all technical risk items after mitigation procedures have been implemented (b)

18.4 Sustainability Analysis

The sustainability requirements were included in this design process to ensure that any negative impacts on the Earth and Mars environments are minimal. The requirements arose from a sustainability analysis in the Baseline Report [1], which identified relevant sustainability issues for each stage of the mission, whether they are related to environmental, social, or economic issues (the three pillars of sustainability). After listing these requirements, a short discussion about their compliance is presented below.

18.4.1 Requirements and Constraints

The top-level and lower-level sustainability requirements for this mission are listed in Table 18.1. Each requirement’s indicated compliance (given in the table’s rightmost column) is explained in the next subsection.

Table 18.1: Requirements related to ground operations and their expected compliance

Index: DME-REQ-	Requirement	Compliance
TL-SUST-01	The design shall not use any hazardous/toxic materials.	Satisfied
TL-SUST-02	The design shall minimize the environmental impact of an UAV on Mars.	Satisfied
TL-SUST-03	The design shall have maximum material re-usability after the end-of-life.	Satisfied
STN-01	At least 15% of the materials used in the design (by mass) shall be from recycled sources.	Satisfied
STN-02	The process of manufacturing the design shall not involve any toxic/hazardous processes which would endanger the production workers past the threshold set by local guidelines.	Satisfied
STN-03	All parts, components, and peripheral equipment which are part of the design and which are to be delivered to Mars shall be sterilized on Earth before launch such that the entire UAV is restricted to a surface biological burden level of ≤ 30 spores.	Satisfied
STN-04	Information about the sustainability risks and impacts of the mission shall be made publicly available via the mission website, media coverage, and social media posts.	Satisfied
STN-05	The scientific data resulting from the mission shall be made available to scientists and scientific institutions for which this data is relevant to research.	Satisfied
STN-06	During the operational phase, components of the UAV relating to soil collection shall be sterilized at the base such that these components are restricted to a surface biological burden level of ≤ 30 spores before they are used for soil collection purposes.	Satisfied
STN-07	The design shall not leave behind any stray material on the Martian surface during mission operations.	Satisfied
STN-08	It shall be possible for the operators on Mars to disassemble the UAV to access reusable components after end-of-life.	Satisfied
STN-09	The instruments and sensors used on the UAV shall have expected minimum lifetimes of 2 years.	Satisfied
STN-10	All parts, components, and spares needed to sustain the mission for 10 years shall be included in a single launch vehicle.	Satisfied

18.4.2 Discussion

As can be seen from the indicated compliance column, this design is expected to meet all of the sustainability requirements which have been set out. This is an important achievement, since it ensures that carrying out this mission will result in an acceptable level of impact on the environment.

Requirements **TL-SUST-01** and **STN-02** are met through the choices in materials. The primary materials used for the body, structures, and propeller blades of the UAV (and its supporting ground equipment) are aluminium and carbon fibre reinforced polymer (CFRP). The production and processing of these materials is well understood, well established, and is not particularly dangerous. Much of the rest of the mass of the UAV comes from the batteries, the power system, and the payload instruments, which will not require any unusual or dangerous materials (there are no radioactive elements, for example).

ability risks (since there are still some risks, despite the precautions taken) and potential impacts are included in media and on the mission website. The mission website can also be used as a hub for scientists to request access to the scientific data collected during the mission which they can use for their research.

It is assumed that the production facility in which the drone components are built and prepared for launch will be equipped with sterilization equipment, since sterilization prior to launch is a standard process for space vehicles. Therefore, the design will be able to comply with requirement **STN-03**. In Chapter 16 it is assumed that sterilization equipment will already be present at the base. This is a safe assumption as contaminated samples have little to no scientific value; thus, ensuring all sample collection equipment is clean is an important step. As a result of this assumption, completing requirement **STN-06** will not be an issue.

During flight operations, the aircraft is designed to not leave behind any stray materials or shed any parts. The only cases in which this would happen is if the design were to crash on Mars or if a component suddenly came loose. However, the drone has been designed to try to make such occurrences extremely rare, so it can be said that the design complies with requirement **STN-07**.

An important aspect of the mission is that the aircraft can be assembled when it arrives on Mars. As a result of this, completing requirements **STN-08** and **TL-SUST-03** at the end of the aircraft's life will not be an issue. The design is inherently easy to disassemble, making accessing components quite simple at the end of the mission life.

When addressing requirement **STN-09**, care was taken to select components and instruments that have high reliability, and thus minimum expected lifetimes of 2 years. Requirement **STN-10** is also satisfied by the design presented in previous chapters. This is because, when selecting components and instruments, not only the mass of the instrument but also the mass of all the instrument spares were taken in to account. This means, if a gas analyzer is twice as heavy as another gas analyzer but also four times more reliable, the heavier instrument would be chosen. This is because in the grand scheme of the mission, this is a more efficient allocation of resources.

Satisfying requirement **TL-SUST-02** follows from the compliance with all of the other Mars-related sustainability requirements. This design does not leave any stray material on the Martian surface, it makes use of no non-renewable resources for its operation, and proper measures are taken to prevent forward contamination of the surface as well. Together, these aspects of the design mean that requirement **TL-SUST-02** is satisfied.

19 System Verification and Validation

In this section the verification and validation is done on a system level, in contrast to the compliance matrices given in the different subsystem chapters, which only give requirements and the compliance to them on subsystem specific level. The integration of all subsystem code modules is also verified. Hence, in Section 19.1 the verification of the fully integrated model is described. Furthermore, the system requirements are given in the compliance matrix in Section 19.2. This section also gives a feasibility study on requirements that are not yet expected to be complied with. Furthermore, Section 19.3 describes the methods to validate the integration of the final product before it is actually sent to Mars.

19.1 Verification of Subsystem Code Modules Integration

As described in Chapter 6, all programs written for the subsystems were combined into one iterative loop. The code modules for all subsystems were already written in functions and classes and at this point they have already been verified on their own. Hence, all the functions take inputs and provide verified outputs. The verification of the full model thus follows straightforwardly that only the iterative loop has to be verified.

Convergence Test

As the loop iterates over the mass of the design it must be verified that the final outcome of the code converges to the mass of the final design. The sizing code is given an initial total mass and the total mass is updated with each iteration. In order to avoid an infinite loop the code is terminated once difference between the previous mass and current mass is less than 0.005. In order to test the convergence the initial input mass was varied. With an initial input mass of 80 [kg] the code converged to a final mass of 106.88 [kg], where an input mass of 120 [kg] converged to 106.89 [kg], confirming that the code converges to the final system mass.

Inputs Verification

The inputs were also verified. By checking every module that no global variables were defined that were used by the function instead of an input, it could be verified that the inputs of the iteration loop were actually used. Furthermore, before the final run of the code to obtain the final values described in this report, it was double-checked that the defined inputs actually were the most up-to-date numbers. Finally, the input masses were set to the values from initial sizing, to make sure that converging would not take to long. Using these tests it was verified that the iteration loop uses the correct input values.

19.2 Compliance Matrix and Feasibility Analysis

Beside the compliance matrices already given and evaluated in the chapters on the different subsystems about the subsystem requirements, there are system-wide, top-level, requirements that need will need a more in depth verification in the following phases. Methods to verify these requirements are given in Table 19.1.

Table 19.1: Compliance matrix of top-level requirements and compliance according to the current state of the analysis. A method to verify the requirements in future phases is also provided

Index: DME-REQ-	Requirement	Verification Method	Compliance
TL-PR01	The design shall assess access to remote area with 100 [m] swath width.	Demonstration that the imaging camera can achieve the required swath width at the surveying altitude	Satisfied
TL-PR02	The design shall provide visual imaging over an area of 50 [km ²].	Analysis using a combination of range and swath width (while choosing a route which complies with the available turn radius)	Satisfied
TL-PR03	The design shall provide visual imaging with 10 [cm] resolution.	Test that the imaging camera can achieve the required resolution by flying it to surveying altitude and setting up marks to check the images	Satisfied
TL-PR04	The design shall provide height mapping with 10 [cm] ground resolution.	Testing that the height mapping achieves the required resolution by flying it to surveying altitude and imaging a test setup	Satisfied
TL-PR05	The design shall provide height mapping over an area of 50 [km ²].	Analysis using a combination of range and swath width (while choosing a route which complies with the available turn radius)	Satisfied
TL-PR06	The design shall be able to measure dust composition up to 4 [km] in the atmosphere measured from Martian ground level at the base.	Analysis by determining the service ceiling of the design	Satisfied

TL-PR07	The design shall be able to measure particle size distribution up to 4 [km] in the atmosphere measured from Martian ground level at the base.	Analysis by determining the service ceiling of the design	Satisfied
TL-PR08	The design shall be able to monitor trace gas emissions at a 500 [m] resolution.	Analysis based on the flight velocity and achievable frequency of gas samples	Satisfied
TL-PR09	The design shall assess remote areas for shallow ground ice deposits up to 10 [m] depth.	Analysis based on the specifications of the GPR and the satisfied soil ground composition on Mars	Satisfied
TL-PR10	The design shall assess remote areas for shallow ground ice deposits with 10 [cm] resolution.	Analysis based on the specifications of the GPR and the expected soil ground composition on Mars	Satisfied
TL-PR11	The design shall semi-autonomously collect and return single soil samples up to 100 [g].	Analysis of autonomy systems and soil collection systems and their integration	Satisfied
TL-PR12	The design shall semi-autonomously collect and return single soil samples up to 50 [km] from the base.	Analysis of the semi-autonomous navigation and control system	Satisfied
TL-PR13	The design shall semi-autonomously collect and return single soil samples in a height range of -1 to 2 [km] measured from Martian ground level at the base.	Analysis of service ceiling and flight operations systems	Satisfied
TL-PR14	The design shall collect and return soil samples up to 500 [g] when human controlled.	Analysis of the drill and soil containers	Satisfied
TL-PR15	The design shall collect and return soil samples up to 10 [km] from the take-off location when human controlled.	Analysis of the range in human controlled scenario	Satisfied
TL-PR16	The design shall collect and return soil samples in a height range of -2 to 4 [km] measured from Martian ground level at the base when human controlled.	Analysis of the service ceiling and power requirements	Satisfied
TL-PR17	The design shall collect and return subsurface samples up to a depth of 10 [cm].	Test the soil collection system on comparable soil on Earth keeping in mind the worse heat radiation on Mars	Satisfied
TL-PR18	The design shall be able to detect dust particles of 1 [μm] in radius.	Test the scientific instruments in a wind tunnel or vacuum chamber on Earth	Satisfied
TL-SFTY-01	The design shall be single point failure free.	Analysis of the subsystems and components required to avoid mission failure	In doubt
TL-SUST-01	The design shall not use any hazardous/toxic materials.	Inspection of materials used in the design	Satisfied
TL-SUST-02	The design shall minimize the environmental impact of an UAV on Mars.	Analysis of the expected environmental impact	Satisfied
TL-SUST-03	The design shall have maximum material re-usability after the end-of-life.	Inspection of which materials could be reused after disassembly	Satisfied
TL-BDG-01	The choice of launcher shall be based on existing/foreseeable launchers.	Inspection of the launcher used	Satisfied
TL-BDG-02	The design shall comply with the launcher payload restrictions as stated in the launch vehicle catalog.	Inspection of the dimensions and mass of the launcher payload	Satisfied
TL-BDG-03	The design shall withstand launch loads.	Test the design by subjecting it to the expected loads and vibrations	Satisfied
TL-BDG-04	The design shall withstand entry/landing loads.	Test the design by subjecting it to the expected loads	Satisfied
TL-OPE-01	The design shall be able to be disassembled into sub-components.	Demonstrate by performing the disassembly	Satisfied
TL-OPE-02	The design shall be able to be transported in its disassembled state.	Demonstrate by transporting the design in a mock-up fairing	Satisfied
TL-OPE-03	The design shall allow unloading and assembly by 3 astronauts within 24 hours.	Demonstrate by allowing 3 astronauts in suits to assemble the design on Earth with the same tools as available on Mars	Satisfied

DME-REQ-TL-SFTY-01

As can be seen in Table 19.1, the only top-level requirement currently in doubt is DME-REQ-TL-SFTY-01, the design shall be single point failure free. As a result the requirement and interpretation of it was discussed with the customer. The interpretation was first that every system should have a sort of backup such that the mission can be finished even if a single point had failed. However, since some systems would have a significant increase in mass, it could make the design infeasible due to the snowball effect. The outcome of the discussion was that this interpretation could be nuanced a bit. Instead of requiring that the mission can be finished, the requirement should

be interpreted as no failure may cause the end of the mission in terms of losing the aircraft or sustaining irreparable damage. This is reasonable because if the drone cannot take-off anymore from a remote location due to a failure, it can still be repaired on-site or after retrieval. With the new interpretation it is feasible again to meet the requirement in the future. Modifications will need to be done to the software to make sure it can recognize more types of failures of different subsystems both while standing on the ground or in flight. Furthermore a more in depth analysis into the propulsion and control will need to be done to make sure the drone can still land if a motor has failed.

19.3 Product Validation

After the top-level requirements are verified, the product should also be validated before launch to show that it can be used in the intended situations. The focus is less on proving the design can meet a requirement, but more on proving that the integration of all subsystems can actually perform the required mission.

Software

The software to be used by the drone should also be verified and validated. For this different mission scenarios will be simulated to test whether the software and hardware is able to perform them successfully. Furthermore, it should also be given inputs that are not deemed very likely or even impossible in order to test the robustness of the system.

Integration of the software and hardware should also be validated. First off, it will be validated on a mock-up that the onboard computer and other electrical components are able to run the software fast enough such that it is able to perform all mission scenarios. Secondly, the setup can be placed on a different drone on Earth to validate that it can actually successfully pilot the drone. This testing has to be performed on a different drone, since the design is only properly designed for Mars conditions.

There are a few parts to validate regarding the software and hardware integration on the version to be sent to Mars. Firstly, the integration of internal hardware and the actuators and motors will be validated in order to check that parameters such as motor rpm or control surface deflection are what they are expected to be. Secondly, the inputs from sensors will be put into the software to validate that the software indeed returns the correct outputs and that there are no mistakes in orientations or units.

Structural

Structural tests will have to be performed to validate that the design can actually handle the loads and that it can survive enough loading cycles for the entire mission duration. The scope of these tests will depend on the maturity of the design. Tests on material specimen will have to be done first to validate that the material that will be used has properties close enough to the values used for the code. If this is the case or after the design has been modified, tests on sub-assemblies will be done. These tests function to validate that all failure conditions have been taken into account for the sub-assembly. The final tests aimed at validating the structural design, is to build a full-scale prototype, and test at which loads it fails. A second model will be made to test on fatigue, in order to validate the lifespan.

The version to be sent to Mars is obviously not tested too thoroughly, as to prevent damaging the structure with the tests. It will be carefully examined for micro-cracks in the aluminum and ply rupture or voids in the CFRP.

The design for the frame for landing the components on Mars also has to be validated. The timeline will look approximately the same as for the main design. Specimen tests will have to be performed, but since it is likely that the same aluminum will be used as for the body of the drone, it could be that no additional tests will have to be performed. Furthermore, since the frame is practically one assembly, no sub-assembly tests will have to be performed as well. A full-scale test will need to be performed tested on the loads and with mock-up parts suspended in it for a shake test.

Again, the version to be sent to Mars does not require full-scale tests, but will need careful examination for manufacturing damage.

Communication

Since the ground communication system is created as part of the design, the ability of performing end-to-end communication between the drone and the ground communication system is already verified. However, the system can still be stress tested to test its robustness to unlikely or impossible mission scenarios. Furthermore, the interface between the ground communication system and the base infrastructure does have to be tested, which can be done by testing with a simulation.

The beacons and design to be sent to Mars should also be tested. It will be validated that the communication between the beacon network and the drone works properly. Furthermore the positioning system of the drone based on the beacon network can already be tested and validated on Earth.

Aerodynamic Interactions

The current aerodynamics are simulated in XFLR for the wing, body and winglets. The other components are seen as separate sources of parasite drag. In order to validate the aerodynamic performance of the design a wind tunnel test or an in depth CFD analysis must be performed. To ensure the data gives comparable results with the expected performance in the martian atmosphere the tests should be performed at the same Reynolds numbers. This can be achieved by using a scaled down model of the drone or decreasing the airspeed during the test (or both). This method for validation will also assist in quantifying the exact stall characteristics of the final design

which is beneficial for flight performance. Furthermore, it will need to be validated that aerodynamic interactions from attachments not currently modeled, do not have a detrimental effect on the aerodynamics.

Since the wing box and beams on which the propulsion systems are attached are from CFRP, care should be taken that the required smoothness of the surface is achieved. Hence the version to be sent to Mars will have the aerodynamic parts checked for smoothness.

Propulsion

The performance of the propulsion rotors must be validated to ensure that the expected thrust can be achieved in the martian environment. These tests must be performed at comparable conditions. For the VTOL operations a vacuum chamber can be used to test the rotor thrust. For the forward thrust during cruise a wind tunnel must be used in order to simulate the incoming flow.

Additionally, the propeller blades must be validated in a method similar to that for the structural subsystem. Exact models will be made in order to test the propeller blades for fatigue and ultimate loads. The final blades (to be sent to Mars) will be inspected.

Payload

The scientific instruments on the payload must also be validated to work over the course of the entire mission. For off the shelf systems instruments such as the camera operating temperatures and expected lifetimes have already been evaluated. However, for systems such as the soil collection arm and the particle collection magnet system validation procedures must be performed.

The dust particle collection system must be tested to last a given number of cycles (depending on how often the customer would like to perform dust collection missions).

The electronics and drill of the soil collection arm have already been somewhat validated as the same mechanism as the arm of the Perseverance mission is used. However, the dimensions of the arm have been adjusted to fit the needs of the drone which requires some additional analysis to ensure reliability of the arm with the updated dimensions.

Thermal Control

Validation of the thermal control integration in the assembled body will need to be performed to make sure there are no heat sources that have been overlooked. Since it will be difficult to test realistic mission scenarios, due to the different conditions on Mars, the product validation tests are primarily aimed at measuring heat produced by the components on the version that will be sent to Mars. Heat dissipation of the cooling solutions can also be performed in a vacuum chamber to test with the correct atmospheric conditions.

Power

There are three main components of the power subsystem which will be tested on Earth. Firstly, the solar panels will be tested at the expected light intensity to validate that they produce the expected power. Additionally, by testing the solar panels over a longer period of time the degradation can be modeled. Secondly, the batteries will be tested at the expected operating temperatures to validate their efficiencies and capabilities in the martian environment. Finally, the power processing unit will be connected to the battery, solar panels and a number of instruments that require power in order to validate its ability to distribute power over the systems in the drone.

Off-the-Shelf Components

Detailed validation of off-the-shelf components is not necessary since the manufacturer will provide specifications. However, to limit the chance of there being faulty parts in the final design, the off-the-shelf components should be powered on before the on Earth assembly. The goal being to validate that the components can actually perform the specifications that were provided by the manufacturer. Additionally, small tests should be performed on Earth to ensure that for example; the cameras in the winglets are installed at the correct angles.

20 Project Design and Development

The Project Design and Development focuses on the future outlook of this project. The first section focuses on the progress of the whole project starting with the finalization of the design and ending with the conclusion of the mission. In the second section, the project Gantt chart is presented in which the information from the project design and development logic is placed on a timeline. Next, a production plan is presented for the design, encompassing the work that needs to be done on Earth and on Mars. The focus of this section is how the final design can be manufactured, assembled, and integrated for delivery to the customer. The last section in this chapter is a cost breakdown of the mission. This includes an overview of the costs of the different components of the mission, including margins.

20.1 Project Design and Development Logic

The project design and development logic shows the logical order of activities to be executed in the post-DSE phases of the project. Using the finalized design as a starting point, a work flow diagram from design choice to the final mission review is presented in Figure 20.1. The flow is split into 4 phases. These are: (A) the final design and manufacturing phase; (B) the system assembly, integration and testing, and launch phase; (C) the operations and sustainment phase; and (D) the closeout phase [29]. In Figure 20.1 the associated years with these phases are displayed in line with those displayed in Section 20.2.

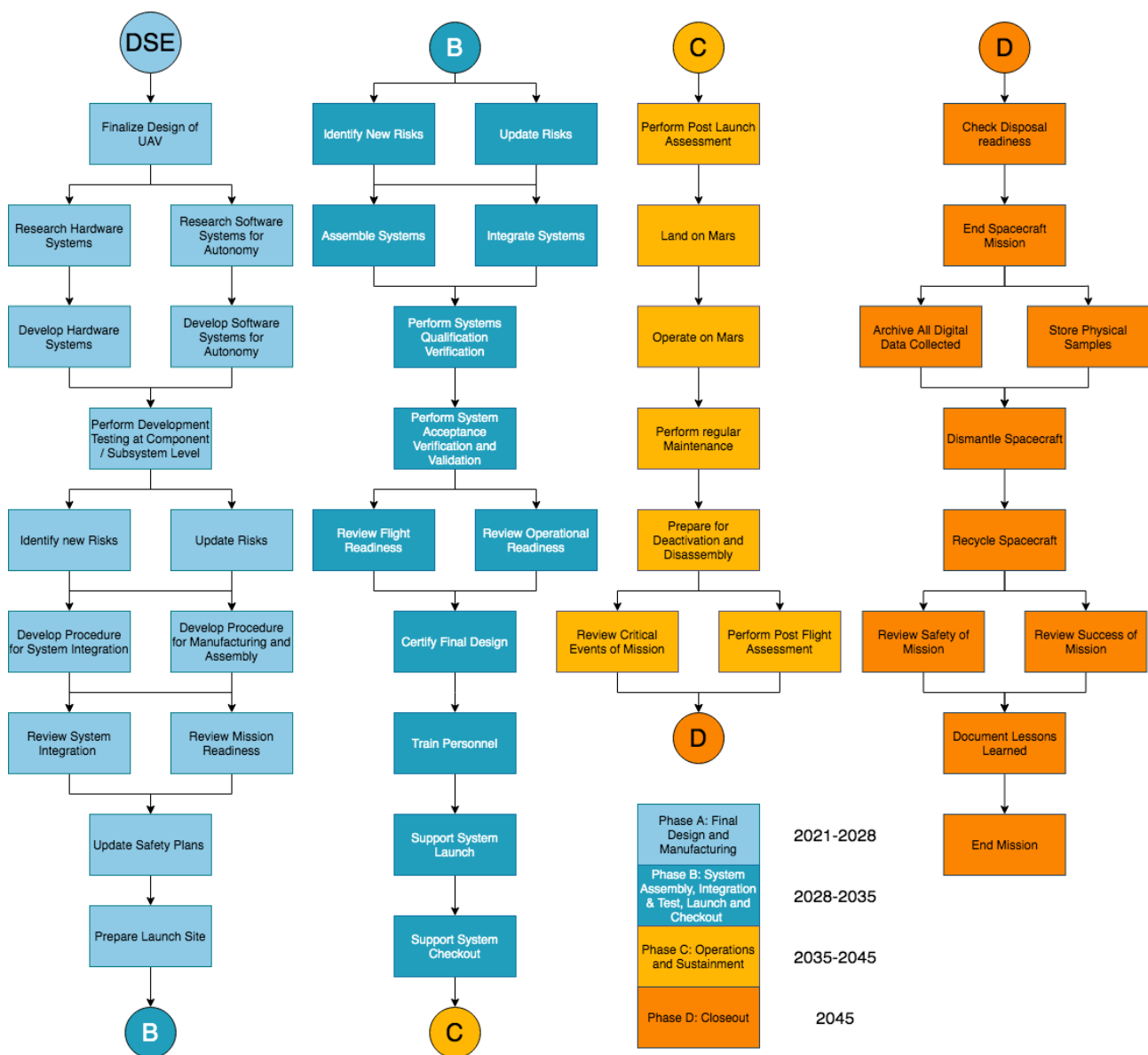


Figure 20.1: Project design and development logic flowchart

In phase A, the design is finalized and manufactured. This phase encompasses the final steps in the DSE and the initial steps after the DSE. It starts with finalizing the design of the drone. After this, the research and development of the specific hardware and software systems associated with the design are carried out. The largest part of the

software will likely be focused on implementing the autonomous aspect of the vehicle required by the top-level requirements. After this, testing will be done at a component and subsystem level. It is typical for spacecraft missions to not build many prototypes, as this would be too costly. Instead, testing is done at each breakdown level of the product throughout the post design phase. Next, a procedure is defined for the UAV systems' integration, manufacturing, and assembly. Integration is checking if all the individually tested systems work together. Based on this plan, the mission readiness and systems integration can be reviewed in parallel to ensure all mission goals are being completed. Lastly, the safety plans are updated based on knowledge gained throughout the phase and the launch site is prepared.

Phase B covers the steps from system integration to launch. After another risk update, the UAV systems are assembled and integrated according to the procedures stipulated in phase A. Then the systems qualification verification is performed, including tests in simulated Martian conditions. System acceptance verification and validation includes end-to-end testing of Earth and Mars ground segments and onboard systems. Once the final design is certified, activities shift towards preparing manuals and handbooks and training personnel to operate the systems. The final activities of phase B are to support system launch and checkout (showing the launch system did what it was meant to do), leading into phase C.

Phase C encompasses the life cycle from launch to end of the mission. The main part of this phase is the operations on Mars and the maintenance. The operations block is related to the main need of the mission which is to fulfil the top-level scientific requirements. These are performing expedition flights on Mars and using the scientific payload to collect the data required to explore new areas that were previously inaccessible. To do this successfully, all the collected data for critical flight events must also be reviewed and post-flight assessments are performed. Regular maintenance must be carried out on the craft to ensure it functions effectively for its full expected lifetime.

The mission is closed out in phase D. It starts with checking if the mission has achieved the goals set at the beginning of the mission, taking into account changes or updates along the way. Once this is established, the UAV's mission is ended. However, the mission as a whole is not finished. First, all the digital data collected in the form of visual imaging, height mapping, gas tracing, and underground visual imaging is archived. At the same time, all the physical samples collected are stored in an appropriate manner. After this, the UAV itself is dismantled and the resources that result from this are recycled for use by the base crew. This ensures sustainability is accounted for while closing out the mission. The final steps before the mission as a whole is ended are to review the safety, successes, and shortcomings of the mission and document all the lessons learned.

20.2 Project Gantt Chart

In this section, the Project Gantt chart is given. The program used for this is Wrike, since this is one of the few planning programs that is able to cover a timeline of more than 30 years, which is necessary for this mission. This Gantt chart shows a schedule for the activities that have to be carried out in order to perform the mission. This covers the same timeline as in the previous section, as can be seen in Figures A.1 and A.2. Please note that the sub-tasks of C.2 as well as sub-tasks C.3.1 to C.3.4 should span the full length of the C.2 and C.3 blocks. This isn't shown in the diagram due to the inability to make tasks of more than 4 years in the Wrike software.

20.3 Production Plan

In relation to Section 20.1, the production plan fits into phases A and B. The focus of the production plan is the manufacturing, assembling, and integrating of the UAV. Integration is not explicitly mentioned in the top layer of the production plan, however it is included within the phases. Integration takes place at two stages between the components and subsystems and also between the subsystems and system level. An example of this integration process could be for the propulsion system. On a component level, the rotor blades and the motor are manufactured by contractors. Then, the components are transported to a shared location and integrated to form the propulsion subsystem. The plan is heavily based on NASA and ESA manufacturing plans [46, 29]. One important block to note in the manufacturing phase is the "send and assign contracts for components." In this phase specialized companies are given contracts to build the scientific equipment required. For example, NASA has a longstanding partnership with Honeybee robotics for building robotic arms for space.

As a result of the fully assembled UAV not fitting in the launch vehicle, it is transported to Mars in a disassembled state. This can be seen in the last step in assembling and testing. As a result of this, a second smaller production plan is made for when the UAV arrives on Mars. This is displayed below in Figure 20.2b.

20.4 Cost Breakdown Structure

In this section, an estimation of the cost budget for the mission is given. In order to get a clear understanding of the different cost components, a cost breakdown structure is made. This cost breakdown structure is given below in Figure 20.3. Please note that this cost breakdown structure does not include each separate sub-component. However, these separate sub-components will be discussed below for each phase of the mission. First, some elaborate descriptions on the cost breakdown of the different phases is given. This is followed by an estimation of the costs in the fiscal year of the launch. Then the contingency margins are added to these costs, resulting in the final

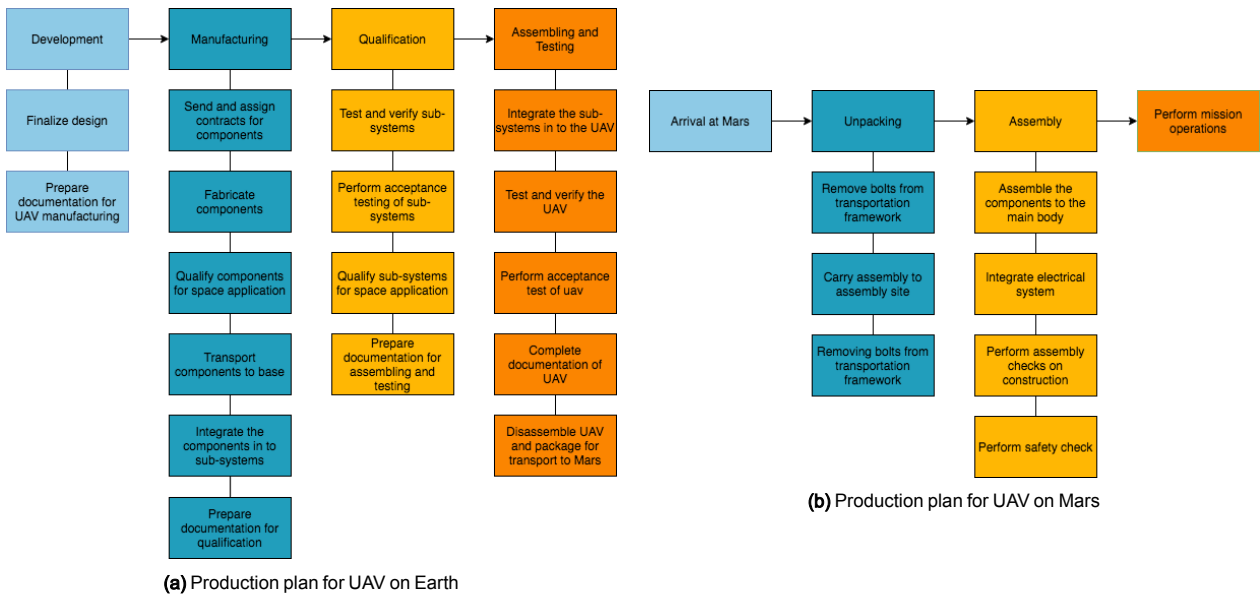


Figure 20.2: Production plans for Earth and Mars

cost estimation. A clear overview of the complete cost breakdown structure including margins is given in Table 20.1.

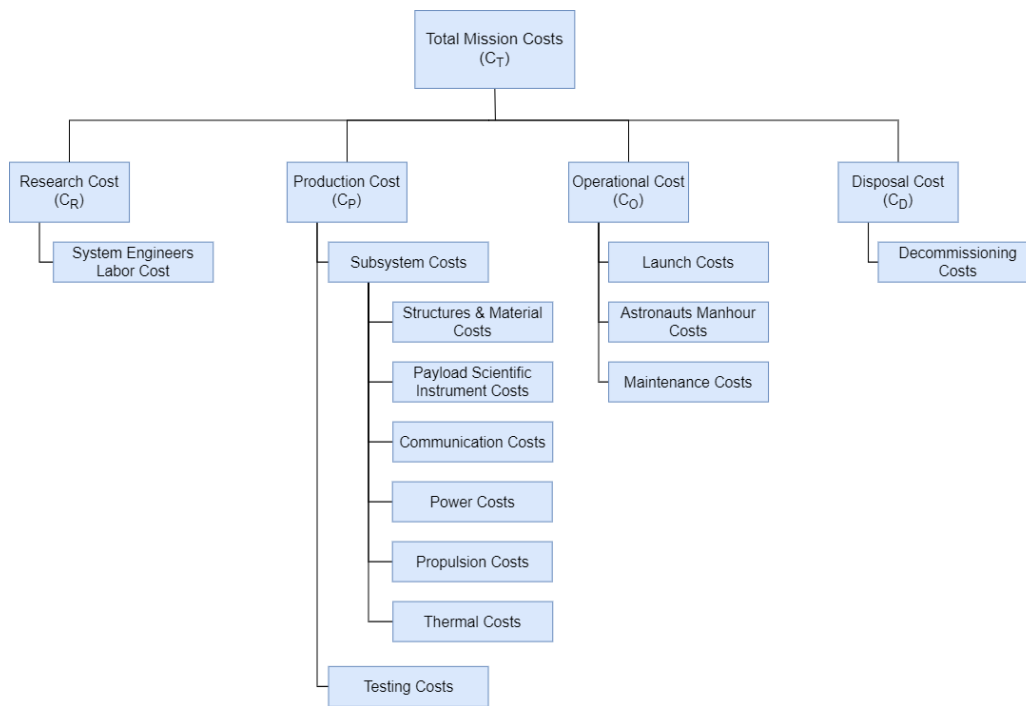


Figure 20.3: Cost breakdown block diagram of the mission

Table 20.1: Cost breakdown table of the mission

Cost Breakdown						
Cost Component	Cost [\$]	Fiscal Year	FY Multiplier	Total Costs [\$]	Margin[%]	Cost with Margin [\$]
<i>System Engineers Labor Cost</i>	11.081.040,00	2021	1	11.081.040,00	10,00%	12.189.144,00
Research Cost	11.081.040,00			11.081.040,00		12.189.144,00
<i>Materials & Structures</i>	1.241,50	2021	1	1.241,50	5,00%	1.303,58
<i>Payload Scientific Instruments</i>	1.253.837,20	2021	1	1.253.837,20	0,00%	1.253.837,20
<i>Communication</i>	266.500.000,00	2021	1	266.500.000,00	5,00%	279.825.000,00
<i>Power</i>	566.869,09	2021	1	566.869,09	5,00%	595.212,55
<i>Propulsion</i>	4.500,00	2021	1	4.500,00	5,00%	4.725,00
<i>Thermal Control</i>	439.165,80	2021	1	439.165,80	5,00%	461.124,09
<i>Testing</i>	865.679.784,31	2009	1,18944449	1.029.678.049,91	10,00%	1.132.645.854,90
Production Cost	1.134.445.397,90			1.298.443.663,50		1.414.787.057,31
<i>Launch</i>	218.000.000,00	2020	1,02	222.360.000,00	5,00%	233.478.000,00
<i>Mission Operations</i>	500.000.000,00	2021	1	500.000.000,00	5,00%	525.000.000,00
Operational Cost	718.000.000,00			722.360.000,00		758.478.000,00
<i>Decommissioning</i>	92.345,00	2021	1	92.345,00	10,00%	101.579,50
Disposal Cost	92.345,00			92.345,00		101.579,50
Total Costs	1.863.618.782,90			2.031.977.048,50		2.185.555.780,81

20.5 Cost Analysis of Different Components

The components must be individually analyzed to obtain a cost estimation for each one. However, due to a lack of information, the costs of some components cannot be found directly. Therefore, an estimation has to be made based on similar components. This leads to an uncertainty in the cost budget estimation. In order to account for this uncertainty, a margin is added to the budget in the next subsection.

20.5.1 Research Cost

The research costs are those incurred during the design phase of the UAV. For this, system engineers are employed to design the UAV subsystems. This includes feasibility studies, mission planning, preliminary design, and detailed design. An average system engineer at NASA has a yearly salary of approximately \$111,000 USD [54]. As an estimate, 10 engineers are expected to be working for 10 years on this research, constantly developing and researching the design. Therefore, the approximate cost for research will be \$11.1 million USD.

20.5.2 Production Cost

The production costs can be divided into two parts: the subsystem costs and the testing costs. The subsystem costs come from the constituent parts of each subsystem. The testing costs consist of the costs that are spent for testing personnel and facilities. The cost estimations for these sub-components are discussed below.

Materials and Structures

For the structural components of the UAV, two materials are used: aluminum 6061 and CFRP (carbon fibre reinforced polymers). These components have to be manufactured, which introduces the manufacturing costs. These manufacturing costs consist of raw material, labor, tooling, equipment, and overhead costs. The manufacturing costs for the UAV are based on mass, namely on cost in [\$USD/kg]. For aerospace-grade aluminum and CFRP, the manufacturing costs per mass are approximately 12 [\$USD/kg] and 85 [\$USD/kg] respectively [98]. Given that the structural masses of these materials used in the design are 5 [kg] and 13.9 [kg] respectively, this results in a total manufacturing cost of \$1,241.50 USD.

Payload Scientific Instruments

In order to execute the mission, the UAV is equipped with a lot of scientific instruments. Some of these scientific instruments are already existing instruments. However, some instruments are specifically for this mission, making it hard to predict their costs. Therefore, the cost of these instruments is estimated based on similar past missions. In order to give a clear overview of the instruments, a table is included below, indicating the costs. The inflation due to the fiscal year and the margins will be discussed in the next sections.

In order to give a better understanding of these cost estimations, the instruments will be discussed individually. The already existing instruments will not be discussed, since these costs are already known. Please note that the sources of these costs are included in the instrument name in the table. However, the instruments that have to be estimated in terms of cost will be discussed below.

The cost of the drill and arm is based on similar components. This is also the case for the soil containers. Due to lack of information on similar components used in past space missions, an estimation will be made from industrial robotic arms. The UAV needs a flight-suitable robotic arm, however, and thus it must be as lightweight as possible. Therefore it is expected that the drill and arm will be approximately 2 times as costly as aforementioned industrial robotic arms. These industrial robotic arms have a cost of \$400,000 USD [72]. Therefore, the cost of the drill and arm for the

Table 20.2: Cost Breakdown of the Payload Scientific Instruments

Payload Scientific Instruments Costs							
Instrument	Amount	Cost [\$]	Fiscal Year	FY Multiplier	Total Costs [\$]	Margin [%]	Cost with Margin [\$]
Drill and Arm	1	800,000	2021	1	800,000	25%	1,000,000
Soil Containers	25	1,000	2021	1	25,000	300%	100,000
Cameras (RunCam 5 Orange) [125]	10	150	2021	1	1,500	5%	1,575
IMU (Bosch BMI088) [132]	2	3.34	2021	1	6.68	10%	7.35
Laser altimeter (LightWare SF30/D) [80]	1	399	2021	1	399	5%	418.95
Onboard computer 1 (DJI Manifold 2-C) [41]	1	1,580	2021	1	1,580	5%	1,659
Onboard computer 2 (DJI Manifold 2-G) [41]	1	1,580	2021	1	1,580	5%	1,659
Computer rack (DJI Manifold bracket) [42]	2	129	2021	1	258	5%	270.90
Servo Motor (D-951TW) [71]	2	470	2021	1	940	5%	987
Thermometer	1	250	2021	1	250	100%	500
Laser airspeed sensor	1	14,580	2021	1	14,580	100%	29,160
Ground Penetrating Radar [157]	1	14,000	2021	1	14,000	100%	28,000
Gas Analyzer [37]	1	12,000	2021	1	12,000	100%	24,000
Magnetic Disks	20	50	2021	1	1,000	300%	4,000
Drill bits [61]	140	400	2021	1	56,000	10%	61,600
Total Costs		846,591.34			929,093.68		1,253,837.20

UAV are estimated to be \$800,000 USD. There is also limited information on the costs of Martian soil sample containers, meaning a large margin will be taken. However, it is known that these containers have to be developed with extreme accuracy. The maximum allowable contamination on the tubes is 15 [ng] [103]. From this, it can be concluded that it is rather expensive to develop these tubes. The sample containers are estimated to cost \$1000 USD each.

Although the technology has been proven, laser airspeed sensors are not currently available as off-the-shelf components. Thus an approximate cost estimate for this sensor can be made by looking at currently available products which use comparable technologies. The laser airspeed sensor consists of multiple components. An important one is the UV laser. The continuous laser that is chosen for reference is the 355nm Solid State Laser, which costs \$11,000 USD. The laser sensor chosen for reference is the DME5000-115 sensor, which is capable of receiving UV lasers. The price of such a sensor is \$3,580 USD [164], which leads to a total price for the laser airspeed sensors of \$14,580 USD. Since not a lot unknown about the development of these sensors, a margin of 100% is taken. The thermometer that is chosen for the UAV is a the same thermometer that is used on the Perseverance Rover and Curiosity Rover. Due to a lack of direct sources on this, a similar thermometer is used for a cost reference: the RGTF-2 thermometer, costing approximately \$250 USD [147]. A margin of 100% is taken for safety.

For the other scientific payload instruments cost estimations are done based on high-end versions of the components on Earth. For example, \$14,000 USD is found to be a realistic price estimate for the ground penetrating radar [157]. A large margin is taken as certifying such a piece of equipment for Mars is likely a challenge. The same logic is applied to the gas analyzer which is also found to be near \$14,000 USD on Earth [37]. The magnetic disks are not very expensive as they are made from samarium-cobalt and are easily found off-the-shelf. The reason a large margin is taken is because the magnets on the UAV require post-processing to carve valleys in the order of magnitude of millimeters into them for effective dust collection. The last components that add significant cost to the payload are the drill bits. It is decided that 140 drill bits will be taken on the mission. This is because the Perseverance rover has a coring tool for 43 samples. If it is assumed that on average 10 samples will be collected per expedition, and there will be 300 flights a year for the entire mission life of 10 years, and that the drill bits will survive 5 times longer than that of the Perseverance rover (as they can be maintained and inspected), then 140 drill bits are needed. The price per bit is based on the price of diamond-embedded bronze drill bits which will be used on the mission [61].

Communication

The communication subsystem requires a space communication network, but also deep space optical communication as an emergency link. This communication network is rather expensive. According to NASA, such a space communication costs approximately \$400 million USD. However, this includes a Deep Space Network, which is not required for this mission. Since DSN costs about \$10,000 - \$15,000 USD per contact, it is estimated that the costs for the communication network will be around \$256 million USD. For the emergency link, deep space optical communication is necessary, which costs approximately \$10.5 million USD, leading to a total communication subsystem cost of \$266.5 million USD.

Power

Three components are needed for the power subsystem: the solar panels, the batteries, and the power distribution system. The first two components are chosen based on currently existing technology. The solar cells are the Spectrolab XTE-LILT Solar Cells [135]. However, no price can be found for these solar cells. That is why the costs for the solar panels are based on a NASA cost estimation for LILT (Low Intensity, Low Temperature) solar panels. It is found that these are approximately 156,522 [USD/m²] [137]. With a solar panel area of 1.685 [m²], this results in a total solar panel cost of \$263,707.83 USD. The batteries are Saft VL51ES Li-ion cell batteries [127]. 21 of these Li-ion cells are needed. However, there is no price to be found on these Li-ion space batteries. Therefore, the cost

of these batteries is estimated based on existing Li-ion batteries, which cost approximately 140 [\$USD/kWh] [25]. With a total energy storage of 5,822 [kWh] for the UAV and beacons, this results in a total battery cost of \$815,080 USD. Finally, the power distribution system is based on regulators and cabling. Using 35 LM76005-Q1 regulators, costing \$2,354 USD each, with a total cabling length of 54 [m], this results in a power distribution system cost of \$82,498 USD [142]. The total cost of the power subsystem is therefore \$347,020.91 USD.

Propulsion

For the propulsion subsystem, the motors for the propellers are the components that size the cost budget. The motors selected for these propellers are the Aveox UT 5025 24P/4 motors [19]. Comparing this motor to other motors, it is estimated that these motors will cost approximately \$1500 USD each [44]. With three motors, the total propulsion subsystem costs will equal \$4500 USD.

Thermal

The thermal costs are based on heaters, thermal sensors, radiators, and insulation. There are two types of radiators, one for the scientific payload in the body structure and one for the motors of the propellers. The radiators used for both the body structure and the motors are the HiPeR radiators produced by Airbus, which cost approximately 500,000 [\$USD/m²] [7]. With 0.87 [m²] total radiator surface area, the radiators are expected to cost \$435,000 USD. For the navigation cameras, 4 heaters are used. These are the SmartHeat SLT Heaters, which cost \$71.95 USD each [92]. This results in a total heater cost of \$287.80 USD. For the insulation, approximately 0.5 [kg] of graphene aerogel is required, resulting in a total insulation cost of \$1378 USD [57]. The thermal sensors that are used are mass airflow sensors, costing approximately \$30 USD each [65]. Using 30 thermal sensors, this results in a cost of \$900 USD. Finally, there are 4 temperature control units. These cost approximately \$400 USD each, resulting in a temperature control cost of \$1600 USD [129]. The total cost of the thermal subsystem cost is \$TBD USD.

Testing

In order to make sure that all the components of the UAV function properly during the mission, these components have to be tested and certified for space. This happens in testing facilities. In order to give a good estimation of the testing costs, previous missions are analyzed. However, there is no cost percentage to be found in terms of testing facility costs. Therefore, it is assumed that the testing costs are part of the total development costs. Looking at the Curiosity Rover, which has approximately the same operational lifetime, these costs are approximately 60% of the total costs. Therefore, it will be assumed that the *Research* and *Production* costs make up approximately 60% of the total mission costs. Adding all the components, the *Testing* costs are then estimated to be approximately \$865.7 million USD.

20.5.3 Operational Cost

The operational cost of the mission depends on the costs of the mission itself. This includes launch as well as costs for the mission operations.

Launch

For the launch of the mission, the Atlas V launcher is selected. Comparing it to the Perseverance Rover mission, the launch is estimated to cost \$243 million USD. However, as already mentioned in Chapter 3, the launch costs are expected to reduce with approximately 25 million USD due to re-usable rocket boosters [130]. Therefore the launch costs are approximated to be \$218 million USD.

Mission Operations

For mission operations, the operational procedures as well as maintenance are taken into account. However, this element of the cost budget is difficult to predict. Therefore, it is chosen to estimate the operational cost of the mission based on similar previous missions. Comparing the operational costs of previous missions with the approximate same goals, it is found that the operational costs are approximately 50 million [\$USD/year] [146]. Since the operational lifetime of this mission is expected to be 10 years, the total operational costs will be approximately \$500 million USD.

20.5.4 Disposal Cost

The disposal costs are the costs that occur at the end-of-life of the mission. This includes the decommissioning. Since the UAV will be mostly recycled and stored for further use, it is expected that the decommissioning costs for the UAV negligible compared to the costs of the mission. The base and the communication network can still be used for further missions, so therefore it is assumed that the decommissioning costs for these components will be zero. For further end-of-life costs, reports have to be written and data has to be published. It is assumed that the 10 system engineers will work on this for about a month. Given their salary, the total costs for disposal and end-of-life are expected to be \$92,345 USD.

20.6 Fiscal Year

In order to account for the variation in the value of money over the years, the fiscal year is taken into account. All of the cost components have been estimated for a certain fiscal year. In order to account for the components that have a fiscal year before 2021, the inflation of the past years must be considered. Since the oldest fiscal year of a component cost estimate (for solar power) is 1994, the inflation over the decades 1990-1999, 2000-2009 and

2010-2019 is taken. The inflation rates for these decades are 3.08%, 2.54% and 1.75% respectively [149]. Looking at Table 20.2, the FY multiplier takes into account these inflation rates, resulting in the total costs per component. To these total costs, a margin is added, which will be discussed in the next section. Please note that some components have a Fiscal Year rate of 1, such as *Power*, since its sub-components have variable fiscal years. The inflation for these sub-components is already taken into account in the total costs.

20.7 Margins

Due to the fact that the mission will take place in the future, a margin is added to the cost budget. This is not only due to the fact that costs will vary over the years, but also that information is lacking on some components. Therefore, some component costs have to be estimated, leading to an uncertainty in the cost budget. Looking at Table 20.1, the margins of the different cost components can be seen. These will be discussed below.

The *System Engineers Labor Cost* component has a margin of 10%. This is because there is not a certainty that the system engineers will work for exactly 10 years with 10 engineers, nor that the salary paid will be the same as for a system engineer at NASA. The *Materials & Structures* component has a margin of 5%. As CFRPs begin to play a bigger role in structural engineering over the years, the price may increase. The *Payload Scientific Instruments* component has a margin of 0%. This is due to the fact that these instruments each have their own margin in Table 20.2. The margin of the *Communication* component is estimated to be 5%. This is due to the fact that a pretty detailed estimation is made based on earlier missions to Mars. The *Power* component has a margin of 5%. This is due to the fact that the power distribution system cost had to be estimated, while the solar cells and batteries are already existing components and thus their prices are known. For the *Propulsion* component, a margin of 5% is chosen. This is based on the fact that there is not a certain price known for the motors that will be used. However, the cost of these motors is based upon similar existing components, resulting in a reasonably precise estimation. The *Thermal* component has a margin of 5%. Since the components of the thermal subsystem have known prices. However, for some of the components, an estimation had to be made. For the *Testing* component, the margin is taken to be 10%. This is because the testing costs are based on the total development costs. This adds another uncertainty in this estimation. Next to that, the testing costs are different for each space mission. The *Launch* costs have a margin of 5%. This is due to the fact that the same launcher is used as for the Perseverance Rover mission. These launch costs are exactly known. However, it can be that the renewable rocket booster might not yet be available, adding uncertainty to this cost estimation. The *Mission Operations* component of the cost breakdown also has a margin of 5%. This is because the mission costs are based on similar (but not identical) previously performed exploration missions on Mars, such as the Curiosity and Perseverance Rovers. Finally, the *Decommissioning* component has a margin of 10%. The reason why this margin is a bit larger is that it is a rough estimation of the costs at end-of-life. It is expected that the components can be re-used, but it is not certain if components will fail during the mission.

20.8 Total Costs

As can be seen in 20.1, the total costs for this mission are estimated to be \$2.032 billion USD. Including the margins, this increases to \$2.186 billion USD. These costs are comparable to those of the Perseverance Rover. The Return on Investment will not be discussed, because this mission is seen as scientific research, resulting only in scientific value rather than monetary value or profit.

21 Conclusion

The purpose of this report was to design and iterate all the subsystems of a drone for Mars exploration. Based on a design option analysis and trade-off, the vehicle was designed to be a VTOL tilt rotor. Each subsystem was designed based on two expedition profiles: a collect and return expedition and a remote sensing expedition. Four conclusions are made based on this report with respect to the four most important subsystems.

The payload suite is capable of performing all the top-level requirements that were set for the design thus surpassing what any satellite or rover has been capable of before. Using a camera with a resolution of 4000×3000 pixels, a frame rate of 60 fps, and a field of view of 72° detailed visual imaging and height mapping can be conducted. A gas analyzer is employed to perform detailed sensing of methane, carbon dioxide, atomic oxygen, ozone, and argon in the Martian atmosphere. Furthermore, a mechanism that uses 20 filter-and-capture magnets allows for extensive dust collection, the analysis of which can be carried out at the base. In addition, a ground penetrating radar is present in the payload suite capable of scanning up to 10 [m] deep at resolutions of 17 [cm]. Lastly, a robotic arm with an ultrasonic drill coring tool is used to collect subsurface samples which are then placed in hermetically sealed containers and also analysed at the base. These instruments have a total mass of 33.8 [kg] prove the UAV's advantages over rovers and satellites.

The drone must be able to perform expeditions either semi-autonomously or under remote human control. Therefore, an autonomy system is required which can plan flight routes, navigate, and make decisions during flight. The primary navigation system to be used is Visual-Inertial Odometry, which is a method of fusing visual camera data with accelerations data to determine position and orientation. Weather monitoring sensors and processes are also included to allow the autonomy system to make real-time updates to its flight path if it detects dust storms on the horizon, for example.

After a thorough analysis of the propulsion subsystem, it was found that extended flight on Mars is possible by overcoming the challenges related to low Reynolds number design. The results of this analysis were that the tilt rotor cruise thrust is 17.5 [N] with an efficiency of 74%, the tilt rotor hover thrust is 55.2 [N] with an efficiency of 50.6% and the vertical rotor hover thrust is 122 [N] with an efficiency of 53.8%. During VTOL each forward propeller requires 2200 [W] and each rear propeller requires 2311 [W]. During cruise, one forward propeller requires 2400 [W]. Based on these values, a brushless DC motor was selected for propulsion with an optimum efficiency torque of 34.27 [Nm] and an RPM between 1500 and 3000. Based on these analyses, the UAV has sufficient propulsion to complete the expeditions laid out in the first paragraph.

Due to its thin atmosphere, the Martian environment presented a myriad of aerodynamics and flight control challenges. The aerodynamic and flight control sizing resulted in a drone with a tip to tip span of 16.1 [m], a sweep of 19° and a dihedral of 3° . The wing has a chord of 0.613 [m] which provides a Reynolds number of 50,000 in the cruise condition. The design decisions made with respect to the aerodynamic shell resulted in the drone being able to carry the payload and perform the expected mission capabilities on Mars.

A number of main recommendations for future research have been identified as vital to the design. To improve the aerodynamics, controllability and propulsion analysis, Computational Fluid Dynamics simulations or wind tunnel tests should be performed for a better understanding of the stall characteristics. For structures, a Finite Element Analysis should be done on the entire structure. Furthermore, more failure cases can be identified and analyzed, for example if one propeller breaks off. For communication, a detailed analysis of the beacon network could be performed by creating a numerical model that considers the limitations due to surface characteristics. The thermal analysis consists of separate analyses and only takes convection into account once. Integrating these analyses and analysing convection would lead to improved results. For improved power analysis, the degradation of the solar and battery cells has to be accounted for. The orientation of the drone during charging can be analysed for optimum solar incidence angle.

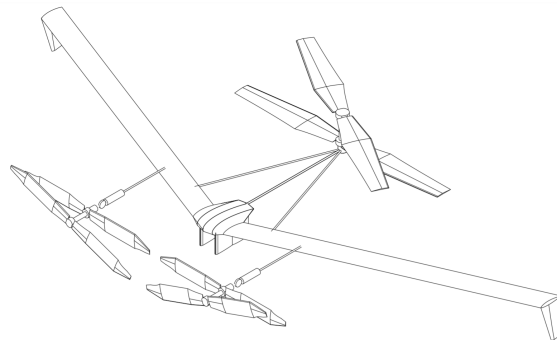


Figure 21.1: Isometric technical drawing of final design in cruise mode (tilt rotors in the horizontal position)

Bibliography

- [1] DSE Group 27. *Drone for Mars Exploration: Baseline Report*. Tech. rep. TU Delft, May 2021.
- [2] DSE Group 27. *Drone for Mars Exploration: Mid-Term Report*. Tech. rep. TU Delft, May 2021.
- [3] DSE Group 27. *Drone for Mars Exploration: Project Plan*. Tech. rep. TU Delft, Apr. 2021.
- [4] United States Naval Academy. *EE302 Lesson 13 Antenna Fundamentals*. 2013. URL: <https://www.usna.edu/ECE/ee434/Handouts/EE302%5C%20Lesson%5C%2013%5C%20Antenna%5C%20Fundamentals.pdf>.
- [5] Aerodesign. *Airfoil Database for Tailless and Flying Wings*. URL: https://www.aerodesign.de/english/profile/profile_s.htm#hs522.
- [6] AGARD. "The Aerodynamics of V/STOL Aircraft". In: (1968). <https://apps.dtic.mil/sti/pdfs/AD0688921.pdf>.
- [7] Airbus Space. *Airbus's space technology gets to Mars with Perseverance*. 2021. URL: https://www.airbus.com/newsroom/news/en/2020/07/Airbus_space_technology_gets_to_mars_with_perseverance_rover.html (visited on 05/10/2021).
- [8] Airfoiltools. *Airfoil Tools*. URL: <http://airfoiltools.com/search/index>.
- [9] Giovanni Alberti et al. "Permittivity estimation over Mars by using SHARAD data: the Cerberus Palus area". In: *Journal of Geophysical research planets* 117 (September 2012).
- [10] Andrea Rusconi et al. "DXTROUS LIGHTWEIGHT ARM FOR EXPLORATION (DELIAN)". In: *13th Symposium on Advanced Space Technologies in Robotics and Automation* (2015).
- [11] B. V. Ratnakumar et al. "Li-Ion Rechargeable Batteries on Mars Exploration Rovers". In: *American Institute of Aeronautics and Astronautics* ().
- [12] Claire E. Newman et al. "Toward More Realistic Simulations and Prediction of Dust Storms on Mars". In: *Decadal Survey on Planetary Science and Astrobiology* (2020).
- [13] Eren Allak et al. "AMADEE-18: Vision-Based Unmanned Aerial Vehicle Navigation for Analog Mars Mission (AVI-NAV)". In: *Astrobiology* 20.11 (2020). PMID: 33179969, pp. 1321–1337. DOI: 10.1089/ast.2019.2036. eprint: <https://doi.org/10.1089/ast.2019.2036>. URL: <https://doi.org/10.1089/ast.2019.2036>.
- [14] United Launch Alliance. *Atlas V Launch Services User's Guide*. 2010. URL: <https://www.ulalaunch.com/docs/default-source/rockets/atlasvusersguide2010.pdf>.
- [15] Peter Annan. *What is Ground Penetrating Radar (GPR)?* 2021. URL: <https://www.sensoft.ca/blog/what-is-gpr/>.
- [16] Eric Apel. *Airbornescience*. 2021. URL: <https://airbornescience.nasa.gov/instrument/TOGA> (visited on 10/10/2018).
- [17] J. Appelbaum and D.J. Flood. "Solar Radiation on Mars". In: (1989).
- [18] Aveox. *8.0" OD 36s32p Series Ultimate Torque Frameless Motors*. URL: https://static1.squarespace.com/static/5931d4becd0f6824d67a243a/t/607a0f26a8c0e02aab2ab3be/1618612007234/Aveox_Ultimate_Torque_Series_80XX-32P_202104.pdf.
- [19] Aveox. *Ultimate Torque Frameless Motors*. URL: https://static1.squarespace.com/static/5931d4becd0f6824d67a243a/t/607a0f861453ca0b05a39c9e/1618612102978/Aveox_Ultimate_Torque_Series_Catalog-50XX-24P_202104.pdf.
- [20] AZUR SPACE. *QJ Solar Cell 4G32C - Advanced*. 2021. URL: http://www.azurspace.com/images/0005979-01-01_DB_4G32C_Advanced.pdf (visited on 06/07/2021).
- [21] Azur Space. *Azur-Space Enabling Technologies*. URL: http://www.azurspace.com/images/0005979-01-01_DB_4G32C_Advanced.pdf (visited on 05/08/2019).
- [22] J. (Bob) Balaram. "Mars Helicopter Technology Demonstrator". In: *2018 AIAA Atmospheric Flight Mechanics Conference*. 2018.
- [23] Rafael Bardera, Suthyvan Sor, and Adelaida García-Magariño. *Aerodynamics of Mars 2020 Rover Wind Sensors*. Mar. 2020. URL: <https://www.intechopen.com/books/mars-exploration-a-step-forward/aerodynamics-of-mars-2020-rover-wind-sensors>.
- [24] Dr. Uri Basson. *Ground penetrating radar*. 2021. URL: <https://geo-sense.com/index.php/methods/ground-penetrating-radar-gpr-surveys/ground-penetrating-radar-gpr/>.
- [25] Battery. *Lithium battery costs have fallen by 98% in three decades*. URL: <https://www.ayesco.ng/lithium-battery-costs-have-fallen-by-98-in-three-decades/>.
- [26] Elena S.f. Berman et al. "Greenhouse gas analyzer for measurements of carbon dioxide, methane, and water vapor aboard an unmanned aerial vehicle". In: *Sensors and Actuators B: Chemical* 169 (2012), pp. 128–135. DOI: 10.1016/j.snb.2012.04.036.
- [27] Rius Billing and Richard Fleischner. "MARS SCIENCE LABORATORY ROBOTIC ARM". In: *European Space Mechanisms and Tribology Symposium* (2011).
- [28] Jasper Bouwmeester. *AE3534 Spacecraft Technology*. [Online; accessed 7-June-2021]. 2018. URL: <https://ocw.tudelft.nl/wp-content/uploads/1.0-Command-and-Data-Handling-Lecture-Notes.pdf>.
- [29] Brian Dunbar. *NASA Program/Project Life Cycle*. 2021. URL: <https://www.nasa.gov/seh/3-project-life-cycle> (visited on 12/12/2019).
- [30] C.D. Browns. *Elements of Spacecraft Design*. American Institute of Aeronautics and Astronautics, 2000.

- [31] Bunting. *Samarium Cobalt Data Sheet*. 2021. URL: https://www.buntingeurope.com/wp-content/uploads/2018/07/BME_Samarium_Cobalt_data_sheet.pdf.
- [32] Dustin Cable. *Would the thin atmosphere and absence of light pollution on Mars make for a fantastic night sky, or would martian dust/twilight spoil the view? Why don't we have broad night-sky pictures?* Oct. 2015. URL: <https://astronomy.com/magazine/ask-astro/2015/10/stargazing-on-mars>.
- [33] Chris Hall. *Future batteries, coming soon: Charge in seconds, last months and power over the air*. 2021. URL: <https://www.pocket-lint.com/gadgets/news/130380-future-batteries-coming-soon-charge-in-seconds-last-months-and-power-over-the-air> (visited on 03/22/2021).
- [34] *Correxit SFII Non-contact optical sensors*. Datasheet. Winterhur, Switzerland: Kistler Group, 2019.
- [35] Fintan Corrigan. *Drone Gyro Stabilization, IMU And Flight Controllers Explained*. May 2020. URL: <https://www.dronezon.com/learn-about-drones-quadcopters/three-and-six-axis-gyro-stabilized-drones/>.
- [36] etalDatta. A. "The Martian Autonomous Rotary-wing Vehicle (MARV)". In: (2000). https://vtol.org/files/dmfile/2000SDC_1_9
- [37] DEMACO. *Residual gas mass spectrometer*. URL: https://www.webshop.demaco.nl/product/residual-gas-mass-spectrometer-with-mass-range-0-200-amu-dual-detector-faraday-and-multiplier/?gclid=CjwKCAjwiLGGbAqEiwAgq3q_mU9gqMPuW0F4Pkkbr6X2_P7SPTjqtqLVJsELeSU0Ti q_hF0nGeX0RoC1v4QAvD_BwE.
- [38] P. H. G. Dickinson. *The Determination of the Atomic Oxygen Concentration and Associated Parameters in the Lower Ionosphere*. London, England: Royal Society, 1980.
- [39] Y. Ding et al. "Automotive Li-Ion Batteries: Current Status and Future Perspectives". In: (2017).
- [40] DJI. *Manifold 2 Series: Product Information*. May 2019. URL: https://dl.djicdn.com/downloads/manifold-2/20190528/Manifold_2_Production_Information_v1.0_Multi.pdf.
- [41] DJI. *Manifold 2-C*. URL: <https://store.dji.com/nl/product/manifold-2?from=search-result-v2&position=1&vid=80932>.
- [42] DJI. *Manifold bracket*. URL: <https://store.dji.com/nl/product/manifold-2-mounting-bracket?from=search-result-v2&position=2>.
- [43] Y. El khchine and M. Sriti. "Tip Loss Factor Effects on Aerodynamic Performances of Horizontal Axis Wind Turbine". In: *Energy Procedia* 118 (2017). 2017 2nd International Conference on Advances on Clean Energy Research (ICACER 2017), Berlin, Germany April 7-9, 2017, pp. 136–140. ISSN: 1876-6102. DOI: <https://doi.org/10.1016/j.egypro.2017.07.028>. URL: <https://www.sciencedirect.com/science/article/pii/S1876610217325547>.
- [44] Electric Motorsport. *Brushless PMAC Motors*. URL: <https://www.electricmotorsport.com/ev-parts/motors/brushless-motors?limit=all>.
- [45] Erica Hupp, Dwayne Brown. *Mars Reconnaissance Orbiter Reaches Planned Flight Path*. 2021. URL: <https://mars.nasa.gov/mro/newsroom/pressreleases/20060912a.html> (visited on 05/19/2021).
- [46] ESA. *Building and testing spacecraft*. URL: https://www.esa.int/Science_Exploration/Space_Science/Building_and_testing_spacecraft.
- [47] ESA. "Margin philosophy for science assessment studies". In: (2012). https://sci.esa.int/documents/34375/36249/15672_Margin_philosophy_for_science_assessment_studies_1.3.pdf.
- [48] ESA. *Nobel-winning lithium-ion batteries powering space*. 2021. URL: https://www.esa.int/Enabling_Support/Space_Engineering_Technology/Nobel-winning_lithium-ion_batteries_powering_space (visited on 10/15/2019).
- [49] ESA. *Who does what in the OCC*. URL: http://www.esa.int/Enabling_Support/Operations/Who_does_what_in_the_OCC.
- [50] The Carlson Law Firm. *How do police detect speeds before making a traffic stop?* Dec. 2019. URL: <https://www.carlsonattorneys.com/news-and-update/police-detect-speeds>.
- [51] Dennis Jack Flood. "Solar Radiation on Mars". In: *Solar Energy* (1989).
- [52] Bruno Gagnon, R. Leduc, and Luc Savard. "Sustainable Development in Engineering: A Review of Principles and Definition of a Conceptual Framework". In: *Environmental Engineering Science* 26 (Feb. 2008). DOI: 10.1089/ees.2008.0345.
- [53] Martin Garland. "Design and implementation of the lightweight advance robotic arm demonstrator (LARAD)". In: *European Space Mechanisms and Tribology Symposium* (2017).
- [54] Glassdoor. *NASA Systems Engineer Salaries*. URL: https://www.glassdoor.com/Salary/NASA-Systems-Engineer-Salaries-E7304_D_K05,21.htm#:~:text=The%5C%20typical%5C%20NASA%5C%20Systems%5C%20Engineer,estimated%5C%20based%5C%20upon%5C%20statistical%5C%20methods..
- [55] I. Pérez Grande et al. "Thermal design of the Air Temperature Sensor (ATS) and the Thermal InfraRed Sensor (TIRS) of the Mars Environmental Dynamics Analyzer (MEDA) for Mars 2020". In: *47th International Conference on Environmental Systems* (July 2017).
- [56] Graphene Supermarket. *Graphene Aerogel*. URL: <https://graphene-supermarket.com/Graphene-Aerogels.html> (visited on 06/22/2021).
- [57] Graphene Supermarket. *Graphene Aerogel*. URL: <https://graphene-supermarket.com/Graphene-Aerogels.html>.
- [58] Håvard Fjær Grip. *Flight Control System for NASA's Mars Helicopter*. Tech. rep. Jet Propulsion Laboratory.

- [59] Sergio Guarro. "On the estimation of space launch vehicle reliability". In: (Nov. 2013).
- [60] Valentyn Halunko. "Space Law: the Present and the Future". In: *Advanced Space Law* 3 (May 2019). DOI: 10.29202/asl/2019/3/3.
- [61] Heiz24. *Rems universal diamond core drill bit*. URL: <https://www.heiz24.de/Rems-universal-diamond-core-drill-bit-UDKB-250x420xUNC-1-1/4-number-of-segments-new?curr=EUR>.
- [62] Myron Hecht Herbert Hecht. *Reliability Prediction for Spacecraft*. Technical Report. Rome Air Development Center (RADC), Dec. 1985.
- [63] R.C. Hibbeler. *Mechanics of Materials*. 10th ed. in SI units. Harlow, United Kingdom: Pearson, 2017.
- [64] Mera Fayez Horne. "Drilling on Mars – Mathematical Model for Rotary-Ultrasonic Core Drilling of Brittle Materials". In: (Fall 2015).
- [65] IST INNOVATIVE SENSOR TECHNOLOGY. *FS2T.0.1E.025*. URL: <https://nl.farnell.com/en-NL/ist-innovative-sensor-technology/fs2t-0-1e-025/sensor-gas-flow-2v-5v/dp/3586997>.
- [66] Jeff Foust. *Space insurance rates increasing as insurers review their place in the market*. URL: <https://spacenews.com/space-insurance-rates-increasing-as-insurers-review-their-place-in-the-market/> (visited on 2011).
- [67] Julien Salomon Jeremy Ledoux Sebastián Riffo. "Analysis of the blade element momentum theory". In: (2020). <https://hal.archives-ouvertes.fr/hal-02550763/document>.
- [68] Grey Hautaluoma Jia-Rufi Cook and Alana Johnson. *6 Things to Know About NASA's Ingenuity Mars Helicopter*. Ingenuity facts. Apr. 2005. URL: <https://www.nasa.gov/feature/jpl/6-things-to-know-about-nasas-ingenuity-mars-helicopter>.
- [69] Shervin Shambayati Jim Taylor Dennis K. Lee. *Deep Space Communications: Mars Reconnaissance Orbiter*. first. Jet Propulsion Laboratory, 2014.
- [70] Ali Bin Junaid. "Design and Implementation of a Dual-Axis Tilting Quadcopter". In: (2018).
- [71] K-Power. *K-Power Hb150t 100kg-Cm Torque Giant Titanium Gear Brushless Industrial Servo*. URL: <https://www.made-in-china.com/showroom/kpower88/product-detailWNXEKFOydqcS/China-K-Power-Hb150t-100kg-Cm-Torque-Giant-Titanium-Gear-Brushless-Industrial-Servo.html>.
- [72] Ken Thayer. *What Is the Real Cost of an Industrial Robot Arm?* URL: <https://insights.globalspec.com/article/4788/what-is-the-real-cost-of-an-industrial-robot-arm>.
- [73] T.W. Kerslake and L.L. Kohout. "Solar Electric Power System Analyses for Mars Surface Missions". In: (1999).
- [74] A. Kiely and M. Klimesh. *The ICER Progressive Wavelet Image Compressor*. IPN Progress Report. Jet Propulsion Laboratory, Nov. 2003.
- [75] Ki C. Kim. "Analytical Calculations of Helicopter Torque Coefficient (CQ) and Thrust Coefficient (Or) Values for the Helicopter Performance (HELPE) Model". In: *Army Research Laboratory* (1999). <https://apps.dtic.mil/sti/pdfs/ADA>
- [76] Paul Knightly. *Record-Setting Mars Dust Storm was Overdue*. Spaceflight Insider. June 2018. URL: <https://www.spaceflightinsider.com/missions/solar-system/record-setting-mars-dust-storm-was-overdue/>.
- [77] NOAA Chemical Science Laboratory. *How is ozone measured in the atmosphere?* 2006. URL: <https://csl.noaa.gov/assessments/ozone/2006/chapters/Q5.pdf>.
- [78] Sugyu Lee. "Effective Length K-Factors For Flexural Buckling Strengths Of Web Members In Open Web Steel Joists". In: (2013).
- [79] G. Li, L. Yu, and S. Fei. "A Binocular MSCKF-Based Visual Inertial Odometry System Using LK Optical Flow". In: Dec. 2020.
- [80] Lightware. *SF30/D (200m)*. URL: <https://lightwarelidar.com/products/sf-30-d-200-m>.
- [81] *LightWare SF30/D LIDAR Sensor Datasheet*. LightWare Optoelectronics Ltd. 2019.
- [82] C. Lindenburg. "MODELLING OF ROTATIONAL AUGMENTATION BASED ON ENGINEERING CONSIDERATIONS AND MEASUREMENTS". In: (2004). European Wind Energy Conference London 22-25 November 2004. URL: <https://publicaties.ecn.nl/PdfFetch.aspx?nr=ECN-RX--04-131>.
- [83] Sarah Loff and Rocky Lind. *NASA's Space Exploration Vehicle (SEV)*. NASA. Aug. 2012. URL: https://www.nasa.gov/exploration/technology/space_exploration_vehicle/index.html.
- [84] Compact Instruments Ltd. *MiniVLS 111 Speed Sensor Threaded Housing (Specifications)*. URL: <https://compactinstruments.co.uk/product/minivls-111-speed-sensor-threaded-housing-5vdc/>.
- [85] MB Madsen. "Magnetic Properties Experiments on the Mars Exploration Rover mission". In: *Journal of Geophysical research planets* 108 (December 2003).
- [86] David A. Maluf and Yuri O. Gawdiak. *ON SPACE EXPLORATION AND HUMAN ERROR*. NASA. URL: http://infolab.stanford.edu/~maluf/papers/hicss_ieee05.pdf.
- [87] *Mars Fact Sheet*. URL: <https://nssdc.gsfc.nasa.gov/planetary/factsheet/marsfact.html>.
- [88] *MARTIAN ATMOSPHERE*. URL: <http://www.braeunig.us/space/atmmars.htm>.
- [89] Lyndsey McMillon-Brown et al. "Dust Abrasion Damage on Martian Solar Arrays: Experimental Investigation and Opportunity Rover Performance Analysis". In: *2019 IEEE 46th Photovoltaic Specialists Conference (PVSC)*. 2019, pp. 2838–2844. DOI: 10.1109/PVSC40753.2019.8980876.
- [90] MEPAG. *10. Mars Radiation Environment*. URL: <https://mepag.jpl.nasa.gov/topten.cfm?topten=>

- 10.
- [91] Kathryn Mersmann. *The Fact and Fiction of Martian Dust Storms*. [Online; accessed 29-April-2021]. 2015. URL: <https://www.nasa.gov/feature/goddard/the-fact-and-fiction-of-martian-dust-storms>.
- [92] Minco. *SmartHeat SLT Heaters*. URL: https://www.minco.com/catalog/?catalogpage=product&cid=3_7-smartheat-heaters&id=HL6500.
- [93] Yacoubi Moaad. "Design and optimization of a ducted fan VTOL MAV controlled by Electric Ducted Fans". In: *EUROPEAN CONFERENCE FOR AERONAUTICS AND AEROSPACE SCIENCES* (2019). <https://www.eucass.eu/doi/10108.pdf>.
- [94] Luca Montabone and François Forget. "Forecasting Dust Storms on Mars: A Short Review". In: (2017).
- [95] B. Montgomerrie. "Methods for Root Effects, Tip Effects and Extending the Angle of Attack Range to 180 degrees, with Application to Aerodynamics for Blades on Wind Turbines and Propellers". In: (2004). URL: <https://www.foi.se/rest-api/report/FOI-R--1305--SE>.
- [96] Morgan McFall-Johnsen. *A scientist's simple animation shows why there won't be a way to communicate with astronauts on Mars in real time*. 2020. URL: <https://www.businessinsider.com/animation-explains-mars-communication-delay-nasa-astronauts-2020-9?international=true&r=US&IR=T> (visited on 06/18/2021).
- [97] Morgan Stanley. *Space: Investing in the final frontier*. URL: <https://www.morganstanley.com/ideas/investing-in-space>.
- [98] N. Shama Rao, T.G.A. Simha, K.P. Rao, G.V.V. Ravi Kumar. "Carbon Composites Are Becoming Competitive And Cost Effective". In: (2018).
- [99] et al N.C. Rogers. *A Generic Model of 1-60 GHz Radio Propagation through Vegetation - Final Report*. Final Report. Qinetiq, May 2002.
- [100] NASA. *Cost*. URL: https://www.nasa.gov/pdf/140643main_ESAS_12.pdf.
- [101] NASA. *Mars Perseverance Rover: Communications*. 2021. URL: <https://mars.nasa.gov/mars2020/spacecraft/rover/communications/> (visited on 05/07/2021).
- [102] NASA. *MEDA (The Mars Environmental Dynamics Analyzer)*. URL: <https://mars.nasa.gov/mars2020/spacecraft/instruments/meda/>.
- [103] NASA. *NASA's Perseverance Rover Sample Tubes*. URL: <http://spaceref.com/mars/nasas-perseverance-rover-sample-tubes.html>.
- [104] NASA. *Pitot-Static Tube (Prandtl Tube)*. URL: <https://www.grc.nasa.gov/www/k-12/airplane/pitot.html>.
- [105] NASA. *State-of-the-Art - Power Generation*. 2021. URL: <https://www.nasa.gov/smallsat-institute/sst-soa-2020/power> (visited on 06/07/2021).
- [106] Michael Chun-Yung Niu. *Composite Airframe Structures*. Third Edition.
- [107] André Noth. "Design of Solar Powered Airplanes for Continuous Flight". In: *ETH Zürich* (2008).
- [108] OECD. *The Space Economy at a Glance 2011*. Paris: OECD Publishing, 2011.
- [109] Avi B. Okon. "Mars Science Laboratory Drill". In: *40th Aerospace Mechanisms Symposium* (2017).
- [110] MIT OpenCourseWare. "Lecture 11: Buckling of Plates and Sections". In: (2013).
- [111] Optics.org. *BAE Systems develops laser airspeed sensor for aircraft*. July 2016. URL: <https://optics.org/news/7/7/20>.
- [112] P.Sidiropoulos. "On the status of orbital high-resolution repeat imaging of Mars for the observation of dynamic surface processes". In: *Planetary and Space Science* 117.2 (2015), pp. 207–222.
- [113] performanceanddrag. "Simple Performance Estimation". In: *AA241X* (2009).
- [114] E.V. Petrova et al. "Optical depth of the Martian atmosphere and surface albedo from high-resolution orbiter images". In: *Planetary and Space Science* 60.1 (2012), pp. 287–296. ISSN: 0032-0633. DOI: <https://doi.org/10.1016/j.pss.2011.09.008>. URL: <https://www.sciencedirect.com/science/article/pii/S0032063311002960>.
- [115] Z. R. Putnam, R. D. Braun, and R. R. Rohrschneider. "Entry System Options for Human Return from the Moon and Mars". In: (2007).
- [116] Mir Mustafizur Rahman. "A workflow to minimize shadows in UAV-based orthomosaics". In: *Journal of Unmanned Vehicle Systems* (2019).
- [117] Manikandan Ramasamy. "Measurements comparing hover performance of single, Coaxial, Tandem, and tilt-rotor configurations". In: 4 (Jan. 2013), pp. 2439–2461.
- [118] Z. Ramlakhan. *Feasibility study of fog detection and visibility estimation using camera images*. Internal Report. Royal Netherlands Meteorological Institute (KNMI), May 2015.
- [119] Research and Markets. *Space Equipment - Global Market Trajectory Analytics*. URL: <https://www.prnewswire.com/news-releases/global-space-equipment-market-report-2020-2027-growing-pressure-to-reduce-design-manufacturing-costs-and-lead-times-encourages-supply-chain-transformation-301234772.html>.
- [120] Bryelle Reyes. *Thermal Control Handbook*. Second Edition.
- [121] E. Rieger et al. "A 154-day periodicity in the occurrence of hard solar flares?" In: *Nature* (July 1984).
- [122] J.A. Rodriguez-Manfredi, M. de la Torre Juárez, and A. Alonso. "The Mars Environmental Dynamics Analyzer, MEDA. A Suite of Environmental Sensors for the Mars 2020 Mission." In: *Space Sci Rev* 217.48

- (2021).
- [123] Sukanta Roy et al. "Design of an Offshore Three-Bladed Vertical Axis Wind Turbine for Wind Tunnel Experiments". In: June 2017, V010T09A046. DOI: 10.1115/OMAE2017-61512.
- [124] RunCam. *RunCam 5 Orange*. 2020. URL: <https://shop.runcam.com/runcam-5-orange/> (visited on 05/22/2021).
- [125] Runcam. *RunCam 5 Orange 12MP 4*. URL: https://www.banggood.com/nl/RunCam-5-Orange-12MP-4-3-145FOV-56g-Ultra-light-4K-HD-FPV-Camera-for-RC-Drone-p-1623803.html?utm_source=googleshopping&utm_medium=cpc_organic&gmcCountry=NL&utm_content=minha&utm_campaign=minha-nl-nl-pc¤cy=EUR&cur_warehouse=CN&createTmp=1&utm_source=googleshopping&utm_medium=cpc_bgs&utm_content=sandra&utm_campaign=sandra-SSC-NL-0519-sku-7ysale&ad_id=522431266522&gclid=CjwKCAjwn6GGBhADEiwAruUcK0z4mJ-5Rx-3U9NVTcaDwn1zKq0KmYcZ6RqE6oSACMmjD90_HS5bxoCm2EQAvD_BwE.
- [126] M. K. Rwigema. "PROPELLER BLADE ELEMENT MOMENTUM THEORY WITH VORTEX WAKE DEFLECTION". In: 2010.
- [127] Saft. *MP & VL Batteries for launchers*. 2021. URL: <https://www.saftbatteries.com/products-solutions/products/mp-vl-batteries-launchers?text=&tech=76&market=331&brand=&sort=newest&submit=Search> (visited on 05/10/2021).
- [128] Saft. *Saft's primary lithium battery earns CNES congratulations for powering ESA/CNES' Philae Lander on its historic comet touchdown*. URL: <https://www.saftbatteries.com/media-resources/press-releases/saft%5C%E2%5C%80%5C%99s-primary-lithium-battery-earns-cnes-congratulations-powering> (visited on 11/20/2020).
- [129] Salvatore Cutrona. *Thermostat Costs*. URL: <https://www.homeadvisor.com/cost/heating-and-cooling/install-a-thermostat/>.
- [130] Sandra Erwin. *SpaceX's GPS contract modified to allow reuse of Falcon 9 boosters*. URL: <https://space.news.com/spacexs-contract-to-launch-gps-satellites-modified-to-allow-reuse-of-falcon-9-boosters/>.
- [131] T.M. Schmidt et al. "Thermal Design of a Mars Helicopter Technology Demonstration Concept". In: *48th International Conference on Environmental Systems* (2018).
- [132] Bosch Sensortec. *BMI088 Data Sheet: 6-Axis Motion Tracking for High-performance Applications*. Nov. 2020. URL: <https://www.bosch-sensortec.com/media/boschsensortec/downloads/datasheets/bst-bmi088-ds001.pdf>.
- [133] *SF Radiation*. URL: https://www.nasa.gov/sites/default/files/atoms/files/space_radiation_ebook.pdf.
- [134] Spectrolab. *XTE-LILT (Low Intensity Low Temperature)*. URL: https://www.spectrolab.com/photovoltaics/XTE-LILT%5C%20Data%5C%20Sheet%5C%20_12.23.19.pdf.
- [135] SPECTROLAB A Boeing Company. *XTE-LILT (Low Intensity Low Temperature) Space Qualified Triple Junction Solar Cell*. 2021. URL: https://www.spectrolab.com/photovoltaics/XTE-LILT%20Data%20Sheet%20_12.23.19.pdf (visited on 06/07/2021).
- [136] Rob Spurrett. *The Future of Lithium-ion Space Batteries: A Supplier's Perspective*. [Online; accessed 21-June-2021]. 2008. URL: https://www.nasa.gov/sites/default/files/atoms/files/01_future_of_lithium-ion_batteries_rspurrett.pdf.
- [137] P.M. Stella et al. "PV technology for low intensity, low temperature (LILT) applications". In: (1994).
- [138] Steven Gordon. *Talking to Martians: Communications with Mars Curiosity Rover*. 2021. URL: <https://sandilands.info/sgordon/communications-with-mars-curiosity#:~:text=The%5C%20UHF%5C%20transceiver%5C%20has%5C%20a,needs%5C%20to%5C%20receive%5C%20stronger%5C%20signals.> (visited on 05/07/2021).
- [139] ESA ESTEC Team. *MarsFAST: Assessment of an ESA Fast Mobility Mars Rover*. Tech. rep. ESA.
- [140] Tec-Science. *Calculation of the Nusselt numbers for forced flows over plates and in pipes - tec-science*. Apr. 2021. URL: <https://www.tec-science.com/thermodynamics/heat/calculation-of-the-nusselt-numbers-for-forced-flows-over-plates-and-in-pipes>.
- [141] Texas Instruments. *LM76005-Q1*. 2021. URL: <https://www.ti.com/product/LM76005-Q1#order-quality> (visited on 06/21/2021).
- [142] Texas Instruments. *LM76005-Q1*. URL: <https://www.ti.com/product/LM76005-Q1#order-quality>.
- [143] Texas Instruments. *TLVM13630*. 2021. URL: <https://www.ti.com/product/TLVM13630> (visited on 06/21/2021).
- [144] Texas Instruments. *TPS57140-Q1*. 2021. URL: <https://www.ti.com/product/TPS57140-Q1> (visited on 06/21/2021).
- [145] Texas Instruments. *TPSM63603*. 2021. URL: <https://www.ti.com/product/TPSM63603> (visited on 06/21/2021).
- [146] The Planetary Society. *Planetary Science Budget Dataset*. URL: https://docs.google.com/spreadsheets/d/12frTU01gfT1CXGWFimN3whf4348F_r3Xo1TqBt020yM/edit#gid=244635107.
- [147] Thermasgard. *RGTF-2 Thermometer*. URL: https://www.sensors.nl/wp-content/uploads/2020/09/RGTF-2__GB-safe.pdf.
- [148] et al Thomas E. Noll. *Investigation of the Helios Prototype Aircraft Mishap*. Jan. 2004. URL: <https://www>.

- nasa.gov/pdf/64317main_helios.pdf.
- [149] Tim McMahon. *Average Annual Inflation Rates by Decade*. URL: <https://inflationdata.com/Inflation/Inflation/DecadeInflation.asp> (visited on 2020).
- [150] S. Tkatchova. *Emerging Space Markets*. Berlin, Germany: Springer, 2018.
- [151] Engineering ToolBox. *Carbon dioxide - Thermal Conductivity*. URL: https://www.engineeringtoolbox.com/carbon-dioxide-thermal-conductivity-temperature-pressure-d_2019.html.
- [152] Engineering ToolBox. *Carbon Dioxide Gas - Specific Heat*. URL: https://www.engineeringtoolbox.com/carbon-dioxide-d_974.html.
- [153] Engineering ToolBox. *Emissivity Coefficients Materials*. URL: https://www.engineeringtoolbox.com/emissivity-coefficients-d_447.html.
- [154] Engineering ToolBox. *Radiation surface absorptivity*. URL: https://www.engineeringtoolbox.com/radiation-surface-absorptivity-d_1805.html.
- [155] Engineering ToolBox. *Thermal Conductivity - selected Materials and Gases*. URL: https://www.engineeringtoolbox.com/thermal-conductivity-d_429.html.
- [156] Arizona State University. *JMars*. 2021. URL: <https://jmars.mars.asu.edu/> (visited on 12/24/2020).
- [157] USRadar. *Ground Penetrating Radar Cost*. URL: <https://usradar.com/ground-penetrating-radar-cost/>.
- [158] I. Varatharajan. "Hellas Planitia: Weather and Geology, Sort Introduction on Hellas". In: ().
- [159] D. Way et al. "EDL Simulation Results for the Mars 2020 Landing Site Safety Assessment". In: (2020).
- [160] James R. Wertz, David F. Everett, and Jeffrey J. Puschell. *Space Mission Engineering: The New SMAD*. Microcosm Press, 2011.
- [161] James R. Wertz and Wiley J. Larson. *Space Mission Analysis and Design*. Third Edition. Kluwer Academic Publishers, 2005.
- [162] David R. Williams. *A Crewed Mission to Mars*. Nov. 2015. URL: <https://nssdc.gsfc.nasa.gov/planetary/mars/marsprof.html>.
- [163] Colin F. Wilson. "Measurement of wind on the surface of Mars". PhD thesis. University of Oxford, 2003.
- [164] World Industrial Automation. *DME5000-115 SICK - Laser sensor*. URL: <https://nl.wiautomation.com/sick/general-automation/sensors/DME5000115>.
- [165] Kris Zacny. "Strategies for Drilling on Mars". In: *Journal of Geophysical research* (2005).
- [166] B.T.C. Zandbergen. *Aerospace Design Systems Engineering Elements I Part: Launch Vehicle design and sizing*. Vol. 06.1. 1. Delft: Delft University of Technology, 2017.
- [167] Miro Zeman. *Photovoltaic Systems*. Delft, The Netherlands: TUDelft.
- [168] J. Zhang et al. "Measurement of Unmanned Aerial Vehicle Attitude Angles Based on a Single Captured Image." In: *Sensors* 18.8 (2018), p. 2655.
- [169] Zhengdong Zhang et al. "Visual-Inertial Odometry on Chip: An Algorithm-and-Hardware Co-design Approach". In: July 2017. DOI: 10.15607/RSS.2017.XIII.028.

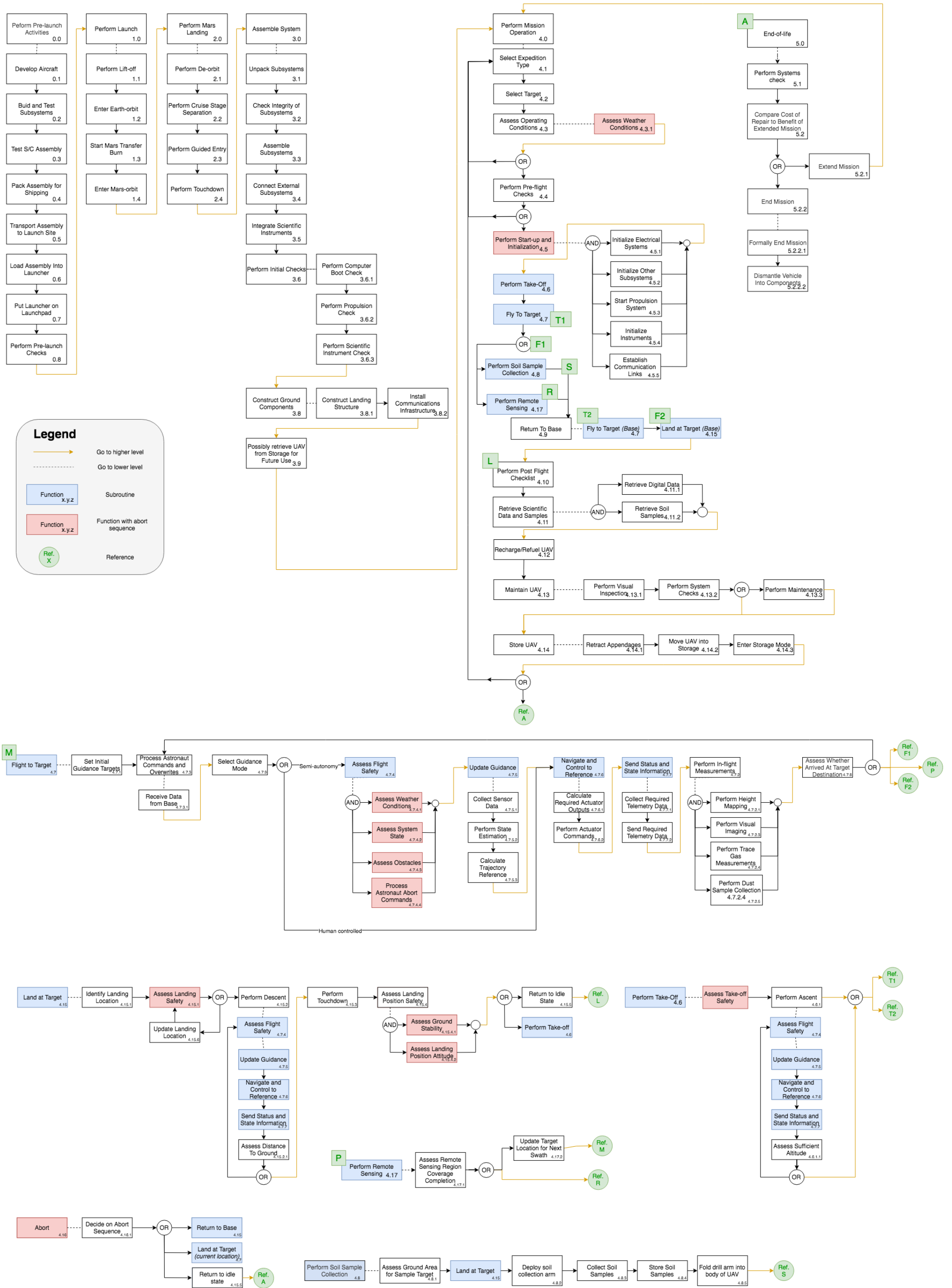


Figure A.3: Functional flow diagram



Figure A.4: Functional breakdown structure

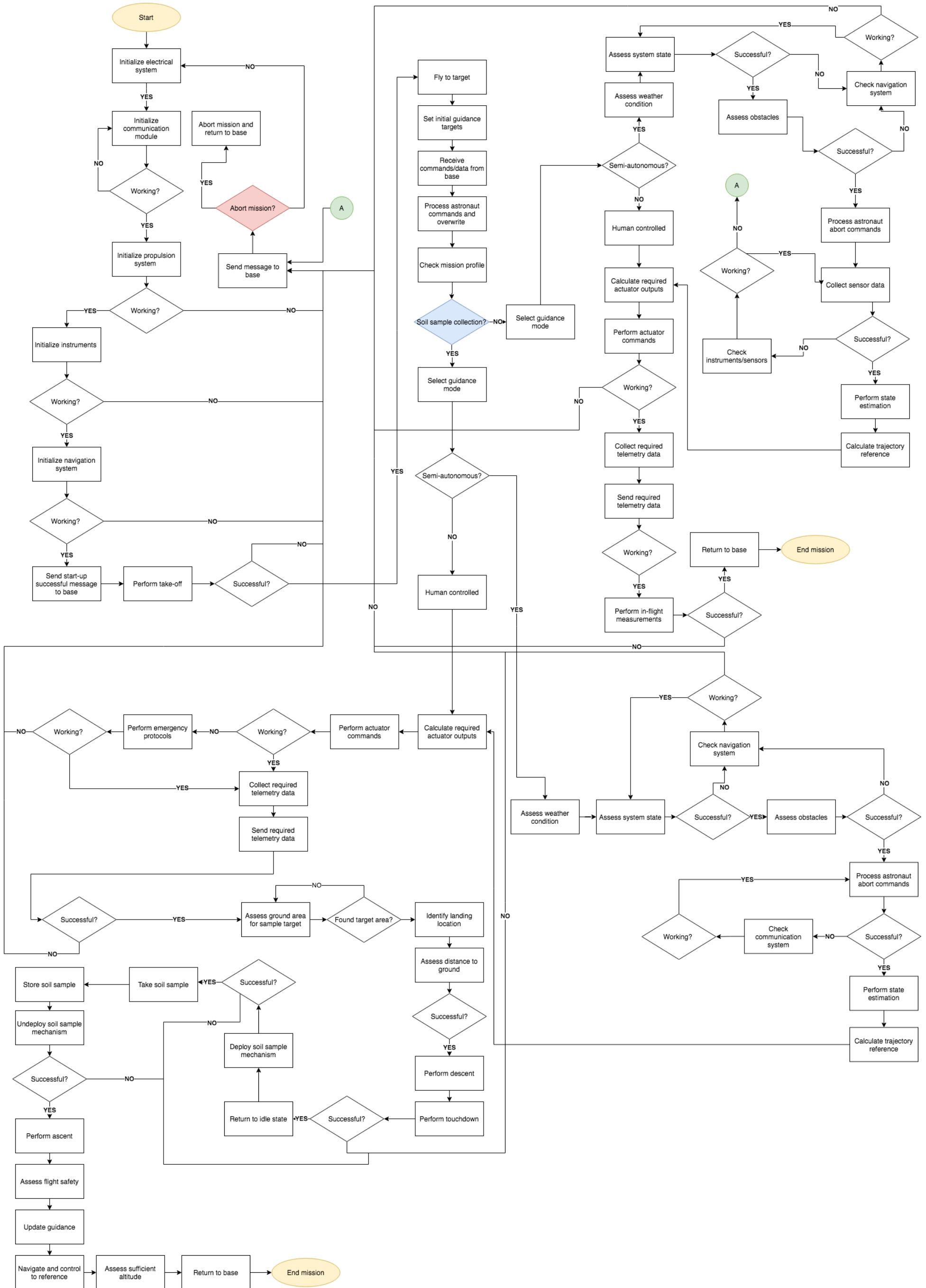


Figure A.5: Flight procedure / software flow diagram